INVESTIGATION OF THE IMPACT OF AZIMUTHAL MAGNETIC FIELD GRADIENT ON PERFORMANCE CHARACTERISTICS AND STABILITY OF HALL EFFECT THRUSTERS

A Dissertation
Presented to
The Academic Faculty

by

Chhavi.

In Partial Fulfillment
of the Requirements for the
Doctorate in Philosophy in the
Daniel Guggenheim School of Aerospace Engineering

Georgia Institute of Technology
AUGUST 2024

INVESTIGATION OF THE IMPACT OF AZIMUTHAL MAGNETIC FIELD GRADIENT ON PERFORMANCE CHARACTERISTICS AND STABILITY OF HALL EFFECT THRUSTERS

Approved by:

Dr. Mitchell L. R. Walker, Advisor
School of Aerospace Engineering
Georgia Institute of Technology

Dr. Lukas Graber
School of Electrical and Computer Engineering
Georgia Institute of Technology

Dr. Wenting Sun
School of Aerospace Engineering
Georgia Institute of Technology

Dr. Sedina Tsikata
School of Aerospace Engineering
Georgia Institute of Technology

Dr. Kunning Xu
Mechanical and Aerospace Engineering
University of Alabama, Huntsville

Date Approved: July 15th, 2024

To my Mom, Dad and Di

.

ACKNOWLEDGEMENTS

This dissertation has been a strenuous, long journey with extreme support, efforts, and sacrifices by the people in my life. As this journey ends, I have gained a lot of valuable experiences and made bonds for a lifetime. Spending the journey far away from home was not only challenging but also pushing boundaries that allowed me to emerge as a strong person. I want to thank my family and friends back home for their patience and understanding throughout these years, and I genuinely appreciate your support for me and my goals.

I want to thank my doctoral committee for providing guidance and resources during my dissertation work. I would like to thank my advisor, Prof. Mitchell Walker, for allowing me the opportunity as an international student to conduct experiments in the field of electric propulsion and for allowing me to get hands-on expertise with Hall thruster operation. Throughout this process, not only did I gain valuable skills and technical knowledge, but I was also able to help in opening new vistas for international students to conduct research in our field. I want to thank Prof. Sedina Tsikata for your patience and willingness to help me understand new diagnostic technology in a short duration of time. Your work in the field of electric propulsion is truly inspiring to women around the world. Through your guidance, I better understood and clarified my research ideas. I would also like to thank Prof. Lukas Graber for discussing the mechanical challenges of building a moving diagnostic and lending us the spectrometer that allowed me to conduct my research work.

I cannot imagine surviving this journey without the help of my amazing and most supportive HPEPL labmates. Firstly, I would like to thank the older generation, David and

JL, for showing me how it is done. David “Sensei,” you have been my mentor, my brother, and my friend throughout this grad school life. I still remember the first day I came to the lab and how you ensured that I felt as a part of the community. From day one to now, your research expertise and depth of knowledge are something that I look up to you for. Our long technical discussions and fun times around the lab are genuinely close to my heart. I would still be bothering you and asking for advice. JL, a doc, from our days of spending hours studying for quals to now, I salute your discipline, focus, and soft heart (that not many people know); it has helped me tackle this process better.

The next round goes to my current colleagues at HPEPL. You all have played a crucial role in completing my research work, and it would not have been possible without you. Muhannad, my twin, you have been my ride-or-die throughout these last few years. From texting you at 3 AM to contacting and panicking during experiments, you have provided me with invariable support to complete my experiments. With your wide area of technical expertise, be it running thrusters, fixing the cathodes, or doing groundbreaking Terahertz research (that is far beyond my understanding), I cannot wait to see your excellent work in revolutionizing the field. Janice, the K-pop veteran, firstly thanks for being the only introvert, so I wasn’t left alone. Words fail me to thank you for all your support, from our long talks at H-Mart to teaching me how to run VTF2 has been a constant support. Your determination and hard work will take you to places, and I can’t wait to be on the sidelines cheering you on. William, our 24-hour day testing and losing our minds together is exactly how I imagined my first testing. While working with you, not only did your depth of knowledge amaze me, but your always-helping attitude was something that I admired a lot. I am excited to see your fantastic work in using molecular propellants.

Aregi, thank you for caring for me and ensuring I got outside my house. Your care and warmth provide the comfortable environment that is much needed in this lab. Naia, the cathode queen, your pure heart, extreme positivity, and badass cathode skills allowed me to finish my work amidst all the chaos. Jacob, the Labview guru, I appreciate your outstanding Labview skills, without which I would not have been able to do any diagnostic measurements; good luck with quals and see you on the other side soon. Julian, thank you for helping me with my experiment without even a slight hesitation. Your long night shifts were the only reason I could get my data on time, and I owe you for that. Adrian, I knew you were the guy when I needed to get something done. Building that new probe arm in a matter of days proves what you're capable of, and I cannot wait to see your fantastic work in breaking down the breathing mode instabilities. Jeff, I can't thank you enough for pulling through with the OES; it facilitated one less thing to worry about during experiments. I wish you good luck in your future endeavors. Ebise and Max, I appreciate your help during the diagnostics build process. Dongho, I really appreciate you sharing your OES knowledge and expertise, which helped me understand the scope of the diagnostic. Dan, thank you for making sure I met my deadlines for this work and accommodating me in the testing schedule. Lastly, I thank Scott, Greg, and Greg at Machine Shop for making me meet the most unrealistic deadline for machining the probe.

My friends, Khushboo, I really appreciate you motivating me and keeping me in check whenever the pressure gets to me. Preyansh, I cannot thank you enough for ensuring I was well-fed and didn't lose my mind while navigating this journey. Shubham, your support over the past six years has helped me and allowed me to have someone who will always have my back. Just keep pushing through; I can already see the light at the end of

the tunnel. I can't wait to take the graduation walk with you. Manasvini, you have been the best person I could ask to be my roommate during this PhD. You listen to my hour-long rants with utmost attention and patience, allowing me to be calm and collected daily. I would have lost my mind if you had not been there to keep me in check. Devanshi and Saurabh, thank you for providing me with constant motivation and setting up travel goals to achieve after grad school.

Finally, I would like to thank my family for all their support in achieving my goals. Mom and Dad, since childhood, you never stopped me from pursuing my dreams and goals. Your unwavering support and belief in me allowed me to reach my potential and complete this journey of grad school. Your constant motivation and guidance were a continuous compass that gave me the right direction to solve any problem. These last few months have been tough, and the completion of my work would not have been possible without your understanding, patience, and extreme positivity. My sister, you have always been my role model and provided me with a direction and mirror of what I can achieve. I aspire to be half as good as you one day. My grandma, I appreciate you constantly pushing us to reach our full potential. I love you guys, and this Ph.D is for you.

TABLE OF CONTENTS

LIST OF TABLES

LIST OF FIGURES

NOMENCLATURE

η_T	thrust efficiency
m_i	ion mass, kg
I_a	acceleration current, A
η_u	propellant utilization efficiency, %
η_a	acceleration efficiency, %
η_E	beam energy efficiency, %
V_m	average beam-ion energy, eV
β	coefficient of ion production
a	ion loss fraction
$\sigma_i(v_e)$	atom ionization cross section, m^2
n_a	atom number density, m^{-3}
N_a	atom flow rate density, $m^{-3}s^{-1}$
V_{az}	z component of the mean value of atom velocity, m s^{-1}
$\dot{m}_A$	total mass flow rate through the accelerating channel, s^{-1}
K_λ	numerical factor
L_a	length of accelerating channel, m
V_d	discharge voltage, V
V_a	accelerating voltage, V
V_p	Plasma potential, V
$\triangle V$	voltage loss parameter, V
η	anode efficiency
T	thrust, mN
v_e	average electron velocity, m s^{-1}
I_d	discharge current, A
i	electron loss parameter
P_d	discharge power, W
m_p	mass of propellant atom, kg
e	electron charge, C
η_b	current utilization efficiency,%
I_b	ion beam current, A
n_i	ion number density, m^{-3}

v_i	average ion velocity, m s^{-1}
A	cross-sectional area of the discharge chamber, m^2
n_e	electron number density, m^{-3}
η_m	mass utilization efficiency
$\dot{m}_b$	ion beam mass flow rate, mg s^{-1}
$\dot{m}_a$	anode mass flow rate, mg s^{-1}
$\dot{m}_c$	cathode mass flow rate, mg s^{-1}
η_v	voltage utilization efficiency
I_{s_p}	specific impulse, s
g	acceleration due to gravity, m s^{-2}
τ	measurement time, s
$\bar{I}_d$	average oscillation discharge current, A
$\triangle$	oscillation amplitude
v_{e_z}	axial electron velocity, m s^{-1}
ϑ_e	electron collision frequency, s^{-1}
m_e	mass of electron, kg
E_z	axial component of the electric field, V m^{-1}
j_{ex}	azimuthal electron current density, A m^{-2}
B_r	radial component of the magnetic field, T
P_e	electron pressure, Pa
j_{e_z}	axial electron current density, A m^{-2}
Ω_e	electron Hall parameter
μ_{eff}	effective mobility
μ_{ez}	axial effective mobility
μ_{ex}	azimuthal effective mobility
T_e	electron temperature, eV
ϑ_{eff}	effective electron collision frequency, s^{-1}
B	magnitude of the magnetic field, G
ω_c	cyclotron frequency, s^{-1}
ϕ	plasma potential, V
c	speed of light, m s^{-1}
ϑ_1	frequency of elastic collision, s^{-1}
ϑ_2	frequency of inelastic collision, s^{-1}
ϑ_i	ionization collision frequency, s^{-1}
b_c	accelerating channel width, m
q_i	propellant ion charge, C

σ_{d_i}	atom ionization collision cross-section, m^2
I_e	electron current, A
B_l	maximum local magnetic field in the azimuthal gradient region, G
$\nabla_\theta B_r$	azimuthal magnetic field gradient, G/°
m_{prop}	propellant mass, kg
m_f	final propellant mass, kg
v_b	ion beam velocity, m s^{-1}
RMS	root mean square of discharge current, A
$v_\perp$	velocity of electron perpendicular to magnetic field lines, m s^{-1}
r_L	Larmor radius, mm
k	Boltzmann constant, J/K
θ_{div}	half-divergence angle, °

SUMMARY

Hall effect thrusters (HETs) are intended to function with a uniform axisymmetric magnetic field. Imperfections in the manufacturing process and electrical shorts that occur during operation might lead to the formation of non-uniformities in the channel. Azimuthal magnetic field gradients are one type of non-uniformity that can arise in the magnetic field. As a result, it is imperative to comprehend the impact of the non-uniform azimuthal magnetic field gradient on the thruster's performance. This thesis aims to quantify the alteration in thruster performance parameters, including efficiency, stability, and thrust, as a result of introducing an azimuthal magnetic field gradient. In order to achieve this, the thruster is modified to enable independent control of the outer magnetic circuit, which in turn allows the current to be adjusted. A three-dimensional sweep probe instrument was constructed to show how the azimuthal magnetic field gradient affects the thrust vector direction. The research results indicate that the azimuthal magnetic field gradient has the most significant impact on the thruster's stability, leading to increased instability during operation. The thrust and efficiency decrease as the gradient increases, with the thrust experiencing the most negligible impact. The introduction of the gradient is indicative of the thrust vector's deviation from the centerline, which leads to a three-dimensional shift in the thrust vector's position. The research offers a physics-based model to explain the observed trends in thruster performance that result from changes in the plasma parameters.

CHAPTER 1 INTRODUCTION

This chapter aims to provide the reader with an overview of electric propulsion (EP) and why it is an active choice for space propulsion. The chapter will provide the reader with knowledge about different kinds of EP systems. Subsequently, an overview of HET operating principles is presented with an elaboration of phenomena affecting the performance of HET. It highlights the crucial role of the magnetic field in HET operation through the review of magnetic field variations in HETs. The goal of this chapter is to provide a brief overview of the impact of magnetic fields on HET performance and emphasize the importance of exploring their effects on HET operation. The chapter progresses toward the motivation required to do the current research and establish the research objectives for the study.

1.1 Electric Propulsion Overview

Space propulsion has been an area of wide interest for a prolonged period. The industry started exploring different kinds of propulsion techniques since the early 1600's[1]. The propulsion techniques varied in terms of fuels and power, dictating how energy is utilized for thrust generated using the respective propulsion system[2,3]. Chemical rockets are primarily used for propelling objects outside the Earth's atmosphere[4]. The propulsion systems are designed to provide the desired specific impulse and thrust as per the mission requirements. The amount of propellant required to conduct specific measurements is given by Equation 1.

$$m_{prop} = m_f[\exp\left(\frac{\Delta v}{g\ I_{sp}}\right) - 1] \quad (1)$$

The equation demonstrates the inverse relationship between mass requirement and impulse associated with mission requirement. The space mission strives towards the objective of achieving the highest impulse. The traditional space propulsion system, being chemical, relies on the energy stored in the chemical bonds to get converted during the combustion/ignition process to produce thrust. Based upon the state of the fuel utilized, the chemical propulsion system was categorized as solid, liquid, and hybrid propellant system[5–7]. Figure 1 provides the performance of various propulsion systems. Irrespective of the propellant kind, due to the chemical propulsion system relying on chemical bond energy, these propulsion means are limited in the amount of impulse that can be achieved. In such scenarios, the utilization of external sources of energy comes into play for the various space missions. EP systems utilize electrical energy to ionize and accelerate propellant particles to produce a plasma plume, enabling thrust production. EP's ability to use external power sources allows it to produce high specific impulse, making it the ideal candidate for space missions[8].

EP devices have been continuously used for various space missions[9,10] and continue to be highly in demand for commercial satellite missions[11]. EP comprises of three types of devices: *i.e.*, electrostatic, electrothermal, and electromagnetic[12,13]. Electrothermal devices use heating elements such as a resistor or arc to ionize the propellant particles and accelerate them through a nozzle to produce thrust. Examples of such devices are arcjet and resistojet. [12,14,15]. The electromagnetic propulsion system uses the

Lorentz force to accelerate ionized propellant particles using electric and magnetic fields. Examples of electromagnetic propulsion devices are pulsed plasma thrusters (PPT) and Magnetoplasmadynamic thrusters (MPDTs)[12,16,17]. Lastly, electrostatic EP devices use Coulomb force to accelerate the charged particles using electromagnetic fields, examples being Hall effect thrusters (HET) and gridded ion thrusters (GIT) [12,18,19]. When comparing all EP systems, HET has been widely used for space missions due to its simplistic designs and high impulse with high efficiency. To aid the development of high-performing HET, it is crucial to understand the operating principles of these electrostatic devices.

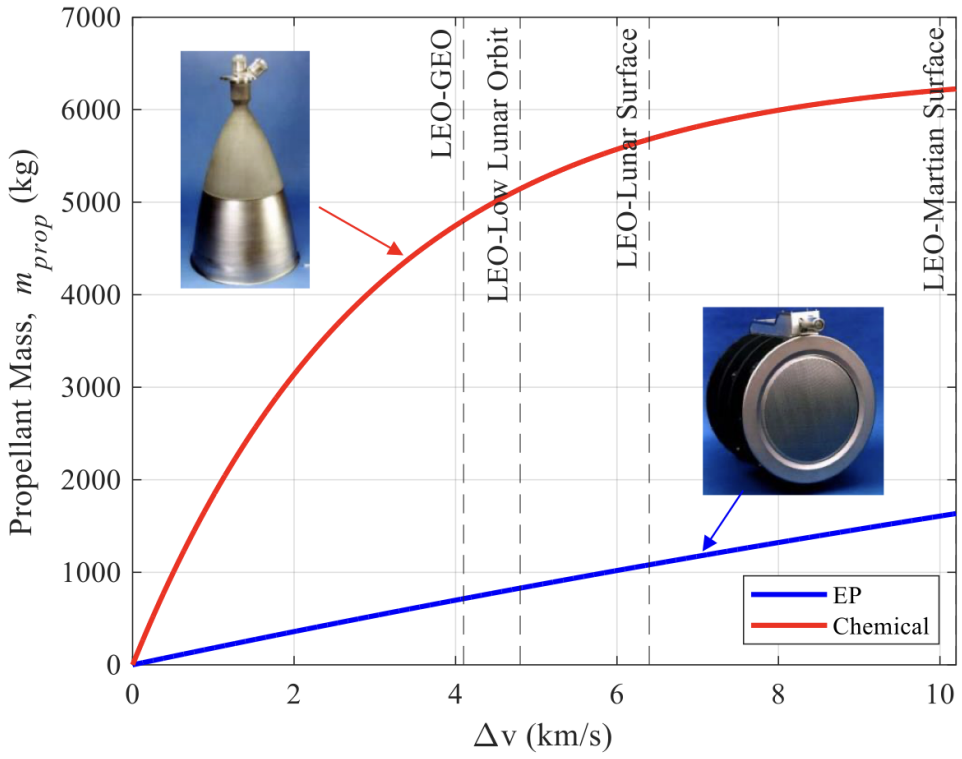

Figure 1 – Propellant mass requirement for different propulsion systems [20]

1.2 Hall Effect Thruster Overview

1.2.1 Operating Principles

The 1960s categorizes the beginning of the HET era in the United States, with EP development taking place in the early-mid 1900s in the Soviet Union [21]. The HET propulsion mechanism is deemed electrostatic because it relies on an electric field to accelerate ions. High specific impulse, viable thrust-to-power ratio, simple annular structure, and high efficiency (~75%) result in the extensive use of this propulsion technology for LEO satellite maneuvers and commercial use[22]. Understanding the operating principle and science behind HETs is now crucial because of their continuous commercial usage and demand.

HETs are electrostatic devices that provide thrust by the acceleration of ionized particles utilizing an electric field. HET propulsion system mainly consists of an anode, cathode, magnetic circuit, and ceramic discharge channel, as shown in Figure 2. Propellant is supplied through the anode, which consists of slotted plates with openings through which the propellant flows to the discharge channel. The anode is maintained at a positive potential utilizing an external power supply. The cathode is an essential component of the system. It can be externally mounted [23] and centrally mounted [24], as shown in Figure 3. The cathode is maintained at a negative potential and supplies electrons necessary for the ionization of the propellant gas as well as to maintain the plume's quasi-neutrality. The HET discharge channel is made of ceramic due to its electrically insulating nature, high thermal conductivity, and thermal shock resistance. The ceramic channel helps reduce wall emission and anode power loading effects observed in the case of TAL thrusters [25].

Lastly, the magnetic circuit present in the HET consists of either a configuration of permanent magnets or inner and outer coils. The magnetic circuit provides the magnetic field requirement for the confinement of electrons for stable operating conditions. The electric field is produced using an external power supply to maintain the potential difference between the cathode and the anode.

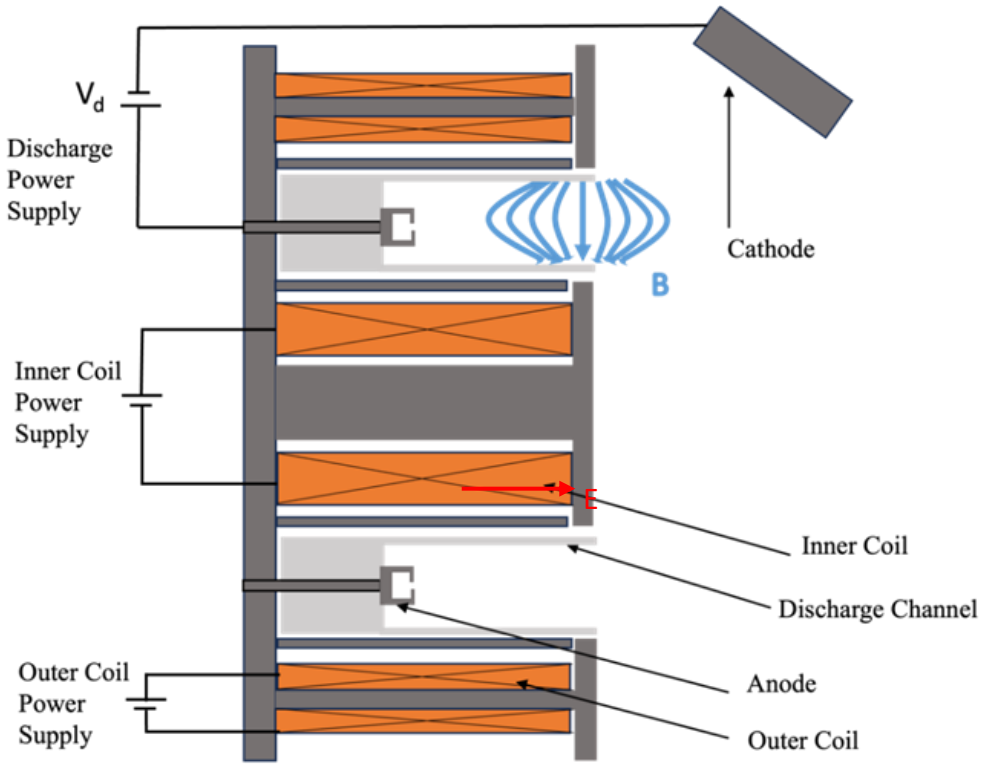

Figure 2 – Schematic representation of HET components [26]

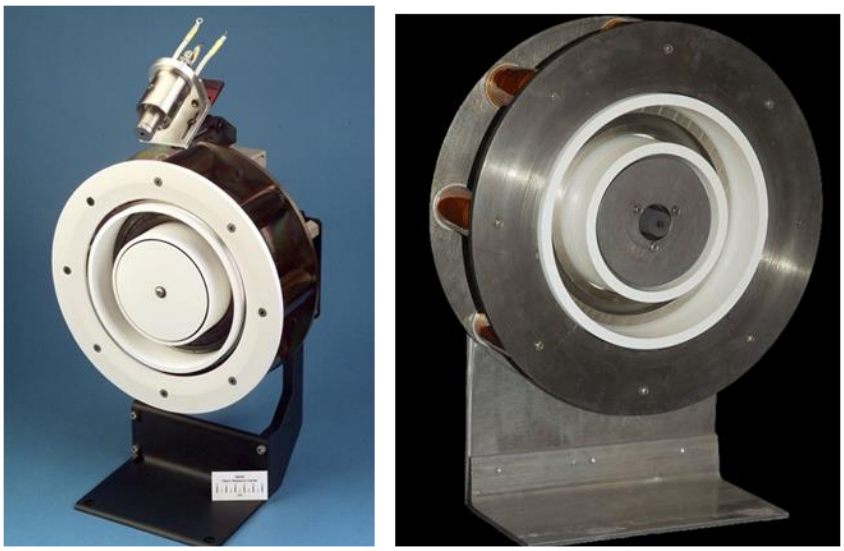

Figure 3 – Externally mounted cathode on NASA 173mV1 [23] (left) and centrally mounted cathode on H6[24] (right)

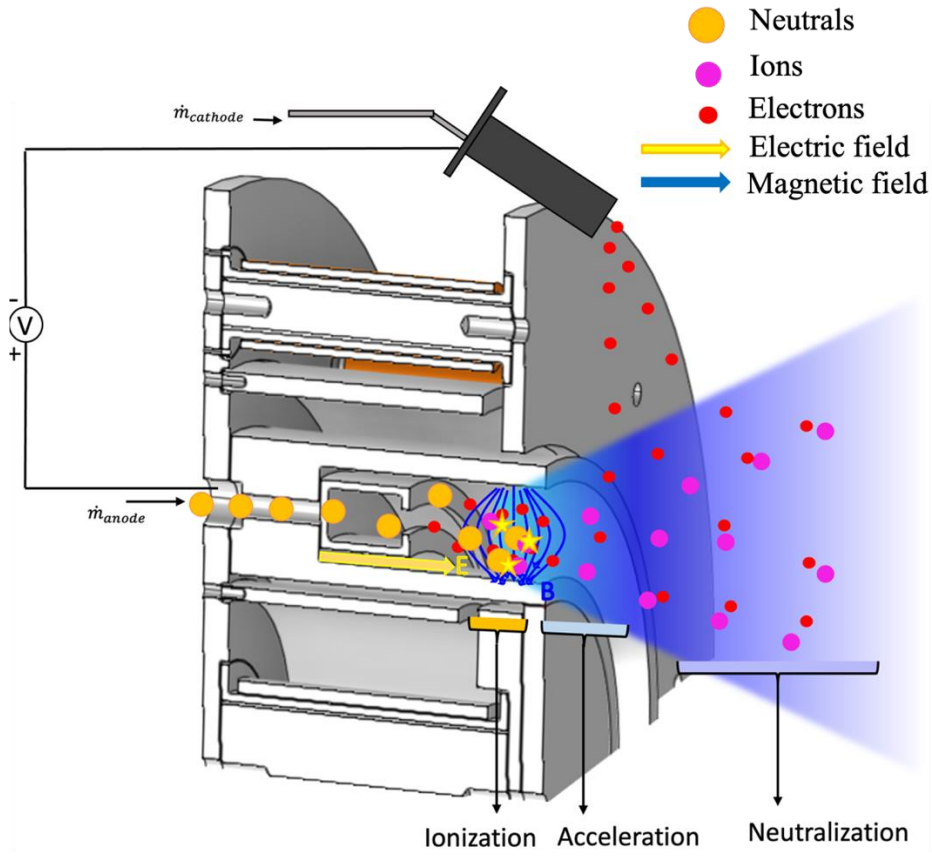

Figure 4 – Cross-sectional view of ionization, acceleration, and neutralization process in HET.

HET receives its name from the Hall current. The Hall current is created when an electric field perpendicular to an applied magnetic field permeates the gases after ionization due to the guiding center's well-known E×B drift [27]. The radial magnetic field generated by the magnetic circuit and the axial electric field result in the azimuthal drift of the magnetically confined electrons. These electrons collide with the gas atoms, ionizing the gas, resulting in counter-streaming electron and ion currents. The ions accelerate by the potential difference due to the electric field, resulting in the thrust, and are neutralized in the plume by the neutralizing electrons supplied by the cathode. This neutralization results in a quasineutral plasma that reduces the near surfaces' electrification. The process involved in HET operation is mainly categorized into three parts: 1) neutral particle ionization, 2) ion acceleration, and 3) plume neutralization, as visualized in Figure 4. These processes are detailed to give the reader a better understanding of the plasma plume production processes in the thruster.

1.2.2 *Ionization*

The cathode supplies electrons through thermionic emission, which possesses distributions of thermal kinetic energy as they exit the cathode. The electrons are guided towards the anode by the electric field established in the discharge channel by the potential difference between the cathode and anode, also known as the discharge voltage. The magnetic field confines the electrons as they move across the channel, resulting in a close drift motion of electrons. The electric and magnetic field results in the development of the Lorenz force, which facilitates the drifting of the guiding center of the electrons azimuthally in the E×B direction. Electron transportation towards the anode causes an increase in the energy distribution possessed by the electrons. During the electron motion,

interaction with neutral atoms results in inelastic collisions. Collisions of electrons possessing energy greater than or equal to the ionization potential of the propellant result in the ionization of the neutral atoms. Ionization collisions result in the production of an ion and low-energy electron. The electrons drift towards the anode after collisions and close the circuit by arriving at the anode. Ionization is impacted by various aspects such as the type of propellant, magnetic field, electric field, and the electron number density distribution [28].

Ionization occurs near the maximum magnetic field region, as seen in Figure 4. The region's location can be varied by changes in the magnetic field, thus affecting HET operation.

1.2.3 Acceleration

After the ionization process, the electrons transverse toward the anode while the ions get accelerated downstream toward the exit plane by the electric field established in the system. The number density distribution of electrons varies axially in the axial direction and peaks where the local magnetic field strength is maximum near the thruster exit plane. The localized potential difference is due to a change in the number density distribution of the electrons, hence accelerating ions in the direction of the exit plane. The ions, due to their large mass, possess a higher Larmor radius than the thruster dimensions, and hence, the motion of ions is unaffected by the magnetic field.

The acceleration of the ions depends on the amount of discharge voltage utilized by the ions for acceleration. Thus, the acceleration voltage (10-15% of V_d) influences the thruster's impulse, thrust, and voltage utilization efficiency. Acceleration and ionization

processes are intertwined and cannot be distinguished as having clear boundaries during standard HET operation.

1.2.4 Neutralization

The accelerated ions exiting the thruster form a positive ion beam cloud. Neutralization becomes essential to avoid charge accumulation on the thruster and spacecraft and to maintain the plasma plume's quasi-neutrality. The recombination process of the ions and electrons takes place in the plasma plume, maintaining a charge-neutral environment during operation. Electrons are supplied by the cathode to the plume for neutralization.

The brief overview of the three major processes occurring in the HET provides information regarding the various operating and plasma parameters that influence the HET performance. These parameters have been evaluated and investigated extensively to establish a direct relationship between the plasma parameters and the HET performance [28,29]. The magnetic field impacts the electron motion and distribution across the discharge channel, making it one of the most crucial and complex parameters influencing thruster performance. Hence, it is essential to analyze the magnetic field's effect on HET operation.

1.3 Motivation

The magnetic field’s crucial role in stable HET operation drives the research toward understanding various magnetic field effects significantly impacting HET performance. Magnetic fields are generated using either permanent magnets or an inner coil and outer

coils in concentric or non-concentric configurations. The magnetic field is axisymmetric for a conventional HET to establish uniform plasma generation. Magnetic field topology in the axial direction consists of concavity of magnetic field lines axial in both directions from the thruster exit plane, as seen in Figure 5a).

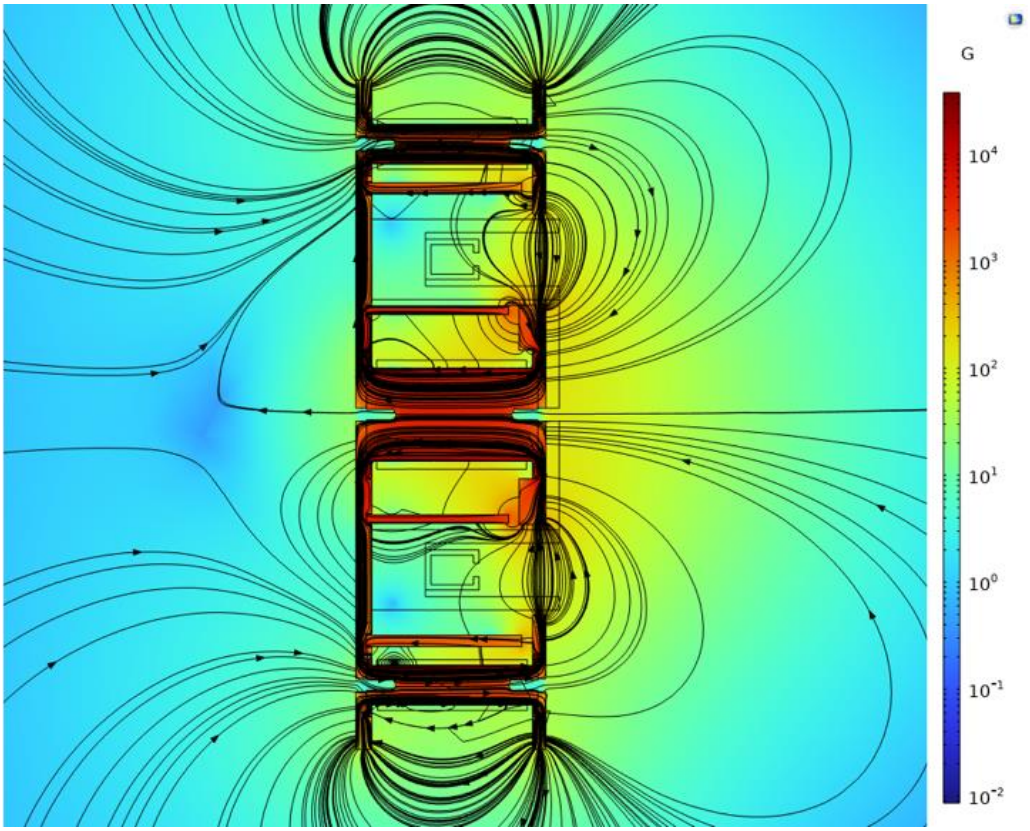

a)

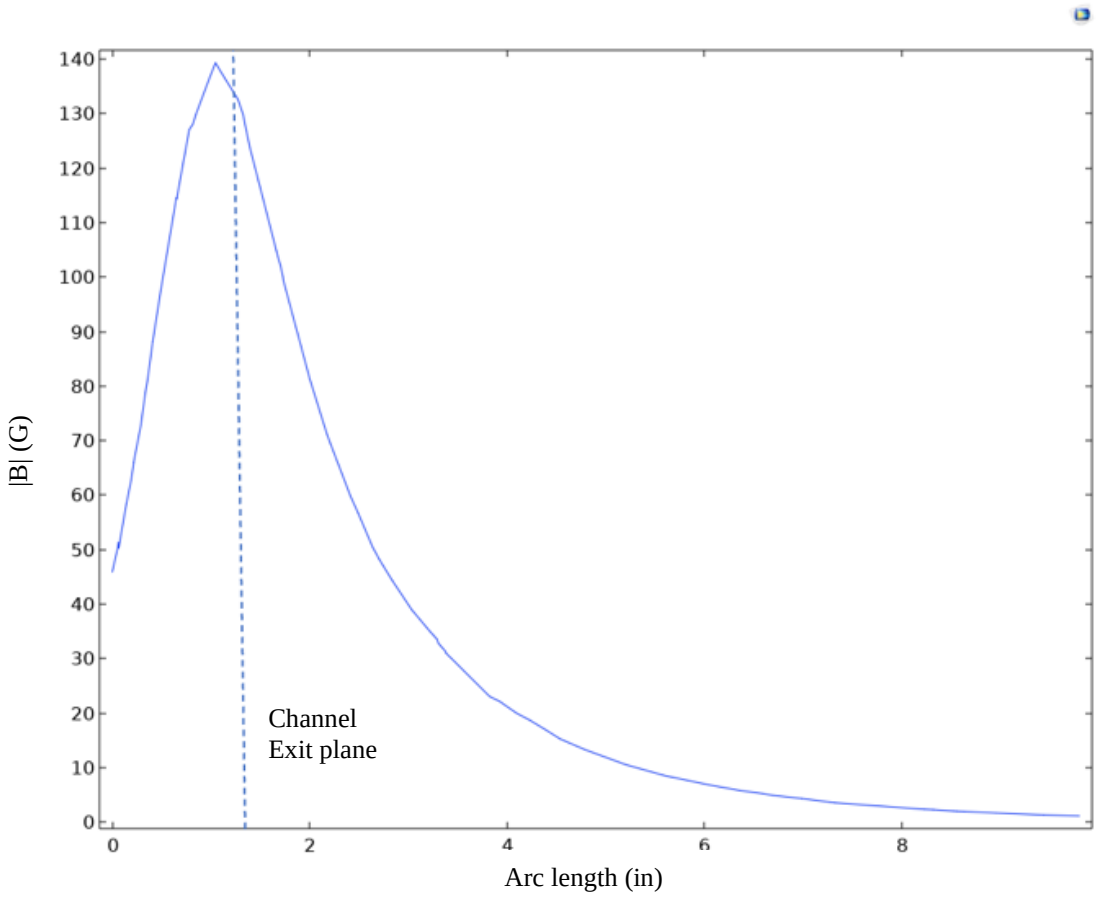

b)

Figure 5 – a) Simulated magnetic field profile for the P5 thruster (IC: 3 A, OC: 2 A) b) Axial variation of the magnetic field at the centerline.

1.3.1 Background on Axial Magnetic Field Gradient Effects

The compactness of the magnetic field lines across the discharge channel represents the magnetic field density. As shown in Figure 5b), the magnetic field density is significantly higher near the thruster exit plane and axially decreases away from the exit plane in both directions. The axial magnetic field gradient results in electron mobility variation across the magnetic field in the discharge channel. Axial magnetic field gradients

have been extensively researched to provide an understanding of the requirement of the gradient in the magnetic field [30–32]. Morozov [31] demonstrates the need for a vanishing magnetic field towards the anode to maintain current continuity. The axial gradient of the radial magnetic field $\nabla \mathbf{B}$ is varied along the discharge chamber centerline from the anode to the thruster exit. The study finds that the electron current fraction (I_e/I_d) for the negative gradient is 0.85, the uniform gradient is 0.5, and the positive gradient is 0.35. The markedly higher electron transport for the negative gradient is attributed to increased plasma oscillations. The uniform gradient provides marginally stable operating conditions; hence, a positive gradient for the magnetic field is essential for stable HET operation. Gao [32] investigated the effects of axial magnetic field configuration on the plume characteristics for miniaturized cylindrical HETs. Current variations in the adjustment coil near the thrust exit plane provide axial magnetic field gradient variation. It is observed that under the lowest magnetic mirror field with a 44.8 G/mm axial gradient, a bulb-like plasma discharge region is radiated near the thruster exhaust with a divergence angle of 77°. The bulb-like plasma discharge gradually disappears with an increase in the upstream mirror-like magnetic field to 74.5 G/mm with a plume divergence angle of 65°, providing enhancement of anode efficiency from 16% to 28%.

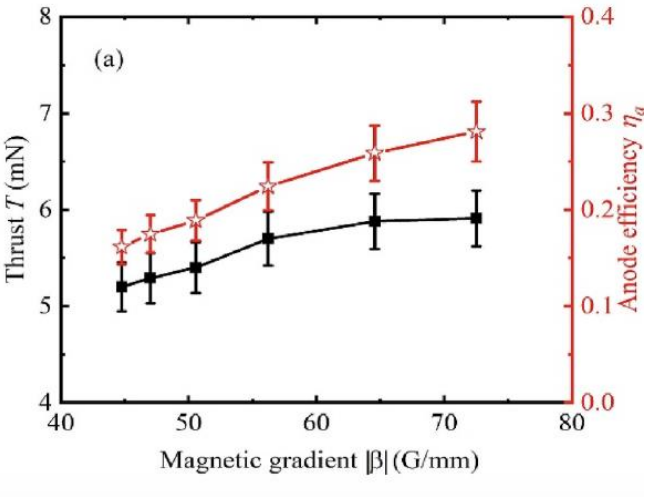

Figure 6 – Thrust and anode efficiency as a function of the magnetic field gradient [32]

1.3.2 Background on Radial Magnetic Field Gradient Effects

While axial gradient effects are widely studied, radial magnetic field effects in the discharge channel are significant. Topology of the magnetic field in the discharge channel results in a radial distribution such that higher magnetic field density is present near the inner wall of the channel. The magnetic field density decreases in the centerline and increases near the outer channel wall—the variation in the density of the magnetic field results in the formation of a magnetic field mirror effect. As electrons travel along the magnetic field in the discharge channel, they experience variation in their velocities, resulting in oscillating motion in the radial direction, as shown in Figure 7. The motion of electrons in the radial direction is assisted by the local charge density buildup, resulting in the localized potential difference in the radial direction.

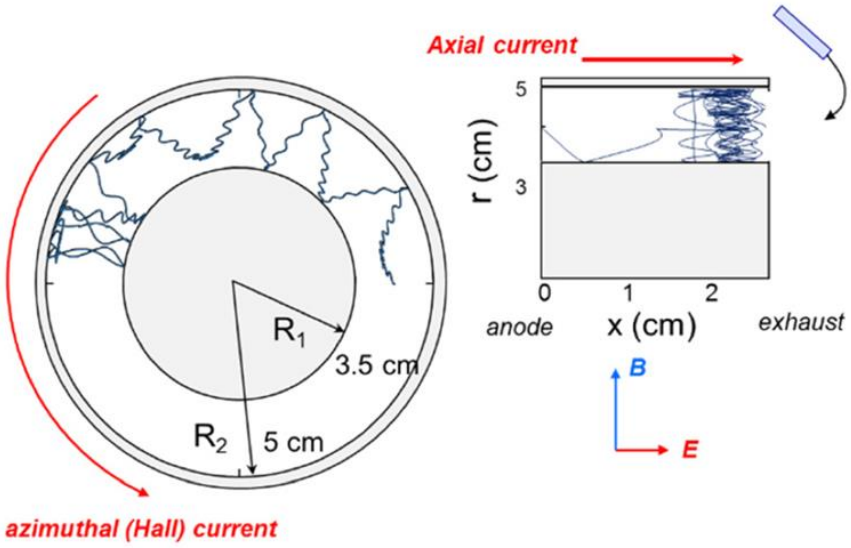

Figure 7 – Simulated results of electron trajectory predictions for a HET, in the radial-azimuthal plane (left), and in the axial-radial plane (right)[3].

Research has taken place to understand the role of the magnetic field gradient on HET operation [33–35]. Through the development of the 2-D plasma Flow Model, Keidar [34] established the relationship between the mirror effect and the potential distribution in the HET discharge channel. The research presents that the magnetic field gradient affects important flow characteristics, such as the radial presheath potential decrease, the presheath length, and the two-dimensional potential shape in the channel. The mirror effect is said to influence the potential line shape, resulting in ion motion variation through the discharge channel. A higher magnetic mirror ratio influences the concavity of potential profiles such that a stronger ion focus occurs in the exhaust area. This information is essential for improving the current state-of-art models used for HET plasma flow simulations. Yu *et al*. [35], utilizing the test particle method, highlighted the asymmetric radial electron mobility due to the magnetic mirror effect. Through theoretical analysis, we know that the near-wall

electron mobility is inversely proportional to the magnetic mirror ratio, thus preventing electron wall collision. Jiang [33] also investigated the mirror effect in cylindrical HETs.

The magnetic mirror effect on the electron density and temperature is understood using a 2D axisymmetric particle-in-cell (PIC) code [36–40]. The electron temperature reaches the maximum (38.4 eV) at the strongest magnetic mirror, along with a temperature barrier between channel walls. In addition, the research evaluates the effect of a magnetic mirror on the secondary electron yield rate, propellant utilization, and multi-charged ion dynamics. The results display that the largest magnetic mirror ratio can maximize and elevate the average yield rate by increasing electron energy. The magnetic mirror effect on the potential distribution is the reason for the electron energy increase. The relationship between thruster performance parameters and magnetic mirror is discussed, with the highest magnetic mirror ratio resulting in the maximum propellant utilization efficiency. Despite all the benefits, the magnetic mirror effect possesses disadvantages regarding wall erosion.

Studies on the axial and radial magnetic field effects have effectively contributed to establishing the crucial role of the magnetic field in HET operation [41–46].This results in the utmost need for the development of a performance model that highlights the relationship of the magnetic field on the thruster performance parameters using plasma parameters to provide a complete understanding of the dependency on the magnetic field. In conventional HET operation, the magnetic field is also considered axisymmetric. However, engineering production issues can lead to manufacturing faults in HET components[22], resulting in a non-uniform magnetic field. The non-uniformities in the

magnetic field can be observed azimuthally in the channel in various conditions resulting from electrical shorting, material processing, and geometrical constraints.

Azimuthal magnetic field gradients forming as a result of manufacturing defects, as well as in devices possessing thrust vectoring capabilities, provide the platform to explore these magnetic field gradients. It is essential to understand how variations in the radial magnetic field strength in the azimuthal direction affect the thruster's performance parameters to address the current requirement for the efficient production of HET components and a high success rate in qualification testing. This will assist in accurately quantifying and predicting the resulting effects on thruster performance. Quantification enables quality assessment through performance prediction and optimizing the manufacturing and testing process. This current research drives towards providing knowledge on the impact of magnetic field gradient on HET performance and a pathway to extend it to understand the impact of azimuthal magnetic field gradient on HET performance and stability utilizing plasma parameters.

1.4 Research Question

In this chapter, we have established a solid foundation for processes associated with HET and the impact of different parameters on the performance of the HET. In previous research, we emphasized the impacts of axial and radial magnetic field gradients. The need for a performance model emphasizing the effects of magnetic fields on particle dynamics that affect the performance of the thruster is well established. The effect of particle dynamics on plasma parameters and thruster performance necessitated magnetic field optimization for thruster performance. While previous studies yielded data regarding

symmetrical magnetic fields, none revealed the underlying mechanism or the effect of magnetic fields on the dynamics of charged particles and also how the performance gets affects by non-uniformities in the magnetic fields. Previous computational studies on azimuthal asymmetry needed to be more comprehensive in offering an explanation for the observed effects. These discussions bring us to the thesis's research question:

"How does azimuthal magnetic field gradient affect Hall effect thruster performance and stability?"

1.5 Objectives

The principal objective of this study is to estimate the impact of azimuthal magnetic field gradients on HET performance. In order to gain insight into the influence of the magnetic field on the processes of ionization, acceleration, and, ultimately, the performance of the thruster, is required to establish a correlation between the magnetic field and plasma properties. To accomplish the aims, the subsequent objectives are:

1) Determine the relationship between the magnetic field, electron temperature, and electron number density.

2) Describe the relationship between azimuthal magnetic field oscillations and discharge current oscillations.

3) Determine correlations between thrust and efficiency in relation to variations in the azimuthal magnetic field

4) Offer an analysis of the influence of azimuthal gradients on the performance of HETs by incorporating variations in plasma properties.

1.6 Assumptions and Approach

1.6.1 Assumptions

The investigation of plasma physics consists of various challenges owing to its intricate characteristics. The first challenge is establishing a link between 3-D varying plasma properties across the plume and thruster performance. In this case, we will consider the plasma properties measurement at the centered radial location of the discharge channel width to eliminate radial variations in plasma properties. The model is simplified to address the impact of the magnetic field in the region of the maximum magnetic field, thus reducing it to a one-D model to provide a theoretical relationship between the magnetic field and performance. The thesis progresses to discussing the axial variations of various parameters presented. In the case of an azimuthal magnetic field, the model observes parameters at the plane of maximum magnetic field location within the channel. A cartesian coordinate system is used instead of a radial coordinate system to provide a simplified solution. The model considers a small area under observation in the channel exhibiting variation in the magnetic field. The model consists of analyzing electron motion along the azimuthal gradient region in the absence of magnetic mirror effect variations.

1.6.2 Approach

The second obstacle that arises in the case of azimuthal gradient is the visualization and measurement of plasma properties in order to determine their stability and efficiency.

The present probe configuration yields measurements at a radial distance of 1 meter by scanning the thruster's center plane. This data is then extrapolated for 3-D plume characteristics while assuming symmetry. In order to gain insight into the fluctuations in the charged particle's properties and the distribution of the plasma plume caused by the asymmetric magnetic field, it is necessary to fabricate a 3-D probe scan arm that facilitates a 3-D Faraday probe scan. The Faraday probe provides current density data about the plume. The proposed design for a hemispherical sweep apparatus entails the incorporation of a motorized setup enabling measurements to be conducted in a 3-D planar format, facilitating the assessment of the thruster's plume. The probe's trajectory is a circular path with a radius of 1 meter. The apparatus incorporates a gear mechanism to regulate and manipulate the movement of the probe. This sweep apparatus design enables future probe deployments for facilitating precise data measurement.

The initial investigations and subsequent model development establish a correlation between the magnetic field, electron temperature, and plasma properties. The created model undergoes modifications to examine the impact of the azimuthal magnetic field gradient. This modification is achieved by including localized magnetic field changes inside the channel near the exit plane. The model is modified to convert the radial coordinate system to cartesian coordinates for analysis of electron motion. Analyzing electron motion in the azimuthal direction makes it possible to quantify the variation in plasma properties along the azimuthal direction.

CHAPTER 2 BACKGROUND

Analyzing the plasma properties that have an impact on the performance metrics helps promote a better understanding of the performance of HETs. Several studies have been undertaken to establish a solid foundation for evaluating the performance of HETs. This chapter will examine several experimental and computational performance studies that have been performed to understand the operational parameters that impact the thrust and efficiency of HETs. In this chapter, we investigate the conventional HETs having uniform magnetic fields and non-conventional HETs that possess non-uniformities in the magnetic field by virtue of their channel shape. These non-conventional HETs provide a case where non-uniformities in the magnetic field are present, allowing for an overview of the effect of these non-uniformities on the performance of the thruster.

2.1 Parametric Effects on HET Performance

2.1.1 Experimental Studies

Komurasaki[47] investigated the performance and acceleration mechanisms of HETs, employing experimental thrust and beam property measurement techniques. HET utilized in this work comprised of standard components found in typical HET systems, including an anode, cathode, and magnetic circuit. The performance of the HET was evaluated by employing a pendulum-type thrust stand. A linear differential transformer was used to convert the thrust stand's deflection into electricity. The thrust stand was comprised of a copper plate that was cooled by water in order to mitigate any potential fluctuations in the signals used for thrust measurement. The measurement of the ion beam

was conducted by positioning an ion beam collector at a distance of 10 cm downstream from the thruster exit plane. The energy distribution of ions was acquired using a multi-grid energy analyzer using a negatively-biased collector. Langmuir probes were used to learn about plasma parameters and how they affect thruster performance. Performance measurements were derived using the following equations.

$$\eta_E = (V_m/\mathrm{V_a}) \tag{2}$$

$$\eta_u = (m_i I_b/\dot{m}_a) \tag{3}$$

$$\eta_a = I_b/I_a \tag{4}$$

$$\eta_T = \eta_u \eta_a \eta_E \tag{5}$$

$$T = I_b\sqrt{2MV_m/e} \tag{6}$$

$$\eta_a = \frac{\beta(1-a)}{\beta(1-a)+1} \tag{7}$$

Table 1 – Thruster operating and performance parameters of SPT [47]

$\dot{m}$, A-eq	V_a, V	I_a, A	I_b, A	η_a, %	η_u, %	η_E, %	η_T^*, %	η_T, %
Ar 0.75	200	0.45	0.10	22	13	63	1.8	1.0
1.00	175	0.97	0.22	23	22	60	3.0	3.3
1.00	200	1.24	0.29	23	29	60	4.0	4.9
1.00	225	1.49	0.36	24	36	63	5.4	6.9
1.00	250	1.70	0.42	25	42	63	6.6	7.0
1.25	200	1.85	0.50	27	40	60	6.5	7.0
1.75	200	3.08	0.92	30	52	63	9.8	11.2
Xe 0.30	150	0.82	0.23	28	77	66	14	12
0.50	100	1.49	0.37	25	74	65	12	13
0.50	130	1.40	0.38	27	76	65	13	16
0.50	150	1.45	0.40	28	80	62	14	15
0.70	150	2.21	0.65	29	97	62	17	15

Operating parameters, including the acceleration voltage and propellant mass flow rate, were deemed to have an impact on β in Equation 5, whereas the thruster geometric parameters determined a. Additional assessment of the efficiency of ion acceleration via the constructed model indicated that an increase in both the mass flow rate of the propellant and the acceleration voltage led to a corresponding enhancement in acceleration efficiency. While neglecting beam divergence and double charge effects, as shown in Table 1, a fair agreement was established between the thrust and acceleration efficiency as determined through the experimental data. The acceleration efficiency was established as a predominant factor of thrust efficiency. The analysis presented in this research paper [47] offers a solid foundation for establishing a correlation between plasma properties, especially mass flow rate, and the performance parameters of a thruster, such as acceleration efficiency.

Kim [48] investigated the impact of primary physical characteristics and processes on the performance of SPTs, explicitly focusing on the ionization process and ion dynamics within the channel. The mass flow rate was stated as an essential parameter for achieving

optimized thruster performance in terms of high efficiency, thus making it the primary focus of the work. As seen in Equation 8, ionization dynamics were depicted in terms of number density variation.

$$\frac{dn_a}{dt} = -(\sigma_i v_e) n_e n_a \tag{8}$$

$$\frac{dN_a}{N_a} = -\frac{(\sigma_i v_e) n_e}{V_{az}} \mathrm{d}z \tag{9}$$

$$\lambda_i(z) = \frac{V_{az}}{(\sigma_i v_e) n_e} \approx const \tag{10}$$

$$\frac{\dot{m}_A}{m_i A} \geq \frac{v_i V_{az}}{(\sigma_i v_e) K_\lambda L_a} \tag{11}$$

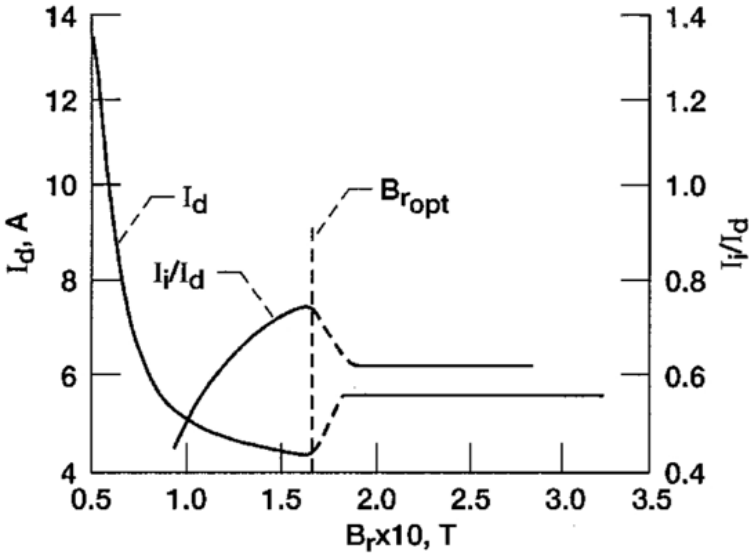

Figure 8 – Discharge current and ion-to-discharge current ratio as a function of magnetic field [48]

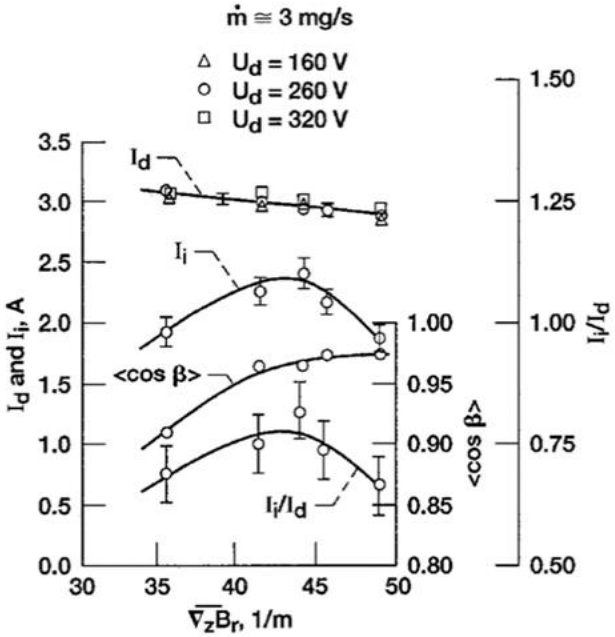

Figure 9 – Discharge current, cos*β*, and ion-to-discharge current ratio as a function of the axial magnetic field gradient for discharge voltage of 160, 260, and 320 V [34].

The ion flow rate density distribution was employed to achieve high ionization efficiency, supported by experimental data. Through the I-V graph, ion current was observed equating to current associated with acceleration voltage at the corresponding mass flow rate. The rate of magnetic field induction in managing electron current was demonstrated using classical conductivity in plasma in the acceleration area of HET. Maximization of I_i/I_d resulted in maximum ion yield, and experimental findings confirmed the requirement as a criterion for magnetic field optimization Figure 8. The study emphasized the relevance of magnetic field topology for concentrating ion flow by asserting the function of magnetic field topology in influencing the electric field structure responsible for ion trajectory variation. The effect of a radial magnetic field gradient on impeller parameters was also investigated, as shown in Figure 9. The discharge current

reduced as the radial magnetic field gradient increased. In contrast, the ion yield ratio peaked at around 30 (1/m) and subsequently fell. The intricate characteristics of the plasma process occurring in the HET necessitate the creation of a model that elucidates the electrons and plasma dynamics within the acceleration channel.

Hofer [49] presented a comprehensive performance model that incorporates utilization efficiencies for partially ionized plasma, with the aim of examining the influence of electron and ion current on thruster performance. To calculate properties that are difficult to measure with a probe, the performance model supplied a combination of thruster performance and plasma parameters. The correlations in this study establish a connection between the dynamics of charged particles and plasma properties. These connections specifically emphasize the impact of accelerating potential on the ion velocity, affecting both thrust and efficiency.

$$V_d = V_a + \triangle V \tag{12}$$

$$\eta = \frac{T v_e}{2 I_d V_d} = \left(1 - \frac{\triangle V}{V_d}\right)(1 - i) \tag{13}$$

$$T = (1 - i)\left(\frac{P_d}{V_d}\right)\sqrt{\frac{2 m_p (V_d - \triangle V)}{e}} \tag{14}$$

The study provided performance parameters as a function of acceleration voltage or a combination of discharge and loss voltage. The model worked effectively for power

ranges between 2.16 and 21.60 kW and also performed well in multi-charge plasma conditions. The predictions generated by the models were evaluated by comparing them with the experimental data. The results indicated a relatively high level of accuracy, with deviations of less than 5% seen in most cases, as depicted in Figure 10. Both the modeled calculations and the data gained during testing revealed that increasing the discharge voltage led to an increase in the specific impulse as well as the efficiency of the thruster. The estimated thrust closely mirrored the experimental behavior of thrust with changes in discharge voltage. Figure 10 illustrates various data trends and established relationships.

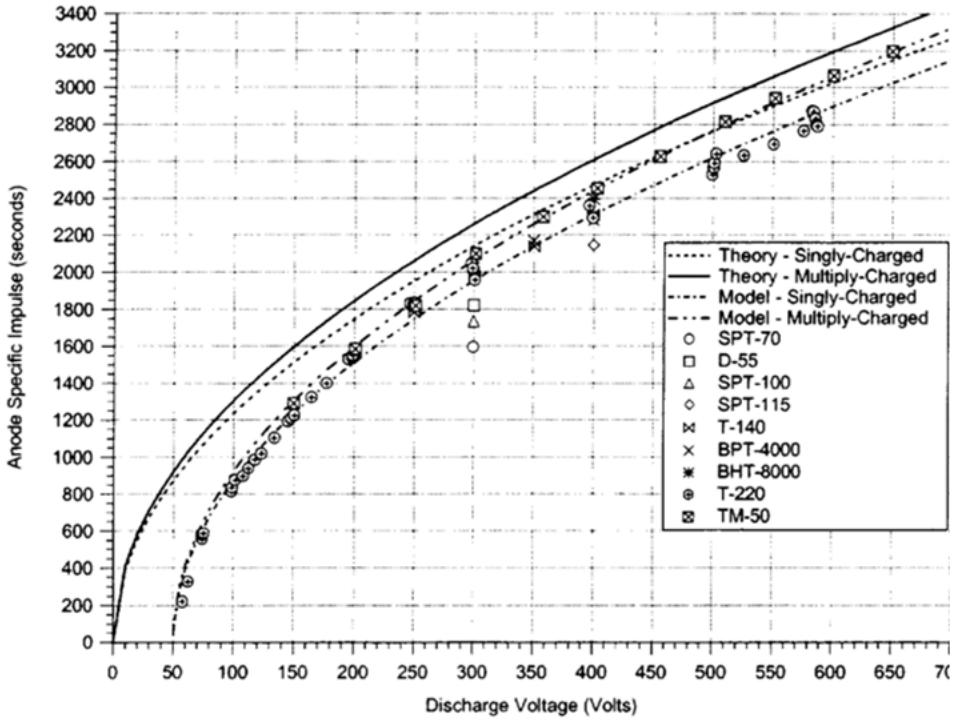

a)

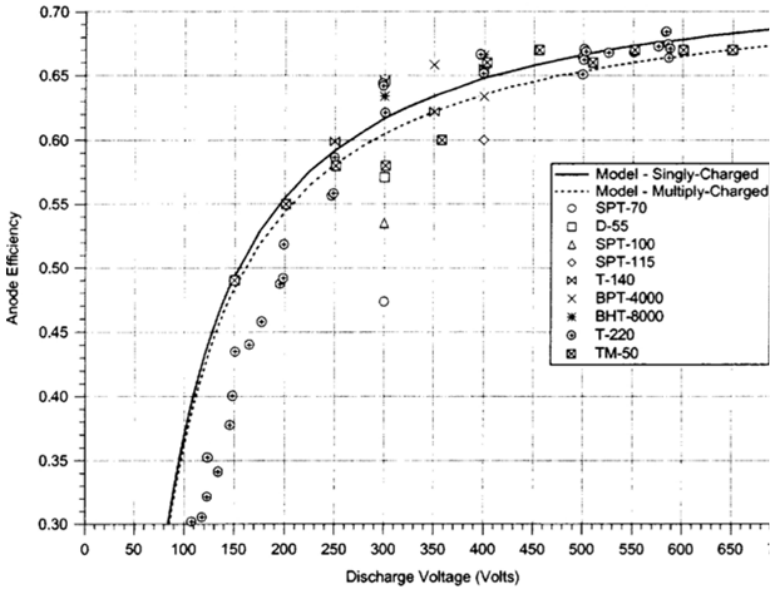

b)

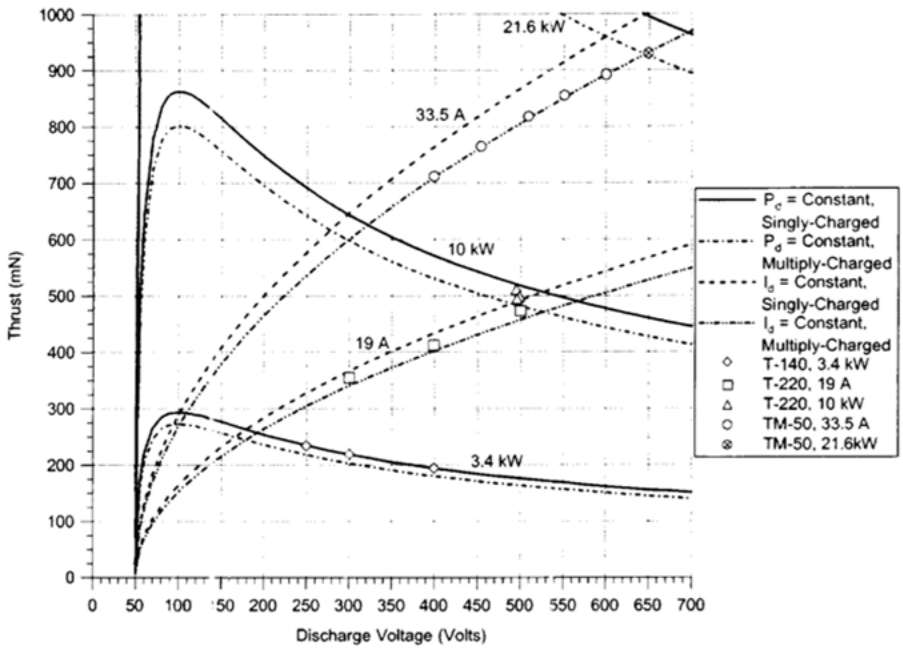

c)

Figure 10 – Thruster performance parameter variations as a function of discharge voltage change a) Anode specific impulse b) Anode efficiency c) Thrust [49]

Despite extensive studies on the correlation between operational parameters (such as mass flow rate and magnetic field) and the impact on ion dynamics and thruster performance, there still needs to be a more comprehensive investigation into the specific impacts of magnetic fields on electron dynamics.

2.1.2 Computational Studies

Regardless of the extensive use of experimental data in the development of a wide range of models, the analytical estimation of charged particle motion and its impact on thrust performance remains a significant challenge. Computational models were developed to enhance the understanding of thruster performance parameters and plasma properties[50–55]. Garrigues[51] developed a quasi-neutral one-dimensional hybrid model to predict SPT performance parameters. The model considered ions as particles and electrons as fluids while retaining quasi-neutrality. The assumption of quasi-neutrality, although helpful in simplifying the governing equation and finding solutions, led to inaccurate estimates of ion density and, consequently, the electric field. In order to simplify this process, the equation for electron momentum was altered to exclude the diffusion term. Subsequently, the model was employed to forecast the impact of alterations in the propellant, the applied voltage, and the anode mass flow rate on the performance of SPT-100-ML. As predicted by modeling, the thruster efficiency at an operational voltage of 300 V deviated from the experimental data by 10%. The modeling results underestimated the thrust by approximately 15 mN for the operational voltage range of 150-400 V. The specific impulse exhibited a discrepancy of 200 s between the model and the experimental result conducted at 350 V. After analyzing the performance of various propellants, it was determined that the calculated thrust remained consistent for both krypton and xenon

despite a 10% difference in efficiencies. The discrepancies between the simulation and experiment performance characteristics were attributed to higher-order ionization states caused by the low energy threshold necessary for excited state ionization. Although the prediction model did not yield precise results, it facilitated the comprehension of the various processes occurring within the channel, enhancing future models through optimization.

Theoretical and computational studies primarily focus on HETs with a uniform magnetic field. The fundamental assumption of a uniform magnetic field significantly influences the precision of the model; hence, it is crucial to investigate the impact of non-uniformities in the magnetic field. The next section presents a comparison of conventional and non-conventional HETs possessing uniform and non-uniform magnetic fields, respectively.

2.2 Conventional HET

Conventional HETs were developed to provide uniform plasma with unchallenging construction[13]. Various design studies continue to take place to optimize HET design and performance[56–58]. After various iterations of the design, the current conventional design of HET with circular channel was deemed suitable for carrying out various mission across wide range of operation.

Now, looking at conventional HET, the channel shape is cylindrical to allow ease of construction. The cylindrical channel shape has various advantages [26]. Characteristics of conventional HET channels allow for the magnetic field to be uniform and radially outwards from the inner to the outer coil, as seen in Figure 11. While the magnetic field is

uniform radially, there is an axial variation of the magnetic field such that the peak magnetic field occurs around the exit plane near the front pole typically present inside the thruster discharge channel. Various research has been conducted in evaluating the advantage of axial magnetic field gradient as seen in section1.3.1.

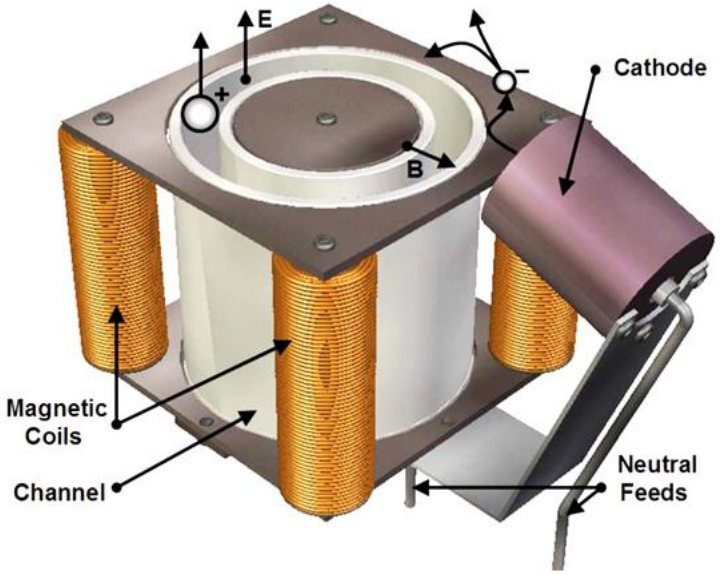

Figure 11 – Conventional HET components and configuration [59]

Electrons, while transversing through the magnetic field, are magnetized. Thus, as the magnetic field decreases axially across the exit plane in both directions, *i.e.*, towards the anode and the cathode, the variation in the magnetic field strength results in varying resistance and thus disparity in electron velocity in the axial direction. The electrons being magnetized move along the magnetic field lines. While moving along the magnetic field, the radially uniform magnetic field with the axial electric field allows for the electrons to experience the E×B drift due to the Lorentz force.

$$F = q(E + vXB) \tag{15}$$

The EXB drift is experienced by electrons inside the channel. The E×B drift causes the electrons to drift in the azimuthal direction as seen in Figure 7. The circular discharge channel shape allows for the electron drift mechanism to occur smoothly without high wall collisions and physical interruptions. This drifting mechanism allows an increase in the possibility of collision of electrons in the channel with the neutrals to result in the ionization of the propellant. The electron azimuthal drift constitutes the Hall current as the name suggests. Hence, the uniform radial magnetic field and electric field play a huge role in the operation and processes associated with HET as discussed in Chapter 1.

2.3 Non-Conventional HET

The need to develop a propulsion system with high efficiency for small satellites has resulted in the development of low-power HET technology. While the core operating concept remains the same, alternative designs of the HET channel aim to provide improved packing efficiency as well as advantages that improve HET operation.

Numerous design initiatives have led to the investigation of various methods for enhancing HET operational capabilities. To increase the thruster's overall efficiency, the two-stage HET is developed as the result of an investigation of the separation and optimization of ionization and acceleration independently[60]. The spacecraft employs many hall thrusters during operation. The circular shape of the HET channel leads to low packing efficiency, resulting in wasted space. Proposed modifications to the discharge

channel shape aim to optimize the packing efficacy of HETs. Numerous research projects have investigated the performance of different channel-shaped HETs, such as linear, cylindrical, racetrack, and wall-less.

Pote[61] at Busek Co. Inc. initiated the development of a novel non-circular racetrack HET, BHT-RT-150, and later on, a higher aspect ratio design, BHT-RT-1500. The racetrack geometry consists of semi-circular halves of the conventional circular HET connected by straight sides, giving a symmetric racetrack cross-section. This unique discharge geometry is believed to increase geometric flow area by scaling the thruster only in the linear direction to eliminate the negative thrust density scaling trends. The racetrack geometry fulfills the specified criteria, which includes a small ion gyroradius, a continuous closed electron drift plasma, and the prevention of electron collisions with the walls. These factors present compelling evidence for the potential of racetrack geometry to exhibit performance on par with that of the standard HET.

The racetrack HET exhibits comparable behavior to the conventional HET in terms of thrust-to-power ratio and I-V changes at low voltages. The thruster produces an 84 mN thrust at 1,675 W and 350 V discharge with a single magnet coil, equating to an anode efficiency of over 41% and an anode-specific impulse of 1,678 s. Unfortunately, non-uniform discharge characteristics are observed at elevated discharge voltages. The discharge intensity increases in the curved sections of the racetrack, accompanied by a noticeable abrupt change in the brightness of the plasma at the upper left and lower right corners. A uniform magnetic field magnitude and a uniform flow distribution at the centerline leads researchers to attribute the asymmetric brightness to the electron drift motion. An additional factor suggested to play a role in the observed non-uniformity is the

radial fluctuation of the B-field. The radial magnetic field exhibited minimal gradient throughout the straight segment of the racetrack, while a substantial gradient is present in the curved segments. This observation implies the necessity of optimizing the magnetic field topology across the channel.

While the majority of thrusters were not tested for an extended time to observe the effects due to stability issues, a racetrack channel configuration study[62] offers valuable insights into erosion processes. The channel erosion is visible in the darkening of the discharge channel wall, as shown in Figure 12, and is primarily assessed based on the magnitude of power deposition on the channel's wall. Although visual inspections have identified areas of power or electron bombardment on the channel walls through discoloration or luminescence, the underlying cause of these wall losses remains uninvestigated. Wall losses are the dissipation of incoming particles' kinetic energy as they collide with the wall. The evaluation of wall losses considers the high energy of electrons and ions.

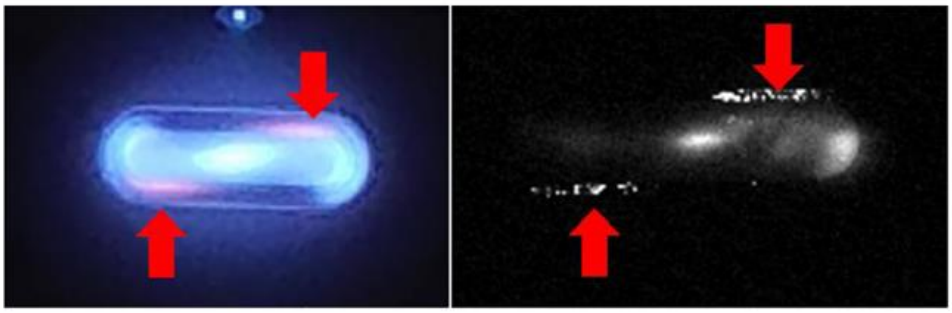

Figure 12 – The non-uniform erosion observed in the Pseudo Linear Thruster [62].

Numerous studies assess energy deposition on the channel wall due to sputtering as a function of the sheath potential, electron temperature, and radial ion velocity. E×B drift and inertial effects of electron motion during the transition from a straight section with a uniform magnetic field to a curved section with a radially varying magnetic field account for the increased power deposition. Through the review of the racetrack HET, the essential role that the magnetic field played in the operation of HET is highlighted. The racetrack HET exhibits non-uniform dispersion of magnetic field lines along its channel during operation. Compacted magnetic field lines in circular sections contribute to an increase in the intensity of the magnetic field within the section. Changes in the magnetic field tend to impact the inertial motion of electrons emanating from the straight section. The electrons coming from the straight section encounter a drastic change in the strength and direction of the magnetic field, which forces the electron to deviate from the straight path motion. However, as a consequence of the high velocity of the electron and the abrupt change in its trajectory within the channel, the electron lacks adequate time to respond to this shift. Consequently, it deviates from the theoretically expected direction of motion. The alteration in motion leads to the accumulation of charge at the beginning of each circular segment, hence increasing the number density, frequency of collisions, and temperature. The increase in temperature leads to an escalation in the thermal erosion of these wall sections, a phenomenon that is considered unfavorable. To allow better operation of non-conventional HETs the magnetic field topology requires modification and optimization with respect to the channel shape. Studying the geometry of the channel and the magnetic circuit governing electron transport in the channel is thus crucial for the advancement of non-conventional HET channel design.

The evaluation of non-conventional HETs where non-uniform magnetic field effects are observed provides a stepping stone to study the potential impact of non-uniform magnetic fields on HET performance. Non-conventional HETs are one case where such gradients are observed; however, manufacturing defects can cause magnetic field non-uniformities to occur in conventional HET[22].

2.4 Azimuthal Magnetic Field Asymmetry

Now, to evaluate the effect of the azimuthal magnetic field gradient effect, few computational studies have been conducted. A study conducted by Lazurenko[63] aimed to generate a three-dimensional model of atom and ion dynamics within the accelerating channel of SPT, utilizing the kinetic equation. Throughout history, models have been devised to analyze axisymmetric magnetic field conditions, sometimes disregarding any potential asymmetry of the magnetic field within the channel. A three-dimensional numeric model was developed rather than a conventional two-dimensional model.

To address the conditions and consequences of a non-axisymmetric magnetic field in HETs, one of the potential applications of asymmetric magnetic fields that was taken into consideration was for thrust vectoring. Deviation of thrust vector for SPT-100 by azimuthal magnetic field asymmetry was simulated by the creation of eight additional coils and four additional outer poles at 300 V and 4.5 mg/s anode conditions. Allowing the electron temperature, potential, and number density to be constant and symmetric for inertial wall calculations resulted in a simplified model. The consideration of ion volume recombination was omitted to enhance the model's ease of compilation. The experimental

and simulated thrust and vector deviation findings showed a high degree of concordance, as shown in .

Table 2 – Measured and calculated thrust and thrust vector deviation [63]

Operation mode	Thrust F (mN)		Thrust vector deviation (deg)	
	Theor.	Expt.	Theor.	Expt.
Azimuthally symmetrical magnetic field	85	80	···	···
Mode 1 (weak asymmetry of magnetic field)	80	72.1	2.2	2.6
Mode 2 (strong asymmetry of magnetic field)	62.7	68.1	4.9	4.8

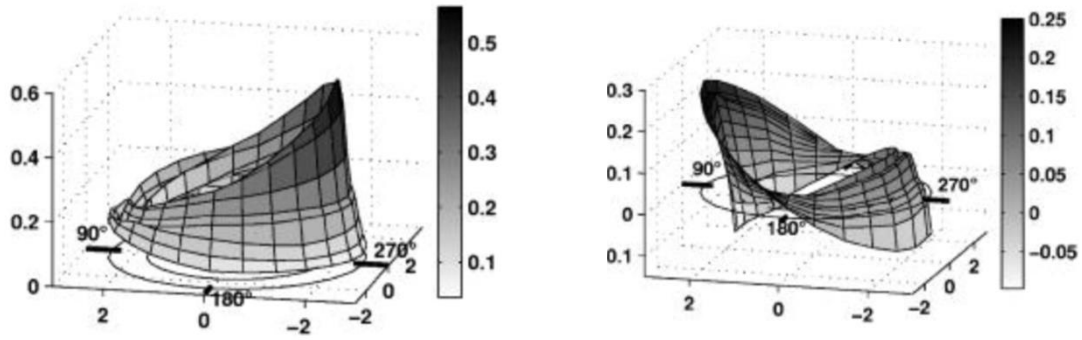

Figure 13 – Distribution of a) ion flux density (m^{-2} s^{-1}) and b) y-component of ion velocity (ms^{-1}) at the exit plane [63]

Using simulation techniques to analyze the distribution of ion flux density and velocity, visual evidence was obtained supporting the concept of thrust vectoring. Similar experiments were conducted on the PPS-flex[64] having a configurable magnetic circuit to analyze the potential use of the magnetic field for thrust vectoring. In order to enable the application of magnetic fields for thrust vectoring, the PPS-Flex design underwent

modifications by augmenting the quantity of independent magnetic flux circuits, hence deviating from the conventional HET design. As a result, an efficient four-stage construction was developed, utilizing 22 coils to operate the thruster. The magnetic circuit architecture had four inner coils, four outer stages with four coils connected in series, and two back coils. A total of 10 distinct power supplies were employed to energize the magnetic circuit for the operation of the HET. The experiment involved testing approximately 100 distinct magnetic field configurations with varying lens angles for the magnetic field lines in the PPS-Flex device, which was operating at 250 V and had a discharge current of 4.28 A. The research gave valuable insights into the uniform configuration with the maximal magnetic field near the exit plane, which is the most optimal state of thruster performance. Although the study did not advance in tracking the thrust vector, it provided valuable knowledge of the operation of the thruster. A more comprehensive understanding of ionization and acceleration variation is necessary to establish a correlation between magnetic field gradients and plasma phenomena.

CHAPTER 3 THEORETICAL MODEL DEVELOPMENT AND VALIDATION

While the previous performance model[49] did offer valuable insights into the potential fluctuations in thruster performance, its failure to investigate the underlying theoretical and physical processes thoroughly underscores the necessity for the present research. This research aims to build a better knowledge of the impact that azimuthal gradients have on plasma parameters and thruster performance, as well as to explore the possibility of estimating thrust vectoring based on azimuthal asymmetry.

The current chapter discusses a model employed for comprehending the influence of magnetic fields in the context of plasma physics that relies on a simplified premise regarding the dynamics of electrons and ions in a HET. The knowledge acquired through the study of various models in Chapter 2 provides a framework for an overview of plasma processes affected by magnetic field variations. The complex non-linear dependence of plasma parameters on the particle dynamics features of a three-dimensional plume is the key issue in designing this model. The new model is simplified by incorporating one-dimensional electron motion dynamics and emphasizing gradients in plasma properties and thruster operating parameters. The model is then modified for taking into account the presence of azimuthal magnetic field gradient, to provide the impact of such gradients on the plasma parameters and thruster performance.

3.1 Axial Variation of Properties

The primary focus of discussion in HET pertains to the radial magnetic field. The magnetic field produced by the inner and outer coil can be observed and represented by magnetic field lines. Examination of the magnetic field distribution displays that the field exhibits a radial increase from the inner channel wall to the outside wall. When examining the axial variation of the magnetic field, it is evident that the magnetic circuit generates a peak near the exit plane, after which the field decreases axially in both directions. Changes in the position of the magnetic field peak lead to corresponding changes in the locations of the ionization and acceleration regions.

The axial magnetic field gradient is required to limit electron velocity and prevent it from bombarding the anode and causing instabilities. A positive magnetic field gradient is associated with more stable HET operation, according to research examining positive, negative, and zero magnetic field gradient conditions in the context of HET operation [22].

An additional gradient observed in the HET channel is the electric field gradient. This gradient is produced by the difference in potential between the cathode and anode, in addition to the influence of electron number density on the localized potential. The variation in electron number density is detectable as a consequence of the gradient in the magnetic field, which induces changes in the energy of electrons as they traverse and move along the magnetic field. An increased magnetic field strength leads to enhanced electron confinement, causing variations in the number density across the plasma plume and thruster channel. The density of electrons directly influences the observed localized potential. Elevated electron number density reduces the local potential, thereby inducing the

formation of an electric field. The location of the maximum electric field is slightly upstream of the maximum magnetic field. In addition to being contingent on the properties of the electron and magnetic field, the location can fluctuate in response to changes in these variables.

The temperature of electrons is an additional feature that exhibits variation within the channel. The electrons in the plume are emitted from the cathode and possess an energy level of around 2-3 eV, exhibiting limited thermal energy. As electrons approach the anode, they encounter fluctuations in the magnetic field. The confinement of electron mobility across the magnetic field causes ohmic heating and an increase in electron temperature due to the magnetic field's resistance. When electrons attain an energy level that is equivalent to or exceeds the ionization energy of the neutral atom, the collision process induces a reduction in electron temperature. Consequently, this leads to variations in electron temperature along the HET channel.

3.2 Theoretical Magnetic Field Performance Model

The development of a model to evaluate the behavior of electrons and ions and their impact on plasma characteristics is a highly intricate and demanding task. Several critical assumptions and conditions are employed to isolate the impact of the magnetic field on the operation of the HET. The fundamental assumptions are as follows:

1) The anode mass flow rate is constant.

The mass flow rate is kept constant throughout the HET operation, thus eliminating the study of its influence on thruster performance.

2) Discharge voltage is constant.

Constant discharge voltage is maintained in the HET to observe the change in discharge current with respect to the change in magnetic field.

3) Only singly-charged particles are considered.

The present model assumes that plasma exclusively comprises of particles with a single charge and does not address the generation of particles with multiple charges.

4) The gradient of the overall magnetic field is constant; however, there may be localized variations in the channel.

The magnetic field magnitudes vary such that the gradient from the anode to the thruster outlet remains constant while local gradients vary across the channel.

5) Facility and cathode effects

The impact of the cathode and the facility is disregarded in the present study, as the primary investigation focuses on the effects of the magnetic field generated by the thruster.

In order to simplify the model, the Coulomb collisions and inertial effects are ignored throughout its development. The development of the model considers steady-state conditions and preserves the quasineutrality characteristic of the plume.

3.2.1 Performance Parameters

The HET performance model, as established by Hofer[22], offers a simplified well-defined formulation for evaluating the efficiency, thrust, and specific impulse of a one-

dimensional far-field quasineutral plasma. The performance parameters are expressed in terms of plasma properties and provide insights on the effects of the plasma properties on the HET performance parameter.

Starting with the efficiencies, the current utilization for the thruster can be interpreted using the beam current and the discharge current. The current utilization efficiency can be further related to the ion and electron velocities that affect the ion beam current and discharge current.

$$\eta_b = \frac{I_b}{I_d} = \frac{n_i e v_b A}{n_i e v_i A - n_e e v_e A} \tag{16}$$

The mass utilization efficiency metric indicates the degree of effectiveness in the conversion of neutral atom flux to ion flux. The utilization efficiency is a function of the ion beam current and the anode propellant mass flow rate for a specific propellant.

$$\eta_m = \frac{\dot{m}_b}{\dot{m}_a} = \frac{m_p I_b}{e\dot{m}_a} \tag{17}$$

Voltage usage efficiency refers to the efficient conversion of discharge voltage into ion acceleration and is represented as a function of the acceleration voltage experienced by the ions and the discharge voltage.

$$\eta_v = \frac{V_a}{V_d} \tag{18}$$

Finally, anode efficiency can be expressed as the total efficiency the HET possesses, indicating how much thrust is efficiently produced by the thruster from the power supplied. Total efficiency is determined by disregarding manufacturing and external defects such as the cathode and magnetic circuit. The total efficiency is also represented as combination of three utilization efficiencies, mass, voltage and current.

$$\eta = \frac{T^2}{2\dot{m}_a P_d} \tag{19}$$

$$\eta = \eta_b \eta_v \eta_m \tag{20}$$

Another performance parameter used for categorizing HETs is thrust. Along with the ion flux, the thrust generated by the HET can be represented as a function of the velocity at which the ions depart the channel as known as the ion velocity.

$$T = \dot{m}_b v_b \tag{21}$$

The estimation of specific impulse can be derived from the measurement of thrust and get influenced by the velocity imparted by the ions exiting the HET channel.

$$I_{sp} = \frac{T}{\dot{m}_a g} \tag{22}$$

Important parameters for determining the performance of a HET are its thrust, efficiency, and stability. Stability offers insights into the HET's effective practicality and

can provide comprehensive information regarding its operation under different conditions. Stability at an operating point not only helps in prolonging thruster operation but also result in efficient operation of the PPU systems.

The magnetic field impacts HET stable operation, as demonstrated in previous studies, and it is an important parameter considered for performance in the scope of the current work. Naoji[65] defines stability as the ratio of the root-mean-square of discharge current oscillations to the discharge current observed under power conditions. This ratio is utilized to observe the effect of the magnetic field on the HET stability and will be considered as one of the stability parameters to observe during experimentation.

$$\triangle = \frac{RMS}{I_d} = \frac{1}{I_d}\sqrt{\int_0^{\tau}(I_d - \bar{I}_d)dt} \tag{23}$$

Along with the ratio of root-mean-square of discharge current oscillations to the discharge current, the magnitude of discharge current oscillation as measured by the peak-to-peak oscillation percentage is also considered the critical indicator for stability with the change in magnetic field.

3.2.2 Uniform Magnetic Field Effect on Plasma Parameters

Having established the study's performance parameters, we now examine the impact of the magnetic field on them by analyzing the dependence of plasma parameters on electron and ion dynamics. Electrons traveling from cathode to anode encounter a magnetic field that causes Lorenz force to act on electrons and gyrate along the magnetic field. The combined effect of the gyration motion and the presence of an electric field in

the channel leads to the azimuthal drift of the guidance center. The purpose of this analysis is to characterize the movement of electrons within a channel centerline using the one-dimensional momentum equation. In this scenario, we will disregard any inertial effects, wall collisions, and radial magnetic field gradients.

$$\vartheta_e n_e v_{e_z} m_e + q n_e E_z + j_{e\theta} B_r + \frac{dP_e}{dz} = 0 \tag{24}$$

The azimuthal current density relation with axial current density is provided by Hofer[22] as:

$$j_{e_\theta} = j_{e_z} \Omega_e \tag{25}$$

Therefore, the electron's velocity can be expressed as a mathematical function of the magnetic field, number density, electron temperature, and electric field.

$$v_{e_z} = \mu_{eff} \left[E_z - \frac{1}{n_e} \frac{d}{dz} (n_e T_e) \right] \tag{26}$$

$$v_{e_z} = \frac{m_e \vartheta_{eff}}{eB^2} \left[E_z - \frac{1}{n_e} \frac{d}{dz} (n_e T_e) \right] \tag{27}$$

The effective mobility at the channel exit is given by the following equation.

$$\mu_{eff} = \frac{e}{m_e}\frac{\vartheta_{eff}}{\omega_c^2} \tag{28}$$

$$\mu_{eff} \propto \frac{1}{B^2} \tag{29}$$

The effective mobility exhibits an inverse relationship with the square of the magnetic field. Consequently, as the magnetic field decreases below the optimum value, the velocity in the axial direction, *i.e.*, across the magnetic field, increases. This deduction is based on the inherent confinement property of magnetic fields. By ohmic heating, we now know that the lower the confinement, the lower the temperature of the electron. Furthermore, according to Choueiri[66], this also applies to potential energy decrease.

$$T_e = \beta_e \phi \tag{30}$$

As the electron traverses the channel, its potential energy increases due to collisions, leading to an accompanying increase in the electron's thermal energy. The relationship between the decrease in magnetic field and confinement, leading to a decrease in electron number density, has been discussed in previous studies. The correlation between electron number density and temperature is established as [67].

$$n_e \geq 1.6X10^{12} T_e^{\frac{1}{2}} (\triangle E)^3 \tag{32}$$

Baranov [68] expresses the relationship based on empirical evidence as follows.

$$E_z^2 \cong B^2 \frac{(T_{e)_{max}}}{m_e c^2} \frac{\vartheta_1}{\vartheta_1 + \vartheta_2} \; or \; E_z^2 \simeq \frac{J_{ez} B T^{0.5}{}_e}{n_e} \tag{32}$$

The potential gradient varies in response to a decrease in the magnitude of the magnetic field, which consequently leads to a decrease in the magnitude of the electric field. Thus far, our discussion has centered around the electrons, the species that become magnetized in the discharge channel. While the magnetic field does not magnetize ions and, therefore, does not alter their direction of motion, it does impact the ionization process and the closely associated acceleration process.

Consequently, the ions are affected, leading to variations in their overall motion and influencing plasma parameters. A decrease in the magnetic field below the optimum operating condition results in a reduction of the electron temperature, thereby decreasing the energy levels of electrons. The lower energy levels result in the shift of the ionization and acceleration region upstream towards the anode. Thereby, the length of the acceleration region increases, as represented by Kim [48].

$$L_a \cong \sqrt{\frac{mV_d}{eB_r^2} \frac{\vartheta_e}{\vartheta_i}} \tag{33}$$

$$\frac{V_d}{B_r^2 L_a b_c} = constant \, , \qquad L_a \propto \frac{1}{B_r} \tag{34}$$

As the magnetic field decreases, the ions experience an increase in potential for acceleration. However, due to the ionization and acceleration region moving upstream results in increase in loss voltage due to wall collision which consequently results in a decrease in acceleration voltage and ultimately decreases the velocity of ions.

$$v_i = \sqrt{\frac{2qV_a}{m_p}} \tag{35}$$

Further discussing potential, it is worth noting that the plasma potential denotes the electrical potential energy of the charged particles with respect to the ground. A decrease in electron temperature affecting the collision process results in a decrease in the plasma potential as the magnetic field decreases. These effects are incorporated in the performance parameters as follows.

$$I_d = n_e(v_e - v_i)qA \qquad v_e \propto \frac{1}{B} \quad I_d \propto \frac{1}{B} \tag{36}$$

$$T = 2n_i q_i A V_a \qquad T \propto B \ , \ T/P_d \propto \sqrt{B} \tag{37}$$

$$I_b = n_i q v_b A \qquad I_b \propto B \tag{38}$$

$$\eta_b = \frac{I_b}{I_d} \qquad \eta_b \propto B \tag{39}$$

$$\eta_m = \frac{\dot{m}_b}{\dot{m}_a} \quad \dot{m}_b \propto B, \qquad \eta_m \propto B \tag{40}$$

$$\eta_v = \frac{V_a}{V_d} \qquad\qquad V_a \propto B \tag{43}$$

$$\eta = \frac{T^2}{2\dot{m}_a P_d} \qquad\qquad \eta \propto \frac{1}{B} \tag{42}$$

Decrease in the magnetic field reduces the thrust and efficiency of the HET despite the increase in discharge current. This efficiency decrease is observed due to the influence of the magnetic field on electron motion being more pronounced. However, as the magnetic field decreases, the acceleration voltage and mass utilization efficiency decrease, further negatively impacting the thruster efficiency.

Naoji[65] also introduced another set of stability criteria for HETs derived from experimental deduction. These criteria are expressed as the following:

$$(Av_e)_{exit} - (Av_e)_{anode} - \left(\sigma_{d_i}\vartheta_e\right)_{T_e} > 0 \tag{43}$$

As the temperature of electrons decrease, the ionization cross-section decreases. This decrease in the velocity of electrons causes the left term to become more negative, resulting in instability. Thus, it is essential to understand how magnetic fields affect ionization and electron velocity. Based on this study, we believe that the farther we are from the optimal magnetic field for the thruster operating conditions, the greater the

likelihood of instability. However, the extent of these effects depends on how far we are from the optimal magnetic field configuration.

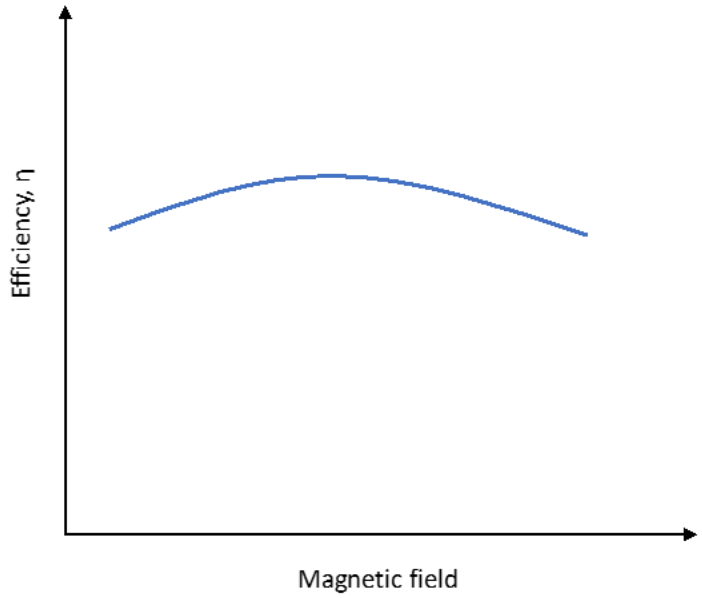

Figure 14 – Predicted thruster efficiency variation as a function of magnetic field strength.

Conducting further research in this field will aid in the validation of this assertion. Importantly, anomalous electron diffusion, wall collision, and thermal effects can alter the motion of electrons across a magnetic field, causing them to deviate from the stated relationship. In such cases, additional research is required to validate the theoretical deduction. The current model incorporates a deviation of the HET from the optimized magnetic field configuration to provide an overview of the effects.

In order to substantiate the inferences drawn in the model regarding the impact of magnetic field variation on plasma parameters, Chapter 4 discusses the experimental

investigation performed to observe the modifications in plasma parameters that the model highlights in response to thruster operating conditions accompanied by magnetic field variation below the optimum value.

3.2.3 Azimuthal Magnetic Field Gradient Effects on Plasma Parameters

The models previously devised assume a uniform magnetic field is present in the HET channel. A modified version of the model presented in the preceding section is built to investigate the effect of a magnetic gradient in the azimuthal direction on the plasma parameters that influence HET performance.

The channel's azimuthal gradient enables the modification of properties in both the radial and axial directions. These gradients result in a complex three-dimensional problem that is exceedingly difficult to resolve. Consequently, it is necessary to make critical assumptions to facilitate the development of the model and establish a correlation between the azimuthal gradient magnitude and the thruster performance parameters. The present model is based on the following assumptions 1) The focus is solely on the azimuthal gradient, disregarding the radial gradient that is present in the channel 2) Ignoring the wall interactions, which could lead to losses as a consequence of recombination and electron emission 3) Developing the model at the maximal magnetic field region near the exit plane and disregarding the gradient in the axial direction.

Now, when examining the specific area of interest in the channel, we divide it into two distinct regions. As depicted in Figure 15, region 1 denotes the presence of a uniform magnetic field with a high magnitude, while region 2 indicates the area where the magnetic field is decreased to establish an azimuthal magnetic field gradient within the channel. A

detailed look at the area shows that electrons enter from the length border and depart from the right boundary, providing a clear visual of the process.

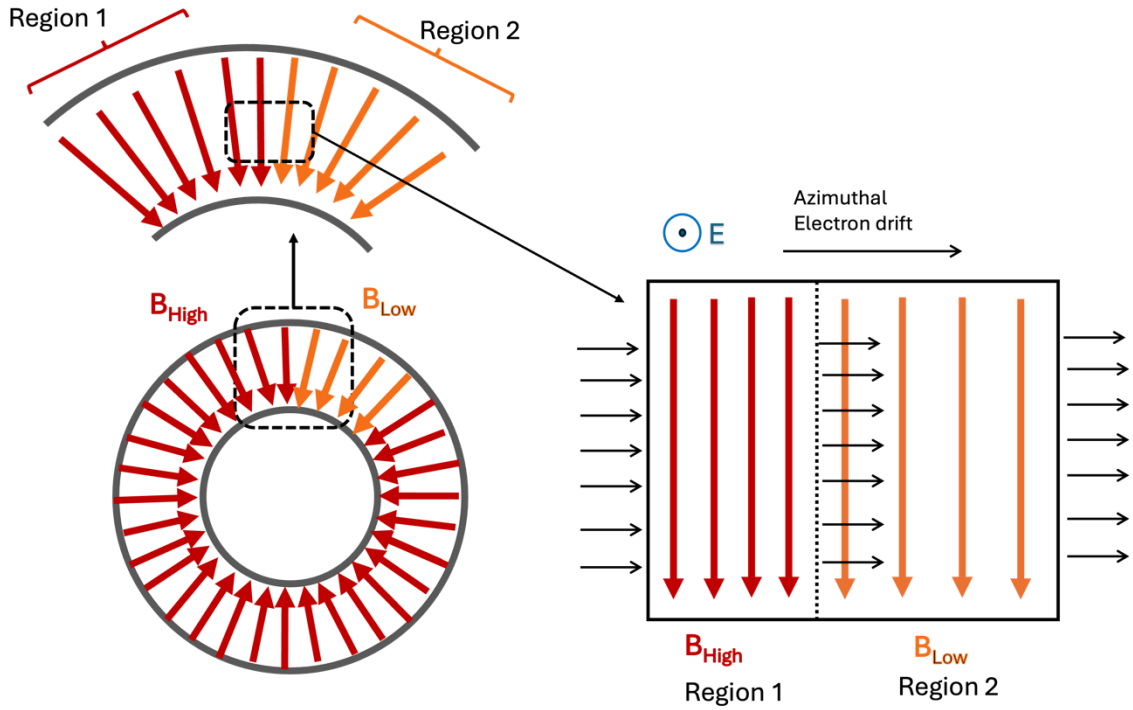

Figure 15 – Azimuthal electron drift motion in the presence of azimuthal magnetic field gradient

Electron trajectories in the HET plume and channel reveal mobility along the magnetic field and azimuthal due to the E×B field, promoting ionization and axial motion. Observing electron trajectories makes it apparent that the movement of electrons in the radial direction is influenced by energy conversion caused by the magnetic mirror effect, leading to oscillatory motion. The electron moves in a helical trajectory along the magnetic field with a gyroscopic radius known as the Larmor radius. The impact of the magnetic field on the Larmor radius is equilibrated to uphold energy conservation. This study will primarily concentrate on the azimuthal motion of electrons, which is dependent on the

strength of the magnetic field and will be the primary focus of the investigation. Electron velocity in the region can be calculated as the sum of the velocity imparted to the electron along the magnetic field and the E×B drift velocity caused by the Lorentz force, which is a consequence of the presence of perpendicular electric and magnetic fields in the channel.

$$\overrightarrow{\mathrm{v_e}} = \overrightarrow{v_\perp} + \overrightarrow{v_{(ExB)}} \tag{44}$$

$$v_e = \frac{eB_r r_L}{m} + \frac{E_z}{B_r} \tag{45}$$

As the magnetic field shifts from one location to another, the velocity along the magnetic field lines is balanced by the potential gradient in the radial direction. Therefore, no magnetic field impact is observed in the first term. Since we are investigating the influence of gradient in the azimuthal direction represented by *x* in Figure 15 , the existing model is utilized to discuss the effect of introducing the azimuthal gradient on the drift velocity component associated with the electron. The 1-D steady-state momentum equation provided in Equation 24 provides a suitable starting point for investigating the effects on plasma properties and HET performance while maintaining the same assumptions as the previous model. When Equation 24 is modified for azimuthal direction and compared, it establishes a relationship between axial current density and azimuthal current density that can be translated into an axial and azimuthal velocity relation.

$$v_{e_x} = v_{e_z}\Omega_e \tag{46}$$

Using Equation 24 and Equation 46, the axial current density is estimated to be influenced by axial mobility, the electric field and the pressure effects.

$$j_{e_z} = \mu_{e_z}\left(-en_eE_z - \frac{dP_e}{dz}\right) \tag{47}$$

For the current model the azimuthal direction is in cartesian coordinate and represented with variable x as shown in Figure 15. Equation 47 can be written for the azimuthal current density as

$$j_{e_x} = \mu_{e_z}\,\Omega_e\left(-en_eE_z - \frac{dP_e}{dz}\right) \tag{48}$$

$$j_{e_x} = \mu_{e_x}\left(-en_eE_z - \frac{dP_e}{dz}\right) \tag{49}$$

The azimuthal mobility is expressed as the sum of the axial mobility and the Hall parameter. It is utilized to establish the connection between the azimuthal drift velocity of electrons and the azimuthal magnetic field gradient within the channel.

$$\mu_{e_x} = \mu_{e_z}\,\Omega_e \tag{50}$$

Thus, the azimuthal velocity of electrons from Equation 46 can be written as a function of electron mobility.

$$v_{e_x} = \mu_{e_x}\left(-E_z - (\frac{1}{en_e})\frac{dP_e}{dz}\right) \tag{54}$$

$$P_e = n_e k\, T_e \tag{52}$$

$$v_{e_x} = \mu_{e_x}\left(-E_z - (\frac{k}{en_e})\frac{d(n_e\, T_e)}{dz}\right) \tag{53}$$

To estimate the changes in the azimuthal direction due to the azimuthal magnetic field gradient, the gradient in velocity is estimated by using Equation 53.

$$\frac{dv_{e_x}}{dx} = \frac{d\mu_{e_x}}{dx}\left(-E_z - \left(\frac{k}{en_e}\right)\frac{d(n_e\, T_e)}{dz}\right) - \frac{d}{dx}\left(\frac{k}{en_e}\right)\frac{d(n_e\, T_e)}{dz} \tag{54}$$

$$\frac{dv_{e_x}}{dx} = \frac{d\mu_{e_x}}{dx}\frac{v_{e_x}}{\mu_{e_x}} - \frac{d}{dx}\left(\frac{k}{en_e}\right)\frac{d(n_e\, T_e)}{dz} \tag{55}$$

The gradient in the azimuthal mobility with position can be determined using the equation presented in Equation 55. The positional gradient is determined by the alterations in the Hall parameters caused by the azimuthal fluctuations in the magnitude of the magnetic field.

$$\mu_{e_x} = \Omega_e \frac{e}{m_e \nu_e (1 + \Omega_e^2)} \tag{56}$$

$$\frac{d\mu_{e_x}}{dx} = \frac{d}{dx} \Omega_e \frac{e}{m_e \nu_e (1 + \Omega_e^2)} \tag{57}$$

$$\frac{d\mu_{e_x}}{dx} \approx \frac{d}{dx} (\frac{1}{B_r}) \tag{58}$$

In order to simplify the equation, the pressure effects are ignored to estimate how the velocity is changing without thermal motion change into account.

$$\frac{dv_{e_x}}{dx} = -\frac{d\mu_{e_x}}{dx} (E_z + \left(\frac{k}{en_e}\right) \frac{d(n_e T_e)}{dz}) \tag{59}$$

$$\frac{dv_{e_x}}{dx} \propto (-\frac{d}{dx}\left(\frac{1}{B_r}\right)) \tag{60}$$

As the electron moves across region one to region two, the magnetic field decreases across the boundary, resulting in a negative azimuthal gradient in the magnetic field. This negative gradient increases the azimuthal drift velocity of electrons from regions 1 to 2, as per Equation 60. According to Equation 46, changes in the azimuthal drift velocity can cause variations in the axial velocity of the electrons.

$$\frac{dv_{e_z}}{dx} = \frac{1}{\Omega_e}\left(\frac{dv_{e_x}}{dx} - v_{e_z}\frac{d\Omega_e}{dx}\right) \tag{61}$$

$$\frac{d\Omega_e}{dx} = \frac{d}{dx}\left(\frac{eB}{m_e v_e}\right) \tag{62}$$

Due to the negative gradient introduced in the channel, the electrons' axial velocity increases as they traverse region 1 to region 2. Therefore, the azimuthal magnetic field gradient in the HET channel can influence the axial motion of electrons, which can lead to modifications in the plasma parameters.

The electron's temperature does not increase to the same extent as in the presence of a uniform magnetic field, thus decreasing the electron's overall temperature. The electron interactions that lead to ionization are diminished due to the electrons' lower overall energy, which is insufficient for collisions to induce ionization. The ionization region in the azimuthal gradient region shifts locally upstream towards the anode in comparison to the region where a uniform magnetic field is present as a result of the increase in the axial velocity of the electron due to the presence of the azimuthal gradient in the channel. This localized shift in the location of the ionization region results in an increase in the length of the acceleration region at that location, which in turn causes non-uniformities in the axial location of the ionization acceleration region in the channel. The voltage loss increases as the ionization region moves upstream at the gradient location, resulting in the ions being lost to the wall rather than being accelerated out of the channel. Therefore, the increase in voltage loss reduces the overall acceleration voltage experienced by the ion particle. The decrease in the available acceleration voltage leads to a decrease

in the ion velocity, affecting the thruster's performance due to a gradient in the azimuthal magnetic field.

Equation 36-42 establishes a correlation between the thruster performance parameters and the plasma parameters. Introducing a gradient in the channel leads to an overall increase in electron velocity, increasing the discharge current. A reduction in the ion velocity and acceleration voltage leads to an overall decrease in the ion beam current. Introducing the gradient in the channel contributes to the overall decrease in the current utilization efficiency, as the discharge current and ion beam current fluctuate. The variations in the ion velocity also contribute to a reduction in the thrust and specific impulse that the ion imparts at the thruster operating configuration, as illustrated in Equation 37. The reduction in the acceleration voltage leads to a corresponding decrease in the voltage utilization efficiency, as indicated by the relationships in Equation (43). Examining the stability equation, when the axial electron velocity increases, the second component of the equation becomes more negative. This reduction leads to a decrease in overall stability, causing the thruster to operate in an unstable state.

The background knowledge of the variations in the plasma properties as the gradient is introduced is provided by the relationships established by the model to analyze the effect of introducing the azimuthal magnetic field gradient, which in turn affects the thruster performance parameters. An experimental test campaign is conducted on HET to substantiate the established relationship and address the research question for the thesis. The experiment involves the introduction of an azimuthal magnetic field gradient of varying magnitudes into the channel, and the effect of this gradient on the thruster performance and plasma parameters is observed.

CHAPTER 4 EXPERIMENT SETUP AND DIAGNOSTICS

This chapter provides a comprehensive summary of the test campaign, including details about the thruster utilized as the test article, the testing facility, and the diagnostics employed for the thesis experiment. The purpose of this chapter is to address the research question posed in the thesis. The chapter acquaints the reader with the experimental configuration and protocol employed to accomplish the aim of the present study.

4.1 Experiment Overview

The present study aims to comprehend the influence of azimuthal magnetic field gradient on the performance of a HET. In order to achieve the objective, it is crucial to observe the impact of modifying the magnetic field on the performance of the HET. The model described in section 3.2.2 helps to establish the correlation between plasma properties and magnetic field and how it affects the performance of the HETs. The homogeneous magnetic field was altered for the initial experiment test to establish experimental justification. The baseline condition for this investigation was the operation of the thruster at a fixed discharge voltage of 300 V, with a fixed anode and cathode mass flow rate of 5.61 mg/sand 0.44 mg/s, respectively. The inner coil current was 6 A, and the outer coil current was 4 A. The first test matrix involved reducing the magnetic field from 145 G to 93 G to monitor the effects on the performance parameters. A FW Bell Gaussmeter 5080 was utilized to measure the magnetic field in the thruster channel. The plasma parameters and thruster operational characteristics were measured using a variety of diagnostics, including Faraday, Langmuir, retarding potential analyzer (RPA),

oscilloscope measurement, and an inverted pendulum thrust stand. The plasma parameters were estimated using far-field measurements at a radial distance of 1m, as it was not feasible to conduct these measurements within the channel due to the facility and experimental constraints. Variations in the magnetic field are believed to affect the location of the ionization and acceleration region, as demonstrated in section 3.2.2 .In order to determine whether these assertions contained observable evidence, optical emission spectroscopy (OES) was employed to monitor the fluctuations in the plume's light intensity as the magnetic field's magnitude was altered. Changes in light intensity can assist in predicting the direction in which the ionization acceleration region moved without direct measurements inside the channel and in establishing the first-level deductions.

After examining the impact of magnetic fields on plasma properties and thruster performance, we proceed to address the research questions of this research. The effect of azimuthal magnetic field gradient on thruster performance is investigated by introducing a deliberate azimuthal gradient in the magnetic field. The magnetic circuit of the HET is divided to enable the control of various sections of the outer circuit using distinct power supplies, which can regulate the magnitude of the gradient in the magnetic field, as illustrated in Figure 16.

The magnetic circuit was divided into two sections, with two coils operating independently with the assistance of two power supplies as OC2 and OC3 coil circuits. The remaining six exterior coils were connected in series and operated by a separate power supply as OC1 coil circuit. The thruster was operated at 300 V with anode and cathode flow rates of 5.61 mg/s and 0.44 mg/s, respectively. At the baseline condition of the thruster, the inner coil power supply gives 6 A of current, while all three power supplies

are utilized for the outer circuit supply 4 A. The azimuthal gradient in the magnetic field is generated by changing the operational capacity of the outer coils from 100% to 0%. The highest azimuthal gradient in the magnetic field for the current operation is introduced when two coils in the outer magnetic circuit (OC2 and OC3) are entirely turned off, resulting in an extreme condition of 0% capacity.

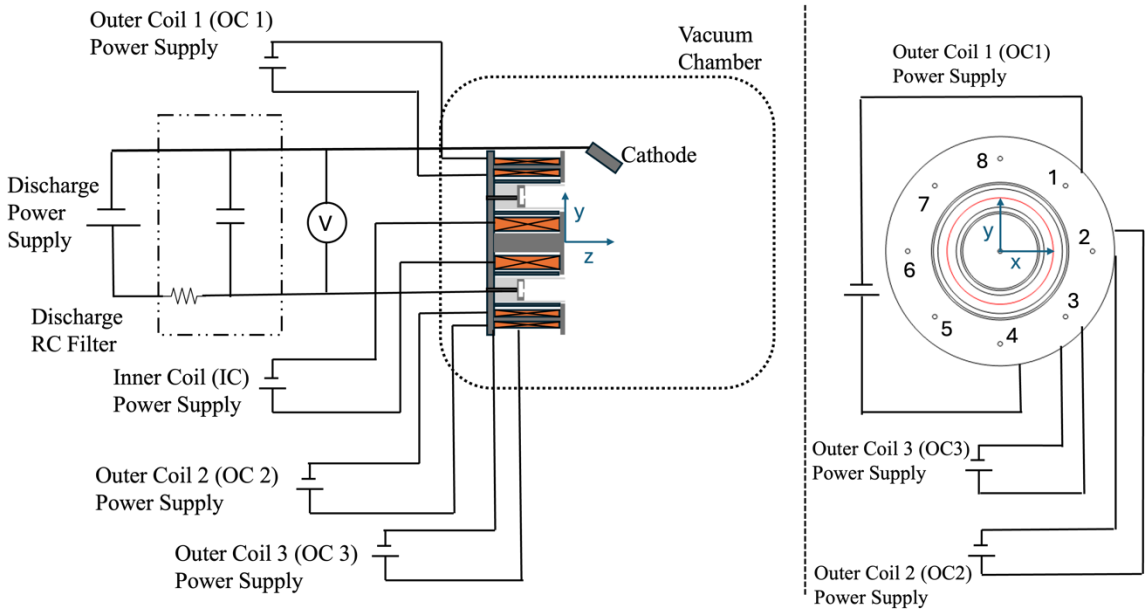

Figure 16 – Electrical schematic of test setup of P5 (left) and magnetic circuit breakdown for the current research(right).

The same diagnostics at 1 m were employed to compare to the uniform condition for measuring change in plasma parameters. The measurements are performed by systematically moving the probe arm in a radial direction, ranging from -90° to 90°, while maintaining a constant distance from the thruster center. Due to the presence of an azimuthal gradient, the plume of the HET will not be uniform; hence, it is essential to take measurements depicting the plume accurately. A three-dimensional mapping of the plume enables the observation of changes in the plume resulting from the introduction of gradients

in the magnetic field. Developing a sweep probe apparatus was necessary to monitor the fluctuations in ion beam current and generate a three-dimensional mapping of the plume. The thrust vector location was presumed to be altered by introducing a gradient, and the sweep probe apparatus could track the thrust vector for the thruster. The OES configuration, which takes measurements along a line parallel to the exit plane, cannot observe the localized shift in the ionization acceleration zone for the azimuthal magnetic field gradient because the gradient was imposed in a specific section of the channel. Consequently, the uniform magnetic fields in the initial test were adjusted to reduce the magnetic field by the same magnitude as that observed in the azimuthal gradient region. This magnetic field variation permits the estimation of the localized shift in the ionization and acceleration region resulting from the gradient's introduction.

4.2 Test Article and Equipment

The experiment presented in this study was conducted using a 5-kW laboratory HET P5, built in 1997, through a collaboration between the Air Force Research Laboratory (AFRL) and the University of Michigan. The P5 HET was used for the experiment due to its comparable performance capabilities to commercial HETs[69]. P5 features a stainless-steel anode with 36 slot holes, a ceramic discharge channel, an inner magnetic core, and eight outside magnetic cores that generate the magnetic field necessary for the functioning of the HET. The thruster comprises a boron nitride and silicon dioxide BN-SiO_2, M26 grade channel with an outside diameter of 173 mm and breadth of 25 mm[42,70]. A hollow cathode of EPL-500 was positioned at a distance of 2.2 cm downstream of the P5 exit plane and 7 cm above the centerline for thruster operation, as depicted in Figure 17.

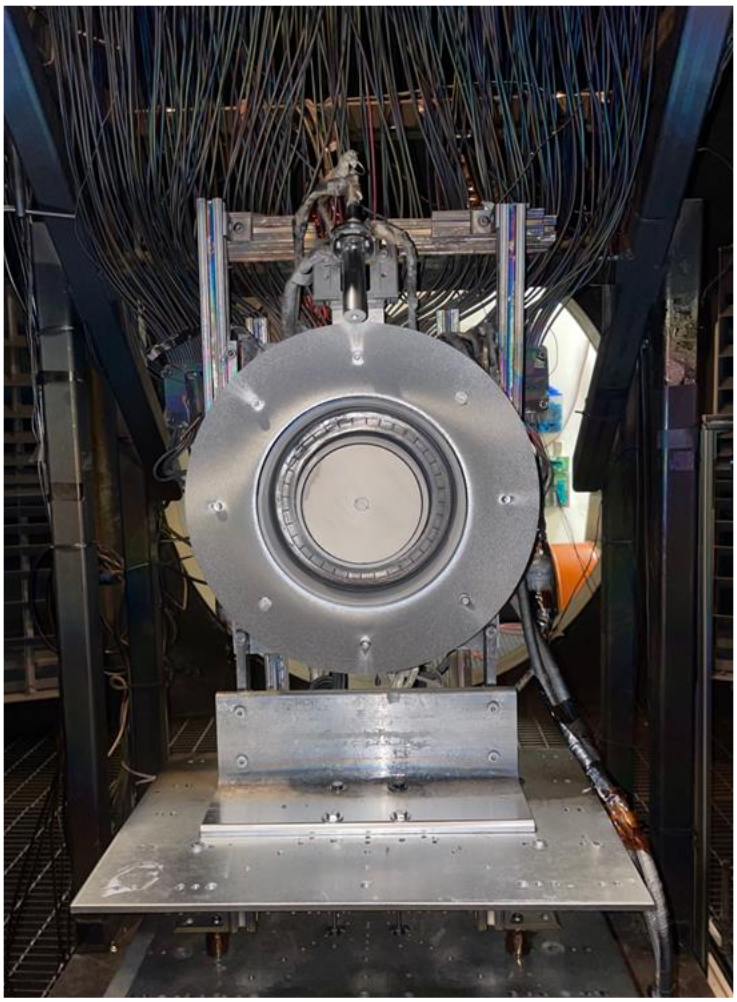

Figure 17 – P5 HET installation in Vacuum Test Facility (VTF-2)

The thruster was operated at a discharge voltage of 300 V, with an anode flow rate of 5.61mg/s and a cathode flow rate of 0.44 mg/s of krypton. MKS GE50A mass flow controllers were utilized to keep the anode and cathode mass flow consistent. The Mesa Labs DryCal 800 calibrated mass flow to ensure that the mass flow uncertainty remained below 2% throughout the test campaign. TDK Lambda GEN power supply was utilized to power the magnetic circuit associated with the HET. We employed a TopCon Quadro Programmable DC power supply to operate the thruster discharge. A high-power RC filter,

which consists of a 0.53-Ω resistor bank and a 100-μF capacitor, is installed in the circuit between the thruster and the discharge power supply to safeguard the discharge power supply from discharge current disturbances. A 1 GHz, 12-bit, up to 2.5 GS/s Teledyne LeCroy HDO6104 oscilloscope was employed to conduct time-resolved discharge current measurements. The discharge current and oscillations were measured with a Teledyne LeCroy CP150 current probe rated for DC up to 10 MHz. One of the four channels with a sampling frequency of 100 MS/s and a ±50 ms collection interval was used to observe thruster-telemetry time traces comprising the oscilloscope's discharge current characteristics.

4.3 Testing Facility

The thesis experiment occurred at Georgia Institute of Technology High-Power Electric Propulsion Laboratory in Vacuum Test Facility 2 (VTF-2). As shown in Figure 18, the facility comprises a stainless-steel cylinder with domed end caps with a diameter of 4.6 m and a total length of 9.2 m. In order to replicate the space environment, a high vacuum is necessary for the operation of HETs. The chamber of VTF-2 creates a high vacuum environment in two stages. Initially, the facility's base pressure is raised from atmospheric conditions to approximately 2.5×10^{-2} Torr by a single-stage, rotary vane SOGEVAC SV630 B mechanical pump, which is supported by a Leybold RUVAC RA 5001 root blower. After the chamber outgases, and the leak rate has decreased to less than 0.1 mTorr/min, the compressor and mechanical pump assembly are deactivated. Consequently, ten liquid nitrogen-cooled CVI TM1200i cryopumps connected to two Stirling Cryogenics SPC-4 compressors are activated to achieve a high vacuum with a base pressure of less than 1×10^{-8} Torr-N_2. A Stirling Cryogenics SPC-8 closed-loop,

recirculating nitrogen liquefaction system supplies liquid nitrogen (LN2) to each cryopump at temperatures ranging from 90 to 110 K via vacuum-jacketed feed lines.

Figure 18 – Vacuum Test Facility (VTF-2) at HPEPL

The pressure is measured using two MKS Granville Phillips 370 Stabil-ion gauges, which are situated 0.3 m downstream of the thruster departure plane and 0.6 m from the thruster centerline, and one Agilent Bayard-Alpert (BA) 571 hot-filament ion gauge on the chamber flange. The Agilent XGS-600 Gauge Controller is employed to modulate the outer ion gauge. In contrast, the Granville Phillips 370 Controller provides precise pressure measurements for the ion gauges within the chamber. The XGS-600 controller's facility

pressure readouts were digitally collected using LabView software at two data samples per second. During testing, the two ion gauges inside the chamber showed nominal operating pressures of 5.9×10^{-6} Torr-N_2 and 1.1×10^{-5} Torr-N_2. The facility maintained a base pressure of 2.55×10^{-9} Torr-N_2 and an operational pressure of 3.1×10^{-6} Torr-Kr throughout the experiment.

4.4 Diagnostics

The diagnostics employed to quantify various plasma parameters included a Sweep probe apparatus, Faraday Probe, Langmuir Probe, RPA, OES, and inverted pendulum thrust stand. The Sweep Probe Apparatus, Faraday Probe, Langmuir Probe, and RPA are mounted on a radial arm driven by a Parker Daedal 200RT rotary motion stage and positioned 1m from the thruster output plane. The OES set-up is situated on a Parker Daedal 406XR precision linear motion stage with a 2000 mm operating length, 0.5 m from the thruster centerline. Figure 19 depicts the P5 HET placed in VTF-2 with all diagnostic probes in the frame.

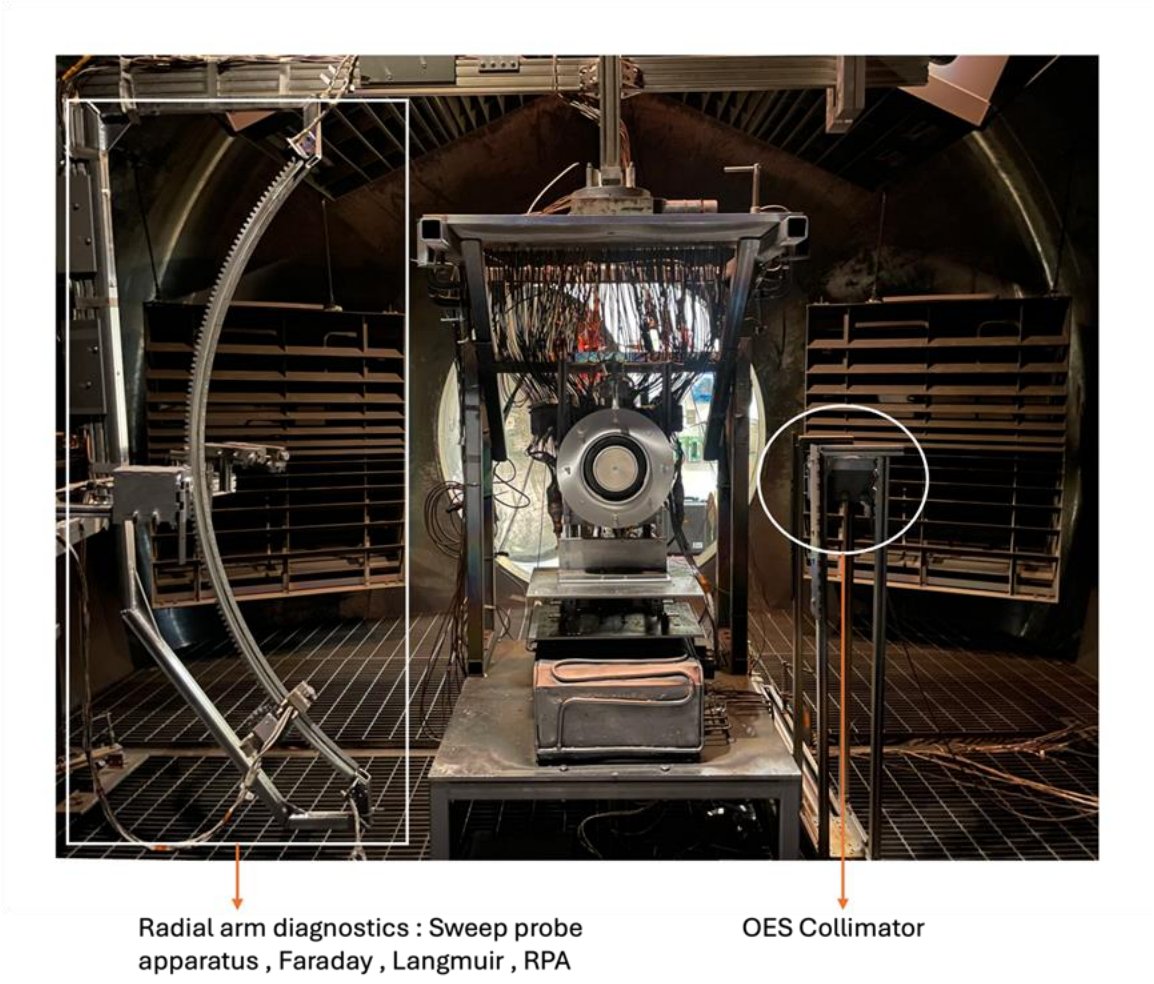

Figure 19 – Experimental test setup providing a full view of all the diagnostics utilized in the study.

4.4.1 Sweep Probe Apparatus

Several investigations have been carried out to examine and study the three-dimensional plume measurements and thrust vectoring capabilities of the thrusters during operation. Various thrust vector measurement systems have been developed utilizing the Faraday probe, double Langmuir, cylinder rods, and retarding potential analyzer (RPA) [71–76]. Though the studies conducted demonstrated promising results, there were limitations due to complex electronic setups with multiple probes and less coverage of ion

beam. Hence, a Sweep probe apparatus is designed to provide the characteristics of a three-dimensional plasma beam, offering a comprehensive measurement setup for plasma non-uniformities and potential use in studying the thrust vectoring capabilities of thrusters. The equipment sweeps a Faraday Probe vertically across the HET plume while spanning radially using a radial arm to gather three-dimensional ion currents. The objective of the current hemispherical sweep probe apparatus is to provide three-dimensional plume characterization of the HET plasma plume in terms of the ion beam current. The three-dimensional mapping of the ion beam current is provided using the Faraday probe as the primary ion beam current measuring device in the apparatus. For this undertaking, the following objectives and requirements are identified:

1) The diagnostic apparatus enables precise and repeatable characterization to facilitate plume measurement.

The objective emphasizes the need for precise and dependable measurement with less than 2° deviations. The criteria are derived from the guidelines outlined in the recommended practices for precise measurements utilizing the Faraday Probe[77]. This criterion restricts measurement uncertainty to less than 2°, enabling the translating mechanism to operate with minimal tremble and optimum position control.

2) Orthogonality must be maintained between the probe collector surface and the ion beam.

The current objective necessitates that the probe collection surface remains orthogonal to the plume to maximize the surface area for ion beam current collection. Additionally, it promotes the reduction of sheath potential effects that occur when ions interact with the collector plate.

3) Capability to provide continuous sweep measurements throughout extended periods of testing.

The objective enables the probe setup to be used for many tests over a long period of time, with the ability to withstand considerable temperature and pressure variations in the vacuum facility environment. The requirement necessitates that the probe instrument possesses robustness and longevity to ensure its sustained utilization in the future.

4) The impact of the probe's presence in the plume on the floating potential of the thruster is negligible.

This objective aims to provide guidance for designing the sweep probe apparatus to minimize its impact on the plasma and the thruster operating conditions, ensuring accurate plasma performance characteristics.

5) Capability to regulate the frequency of measurement or data sweeps of the plume.

The capacity to regulate the frequency of measurements facilitates the acquisition of comprehensive and spatially specific data at the intended locations of interest. The sweep probe apparatus enables the operator to collect more extensive data sets in concentrated areas, such as the centerline for thrust vectoring or plume endpoints for facility effects.

6) A lightweight, simplistic design featuring minimal back sputtering.

The simplistic, lightweight design of the sweep probe apparatus allows for easy installation and utilization of the setup for various testing conditions. It also increases the data collection capabilities of the testing facility, aiding in the advancement of the understanding of the plasma plume.

The design objective provides a detailed requirement needed to be fulfilled by the sweep probe apparatus for successful validation and utilization. These goals are accomplished by the current apparatus consisting of a geared face curved framework/track, a motion-controlled gear, a probe mount, and probe electronics incorporated into the sweep probe apparatus to enable the probe to be swept across the plasma plume. Due to its adaptability and simplicity, the design permits the attachment of diverse probes to acquire plasma properties at distinct locations within the plume. The current design utilizes a Faraday probe to detect the ion beam current across the plume.

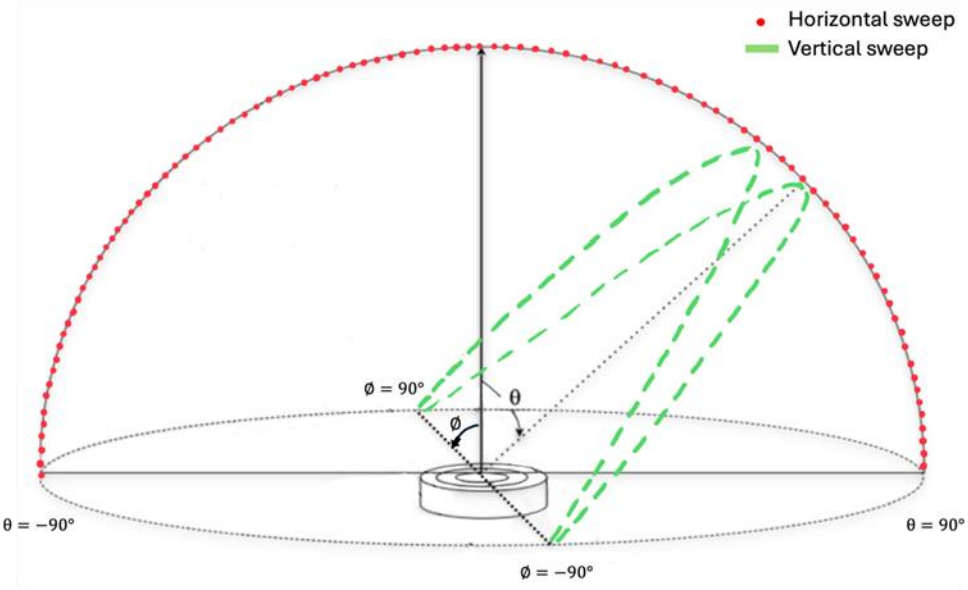

Figure 20 – Schematic of Faraday probe sweep path for the sweep probe apparatus

The apparatus consists of a circular framework with a radius of 1 meter, constructed from lightweight aluminum, as depicted in Figure 21. The framework is composed of a geared track on one side and a curved flat surface insulated from the plume using graphite fragments on the other side. A slot is created in the aluminum structure to accommodate

motion bearings and preserve the orthogonality of the probe while moving along a curved trajectory. The bearing linked to the probe mount guarantees that the probe remains in the correct orientation while sweeping through the plume. The geared track framework currently ranges from -41 to 46 °, providing a measurement span of 87 ° of the plume. The framework can be extended to 180° span in facilities without spatial restrictions such as floor and the thruster mount. The probe mount is fabricated utilizing a combination of aluminum and graphite components. The aluminum brackets are connected with the motion gear as well as the stepper motor employed for motion control. As depicted in Figure 21 the Nema 17 motor with a 50:1 ratio planetary gearbox is utilized to translate the probe along a 1m radius path via a motion gear. The stepper motor, having a step size of 1.8° per step, enables accurate gear movement along the track and provides positional control over the probe. The graphite component of the mount serves the purpose of connecting the Faraday probe to the mount while guaranteeing electrical isolation and reduced interference during measurements as seen in Figure 22. The construction of the Faraday probe adheres to the recommended principles, utilizing a stainless steel casing that is 1 inch in length and a collector coated with tungsten[77]. The Faraday probe consists of 2.31 cm diameter collector and a 2.54 cm outer diameter guard ring with a wall thickness of 0.074 cm. An aluminum collector electrode is tungsten coated to reduce the effect of secondary electron emission (SEE). The collector and guard ring are electrically isolated from each other using Macor ceramic spacers.

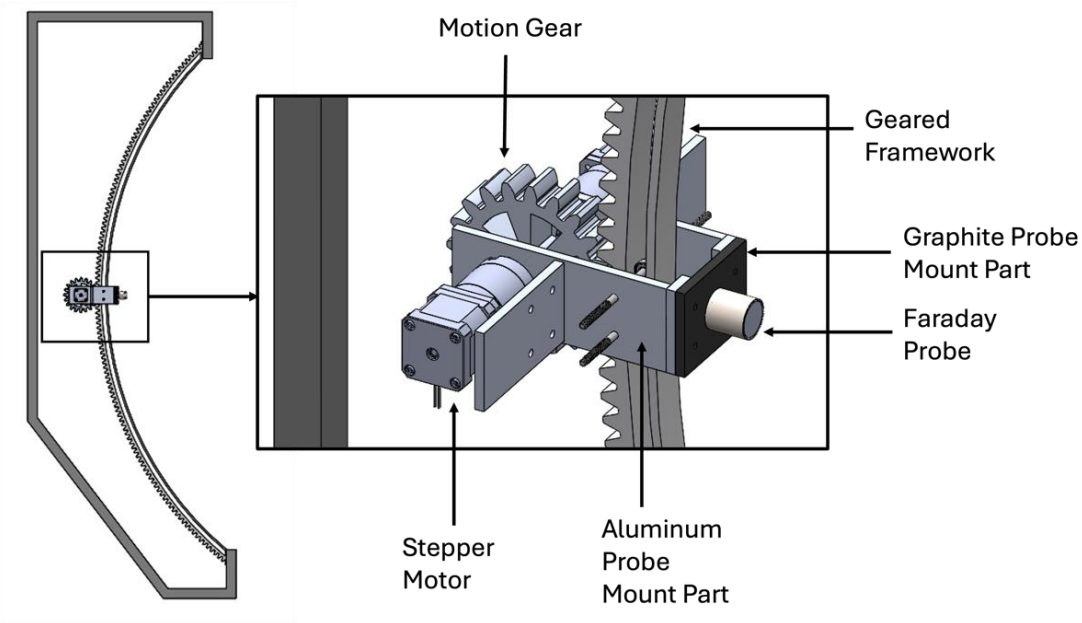

Figure 21 – Detailed rendering of the 1-m Curved Sweep probe apparatus with its components a) Stepper motor b) Motion control gear c) Gear framework d) Faraday probe, and e) Aluminum and Graphite Mount components.

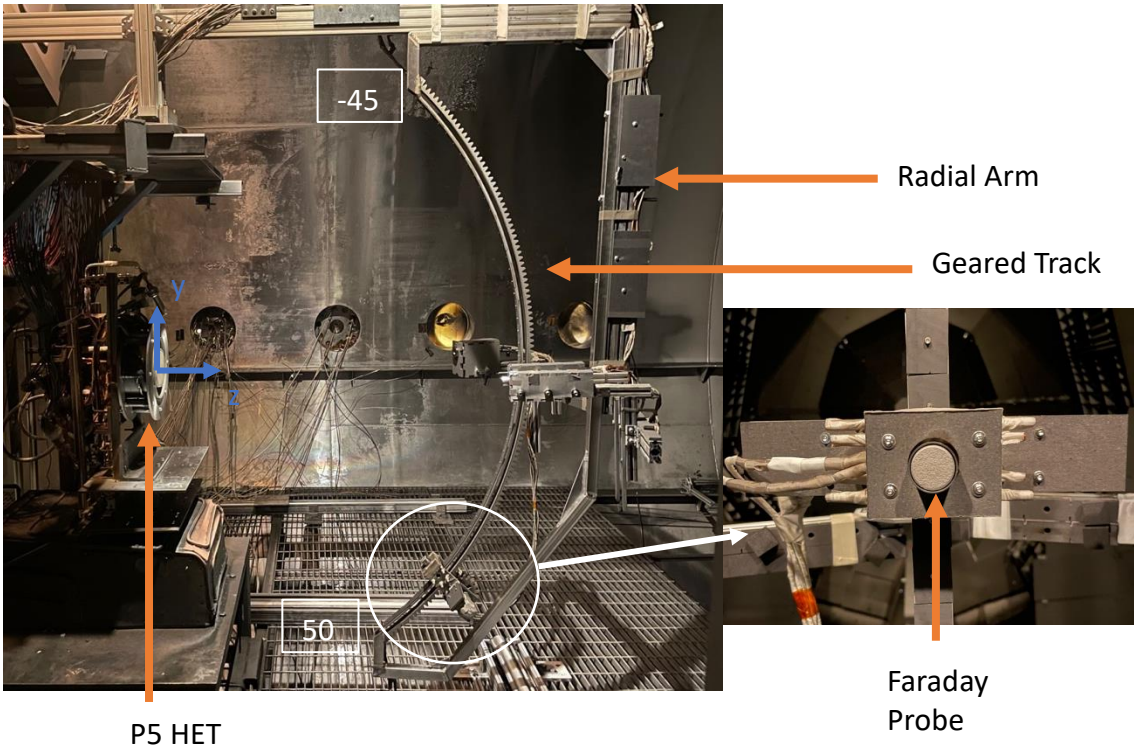

Figure 22 – 1-m Curved Sweep probe apparatus installed in VTF-2.

The Ni motion controller MID-7604/7602 allowed for the adjustment of the motor's speed during operation. A stepper motor is employed in conjunction with limit switches positioned at the endpoints to monitor the probe's location as it moves along a curved path. At -45° and 50° from the track, high-precision limit switches are arranged so that the probe mount contact can activate the limit switch circuit and halt the stepper's motion. The entire sweep probe apparatus is positioned on a radial probe arm, so that there is a 1m distance between the probe collector and the thruster exit plane in VTF-2, as seen in Figure 3. The radial probe arm is designed to undergo a sweeping motion, starting from -90° and ending at 90° with a velocity of 0.63° per second. The probe arm is controlled by a Parker Daedal 200RT series rotary table, which has an accuracy of ±17° [78], as depicted in Figure 23. The angular transverse motion and the stepper motor-driven vertical motion of the Faraday probe are controlled by Agilent 34970A Data Acquisition Unit (DAQ). LabVIEW Virtual Instrument is used to record both the probe location and the ion beam current gathered by the Faraday probe.

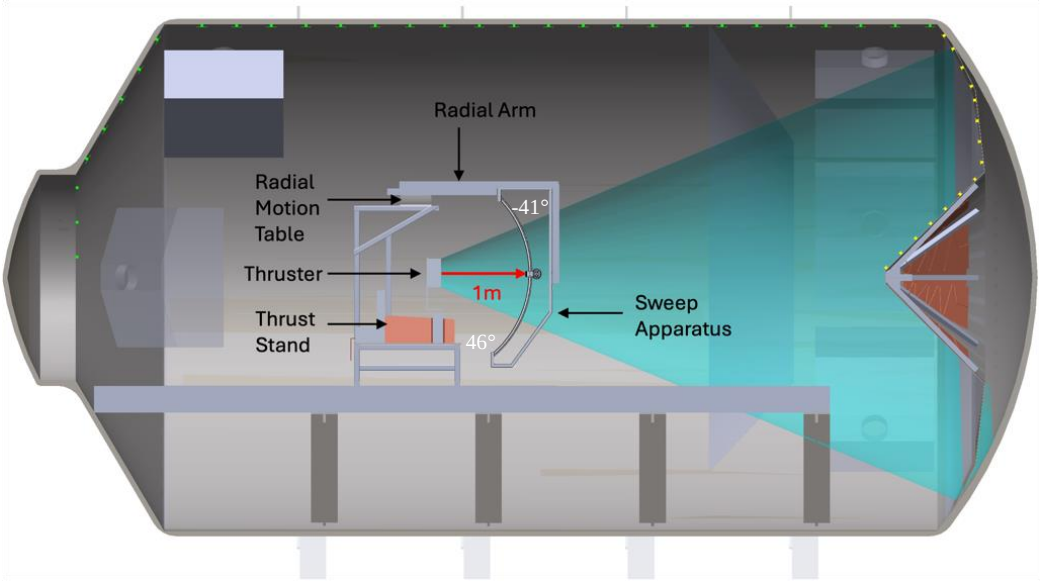

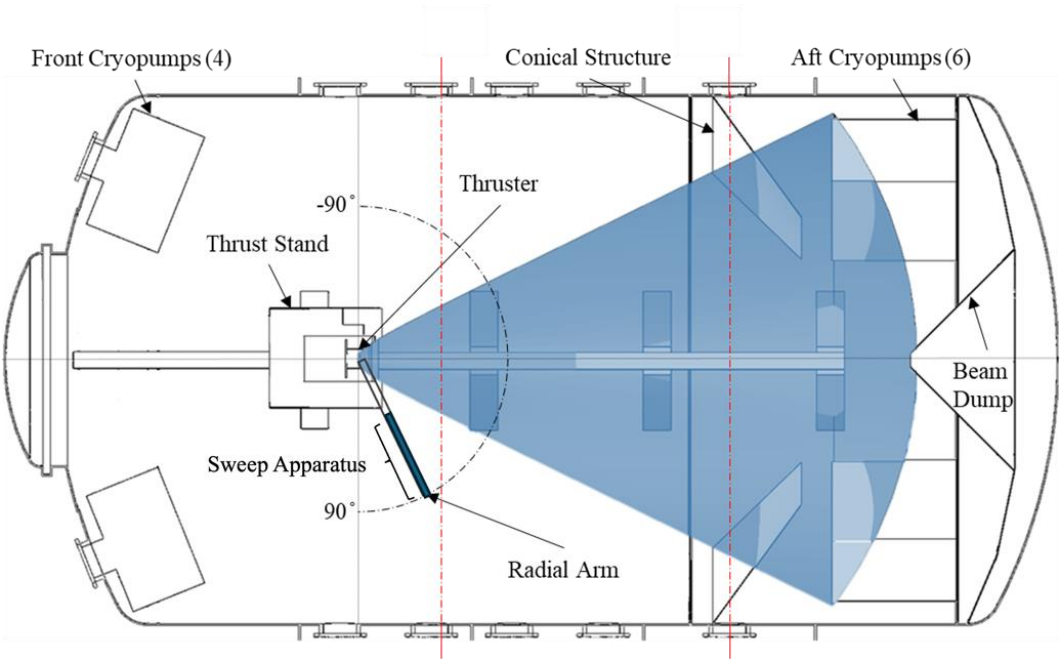

Figure 23 – Schematic of the sweep probe apparatus orientation with respect to P5 in VTF-2 chamber.

The guard and collector of the Faraday probe are biased at -30 V based on the recommended practices [77]. While taking measurements using hemispherical apparatus, three angular vertical sweeps of the Faraday probe are performed consecutively in opposite directions (-41 to 46°, 46 to -41° and again -41 to 46°) to eliminate any systematic inaccuracy caused by the motion control system. Following three vertical sweeps with the sweep apparatus, the probe arm is repositioned in a radial direction to conduct a vertical scan at the next horizontal position. Measurements are collected at intervals of 5° in the horizontal direction in the main plume, near the centerline. The multiple scans conducted using the hemispherical apparatus yielded a standard error of 1.8×10^{-7}, indicating highly repeatable measurements. The duration to perform the mapping of the entire plume region

is two hours. The collected data is subsequently examined utilizing the correction factors and methodologies outlined by Brown[79]. The method mentioned has an error of around 5% for the beam current and 1.5% for the plume divergence half-angle[77, 80]. The sample measurements obtained using the sweep probe apparatus for the baseline configuration of P5 operating at 300V is shown in Figure 24.

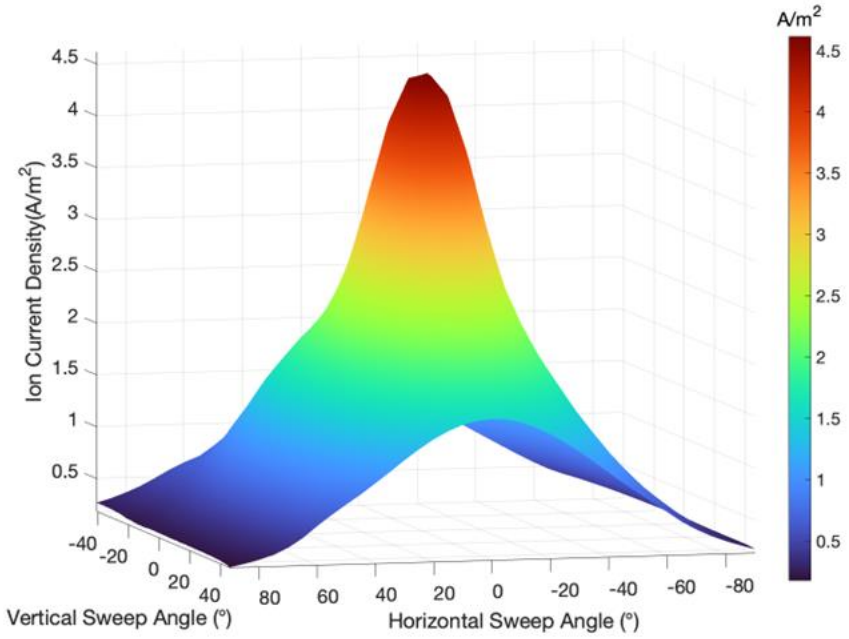

a)

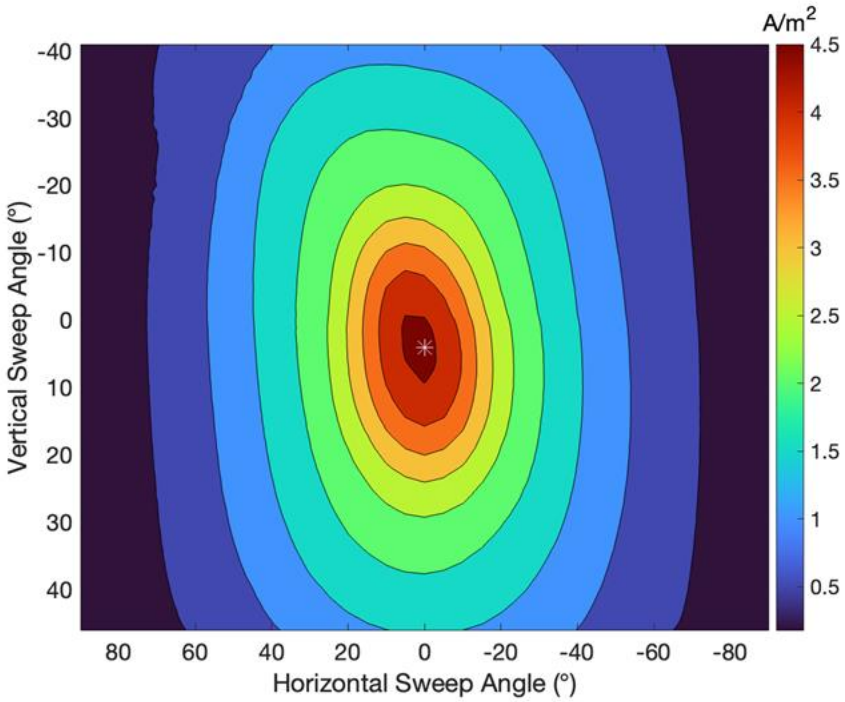

b)

Figure 24 – Sample measurements of a) Three-dimensional ion current density variation with horizontal and vertical sweep b) Contour map of ion current density with marking of the plume center.

4.4.2 Faraday Probe

Faraday probes are flat electrodes specifically designed to measure ion current. The electrode is negatively biased about the local plasma potential, resulting in the collection of only ions. In conventional testing, the Faraday probe crosses the HET plume at a set radial distance, resulting in a spatially specified ion current density distribution function. To estimate the ion beam current and beam divergence half-angle, θ_{div}, the ion current density distribution function is first determined and then integrated across space under the assumption of axisymmetric condition. As previously mentioned, the current research

involves mounting the Faraday probe on a rotary table and sweeping the plasma plume at a radial distance of 1 m to create a semicircle with the thruster at its center. Figure 25 illustrates the conventional Faraday probe's standard trajectory sweep.

The conventional use of the Faraday probe on the radial arm, as illustrated in Figure 25,adheres to the same design principles as the Faraday Probe affixed on the 3D sweep probe apparatus. The collector and guard ring are biased at -30 V relative to the ground using a Keithley 2470 Sourcemeter. A Parker Daedal 200RT series rotary table with a positional accuracy of ±0.17° is employed to scan the probe across the plasma plume at a velocity of 0.63°/s, passing from -90° to +90°. We conducted three scans per operating condition to reduce measurement errors and predict uncertainty. The rotary table encoder position and current measurement from the sourcemeter were captured using a LabVIEW VI program, which also recorded the ion beam current at the respective positions.

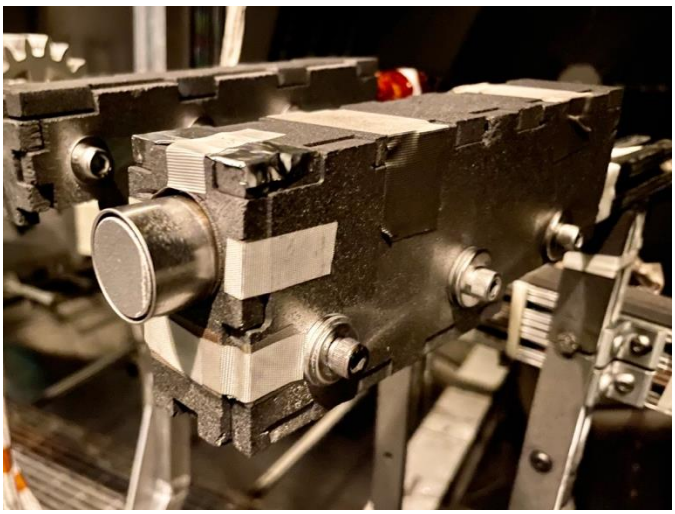

Figure 25 – Faraday probe installed on VTF-2 radial arm for horizontal ion current measurements

4.4.3 Langmuir Probe

The Langmuir probe is a diagnostic tool utilized to assess the condition of the plasma at a specific spot. Plasma parameters that comprise the state of parameters include the plasma potential, V_p, the floating potential, V_f, the electron number density, n_e, and the electron temperature, T_e. An alumina ceramic tube measuring 6.4 mm in diameter and 65 mm in length encases a tungsten tip in the Langmuir probe design. The Langmuir probe is positioned on the radial arm so that the tungsten point is directed toward the thruster. A Keithley 2470 sourcemeter was used to bias the probe from -50 V to +60 V, in 0.1 V increments, with respect to ground and measuring the current. The current is collected at the centerline of the thruster at an angular position of 0 °with respect to the thruster plume center through three consecutive voltage sweeps. A LabView program recorded the Keithley 2470 data output and calculated the local I-V characteristic curve at the centerline. Figure 26 displays an image of a Langmuir probe utilized in this experiment.

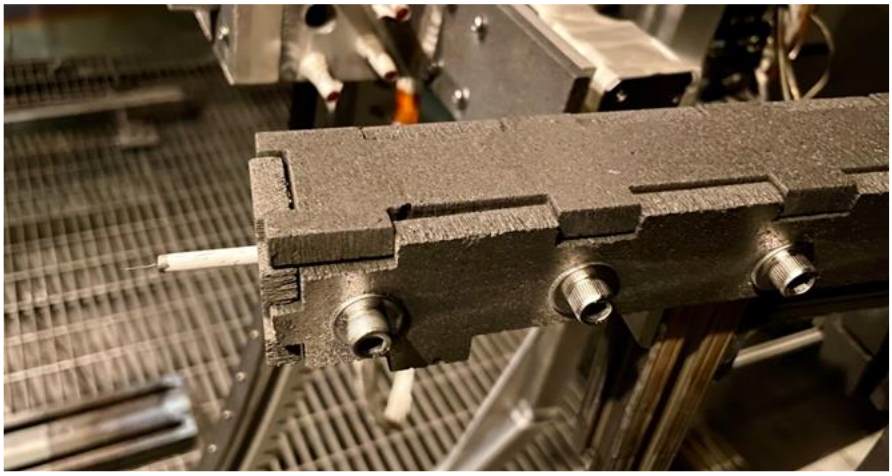

Figure 26 – Langmuir probe installed on VTF-2 radial arm for plume measurements.

The data analysis performed utilizing the I-V trace followed the underlying theories: 1) conventional, thin-sheath approximation for Langmuir probes embedded in the HET plume, or 2) thick-sheath, orbital motion-limited approximation for Langmuir probes immersed in the background plasma [81].

4.4.4 RPA

The RPA is a diagnostic consisting of four electrostatically biased grids that function as a high-pass energy filter, selectively filtering ions based on their energy [82]. The RPA is utilized to quantify the ion energy distribution within the thruster plume. The RPAs consist of four grids: the floating grid, the electron repulsion grid, the ion repulsion grid, and the electron suppression grid. The floating grid is oriented to face the plasma plume. In order to protect the plasma from the perturbations caused by the probe's presence, the floating grid is permitted to float electrically. The electron repulsion and suppression grid are biased to -30 V relative to the ground to prevent plasma electrons and high-energy secondary electrons from reaching the collector. The accumulated density function of the ions in the plasma is measured with a Keithley 2470 source meter, which measures the current that has been collected. The numerical derivative is applied to the voltage and current sweep to derive the ion energy distribution function. In order to impede the motion of the incident ions and subsequently filter the ion population based on directed kinetic energy, the ion repulsion grid is scanned with a bias voltage ranging from 0 to 450 V, with a voltage spacing of 2 V relative to the ground. The RPA is affixed to the radial arm to obtain a measurement of the centerline location with a 0° angular position about the thruster plume. Three successive voltage sweeps are conducted to account for the uncertainty and variability in data. The RPA measurement of the ion energy distribution peak between

scans of the same condition exhibited a variability of ±5%. Figure 27 displays an image of the RPA utilized in this investigation.

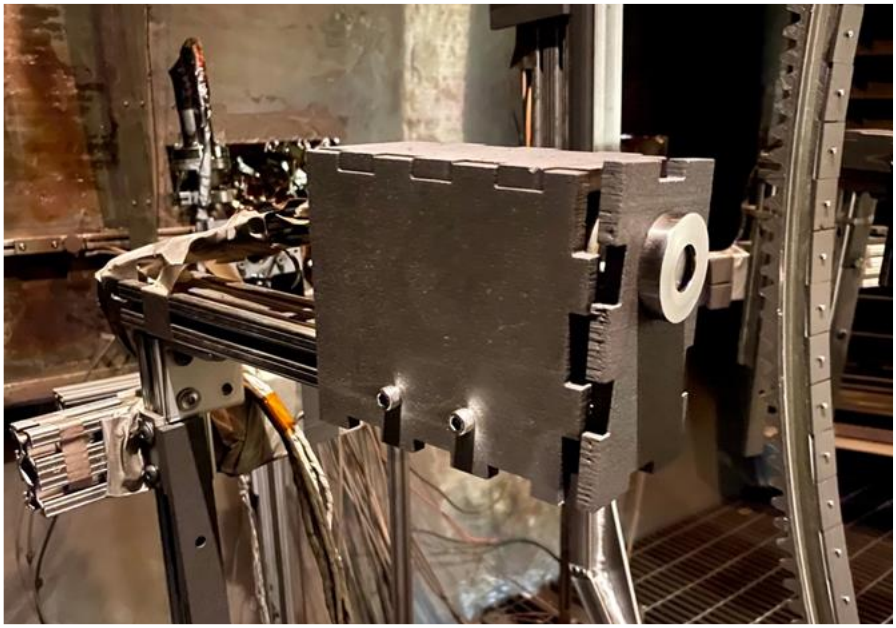

Figure 27 – RPA installed on VTF-2 radial arm for plume measurements

4.4.5 Inverted Pendulum Thrust Stand

A null-type, water-cooled inverted pendulum thrust stand is employed to measure thrust based on the thrust stand design developed by the NASA Glenn Research Center [83]. The thrust stand is composed of a pair of parallel plates connected by a series of four flexures. These flexures support the upper plate and allow it to deflect in response to an applied force as shown in Figure 28. The upper plate's position is monitored by a linear voltage differential transformer (LVDT) and regulated by two electromagnetic actuators. During operation, a pair of SIM 960 Analog proportional-integral-derivative (PID) controllers regulate the current through each actuator by modulating the current through the actuators based on the LVDT signal. This process eliminates any vibrational noise

(damper coil) and maintains the upper plate stationary (null coil). The current through the null coil, necessary to maintain the upper plate's stationary position, is directly proportional to the thrust. The thrust stand is actively water-cooled to facilitate the chilling of the null coil circuit during thruster firings in order to preserve thermal equilibrium. An 1100-W VWR International 1173-P refrigerated recirculation chiller supplies the cooling water, which does not fluctuate by more than 5 °C compared to the thruster-off condition.

The thrust stand is calibrated by employing a collection of weights that are well-known and cover the entire range of anticipated thrust values. In order to provide a measurement of the thrust at an operating condition, a linear fit is established by correlating the null coil current to the force applied to the thrust stand. The thruster was turned off for each of the three consecutive thrust measurements. Following the calibration, the thruster was reactivated, and a thermal steady state was achieved by allowing a change in temperature of less than ±0.5 °C/min before the subsequent set of measurements. This study's average thrust stand uncertainty was approximately ±2 mN (2.6% full scale), defined as the variability associated with the calibrations conducted for each scan at an operating condition.

Figure 28 – VTF2 inverted pendulum thrust stand

4.4.6 Oscilloscope for Time-Resolved Measurements

A high-definition, four-channel oscilloscope was employed to capture time-resolved measurements of the P5 discharge current. The time-resolved measurements for the discharge current I_d, the peak-to-peak variation of the discharge current $I_{d,pk2pk}$, and the root mean square measurement of the discharge current $I_{d,rms}$ were captured using a Teledyne LeCroy HDO6104A oscilloscope. This oscilloscope has a DC – 1 GHz bandwidth and a resolution of 12 bits. The oscilloscope was configured with a time base of ±5 ms and a sampling rate of 50 MS/s, with a maximum discernible frequency of 20 MHz. The characteristics of the discharge current oscillations were measured using a Teledyne LeCroy CP150 current instrument. The CP150 has a maximum rated current of 300 A and a DC – 10 MHz bandwidth. In order to monitor the oscillations generated by the HET plume, the CP150 sensor was installed at the power feedthrough that corresponds

to the anode power line upstream of the RC filter. The frequency measurements for the current study were observed below 300 kHz allowing for low losses in the discharge current measurements using the CP150 sensor. The average values of the discharge current characteristics across the five traces were determined by capturing a minimum of five oscilloscope traces for the HET discharge at each operating condition. The measurements were employed to illustrate the thruster's stability at an operating point and to comprehend the effect of the sweep probe apparatus insertion in the plasma plume on the stability and operation of the HET.

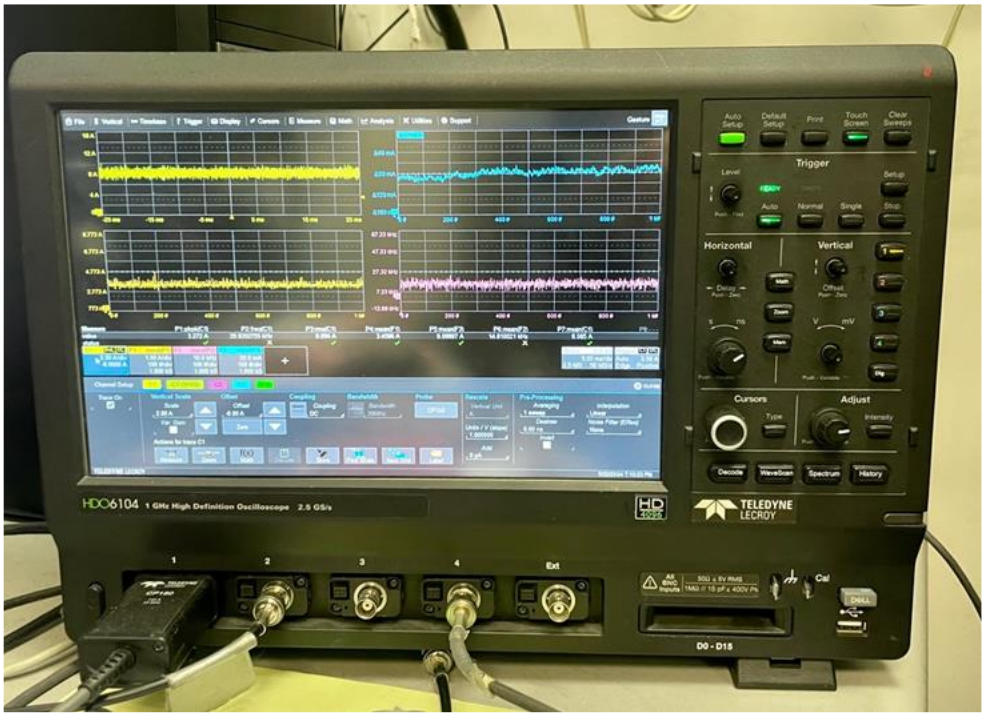

Figure 29 – Teledyne LeCroy HDO6104A oscilloscope used for the study.

4.4.7 OES Setup

OES is a diagnostic test that detects plasma composition, electron temperature, and electron number density without requiring invasive procedures[84]. In general, OES entails

the passive collection of light plasma plumes from the HET using a collimator, which is then directed through a series of fiber-optic cables before being incorporated into a portable spectrometer. A collimator is an optical device that captures the light from the plume at the desired location by arranging three pinholes. The collimator was equipped with a quartz lens to minimize the deposition of sputter material on the aperture, enabling the setup to be used continuously throughout the experiment. The collimator is engineered to concentrate the light collected on the optical fiber, which is then transported to the spectrometer. The present study employed a 100 mm-long collimator with a 0.5 mm pinhole, which enabled an ultimate resolution of 3 mm. Figure 30 illustrates that the collimator was mounted on a custom aluminum extrusion mount, which enabled the measurement to be taken at the thruster's center. The aluminum mount housing is 0.5 m from the thruster centerline and is on a Parker Daedal 406XR precision linear motion stage with a 2000 mm operating length. The linear motion stage enabled spatial measurements at axial distances of 0 mm, 5 mm, and 10mm from the exit plane.

Protecting the fiber optic cable from particle collisions and deposition, the FC-UVIR600-3-BX-VAC is a 3m-long specialized vacuum-rated fiber cable. After going through the chamber feedthrough connection, the optical fiber outside the chamber is attached to the Ocean Insight HDX-XR spectrometer. This spectrometer takes in the optical signal and returns the light spectrum from the plasma plume. The Ocean Insight OceanView software was employed to visualize and record the signals collected by the spectrometer. To carry out the current investigation, the Plasma and Dielectrics Laboratory provided a loan of an Ocean Insight OCEAN-HDX-XR. With an extended wavelength range of 200 nm to 1100 nm, this spectrometer can encompass nearly all of the anticipated

electron and ion emission wavelengths for krypton. This spectrometer has a full-width half-maximum resolution of 1 nm and an integration time range of 6 ms to 10 seconds, with a 10-micrometer aperture. The present experiment entailed the acquisition of five scans at a 100 ms interval. These five scans were averaged across the light spectrum to determine light intensity at different wavelengths. The OES system was calibrated before each scan to ensure that the saturation intensity remained at 75% and the integration time was 4000 ms. We measured the three axial positions in the background, 0.5 meters behind the thruster. The background measurements were employed to eliminate the disturbance observed in the plume measurements due to other light sources, such as the ion gauges.

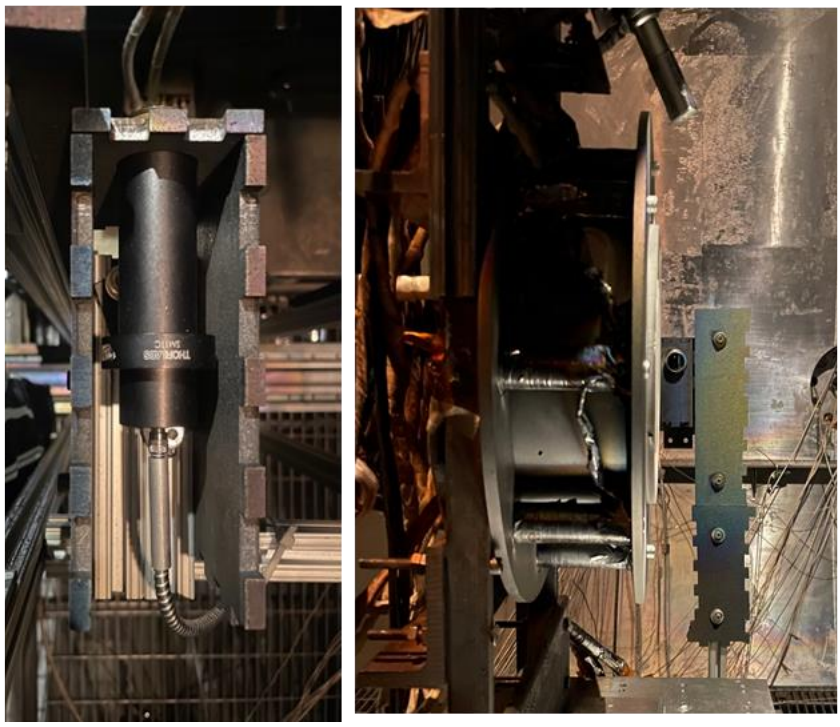

Figure 30 – OES setup collimator (left) and orientation of collimator with respect to thruster for exit plane measurements(right)

CHAPTER 5 RESULTS

This chapter presents the findings derived from the experiment to address the research question posed in the thesis. Initially, an overview of the test matrix is provided to inform the reader of the operating conditions implemented during the experiment. Subsequently, the baseline steady state condition for the thruster is established, which will serve as a basis for comparison as the magnetic field gradient is introduced into the channel. Following the establishment of the baseline test circumstances, the first test matrix occurred, which involved reducing the uniform magnetic field from 145 G to 93 G. The plasma properties, thruster characteristics, and performance parameters were derived using the diagnostics in section 4.4. The azimuthal magnetic field gradient introduced in the channel is discussed following the first test matrix. The plasma parameters and thruster performance with varied azimuthal magnetic field gradients are supplied for the reader's information.

5.1 Test Matrix

As described in section 4.1, the experiment for the present thruster consists of dividing the test matrix into two halves. The initial test matrix is created to evaluate the impact of the magnetic field on the thruster's performance. The second phase of the experiment involves the introduction of a test matrix that introduces a varying magnitude of azimuthal magnetic field gradient into the channel, allowing for the evaluation of its impact on the thruster's performance. Establishing the baseline condition is the first step in

establishing a steady-state operating condition for comparison. The thruster was ignited at a discharge voltage of 300 V, with an inner coil current of 6 A and an outer coil current of 4 A. The thruster's previous test trials determined that the anode and cathode flow rates should be 5.61 mg/s and 0.44 mg/s of krypton, respectively for thruster ignition. Iterations of thruster configurations with varying mass flow and magnetic field magnitude were carried out to identify a stable operating point. The condition with the lowest peak-to-peak discharge current ratio was established as a stable operating point. The discharge current's lowest peak-to-peak ratio was (52%) at 300 V, with an anode and cathode mass flow 5.61 mg/s and 0.44 mg/respectively and a magnetic circuit configuration of 6 A in the inner coil and 4 A in the outer coil. Once the thermal stable state was reached, diagnostic measurements were taken using various instruments such as the sweep probe apparatus, Faraday probe, Langmuir probe, RPA, oscilloscope, OES, and inverted pendulum thrust stand. A thermal steady state is a temperature change of less than 0.5 °C/min in the thruster body. The thruster took approximately three hours to achieve a thermally stable state.

Upon completion of all diagnostic measurements that established the plasma parameters and thruster performance, the test matrix 1 of the experiment, which emphasizes the impact of a change in magnetic field, was undertaken. Keeping the discharge voltage and mass flow conditions consistent with the baseline condition, the test matrix involved uniformly reducing the magnetic field of the HET. Table 3 illustrates that the reduction in magnetic field was achieved by reducing the coil currents while maintaining the same ratio between the inner and outer coils. The magnetic field exhibited a reduction of 3.4% from the baseline, followed by a further decrease of 3.4% to reach the third working condition. Subsequently, there was a 13.7% decrease and a 29.6% decrease

from the baseline. It is essential to acknowledge that the third and fifth operating conditions indicate the magnetic field reduction during the azimuthal magnetic field measurement. These conditions correspond to the deactivation of one and two coils, respectively. At each working state, measurements were obtained for Faraday, Langmuir, RPA, OES, Oscilloscope, and inverted pendulum thrust stand.

Table 3 – Operating test conditions of P5 for test matrix 1 with uniform magnetic field configuration

Test Condition No.	Condition Name	V_d (V)	I_d (A)	B (G)	$\dot{m}_c$ (mg/s)	$\dot{m}_a$ (mg/s)	IC Current (A)	OC1, 2 and 3 Current (A)
1	baseline	300	7.90	145	0.44	5.61	6.00	4.00
2	uniform 1	300	8.03	136	0.44	5.61	5.85	3.90
3	uniform 2	300	8.04	130	0.44	5.61	5.70	3.80
4	uniform 3	300	8.01	125	0.44	5.61	5.55	3.70
5	uniform 4	300	8.14	120	0.44	5.61	5.40	3.60
6	uniform 5	300	8.36	110	0.44	5.61	4.50	3.00
7	uniform 6	300	9.20	93	0.44	5.61	3.00	2.00

Proceeding to the second test matrix, we examine the introduction of the azimuthal magnetic field gradient and its effect on the plasma plume and the HET performance. The outer coil circuit was divided into three sections to facilitate the experiment. Six coils were connected in series and powered by a separate power supply. In comparison, the remaining two coils were separated to function as individual coils and powered separately, as

illustrated in Figure 16 in section 4.1. As shown in Table 4, the test matrix commences by reducing the current in coil circuit 2 by 50%, resulting in a 5.51% decrease in the magnetic field in the localized area. The subsequent operating condition entails a reduction in the current in coil circuit from 2 to 0 A, which leads to a localized reduction in magnetic field by 9.65% and an azimuthal gradient of 0.18 G/°. This is one of the primary points of the study. The subsequent condition necessitated a 50% reduction in coil current in the coil 3 circuit and the complete shutdown of the coil 2 circuit. This operating situation leads to an augmentation in the gradient and the specific region undergoing the alteration in the magnetic field. The third operating state is a 13.79% decrease in the magnetic field. The final operating condition in test matrix 2 is the complete powering off outer coil circuit two (OC2) and outer coil circuit three (OC3), enabling only the outer coil circuit one (OC1) to be operational. A gradient of 0.36 G/° and a reduction in a magnetic field by 16.55% are the outcomes of this extreme condition for the current research. Figure 31 shows the COMSOL simulation of the magnetic field line configuration with a single coil and two coils off. The simulation revealed a decrease in the magnetic field, as illustrated in Figure 32. It is crucial to acknowledge that the gradient introduced and the percentage decrease in the magnetic field for the two conditions are identical to those observed during the experiment. However, the magnetic field's magnitude varied by 48.21%. A possible reason for this is the normal wear and tear of the thruster because of the harsh test conditions used in other HPEPL test campaigns.

Table 4 - Operating test conditions of P5 for test matrix 2 with azimuthal magnetic field gradient configuration

Test No.	Condition Name	V_d (V)	I_d (A)	B_l (G)	$\nabla_\theta B_r$ (G/°)	$\dot{m}_c$ (mg/s)	$\dot{m}_a$ (mg/s)	IC Current (A)	OC1 Current (A)	OC2 Current (A)	OC3 Current (A)
1	baseline	300	7.90	145	0.00	0.44	5.61	6.00	4.00	4.00	4.00
2	gradient1	300	7.91	136	0.18	0.44	5.61	5.85	3.90	2.00	4.00
3	gradient2	300	7.94	130	0.31	0.44	5.61	5.70	3.80	0.00	4.00
4	gradient3	300	7.94	125	0.30	0.44	5.61	5.55	3.70	0.00	2.29
5	gradient4	300	8.05	120	0.36	0.44	5.61	5.40	3.60	0.00	0.00

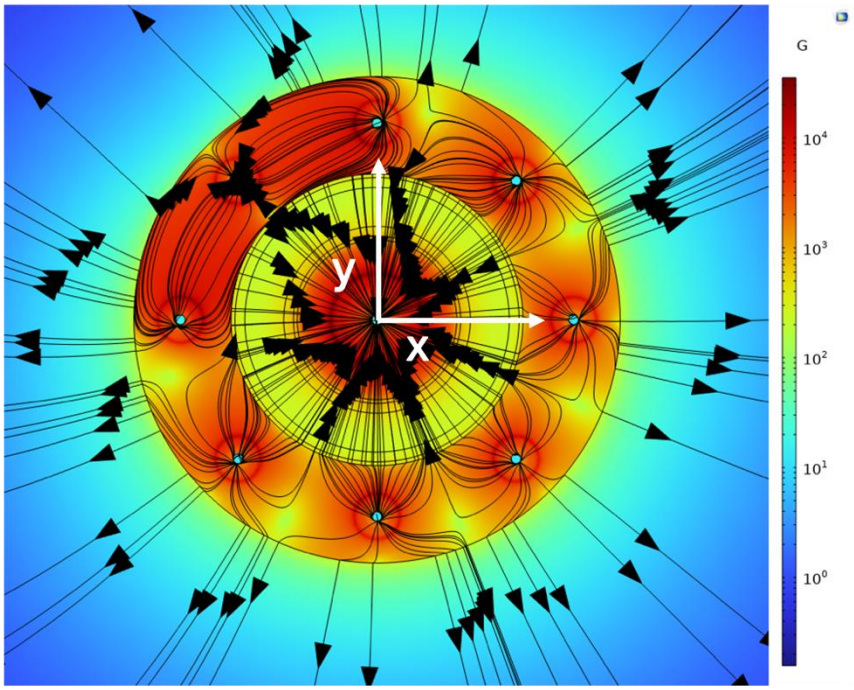

a)

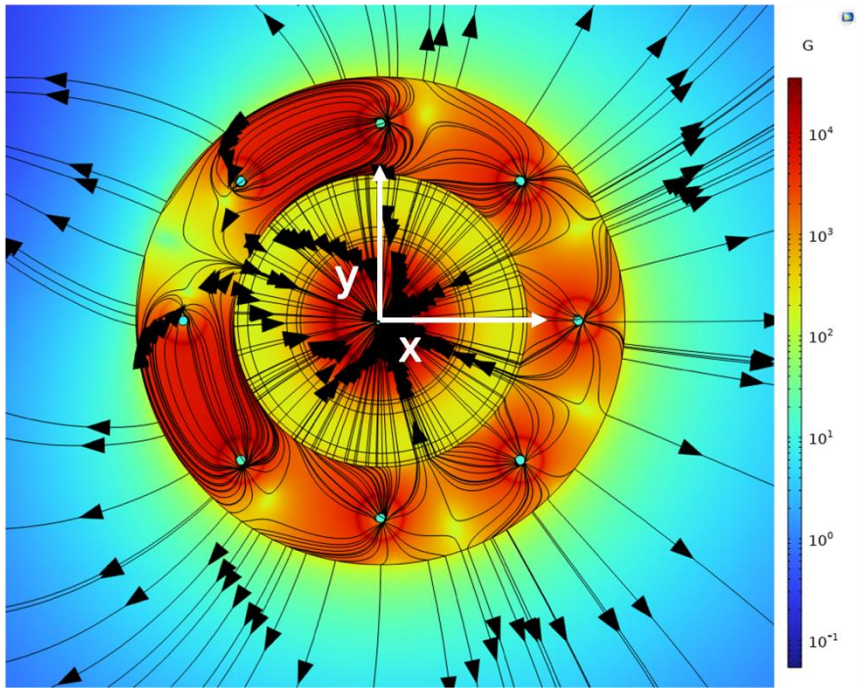

b)

Figure 31 – COMSOL simulation of P5 with 6 A IC and 4 A OC configuration for a) one coil off condition b) two coils off condition.

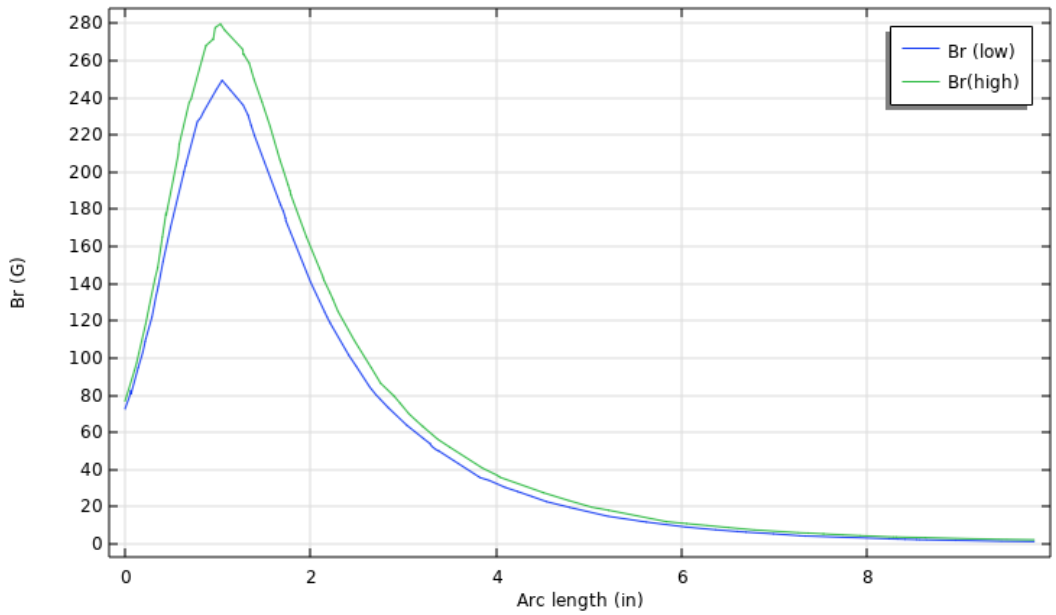

a)

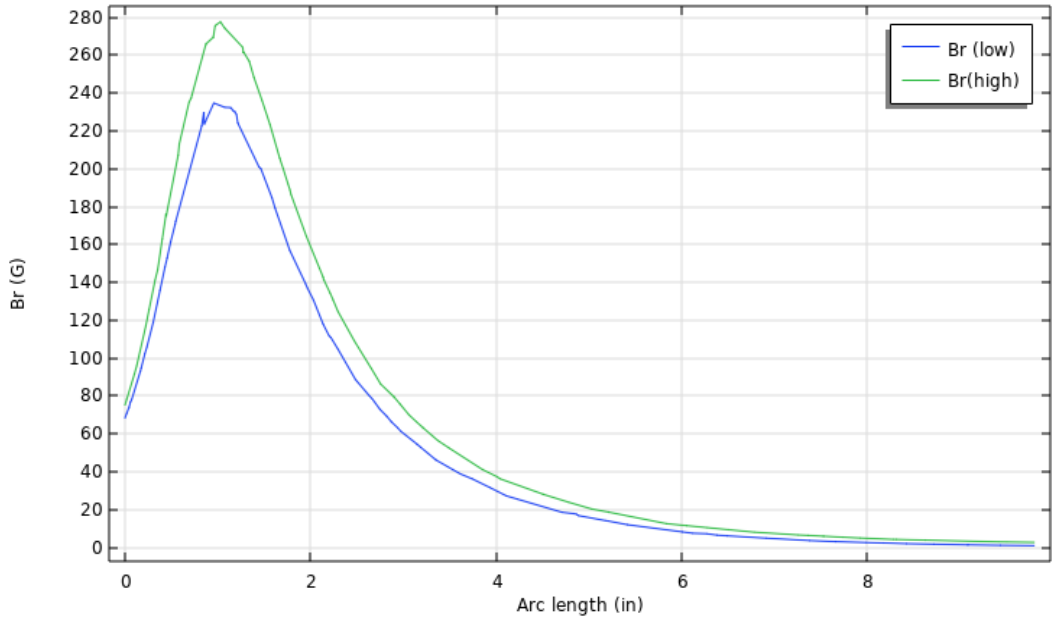

b)

Figure 32 – Axial variation of radial magnetic field [Br(low)] at the centerline of the P5 channel using COMSOL for a) one coil off condition b) two coils off condition with respect to baseline uniform magnetic field condition[Br(high)]

5.2 Baseline Condition

5.2.1 Sweep Probe Apparatus

The Sweep Probe apparatus is operated after the thruster has achieved the thermal steady state condition. The apparatus consists of a Faraday probe that collects ion current across a hemispherical area. The collector and the guard ring of the Faraday are biased to -30 V using the Keithley 2470 source meter. Measurements are conducted with a continuously sweep ranging from -41° to 46° for the probe with a resolution of 0.1°for the measurements for data analysis. After three consecutive vertical sweeps the sweep probe apparatus mounted on the radial arm is swept horizontally with an angular spacing of 5°. This results in a total of 37 horizontally positioned scans ranging from -90° to 90°. The ion current measurements from the three-dimensional sweeping of the plume can be seen in Figure 33. An ion beam current of 3.60 A with a beam divergence of 26° was obtained from the raw data from the Faraday probe. The standard error associated with the reading is of 1.8×10^{-7} deeming the measurements to be highly reliable and accurate. In order to get the total ion beam current of the plume, a horizontal scan was conducted with the sweep probe apparatus with the position of the Faraday probe at 0° in vertical direction resulting in the probe being situated at the centerline. The three-dimensional scan yielded a 37% decrease compared to the horizontal sweep in the measurement of ion beam current due to the restricted vertical sweep range. The vertical scans were extrapolated using the horizontal scan measurements to determine the potential full-scale measurement of the ion beam current while preserving the trend of ion current density variation across the 37 vertical scans. The data extrapolation resulted in measurements that span from -90° to 90° in both the vertical and horizontal directions, thereby enabling the total estimation of the

hemispherical ion current for P5 at 2.3 kW, as illustrated in Figure 34. An ion beam current measurement of 5.71 A and a divergence angle of 33.94° was obtained from the extrapolated three-dimensional ion current. The ion beam current measurements were evaluated after correcting for secondary electron emission and charge exchange at horizontal and vertical angles, yielding a 95% ion beam percentage. The hemispherical sweep mechanism had a negligible effect on the floating potential of the thruster keeping it at -5.84 V, allowing it to be used without impacting its operation. The measurements acquired with the hemispherical apparatus were subject to uncertainty. This uncertainty included a ±10% margin of error connected with the Faraday probe[77] and a margin of error of less than ±1% associated with the gear motion control system for vertical scan and a ±2% for the horizontal motion control system.

Table 5 – Calculated ion beam properties at baseline test condition on krypton using sweep probe apparatus.

Test No.	Condition Name	I_d (A)	I_b (A)	θ_{div} (°)	η_b (%)
1.	baseline	7.90	5.71	33.94	72.30

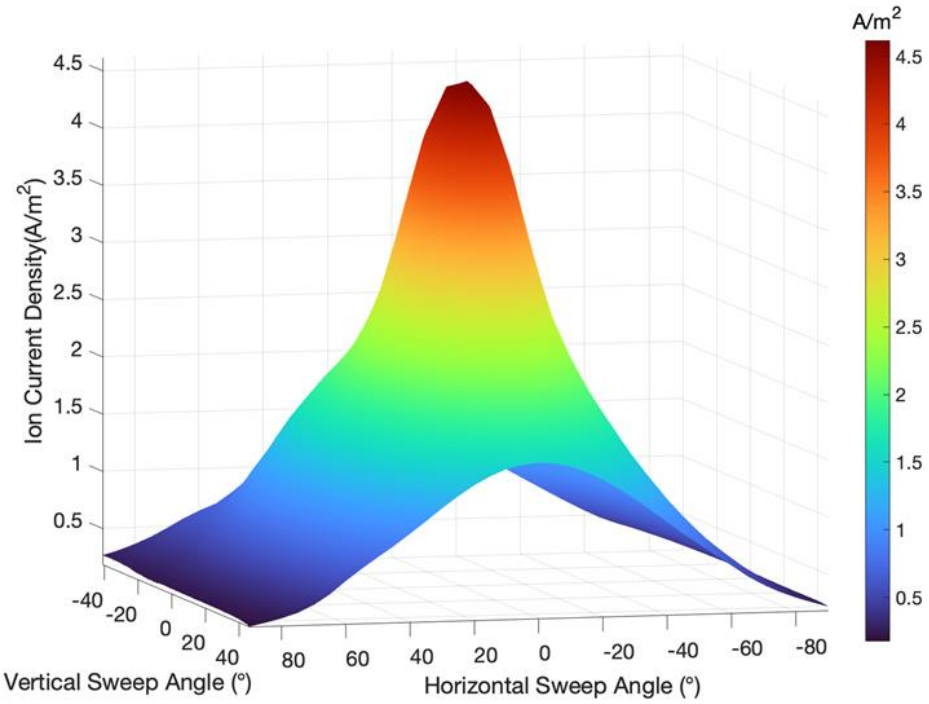

a)

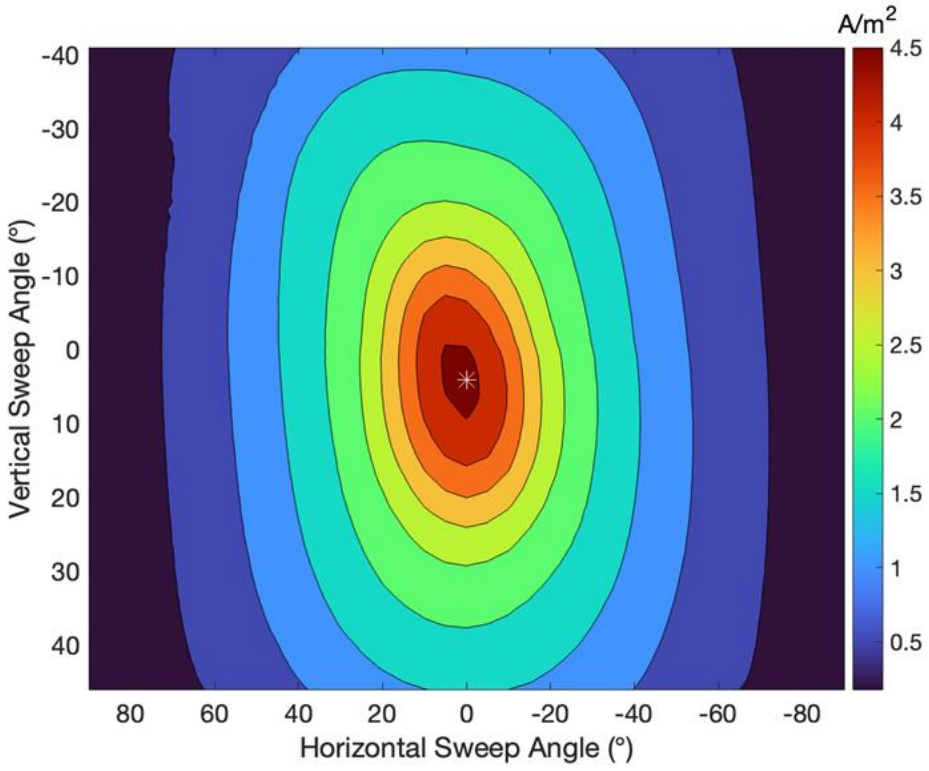

b)

Figure 33 – Raw measurements of a)Three-dimensional ion current density variation with horizontal and vertical sweep b) Contour map of ion current density at baseline test condition

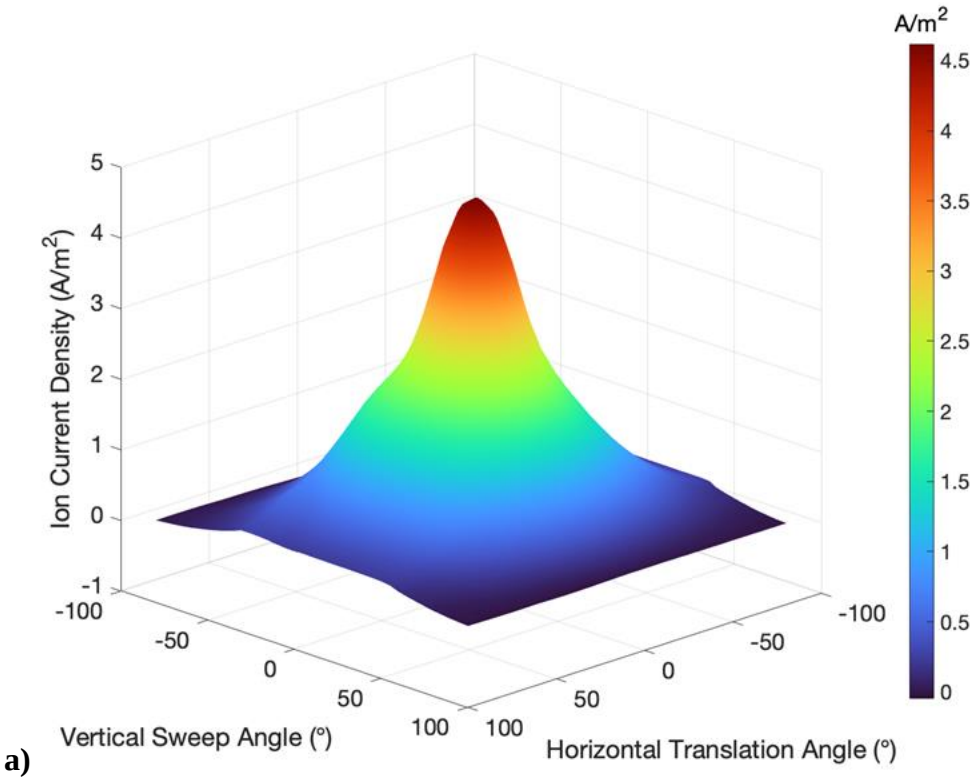

a)

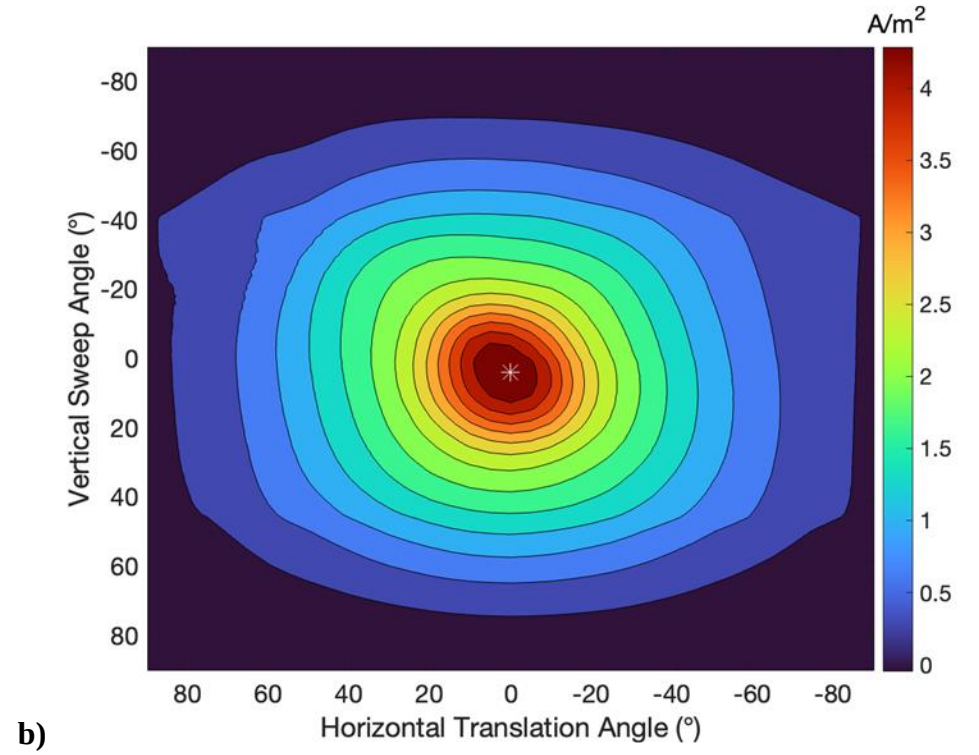

b)

Figure 34 – Extrapolated measurements of a)Three-dimensional ion current density variation with horizontal and vertical sweep b) Contour map of ion current density at baseline test condition

5.2.2 Faraday Probe

The Faraday probe is mounted on the radial arm and swept horizontally from -90° to 90° with a resolution of ±0.17°. The Collector and Guard of the Faraday are biased at -30 V to collect the ion current in the plume. The measurement of the Faraday probe is subject to the same uncertainty margin of ±10% as recommended in Faraday's best practices[77]. The radial arm motion control system is subject to a systemic error of ±2%. The uncertainty associated with the scan measurements was determined by conducting three consecutive scans. Table 6 displays the thruster's current utilization, beam divergence, and ion beam current at the operating condition. Figure 35 displays the revised Faraday probe scan representing the ion current density.

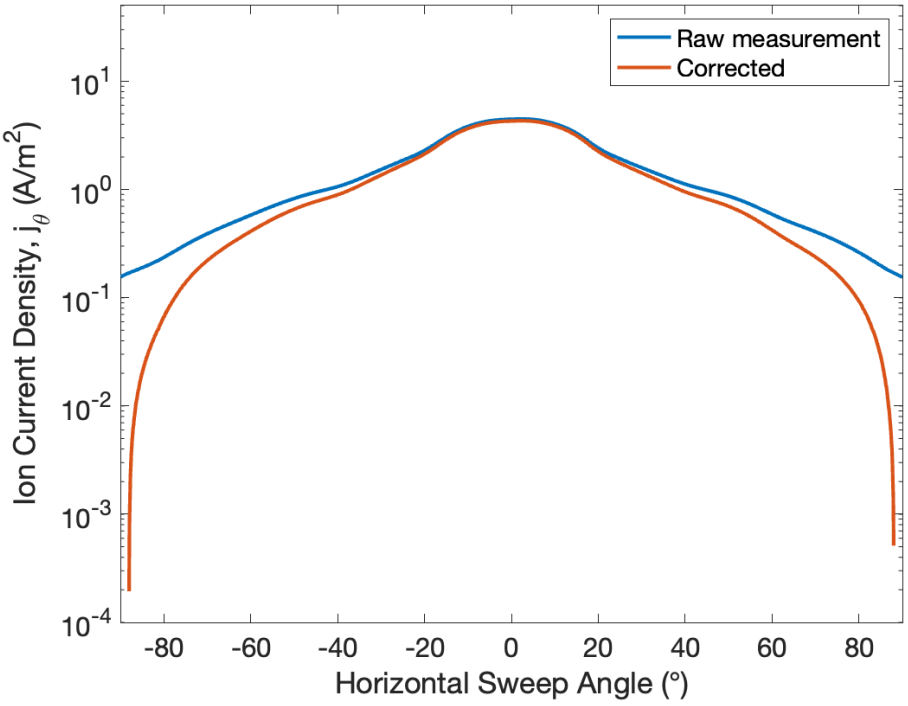

Figure 35 – Raw and corrected ion current density for a horizontal sweep at baseline test condition

Table 6 – Calculated ion beam properties at baseline test condition on krypton using Faraday probe

Test No.	Condition Name	I_d (A)	I_b (A)	θ_{div} (°)	η_b (%)
1	baseline	7.90	4.11	33.23	52.05

5.2.3 Langmuir Probe

The Langmuir probe is positioned on the radial probe arm to collect measurements at the thruster centerline. The radial arm is positioned at 0° at a horizontal sweep angle to allow the measurements to be conducted. The Langmuir probe undergoes three consecutive scans, sweeping from -50 V to 80 V. Table 7 depicts plasma parameters such as electron density, temperature, and potential obtained from the data analysis of the I-V trace. The I-V traces obtained from the HET plume exhibited characteristics that resemble the principles of Langmuir probe theory, suggesting the presence of a Maxwellian electron distribution. The data processing for the trace obtained for the test condition as shown in Figure 36.

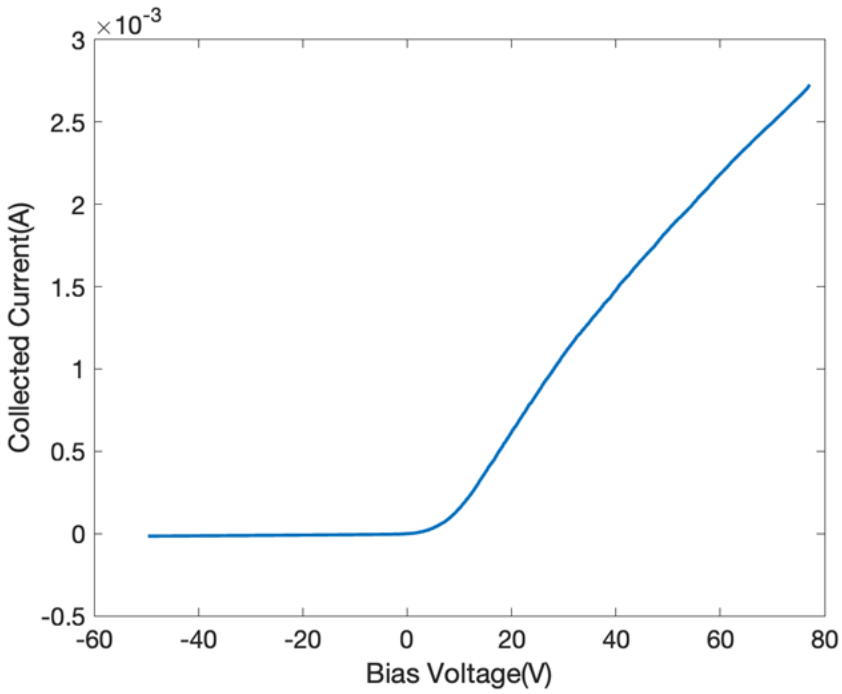

Figure 36 – Average I-V traces collected by Langmuir probe at baseline test condition

Table 7 – Calculated plume properties at baseline test condition on krypton using Langmuir probe.

Test No.	Condition Name	T_e (eV)	n_e (m^{-3})	V_p (V)
1	baseline	4.27	1.99×10^{15}	14.88

5.2.4 RPA Probe

The RPA probe is located on the radial probe arm, and to take measurements at the thruster centerline, the radial arm is positioned at 0° in a horizontal sweep. The RPA was swept from 0 V to 450 V, and three successive scans were performed. The voltage with the largest d*I*/dV must be determined to acquire the plasma parameters, which are the

acceleration voltages experienced by ions. Figure 37 illustrates that the maximum value achieved at the current operating condition was 269.80 V.

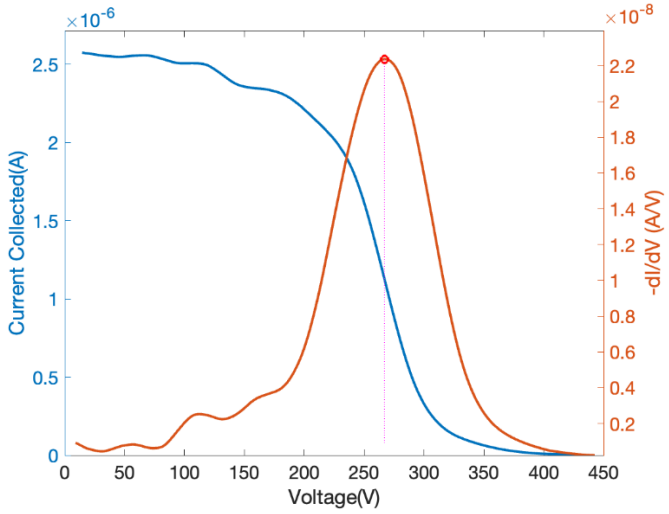

Figure 37 – Average I-V traces collected by RPA(left) and ion energy distribution function represented by -d*I*/dV (right) at baseline test condition

5.2.5 OES

The OES scan was performed at three axial positions starting from the exit plane. The measurements were obtained at distances of 0 mm, 5 mm, and 10 mm from the exit plane. Table 8 displays the location and intensity of light at the exit plane. In order to remove any light collected by external light sources, such as the ion gauges in the chamber, the background noise was eliminated from the OES scan. The OES measurement was obtained at the exit plane, and the background scan is depicted in Figure 38.

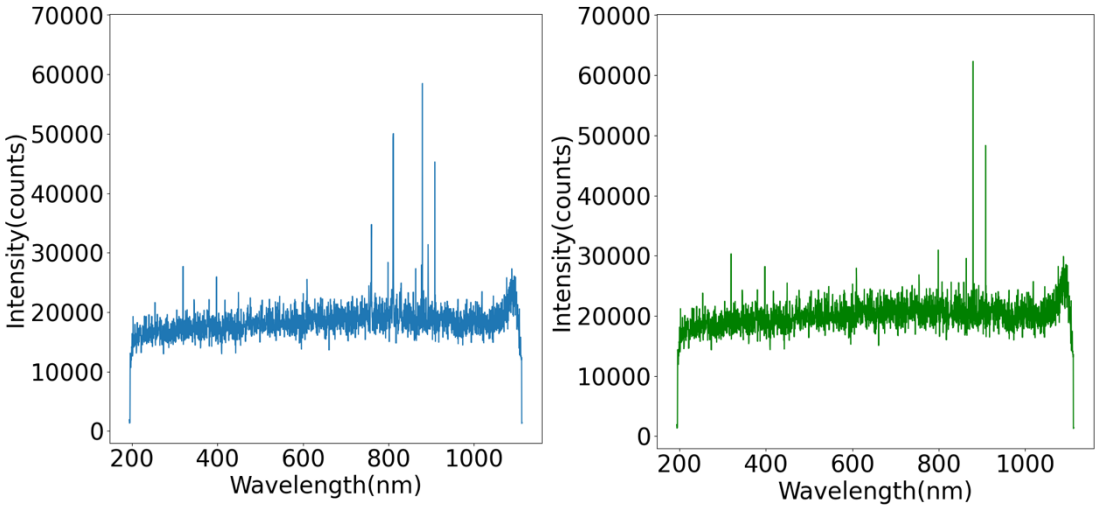

Figure 38 – Plume light intensity spectrum collected using OES at baseline test condition

Table 8 – Plume intensity measurements for baseline test condition at 0 mm, 5 mm and 10 mm from thruster exit plane.

Test No.	Condition Name	Distance from exit plane (mm)	λ_{max} (nm)	*Intensity count*
1	baseline	0	811.24	31622.11
1	baseline	5	811.24	21766.23
1	baseline	10	811.24	16173.11

5.2.6 Oscilloscope

Table 9 shows time-resolved measurements of the thruster discharge characteristics under operating conditions. In order to eliminate any discrepancies in the measurements that may have resulted from plasma fluctuations, five measurements were recorded over a two-hour period and averaged to determine the final discharge characteristics. An analysis

of the oscilloscope's observations of the discharge current oscillation allows us to gather insights into the instabilities in the HET. The power spectral density was obtained by performing a fast Fourier transform on the time-resolved discharge current. The peak frequency was 6.4 kHz ±900Hz, as shown in Figure 39. The peak frequency exhibited a magnitude shift of 2 kHz under the non-uniform test conditions. It is crucial to notice that, despite a gradient in the channel, the oscillations' peak frequency remains below the frequently observed breathing mode instability, which ranges from 10 to 30 kHz. Consequently, the present investigation does not examine breathing mode instabilities but local plasma low-frequency instabilities.

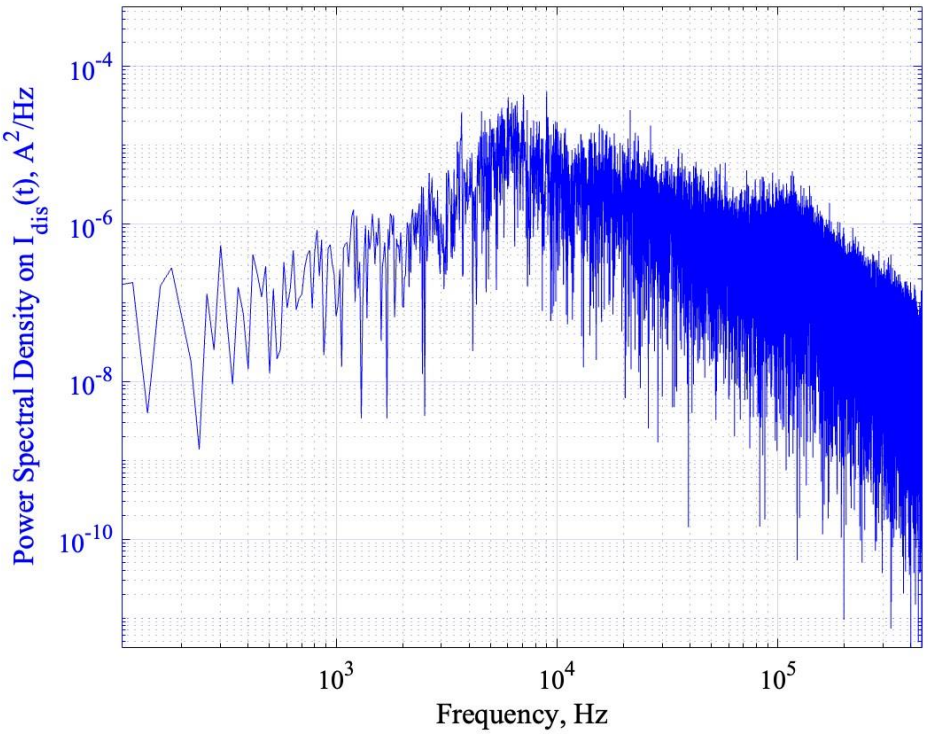

Figure 39 – Power spectral density plots of $I_d(t)$ at 300 V and 7.90 A baseline test condition on krypton

Table 9 – Time-resolved measurements of discharge current at baseline test condition.

Test No.	Condition Name	I_d (A)	$I_{d,pk2pk}$ (A)	$I_{d,rms}$ (A)
1	baseline	7.90	4.15	7.92

5.2.7 Thrust Stand

Following the completion of measurements with all probes, thrust measurements were carried out. The average thrust value was determined by taking consecutive thruster measurements in a row. The thruster was permitted to achieve thermal stable state conditions between each measurement. The current operating condition yielded a thrust of 78.03 mN with an error of ±2 mN. Specific impulse obtained for the current operating condition was 1409.56 s.

5.3 Uniform Magnetic Field Variation Condition

5.3.1 Uniform1 Test Condition

5.3.1.1 Faraday Probe

The Faraday probe is mounted on the radial arm and swept horizontally from -90° to 90° with a resolution of ±0.17°. The Collector and Guard of the Faraday are biased at -30 V to collect the ion current in the plume. The radial arm motion control system is subject to a systemic error of ±2%. The uncertainty associated with the scan measurements was determined by conducting three consecutive scans. Table 10 displays the thruster's

current utilization, beam divergence, and ion beam current at the operating condition. Figure 40 displays the revised Faraday probe scan representing the ion current density.

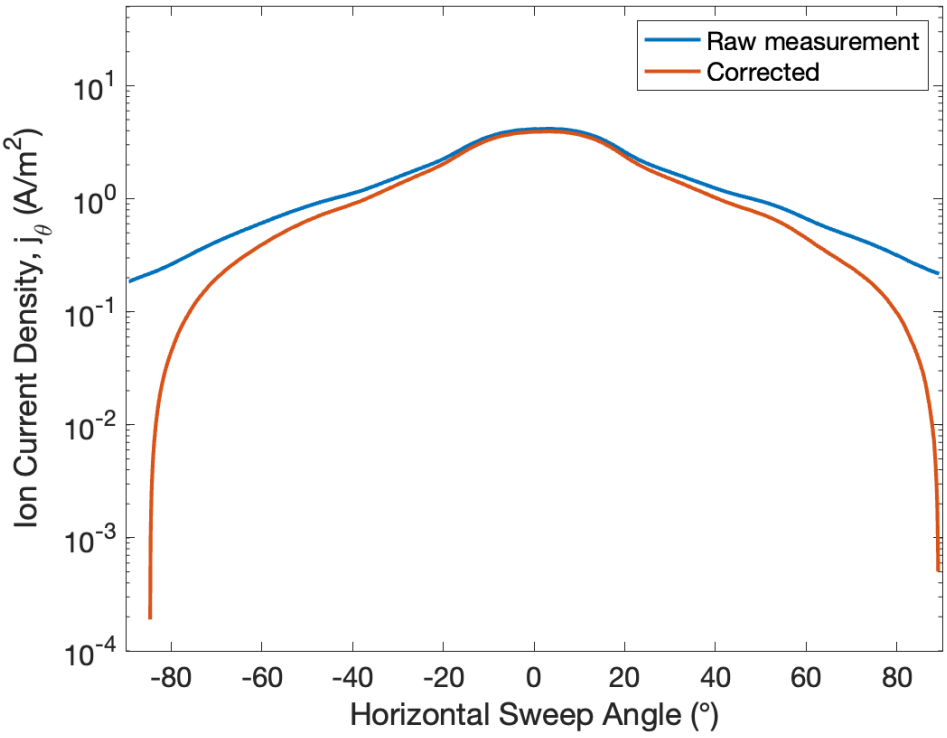

Figure 40 – Raw and corrected ion current density for a horizontal sweep for uniform 1 test condition

Table 10 – Calculated ion beam properties at uniform1 test condition on krypton using Faraday probe

Test No.	Condition Name	I_d (A)	I_b (A)	θ_{div} (°)	η_b (%)
2.	uniform1	8.03	4.08	33.23	50.79

5.3.1.2 Langmuir Probe

The Langmuir probe is positioned on the radial probe arm to collect measurements at the thruster centerline. The radial arm is positioned at 0° at a horizontal sweep angle to allow the measurements to be conducted. The Langmuir probe undergoes three consecutive scans, sweeping from -50 V to 60 V. Table 11depicts plasma parameters such as electron density, temperature, and potential obtained from the data analysis of the I-V trace. The I-V traces obtained from the HET plume exhibited characteristics that resemble the principles of Langmuir probe theory, suggesting the presence of a Maxwellian electron distribution. The data processing for the trace obtained for the test condition is shown in Figure 41.

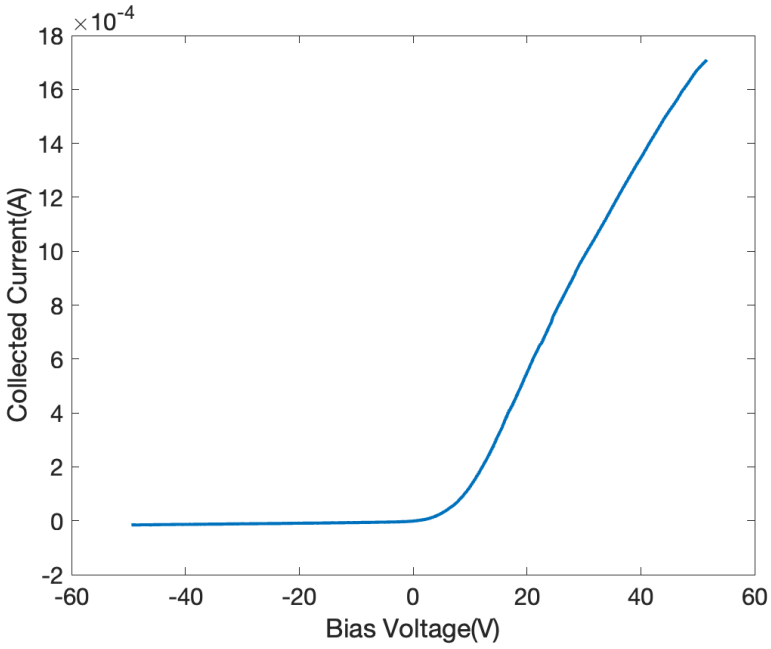

Figure 41 – Average I-V traces collected by Langmuir probe at uniform1 test condition.

Table 11 – Calculated plume properties at uniform1 test condition on krypton using Langmuir probe.

Test No.	Condition Name	T_e (eV)	n_e (m^{-3})	V_p (V)
2.	uniform1	3.96	1.93×10^{15}	14.83

5.3.1.3 RPA Probe

The RPA probe is located on the radial probe arm, and to take measurements at the thruster centerline, the radial arm is positioned at 0 ° in a horizontal sweep. The RPA was swept from 0 V to 450 V, and three successive scans were performed. The voltage with the largest d*I*/dV must be determined to acquire the plasma parameters, which are the acceleration voltages experienced by ions. Figure 42 illustrates that the maximum value achieved at the current operating condition was 267 V.

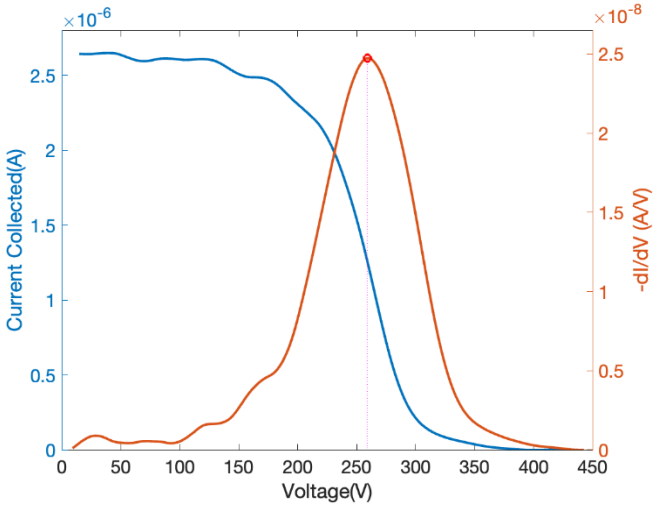

Figure 42 – Average I-V traces collected by RPA(left) and ion energy distribution function represented by -d*I*/dV (right) at uniform1 test condition.

5.3.1.4 OES

The OES scan was performed at three axial positions starting from the exit plane. The measurements were obtained at distances of 0mm, 5mm, and 10mm from the exit plane. Table 12 displays the location and intensity of light at the exit plane. In order to remove any light collected by external light sources, such as the ion gauges in the chamber, the background noise was eliminated from the OES scan. The OES measurement was obtained at the exit plane, and the background scan is depicted in Figure 43.

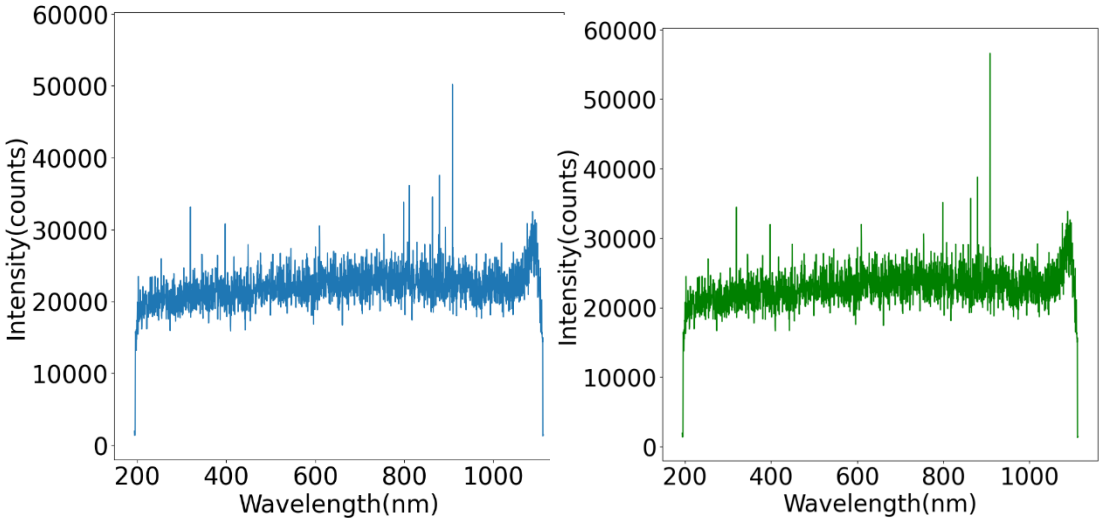

Figure 43 – Plume light intensity spectrum collected using OES at uniform1 test condition.

Table 12 – Plume intensity measurements for uniform1 test condition at 0 mm, 5 mm and 10 mm from thruster exit plane.

Test No.	Condition Name	Distance from exit plane (mm)	λ_{max} (nm)	$Intensity\ count$
2.	uniform1	0	811.24	12057.33
2.	uniform1	5	811.24	7510.33
2.	uniform1	10	811.24	4117.89

5.3.1.5 Oscilloscope

Table 13 shows time-resolved measurements of the thruster discharge characteristics under operating conditions. In order to eliminate any discrepancies in the measurements that may have resulted from plasma fluctuations, five measurements were recorded over a two-hour period and averaged to determine the final discharge characteristics.

Table 13 – Time-resolved measurements of discharge current at uniform1 test condition.

Test No.	Condition Name	I_d (A)	$I_{d,pk2pk}$ (A)	$I_{d,rms}$ (A)
2.	uniform1	8.03	5.81	8.09

5.3.1.6 Thrust Stand

Following the completion of measurements with all probes, thrust measurements were carried out. The average thrust value was determined by taking consecutive thruster measurements in a row. The thruster was permitted to achieve thermal stable state conditions between each measurement. The current operating condition yielded a thrust of 77.06 mN with an error of ±2 mN. The specific impulse obtained for the current operating condition was 1392.03 s.

5.3.2 Uniform 2 Test Condition

5.3.2.1 Faraday Probe

The Faraday probe is mounted on the radial arm and swept horizontally from -90°to 90° with a resolution of ±0.17°. The Collector and Guard of the Faraday are biased at -30 V to collect the ion current in the plume. The radial arm motion control system is subject to a systemic error of ±2%. The uncertainty associated with the scan measurements was determined by conducting three consecutive scans.

Table 14 displays the thruster's current utilization, beam divergence, and ion beam current at the operating condition. Figure 44 displays the revised Faraday probe scan representing the ion current density.

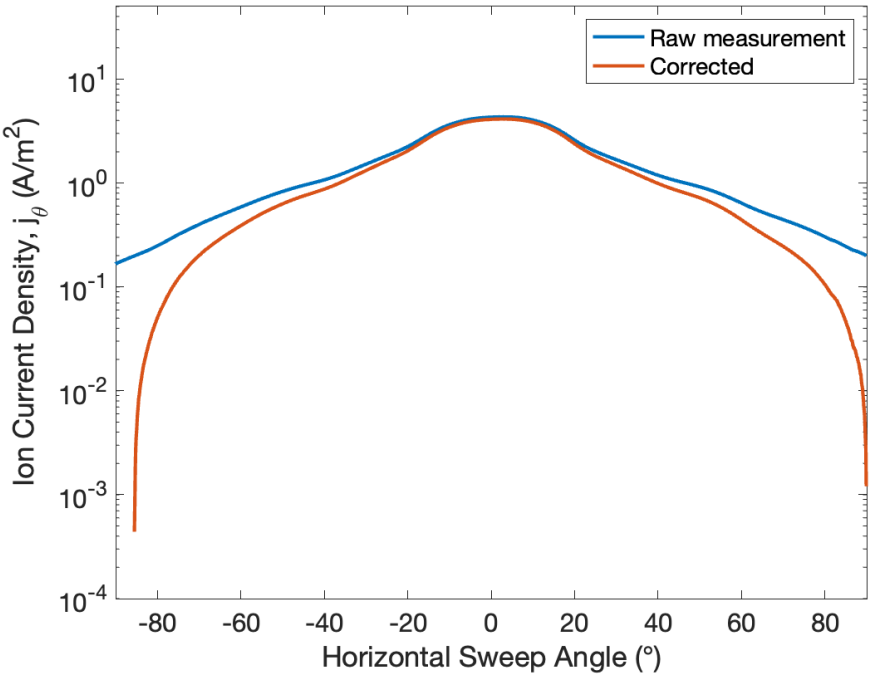

Figure 44 – Raw and corrected ion current density for a horizontal sweep for uniform2 test condition.

Table 14 – Calculated ion beam properties at uniform2 test condition on krypton using Faraday probe

Test No.	Condition Name	I_d (A)	I_b (A)	θ_{div} (°)	η_b (%)
3.	uniform2	8.04	4.04	33.23	50.28

5.3.2.2 Langmuir Probe

The Langmuir probe is positioned on the radial probe arm to collect measurements at the thruster centerline. The radial arm is positioned at 0 °at a horizontal sweep angle to allow the measurements to be conducted. The Langmuir probe undergoes three consecutive scans, sweeping from -50 V to 60 V. Table 15 depicts plasma parameters such as electron

density, temperature, and potential obtained from the data analysis of the I-V trace. The I-V traces obtained from the HET plume exhibited characteristics that resemble the principles of Langmuir probe theory, suggesting the presence of a Maxwellian electron distribution. The data processing for the trace obtained for the test condition as shown in Figure 45.

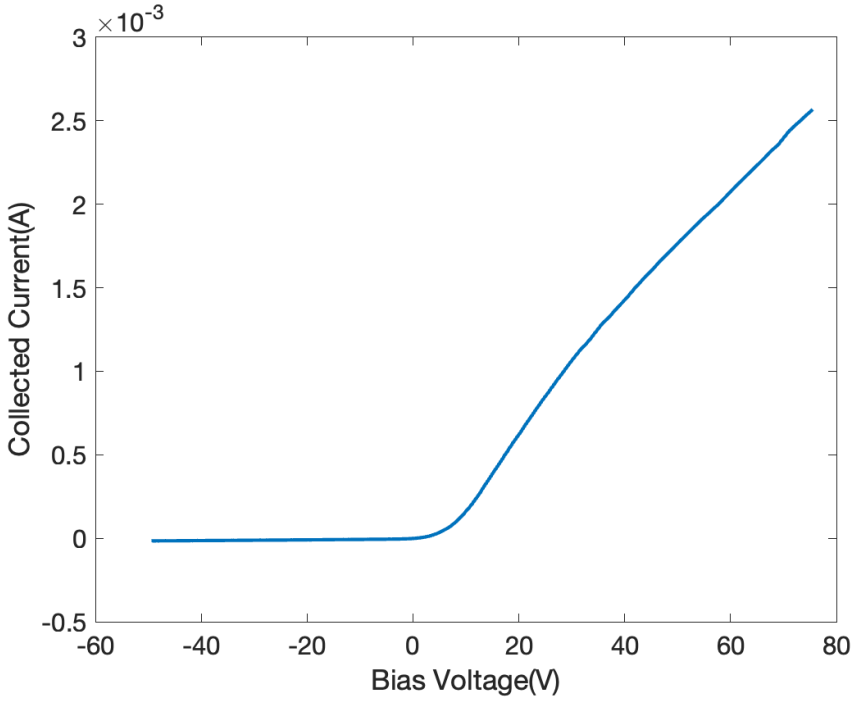

Figure 45 – Average I-V traces collected by Langmuir probe at uniform2 test condition.

Table 15 – Calculated plume properties at uniform2 test condition on krypton using Langmuir probe.

Test No.	Condition Name	T_e (eV)	n_e (m^{-3})	V_p (V)
3.	uniform2	3.64	1.88×10^{15}	14.17

5.3.2.3 RPA Probe

The RPA probe is located on the radial probe arm, and to take measurements at the thruster centerline, the radial arm is positioned at 0 ° in a horizontal sweep. The RPA was swept from 0 V to 450 V, and three successive scans were performed. The voltage with the largest d*I*/dV must be determined to acquire the plasma parameters, which are the acceleration voltages experienced by ions. Figure 46 illustrates that the maximum value achieved at the current operating condition was 266.3 V.

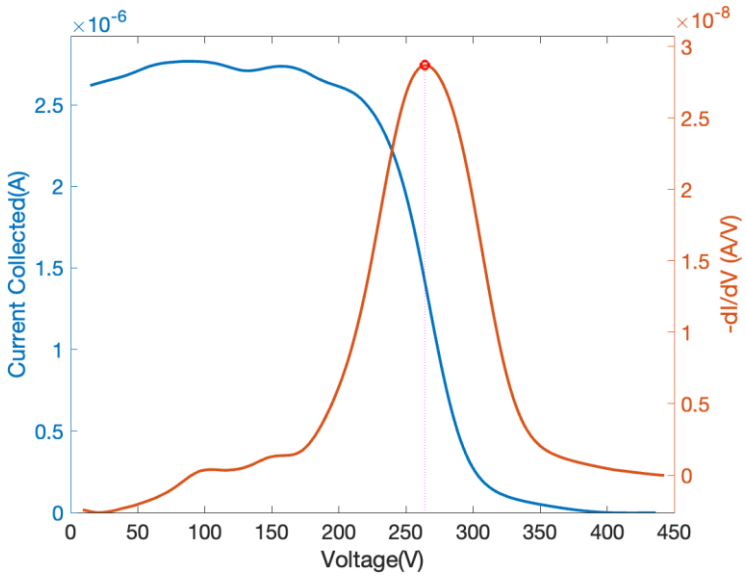

Figure 46 – Average I-V traces collected by RPA(left) and ion energy distribution function represented by -d*I*/dV (right) at uniform2 test condition

5.3.2.4 OES

The OES scan was performed at three axial positions starting from the exit plane. The measurements were obtained at distances of 0 mm, 5 mm, and 10 mm from the exit plane. Table 16 displays the location and intensity of light at the exit plane. In order to remove any light collected by external light sources, such as the ion gauges in the chamber,

the background noise was eliminated from the OES scan. The OES measurement was obtained at the exit plane, and the background scan is depicted in Figure 47.

Table 16 – Plume intensity measurements for uniform2 test condition at 0 mm, 5 mm and 10 mm from thruster exit plane.

Test No.	Condition Name	Distance from exit plane (mm)	λ_{max} (nm)	*Intensity count*
3.	uniform2	0	811.24	13677.31
3.	uniform2	5	811.24	7937.93
3.	uniform2	10	811.24	5042.06

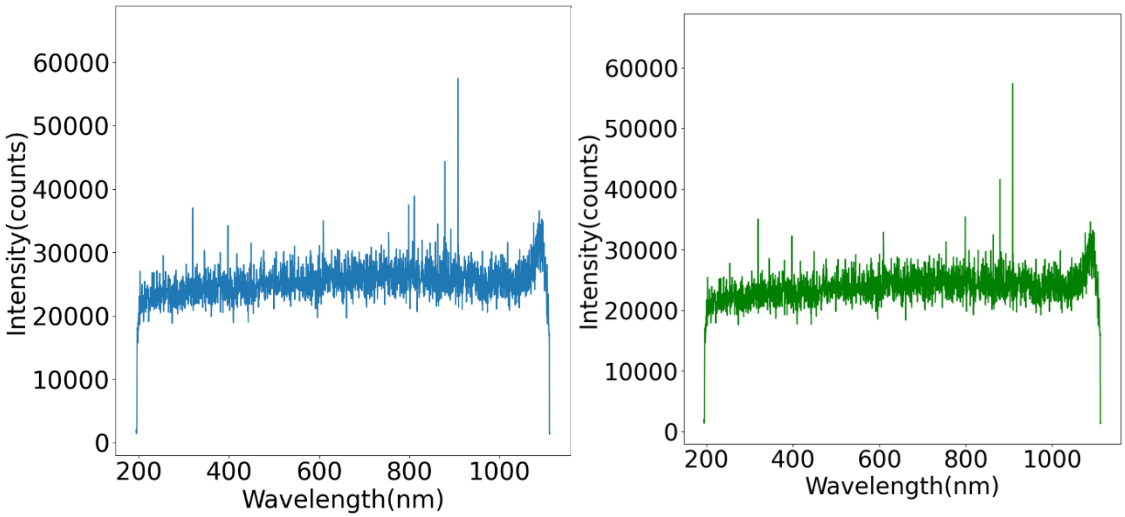

Figure 47 – Plume light intensity spectrum collected using OES at uniform2 test condition

5.3.2.5 Oscilloscope

Table 17 shows time-resolved measurements of the thruster discharge characteristics under operating conditions. In order to eliminate any discrepancies in the measurements that may have resulted from plasma fluctuations, five measurements were

recorded over a two-hour period and averaged to determine the final discharge characteristics.

Table 17 – Time-resolved measurements of discharge current at uniform2 test condition.

Test No.	Condition Name	I_d (A)	$I_{d,pk2pk}$ (A)	$I_{d,rms}$ (A)
3.	uniform2	8.04	5.99	8.05

5.3.2.6 Thrust Stand

Following the completion of measurements with all probes, thrust measurements were carried out. The average thrust value was determined by taking consecutive thruster measurements in a row. The thruster was permitted to achieve thermal stable state conditions between each measurement. The current operating condition yielded a thrust of 76.8 mN with an error of ±2 mN. Specific impulse obtained for the current operating condition was 1387s.

5.3.3 Uniform 3 Test Condition

5.3.3.1 Faraday Probe

The Faraday probe is mounted on the radial arm and swept horizontally from -90° to 90° with a resolution of ±0.17°. The Collector and Guard of the Faraday are biased at -30 V to collect the ion current in the plume. The radial arm motion control system is subject to a systemic error of ±2%. The uncertainty associated with the scan measurements

was determined by conducting three consecutive scans. Table 18 displays the thruster's current utilization, beam divergence, and ion beam current at the operating condition. Figure 48 displays the revised Faraday probe scan representing the ion current density.

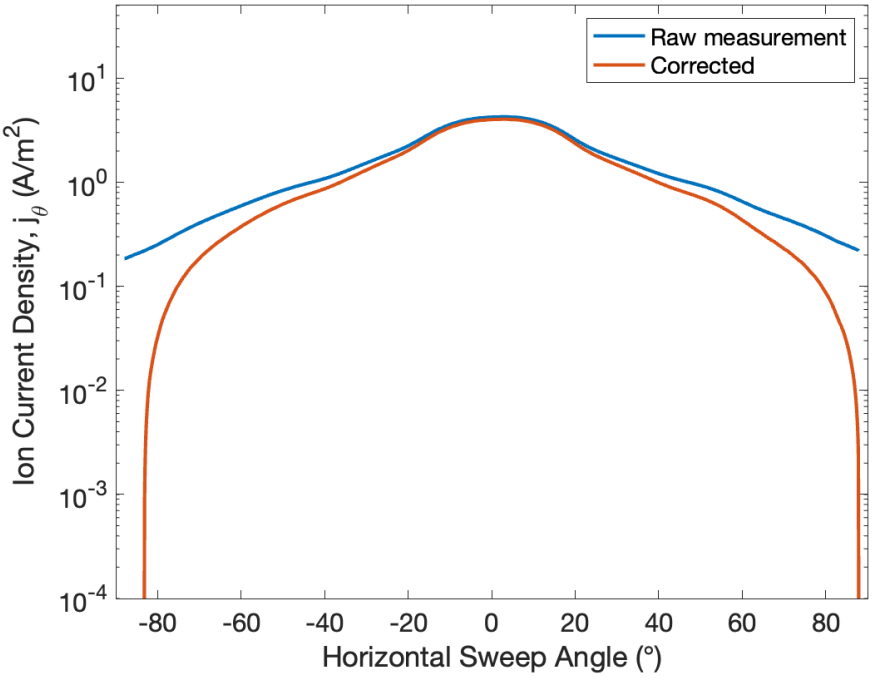

Figure 48 – Raw and corrected ion current density for a horizontal sweep for uniform3 test condition

Table 18 – Calculated ion beam properties at uniform3 test condition on krypton using Faraday probe

Test No.	Condition Name	I_d (A)	I_b (A)	θ_{div} (°)	η_b (%)
4.	uniform3	8.01	4.08	32.83	50.88

5.3.3.2 Langmuir Probe

The Langmuir probe is positioned on the radial probe arm to collect measurements at the thruster centerline. The radial arm is positioned at 0°at a horizontal sweep angle to allow the measurements to be conducted. The Langmuir probe undergoes three consecutive scans, sweeping from -50 V to 80 V. Table 19 depicts plasma parameters such as electron density, temperature, and potential obtained from the data analysis of the I-V trace. The I-V traces obtained from the HET plume exhibited characteristics that resemble the principles of Langmuir probe theory, suggesting the presence of a Maxwellian electron distribution. The data processing for the trace obtained for the test condition is shown in Figure 49.

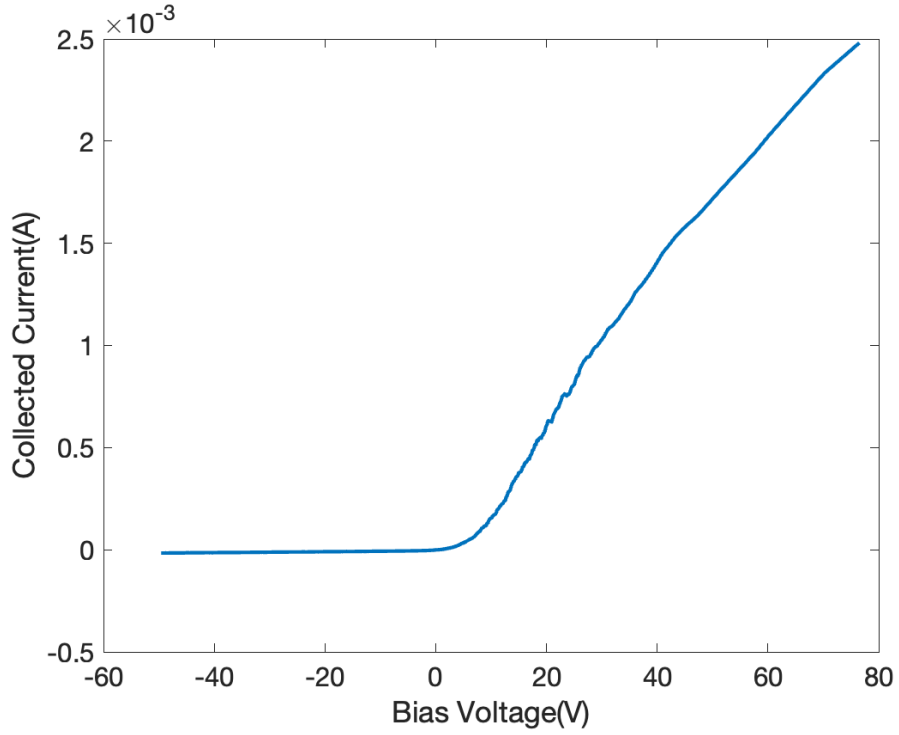

Figure 49 – Average I-V traces collected by Langmuir probe at uniform3 test condition.

Table 19 – Calculated plume properties at uniform3 test condition on krypton using Langmuir probe.

Test No.	Condition Name	T_e (eV)	n_e (m^{-3})	V_p (V)
4.	uniform3	3.79	1.89×10^{15}	13.94

5.3.3.3 RPA Probe

The RPA probe is located on the radial probe arm, and to take measurements at the thruster centerline, the radial arm is positioned at 0° in a horizontal sweep. The RPA was swept from 0 V to 450 V, and three successive scans were performed. The voltage with the largest d*I*/dV must be determined to acquire the plasma parameters, which are the acceleration voltages experienced by ions. Figure 50 illustrates that the maximum value achieved at the current operating condition was 266 V.

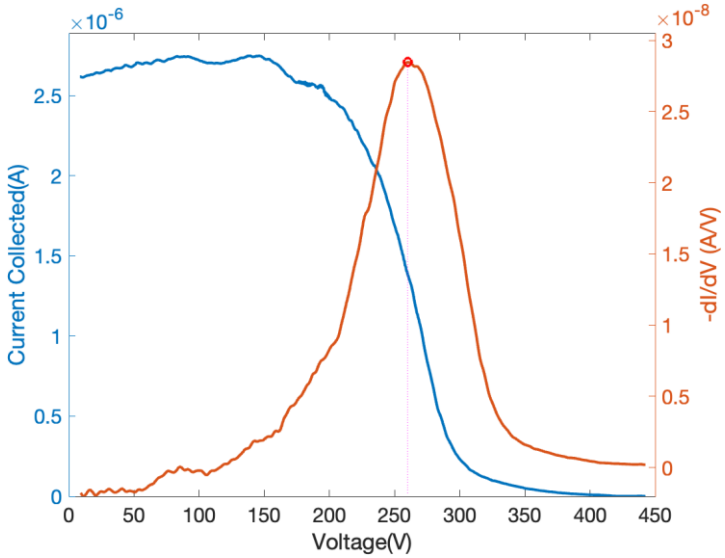

Figure 50 – Average I-V traces collected by RPA(left) and ion energy distribution function represented by -d*I*/dV (right) at uniform3 test condition

5.3.3.4 OES

The OES scan was performed at three axial positions starting from the exit plane. The measurements were obtained at distances of 0 mm, 5 mm, and 10 mm from the exit plane. Table 20 displays the location and intensity of light at the exit plane. In order to remove any light collected by external light sources, such as the ion gauges in the chamber, the background noise was eliminated from the OES scan. The OES measurement was obtained at the exit plane, and the background scan is depicted in Figure 51.

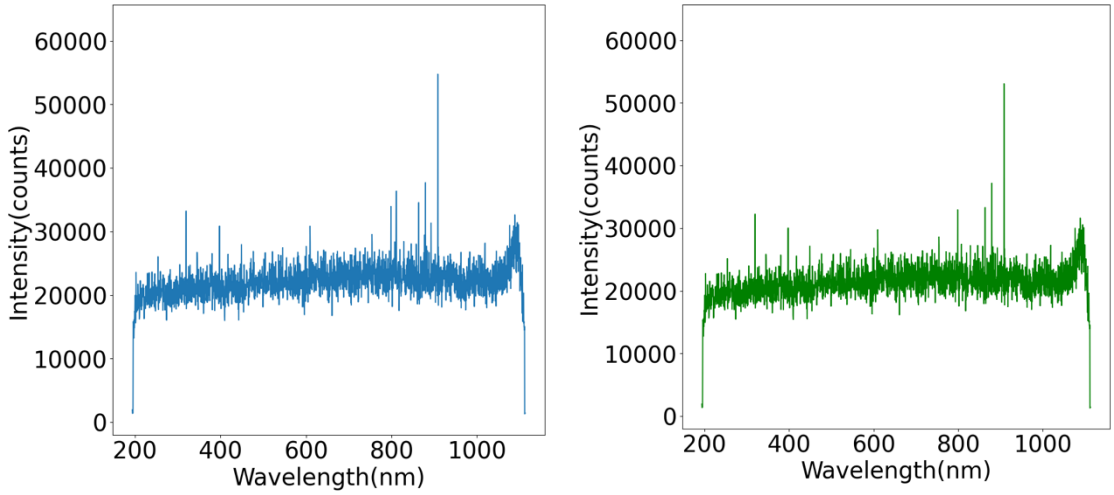

Figure 51 – Plume light intensity spectrum collected using OES at uniform3 test condition.

Table 20 – Plume intensity measurements for uniform3 test condition at 0 mm, 5 mm and 10 mm from thruster exit plane.

Test No.	Condition Name	Distance from exit plane (mm)	λ_{max} (nm)	*Intensity count*
4.	uniform3	0	811.24	14072.11
4.	uniform3	5	811.24	9379.56
4.	uniform3	10	811.24	7356

5.3.3.5 Oscilloscope

Table 21 shows time-resolved measurements of the thruster discharge characteristics under operating conditions. In order to eliminate any discrepancies in the measurements that may have resulted from plasma fluctuations, five measurements were recorded over a two-hour period and averaged to determine the final discharge characteristics.

Table 21 – Time-resolved measurements of discharge current at uniform3 test condition.

Test No.	Condition Name	I_d (A)	$I_{d,pk2pk}$ (A)	$I_{d,rms}$ (A)
4.	uniform3	8.01	5.53	8.37

5.3.3.6 Thrust Stand

Following the completion of measurements with all probes, thrust measurements were carried out. The average thrust value was determined by taking consecutive thruster measurements in a row. The thruster was permitted to achieve thermal stable state conditions between each measurement. The current operating condition yielded a thrust of 76.61 mN with an error of ±2 mN. Specific impulse obtained for the current operating condition was 1384 s.

5.3.4 Uniform 4 Test Condition

5.3.4.1 Faraday Probe

The Faraday probe is mounted on the radial arm and swept horizontally from -90° to 90° with a resolution of ±0.17°. The collector and guard ring of the Faraday are biased at -30 V to collect the ion current in the plume. The measurement of the Faraday probe is subject to the same uncertainty margin of ±10% as recommended in Faraday's best practices[77]. The radial arm motion control system is subject to a systemic error of ±2%. The uncertainty associated with the scan measurements was determined by conducting three consecutive scans. Table 22 displays the thruster's current utilization, beam divergence, and ion beam current at the operating condition. Figure 52 displays the revised Faraday probe scan representing the ion current density.

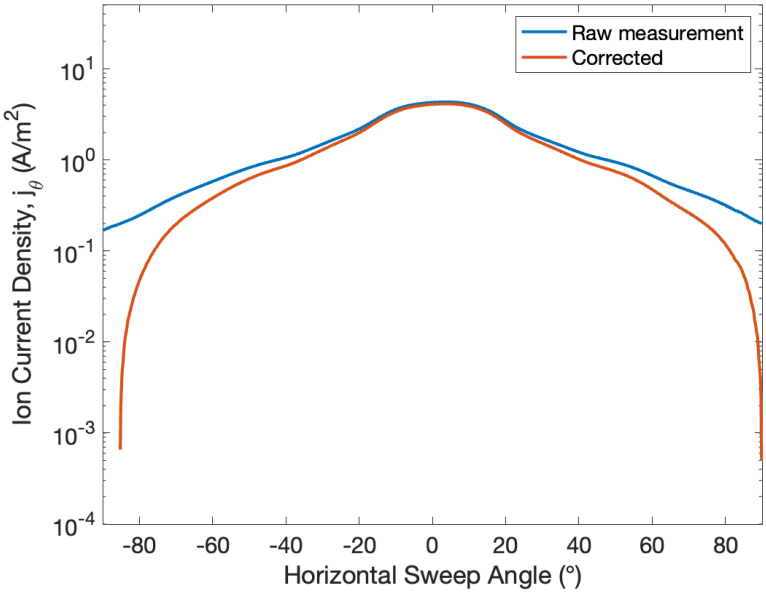

Figure 52 – Raw and corrected ion current density for a horizontal sweep for uniform4 test condition

Table 22 – Calculated ion beam properties at uniform4 test condition on krypton using Faraday probe

Test No.	Condition Name	I_d (A)	I_b (A)	θ_{div} (°)	η_b (%)
5.	uniform4	8.14	4.03	33.46	49.46

5.3.4.2 Langmuir Probe

The Langmuir probe is positioned on the radial probe arm to collect measurements at the thruster centerline. The radial arm is positioned at 0°at a horizontal sweep angle to allow the measurements to be conducted. The Langmuir probe undergoes three consecutive scans, sweeping from -50 V to 80 V. Table 23 depicts plasma parameters such as electron density, temperature, and potential obtained from the data analysis of the I-V trace. The I-V traces obtained from the HET plume exhibited characteristics that resemble the principles of Langmuir probe theory, suggesting the presence of a Maxwellian electron distribution. The data processing for the trace obtained for the test condition is shown in Figure 53.

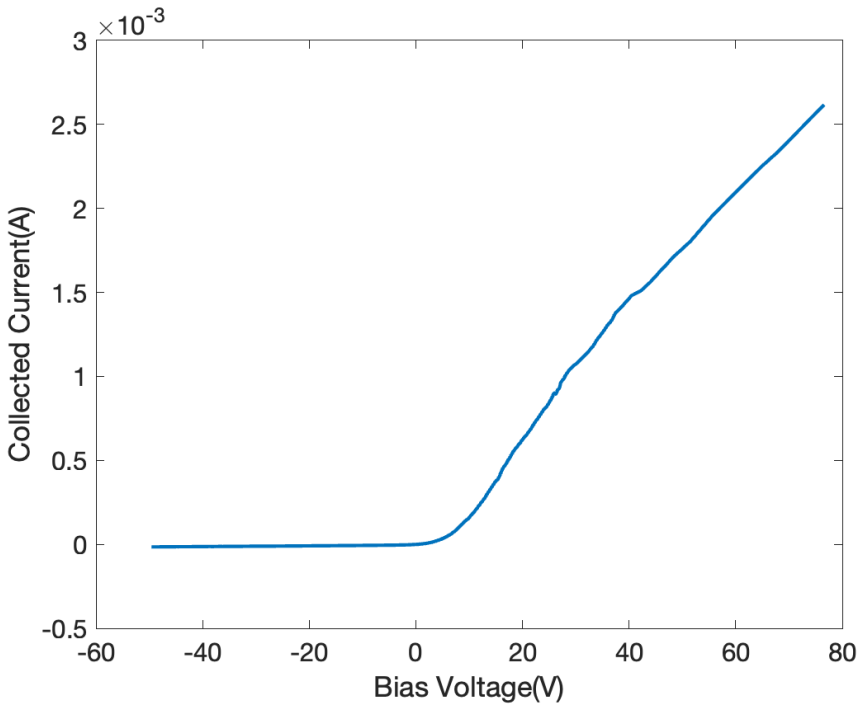

Figure 53 – Average I-V traces collected by Langmuir probe at uniform4 test condition.

Table 23 – Calculated plume properties at uniform4 test condition on krypton using Langmuir probe.

Test No.	Condition Name	T_e (eV)	n_e (m^{-3})	V_p (V)
5.	uniform4	3.53	1.79×10^{15}	13.53

5.3.4.3 RPA Probe

The RPA probe is located on the radial probe arm, and to take measurements at the thruster centerline, the radial arm is positioned at 0 ° in a horizontal sweep. The RPA was swept from 0 V to 450 V, and three successive scans were performed. The voltage with the

largest d*I*/dV must be determined to acquire the plasma parameters, which are the acceleration voltages experienced by ions. Figure 54 illustrates that the maximum value achieved at the current operating condition was 266 V.

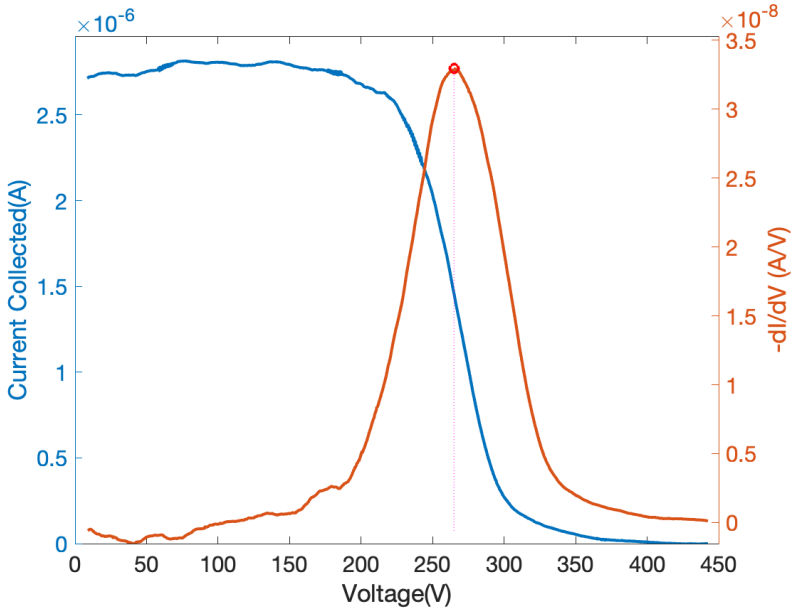

Figure 54 – Average I-V traces collected by RPA(left) and ion energy distribution function represented by -d*I*/dV (right) at uniform4 test condition

5.3.4.4 OES

The OES scan was performed at three axial positions starting from the exit plane. The measurements were obtained at distances of 0 mm, 5 mm, and 10 mm from the exit plane.

Table 24 displays the location and intensity of light at the exit plane. In order to remove any light collected by external light sources, such as the ion gauges in the chamber, the background noise was eliminated from the OES scan. The OES measurement was obtained at the exit plane, and the background scan is depicted in Figure 55.

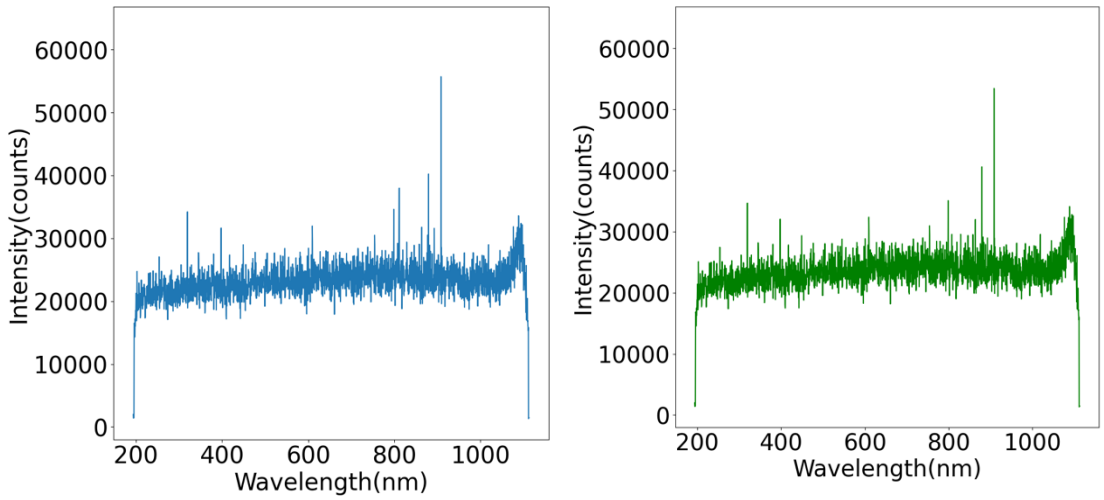

Figure 55 – Plume light intensity spectrum collected using OES at uniform4 test condition.

Table 24 – Plume intensity measurements for uniform4 test condition at 0 mm, 5 mm and 10 mm from thruster exit plane.

Test No.	Condition Name	Distance from exit plane (mm)	λ_{max} (nm)	*Intensity count*
5.	uniform4	0	811.24	12472.68
5.	uniform4	5	811.24	7764.81
5.	uniform4	10	811.24	5462.75

5.3.4.5 Oscilloscope

Table 25 shows time-resolved measurements of the thruster discharge characteristics under operating conditions. In order to eliminate any discrepancies in the measurements that may have resulted from plasma fluctuations, five measurements were recorded over a two-hour period and averaged to determine the final discharge characteristics.

Table 25 – Time-resolved measurements of discharge current at uniform4 test condition.

Test No.	Condition Name	I_d (A)	$I_{d,pk2pk}$ (A)	$I_{d,rms}$ (A)
5.	uniform4	8.14	6.28	8.07

5.3.4.6 Thrust Stand

Following the completion of measurements with all probes, thrust measurements were carried out. The average thrust value was determined by taking consecutive thruster measurements in a row. The thruster was permitted to achieve thermal stable state conditions between each measurement. The current operating condition yielded a thrust of 76.51 mN with an error of ±2 mN. Specific impulse obtained for the current operating condition was 1382 s.

5.3.5 Uniform 5 Test Condition

5.3.5.1 Faraday Probe

The Faraday probe is mounted on the radial arm and swept horizontally from -90°to 90°with a resolution of ±0.17°. The Collector and Guard of the Faraday are biased at -30 V to collect the ion current in the plume. The radial arm motion control system is subject to a systemic error of ±2%. The uncertainty associated with the scan measurements was determined by conducting three consecutive scans. Table 26 displays the thruster's current utilization, beam divergence, and ion beam current at the operating condition. Figure 56 displays the revised Faraday probe scan representing the ion current density.

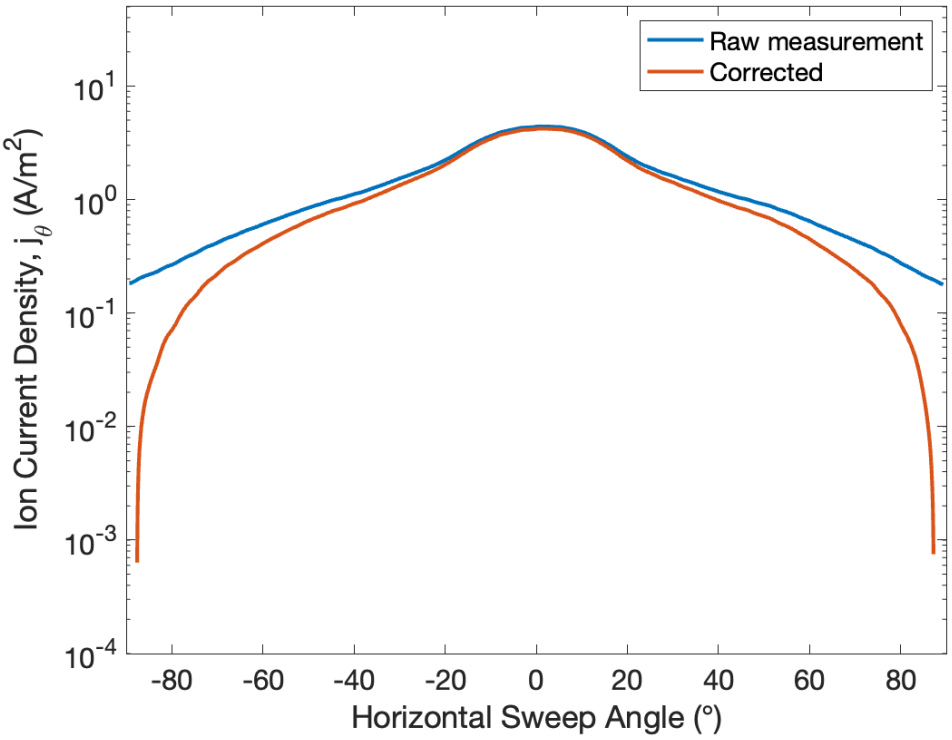

Figure 56 – Raw and corrected ion current density for a horizontal sweep at uniform5 test condition

Table 26 – Calculated ion beam properties at uniform5 test condition on krypton using Faraday probe

Test No.	Condition Name	I_d (A)	I_b (A)	θ_{div} (°)	η_b (%)
6.	uniform5	8.36	4.02	33.64	48.05

5.3.5.2 Langmuir Probe

The Langmuir probe is positioned on the radial probe arm to collect measurements at the thruster centerline. The radial arm is positioned at 0°at a horizontal sweep angle to allow the measurements to be conducted. The Langmuir probe undergoes three consecutive

scans, sweeping from -50 V to 80 V. Table 27 depicts plasma parameters such as electron density, temperature, and potential obtained from the data analysis of the I-V trace. The I-V traces obtained from the HET plume exhibited characteristics that resemble the principles of Langmuir probe theory, suggesting the presence of a Maxwellian electron distribution. The data processing for the trace obtained for the test condition is shown in Figure 57.

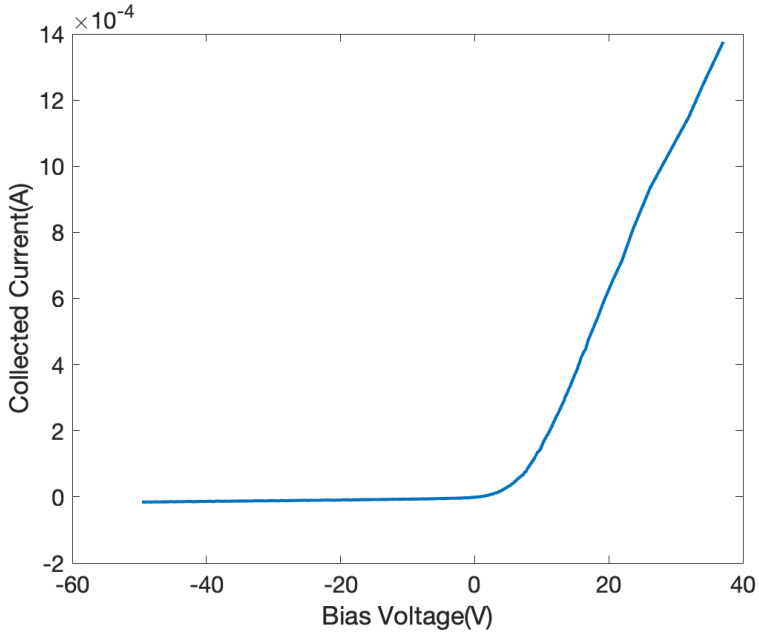

Figure 57 – Average I-V traces collected by Langmuir probe at uniform5 test condition

Table 27 – Calculated plume properties at uniform5 test condition on krypton using Langmuir probe.

Test No.	Condition Name	T_e (eV)	n_e (m^{-3})	V_p (V)
6.	uniform5	3.40	1.49×10^{15}	11.83

5.3.5.3 RPA Probe

The RPA probe is located on the radial probe arm, and to take measurements at the thruster centerline, the radial arm is positioned at 0 ° in a horizontal sweep. The RPA was swept from 0 V to 450 V, and three successive scans were performed. The voltage with the largest d*I*/dV must be determined to acquire the plasma parameters, which are the acceleration voltages experienced by ions. Figure 58 illustrates that the maximum value achieved at the current operating condition was 264 V.

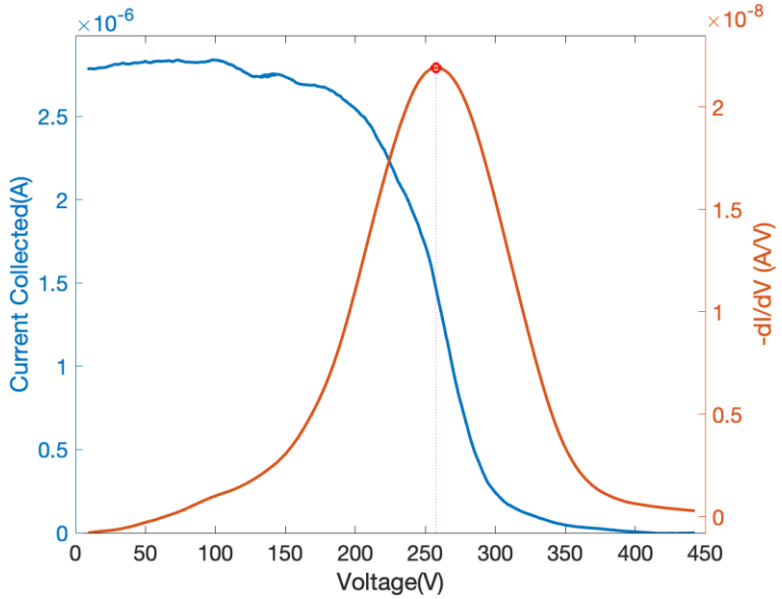

Figure 58 – Average I-V traces collected by RPA(left) and ion energy distribution function represented by -d*I*/dV (right) at uniform5 test condition

5.3.5.4 OES

The OES scan was performed at three axial positions starting from the exit plane. The measurements were obtained at distances of 0 mm, 5 mm, and 10 mm from the exit plane. Table 28 displays the location and intensity of light at the exit plane. In order to remove any light collected by external light sources, such as the ion gauges in the chamber,

the background noise was eliminated from the OES scan. The OES measurement was obtained at the exit plane, and the background scan is depicted in Figure 59.

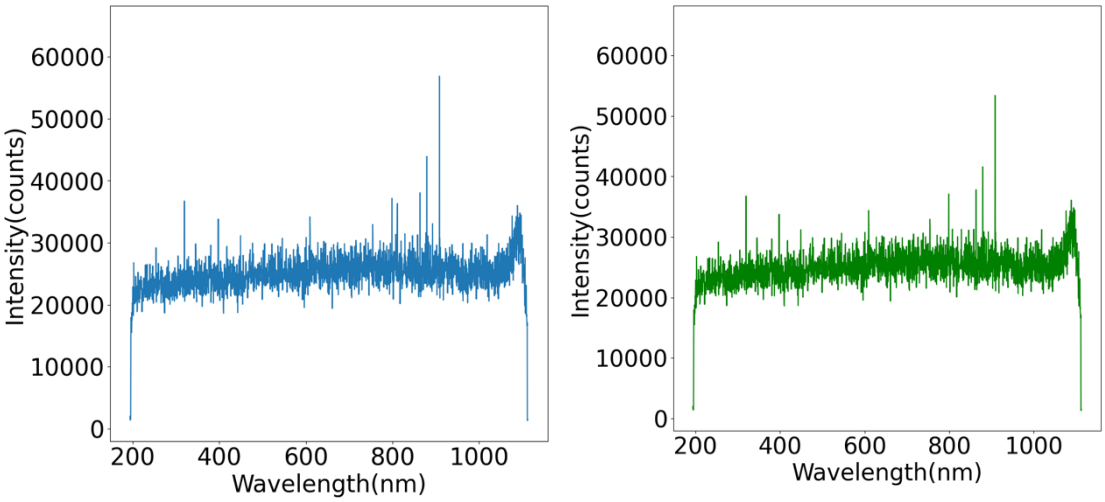

Figure 59 – Plume light intensity spectrum collected using OES at uniform5 test condition

Table 28 – Plume intensity measurements for uniform5 test condition at 0 mm, 5 mm, and 10 mm from thruster exit plane.

Test No.	Condition Name	Distance from exit plane (mm)	λ_{max} (nm)	*Intensity count*
6.	uniform5	0	811.24	8808.18
6.	uniform5	5	811.24	6446.33
6.	uniform5	10	811.24	6191.88

5.3.5.5 Oscilloscope

Table 29 shows time-resolved measurements of the thruster discharge characteristics under operating conditions. In order to eliminate any discrepancies in the measurements that may have resulted from plasma fluctuations, five measurements were recorded over a two-hour period and averaged to determine the final discharge characteristics.

Table 29 – Time-resolved measurements of discharge current at uniform5 test condition.

Test No.	Condition Name	I_d (A)	$I_{d,pk2pk}$ (A)	$I_{d,rms}$ (A)
6.	uniform5	8.36	10.48	8.31

5.3.5.6 Thrust Stand

Following the completion of measurements with all probes, thrust measurements were carried out. The average thrust value was determined by taking consecutive thruster measurements in a row. The thruster was permitted to achieve thermal stable state conditions between each measurement. The current operating condition yielded a thrust of 76.43 mN with an error of ±2 mN. Specific impulse obtained for the current operating condition was 1381 s.

5.3.6 Uniform 6 Test Condition

5.3.6.1 Faraday Probe

The Faraday probe is mounted on the radial arm and swept horizontally from -90°to 90° with a resolution of ±0.17°. The Collector and Guard of the Faraday are biased at -30 V to collect the ion current in the plume. The radial arm motion control system is subject to a systemic error of ±2%. The uncertainty associated with the scan measurements was determined by conducting three consecutive scans. Table 30 displays the thruster's current utilization, beam divergence, and ion beam current at the operating condition. Figure 60 displays the revised Faraday probe scan representing the ion current density.

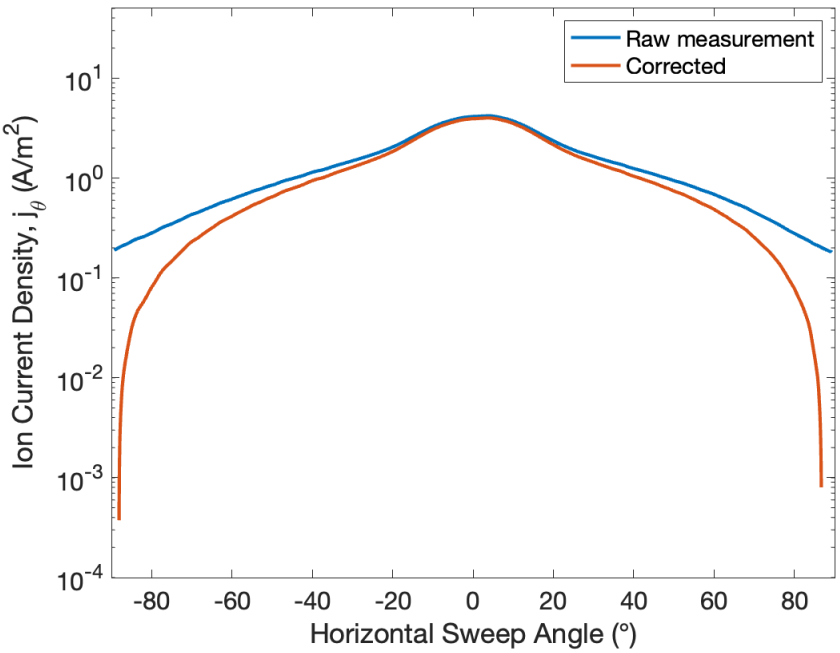

Figure 60 – Raw and corrected ion current density for a horizontal sweep at uniform6 test condition

Table 30 – Calculated ion beam properties at uniform6 test condition on krypton using Faraday probe

Test No.	Condition Name	I_d (A)	I_b (A)	θ_{div} (°)	η_b (%)
7.	uniform6	9.20	3.89	34.46	42.32

5.3.6.2 Langmuir Probe

The Langmuir probe is positioned on the radial probe arm to collect measurements at the thruster centerline. The radial arm is positioned at 0 °at a horizontal sweep angle to allow the measurements to be conducted. The Langmuir probe undergoes three consecutive scans, sweeping from -50 V to 80 V. Table 31 depicts plasma parameters such as electron density, temperature, and potential obtained from the data analysis of the I-V trace. The I-V traces obtained from the HET plume exhibited characteristics that resemble the principles of Langmuir probe theory, suggesting the presence of a Maxwellian electron distribution. The data processing for the trace obtained for the test condition is shown in Figure 61.

Table 31 – Calculated plume properties at uniform6 test condition on krypton using Langmuir probe.

Test No.	Condition Name	T_e (eV)	n_e (m^{-3})	V_p (V)
7.	uniform6	2.96	1.19×10^{15}	10.70

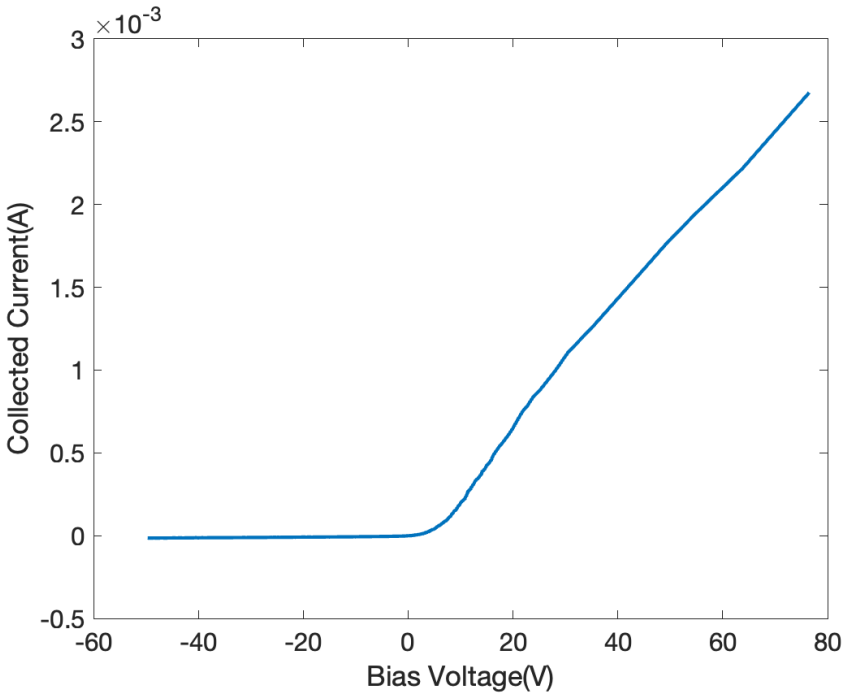

Figure 61 – Average I-V traces collected by Langmuir probe at uniform6 test condition

5.3.6.3 RPA Probe

The RPA probe is located on the radial probe arm, and to take measurements at the thruster centerline, the radial arm is positioned at 0 ° in a horizontal sweep. The RPA was swept from 0 V to 45 0V, and three successive scans were performed. The voltage with the largest d*I*/dV must be determined to acquire the plasma parameters, which are the acceleration voltages experienced by ions. Figure 62 illustrates that the maximum value achieved at the current operating condition was 261 V.

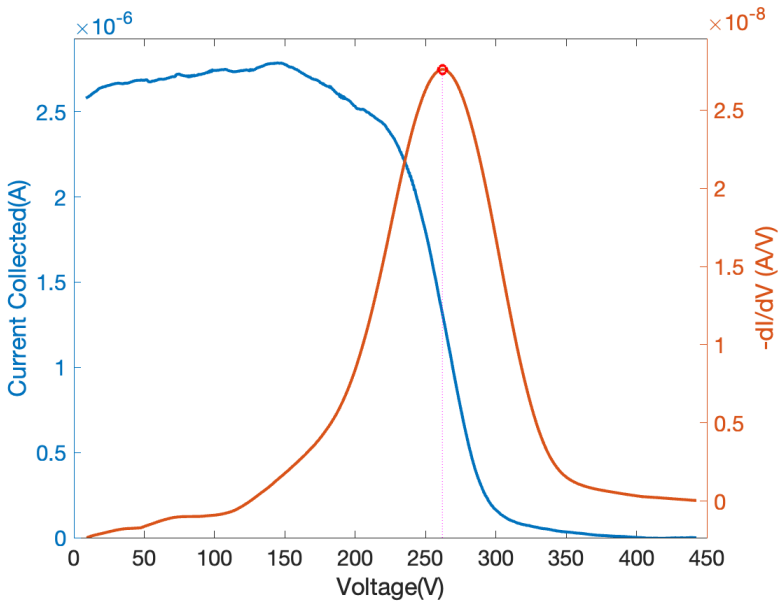

Figure 62 – Average I-V traces collected by RPA(left) and ion energy distribution function represented by -d*I*/dV (right) at uniform6 test condition

5.3.6.4 OES

The OES scan was performed at three axial positions starting from the exit plane. The measurements were obtained at distances of 0 mm, 5 mm, and 10 mm from the exit plane. Table 32 displays the location and intensity of light at the exit plane. In order to remove any light collected by external light sources, such as the ion gauges in the chamber, the background noise was eliminated from the OES scan. The OES measurement was obtained at the exit plane, and the background scan is depicted in Figure 63.

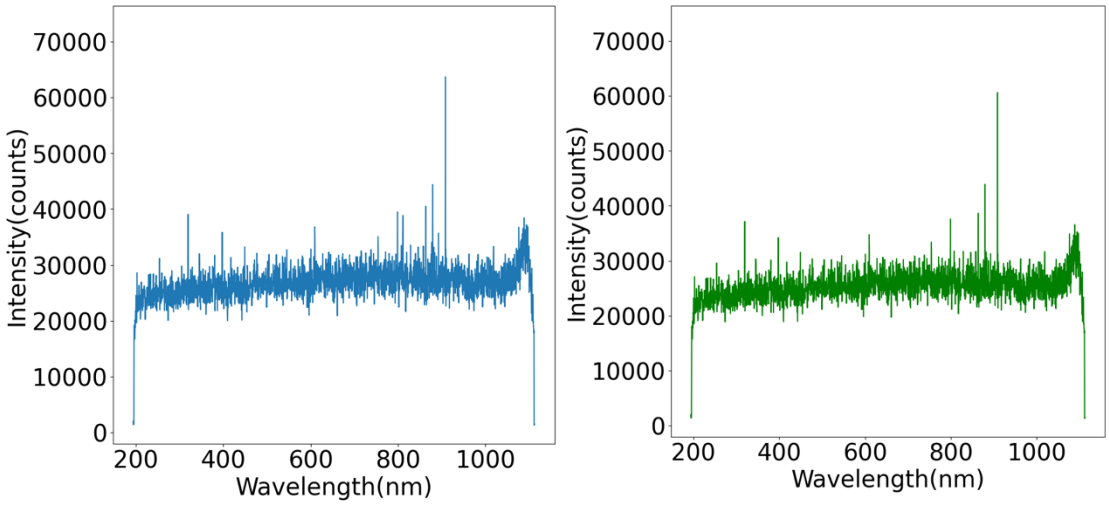

Figure 63 – Plume light intensity spectrum collected using OES at uniform6 test condition

Table 32 – Plume intensity measurements for uniform6 test condition at 0 mm, 5 mm, and 10 mm from the thruster exit plane.

Test No.	Condition Name	Distance from exit plane (mm)	λ_{max} (nm)	*Intensity count*
7.	uniform6	0	811.24	12216.88
7.	uniform6	5	811.24	7995.34
7.	uniform6	10	811.24	5229.44

5.3.6.5 Oscilloscope

Table 33 shows time-resolved measurements of the thruster discharge characteristics under operating conditions. In order to eliminate any discrepancies in the measurements that may have resulted from plasma fluctuations, five measurements were

recorded over a two-hour period and averaged to determine the final discharge characteristics.

Table 33 – Time-resolved measurements of discharge current at uniform6 test condition.

Test No.	Condition Name	I_d (A)	$I_{d,pk2pk}$ (A)	$I_{d,rms}$ (A)
7.	uniform6	9.20	14.21	9.43

5.3.6.6 Thrust Stand

Following the completion of measurements with all probes, thrust measurements were carried out. The average thrust value was determined by taking consecutive thruster measurements in a row. The thruster was permitted to achieve thermal stable state conditions between each measurement. The current operating condition yielded a thrust of 75.7 mN with an error of ±2 mN. Specific impulse obtained for the current operating condition was 1368 s.

5.4 Azimuthal Magnetic Field Gradient Conditions

5.4.1 Gradient 1 Test condition

5.4.1.1 Sweep Probe Apparatus

The Sweep Probe apparatus is operated after the thrust has achieved the thermal steady state condition. The apparatus consists of a Faraday probe that collects ion current

across a hemispherical area. The collector and the guard ring of the Faraday are biased to -30 V using the Keithley 2470 source meter. Measurements are conducted with a continuous sweep ranging from -41 °to 46 °for the probe, with a resolution of 0.1 °for the measurements for data analysis. After three consecutive vertical sweeps, the sweep probe apparatus mounted on the radial arm is swept horizontally with an angular spacing of 5°. This results in a total of 37 horizontally positioned scans ranging from -90° to 90°. The ion current measurements from the three-dimensional sweeping of the plume can be seen in Figure 64. An ion beam current of 2.19 A with a beam divergence of 25.83° was obtained from the raw data from the Faraday probe. The standard error associated with the reading is 1.8×10^{-7}, deeming the measurements to be highly reliable and accurate. In order to get the total ion beam current of the plume, a horizontal scan is conducted with the sweep probe apparatus with the position of the Faraday probe at 0°in vertical direction resulting in the probe being situated at the centerline. The three-dimensional scan yielded a 37% decrease compared to the horizontal sweep in the measurement of ion beam current due to the restricted vertical sweep range. The vertical scans were extrapolated using the horizontal scan measurements to determine the potential full-scale measurement of the ion beam current while preserving the trend of ion current density variation across the 37 vertical scans. The data extrapolation resulted in measurements that span from -90° to 90° in both the vertical and horizontal directions, thereby enabling the total estimation of the hemispherical ion current for P5 at 2.3 kW, as illustrated in Figure 65. An ion beam current measurement of 4.29 A and a divergence angle of 34° were obtained from the extrapolated three-dimensional ion current. The ion beam current measurements were evaluated after

correcting for secondary electron emission and charge exchange at horizontal and vertical angles, yielding a 95% ion beam percentage.

Table 34 – Calculated ion beam properties at gradient1 test condition on krypton using sweep probe apparatus.

Test No.	Condition Name	I_d (A)	I_b (A)	θ_{div} (°)	η_b (%)
2	gradient 1	7.91	4.29	34	54.28

a)

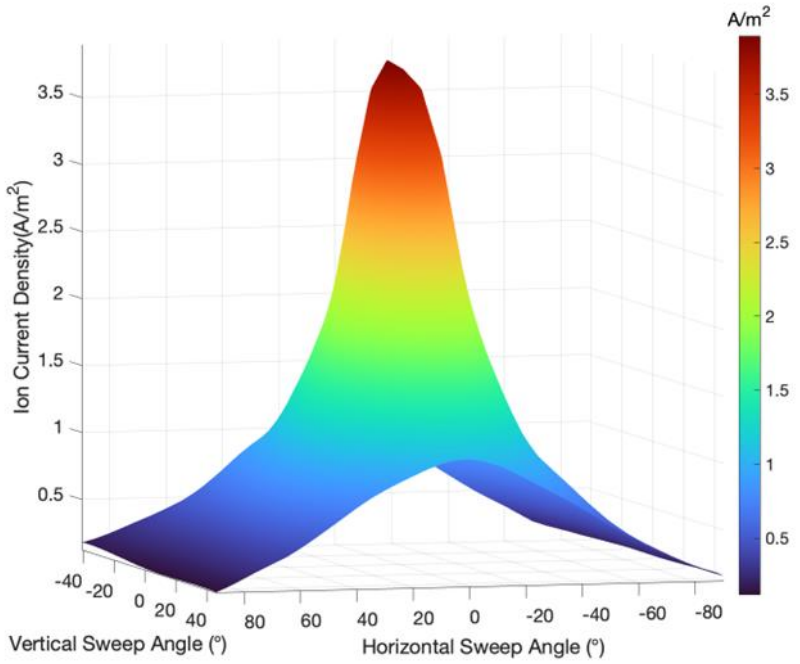

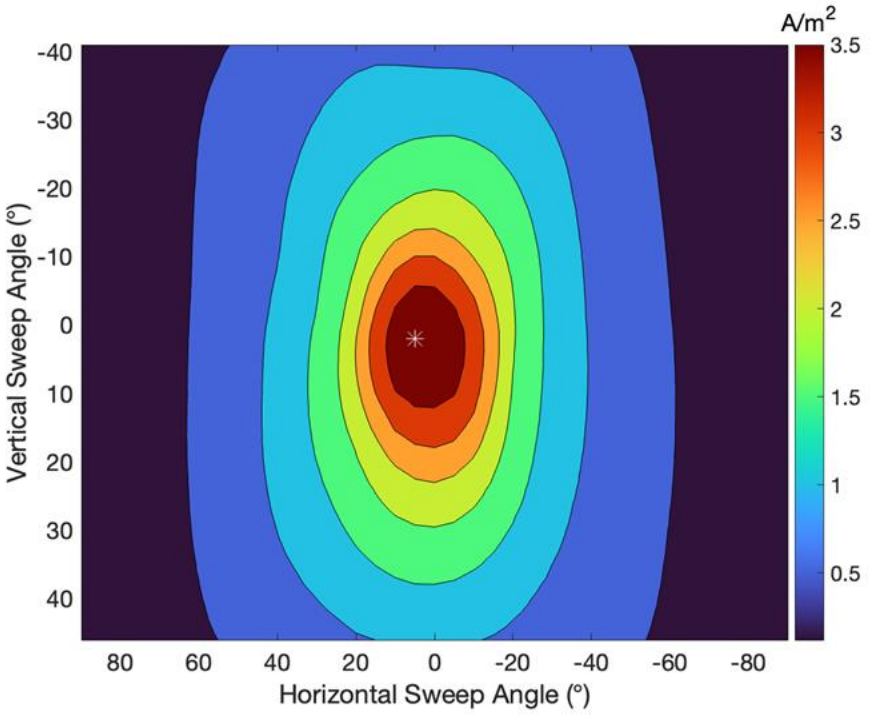

b)

Figure 64 – Raw measurements of a)Three-dimensional ion current density variation with horizontal and vertical sweep b) Contour map of ion current density at gradient1 test condition

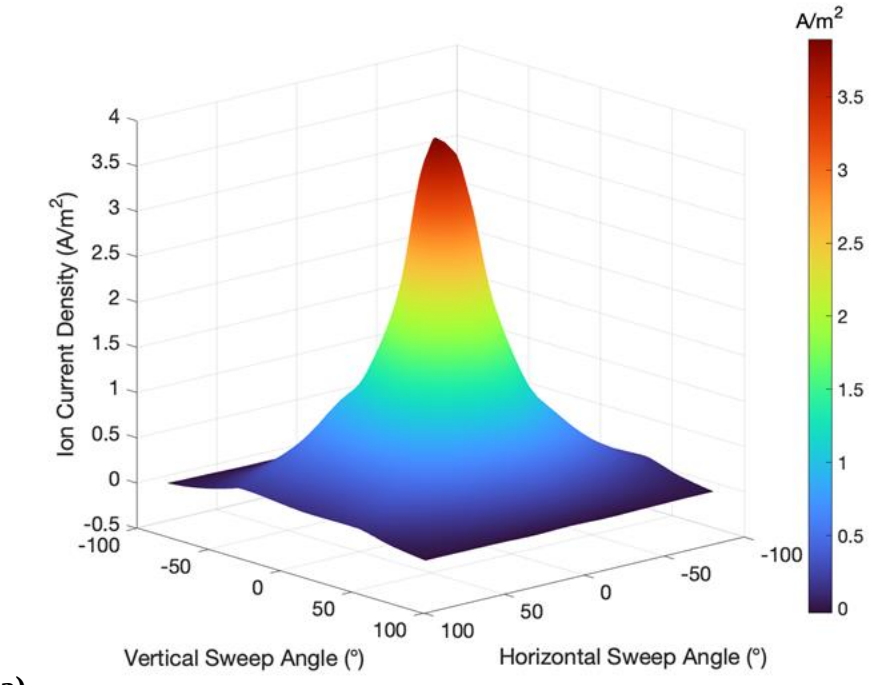

a)

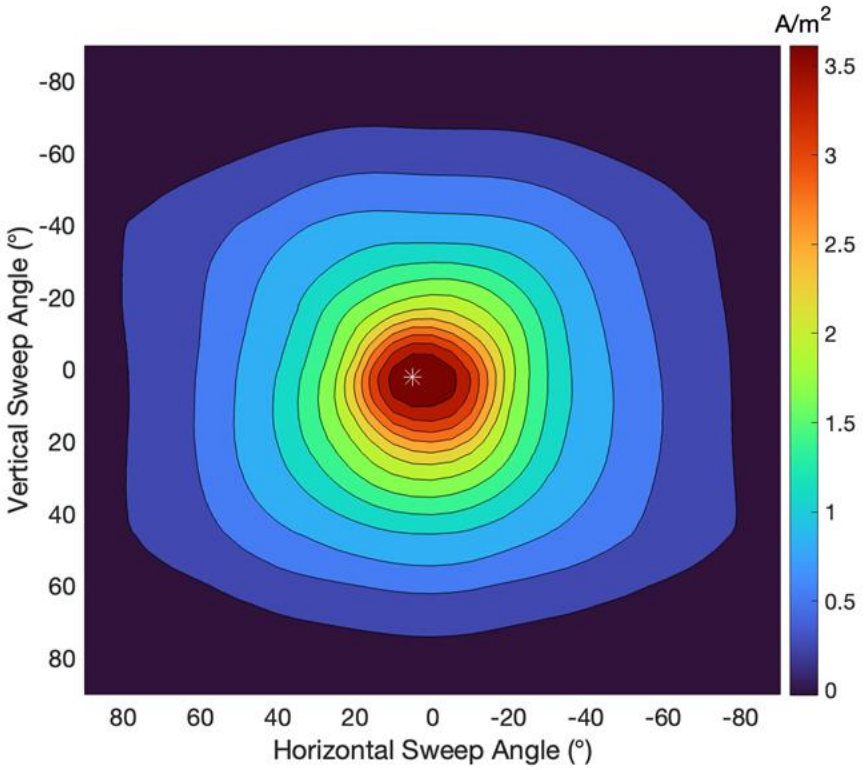

b)

Figure 65 – Extrapolated measurements of a)Three-dimensional ion current density variation with horizontal and vertical sweep b) Contour map of ion current density at gradient1 test condition

5.4.1.2 Faraday Probe

The Faraday probe is mounted on the radial arm and swept horizontally from -90° to 90° with a resolution of ±0.17°. The Collector and Guard of the Faraday are biased at -30 V to collect the ion current in the plume. The measurement of the Faraday probe is subject to the same uncertainty margin of ±10% as recommended in Faraday's best practices[77]. The radial arm motion control system is subject to a systemic error of ±2%. The uncertainty associated with the scan measurements was determined by conducting three consecutive scans. Table 35 displays the thruster's current utilization, beam

divergence, and ion beam current at the operating condition. Figure 66 displays the revised Faraday probe scan representing the ion current density.

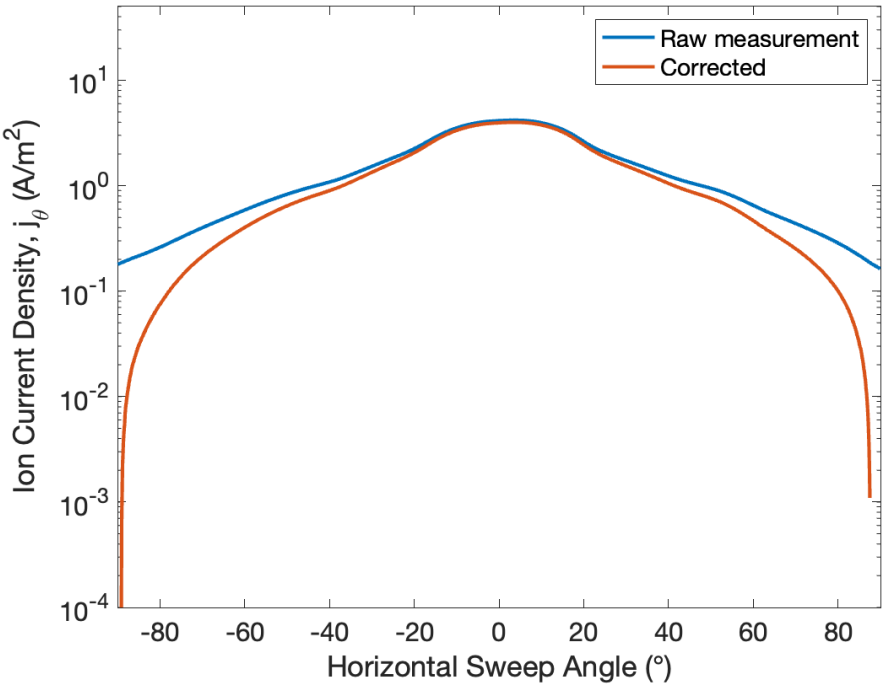

Figure 66 – Raw and corrected ion current density for a horizontal sweep at gradient1 test condition

Table 35 – Calculated ion beam properties at gradient1 test condition on krypton using Faraday probe

Test No.	Condition Name	I_d (A)	I_b (A)	θ_{div} (°)	η_b (%)
2	gradient 1	7.91	4.20	33.67	53.18

5.4.1.3 Langmuir Probe

The Langmuir probe is positioned on the radial probe arm to collect measurements at the thruster centerline. The radial arm is positioned at 0 °at a horizontal sweep angle to allow the measurements to be conducted. The Langmuir probe undergoes three consecutive scans, sweeping from -50 V to 80 V. Table 36 depicts plasma parameters such as electron density, temperature, and potential obtained from the data analysis of the I-V trace. The I-V traces obtained from the HET plume exhibited characteristics that resemble the principles of Langmuir probe theory, suggesting the presence of a Maxwellian electron distribution. The data processing for the trace obtained for the test condition is shown in Figure 67.

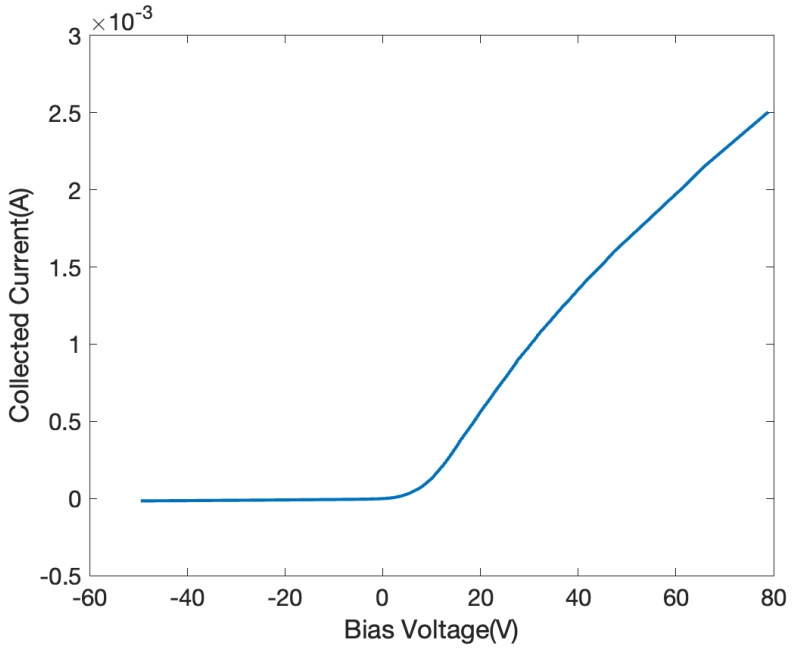

Figure 67 – Average I-V traces collected by Langmuir probe at gradient1 test condition

Table 36 – Calculated plume properties at gradient1 test condition on krypton using Langmuir probe.

Test No.	Condition Name	T_e (eV)	n_e (m^{-3})	V_p (V)
2	gradient 1	3.92	1.93×10^{15}	14.60

5.4.1.4 RPA Probe

The RPA probe is located on the radial probe arm, and to take measurements at the thruster centerline, the radial arm is positioned at 0° in a horizontal sweep. The RPA was swept from 0 V to 450 V, and three successive scans were performed. The voltage with the largest d*I*/dV must be determined to acquire the plasma parameters, which are the acceleration voltages experienced by ions. Figure 68 illustrates that the maximum value achieved at the current operating condition was 251 V.

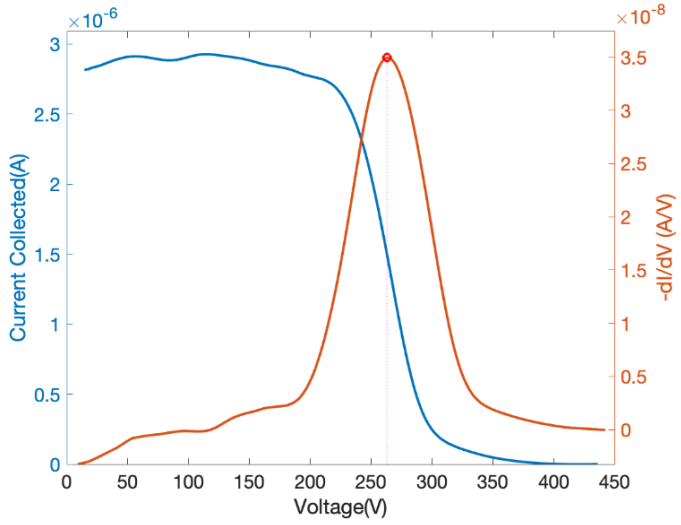

Figure 68 – Average I-V traces collected by RPA(left) and ion energy distribution function represented by -d*I*/dV (right) at gradient1 test condition

5.4.1.5 Oscilloscope

Table 37 shows time-resolved measurements of the thruster discharge characteristics under operating conditions. In order to eliminate any discrepancies in the measurements that may have resulted from plasma fluctuations, five measurements were recorded over a two-hour period and averaged to determine the final discharge characteristics.

Table 37 – Time-resolved measurements of discharge current at gradient1 test condition.

Test No.	Condition Name	I_d (A)	$I_{d,pk2pk}$ (A)	$I_{d,rms}$ (A)
2	gradient 1	7.91	4.22	7.92

5.4.1.6 Thrust Stand

Following the completion of measurements with all probes, thrust measurements were carried out. The average thrust value was determined by taking consecutive thruster measurements in a row. The thruster was permitted to achieve thermal stable state conditions between each measurement. The current operating condition yielded a thrust of 76.02 mN with an error of ±2 mN. Specific impulse obtained for the current operating condition was 1373 s.

5.4.2 Gradient 2 Test Condition

5.4.2.1 Sweep Probe Apparatus

The Sweep Probe apparatus is operated after thrust has achieved the thermal steady state condition. The apparatus consists of a Faraday probe that collects ion current across a hemispherical area. The collector and the guard ring of the Faraday are biased to -30V using the Keithley 2470 source meter. Measurements are conducted with a continuous sweep ranging from -41°to 46°for the probe with a resolution of 0.1 °for the measurements for data analysis. After three consecutive vertical sweeps, the sweep probe apparatus mounted on the radial arm is swept horizontally with an angular spacing of 5°. This results in a total of 37 horizontally positioned scans ranging from -90 °to 90°. The ion current measurements from the three-dimensional sweeping of the plume can be seen in Figure 69. An ion beam current of 2.24 A with a beam divergence of 26° was obtained from the raw data from the Faraday probe. The standard error associated with the reading is of 1.8×10^{-7}, deeming the measurements to be highly reliable and accurate. In order to get the total ion beam current of the plume, a horizontal scan is conducted with the sweep probe apparatus with the position of the Faraday probe at 0° in vertical direction resulting in the probe being situated at the centerline. The three-dimensional scan yielded a 36.9% decrease compared to the horizontal sweep in the measurement of ion beam current due to the restricted vertical sweep range. The vertical scans were extrapolated using the horizontal scan measurements to determine the potential full-scale measurement of the ion beam current while preserving the trend of ion current density variation across the 37 vertical scans. The data extrapolation resulted in measurements that span from -90° to 90° in both

the vertical and horizontal directions, thereby enabling the total estimation of the hemispherical ion current for P5 at 2.3 kW, as illustrated in Figure 70. An ion beam current measurement of 4.40 A and a divergence angle of 33.91° was obtained from the extrapolated three-dimensional ion current. The ion beam current measurements were evaluated after correcting for secondary electron emission and charge exchange at horizontal and vertical angles, yielding a 95% ion beam percentage.

Table 38 – Calculated ion beam properties at gradient2 test condition on krypton using sweep probe apparatus.

Test No.	Condition Name	I_d (A)	I_b (A)	θ_{div} (°)	η_b (%)
3	gradient2	7.94	4.40	34	55.46

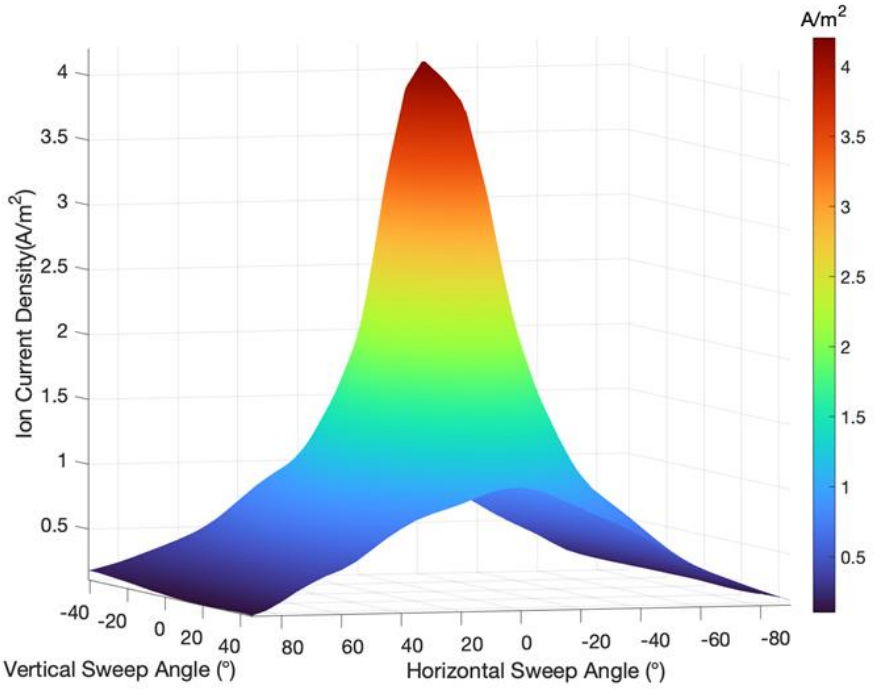

a)

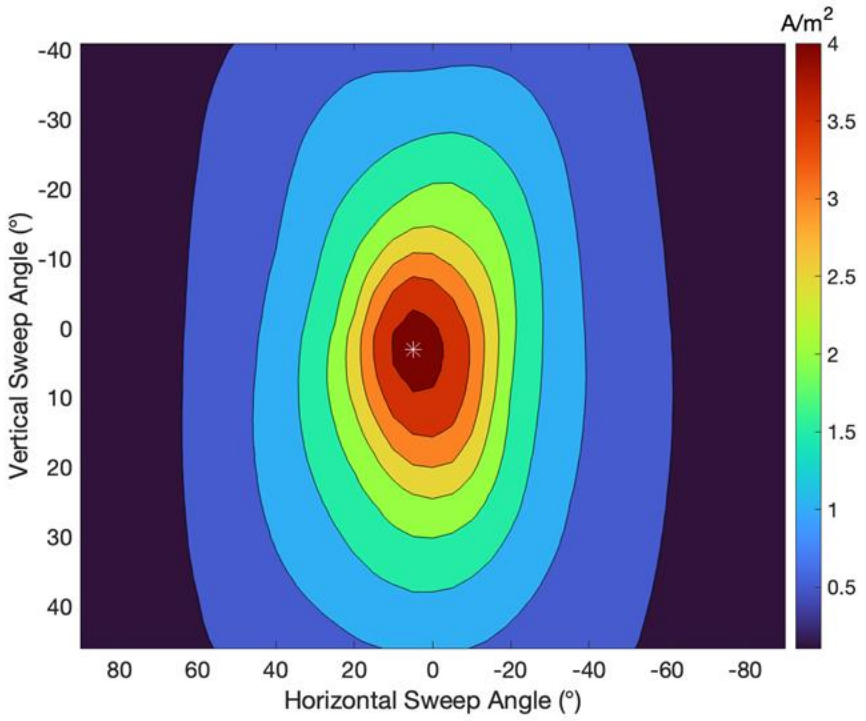

b)

Figure 69 – Raw measurements of a)Three-dimensional ion current density variation with horizontal and vertical sweep b) Contour map of ion current density at gradient2 test condition

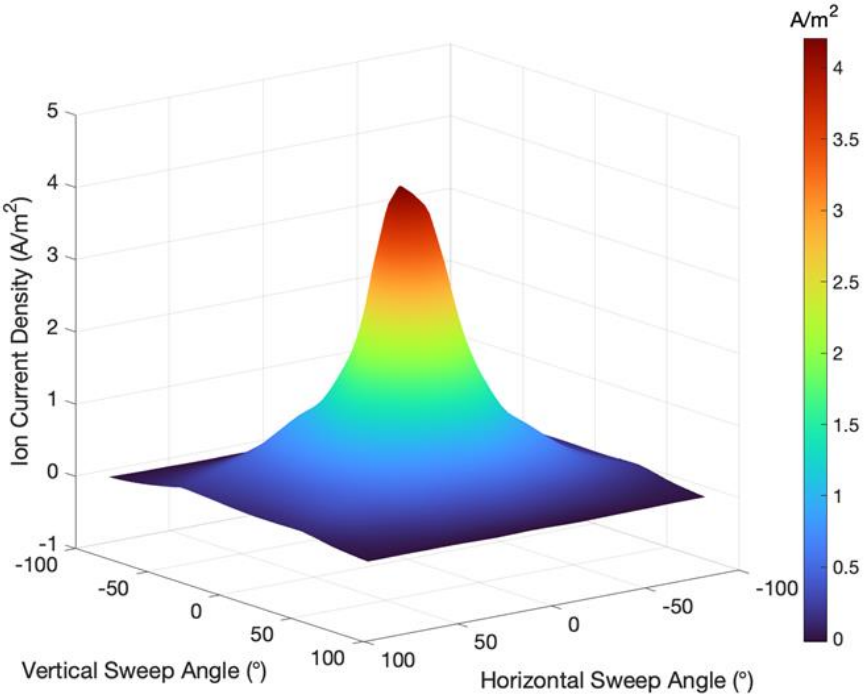

a)

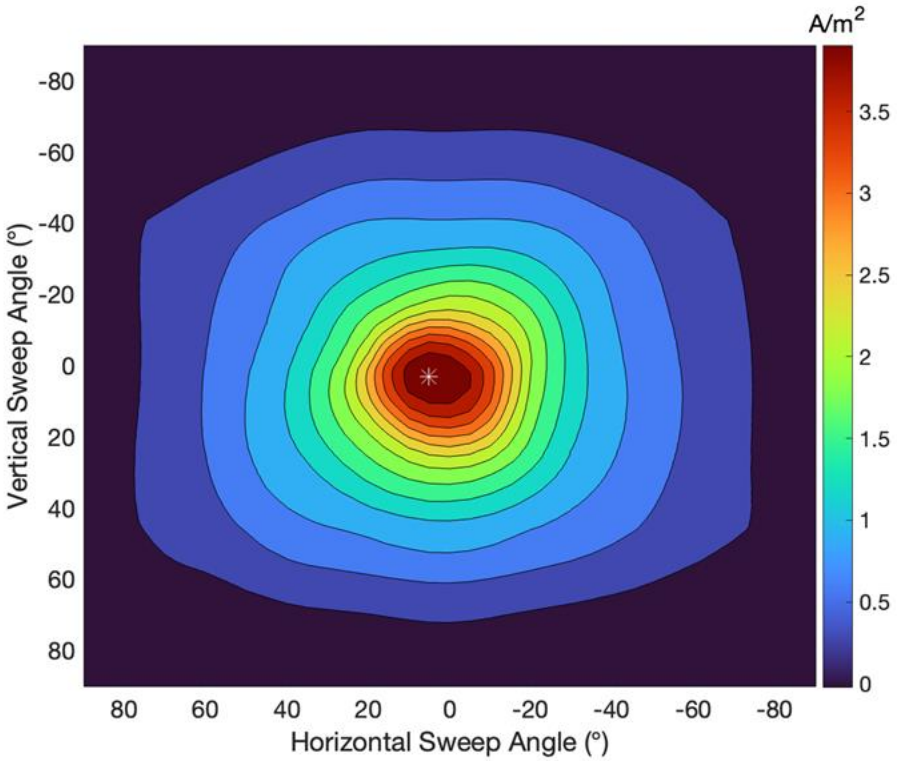

b)

Figure 70 – Extrapolated measurements of a) Three-dimensional ion current density variation with horizontal and vertical sweep b) Contour map of ion current density at gradient2 test condition

5.4.2.2 Faraday Probe

The Faraday probe is mounted on the radial arm and swept horizontally from -90° to 90° with a resolution of ±0.17°. The Collector and Guard of the Faraday are biased at -30 V to collect the ion current in the plume. The radial arm motion control system is subject to a systemic error of ±2%. The uncertainty associated with the scan measurements was determined by conducting three consecutive scans. Table 39 displays the thruster's current utilization, beam divergence, and ion beam current at the operating condition. Figure 71 displays the revised Faraday probe scan representing the ion current density.

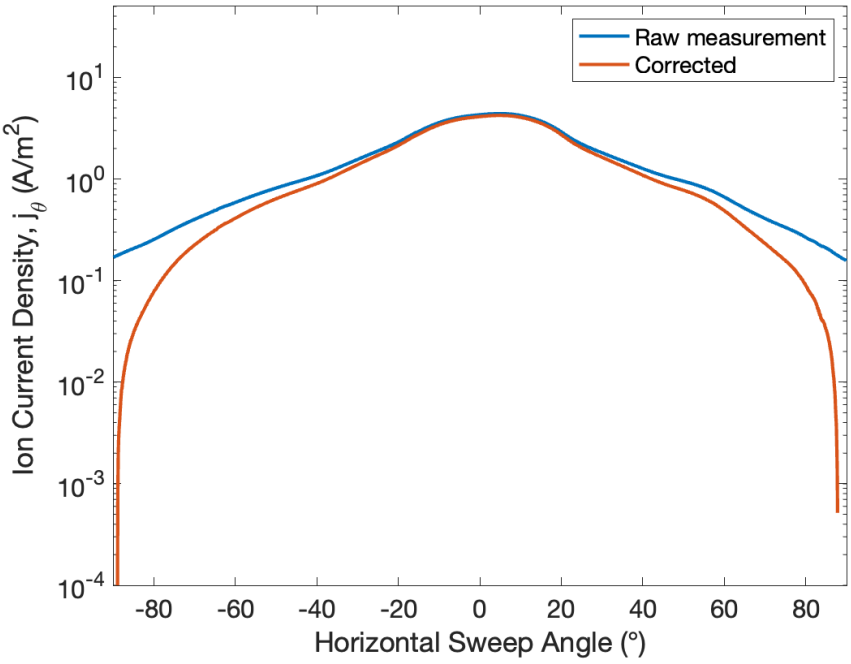

Figure 71 – Raw and corrected ion current density for a horizontal sweep at gradient2 test condition

Table 39 – Calculated ion beam properties at gradient2 test condition on krypton using Faraday probe

Test No.	Condition Name	I_d (A)	I_b (A)	θ_{div} (°)	η_b (%)
3	gradient 2	7.94	4.32	33.32	54.38

5.4.2.3 Langmuir Probe

The Langmuir probe is positioned on the radial probe arm to collect measurements at the thruster centerline. The radial arm is positioned at 0 °at a horizontal sweep angle to allow the measurements to be conducted. The Langmuir probe undergoes three consecutive scans, sweeping from -50 V to 80 V. Table 40 depicts plasma parameters such as electron

density, temperature, and potential obtained from the data analysis of the I-V trace. The I-V traces obtained from the HET plume exhibited characteristics that resemble the principles of Langmuir probe theory, suggesting the presence of a Maxwellian electron distribution. The data processing for the trace obtained for the test condition as shown in Figure 72.

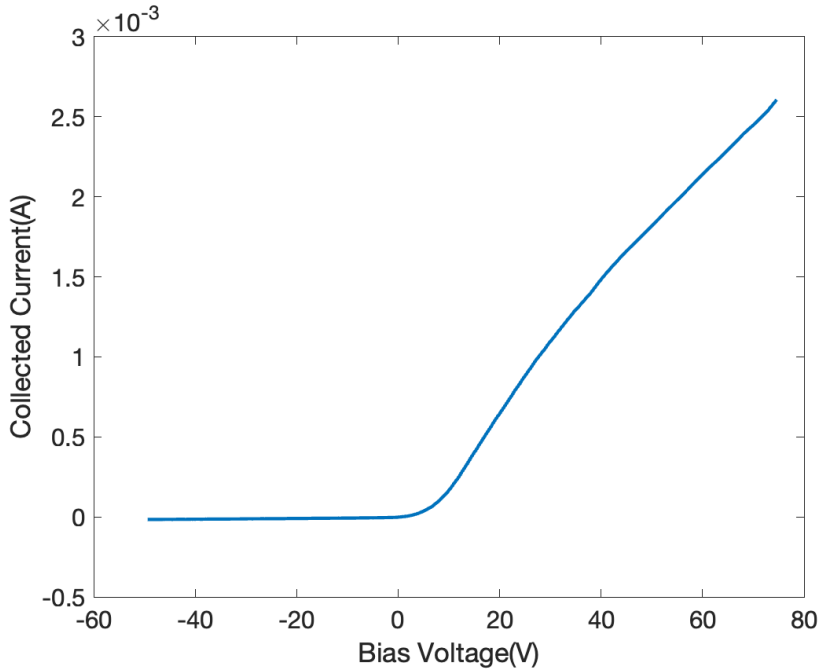

Figure 72 – Average I-V traces collected by Langmuir probe at gradient2 test condition

Table 40 – Calculated plume properties at gradient2 test condition on krypton using Langmuir probe.

Test No.	Condition Name	T_e (eV)	n_e (m^{-3})	V_p (V)
3	gradient 2	3.93	1.94×10^{15}	14.56

5.4.2.4 RPA Probe

The RPA probe is located on the radial probe arm, and to take measurements at the thruster centerline, the radial arm is positioned at 0° in a horizontal sweep. The RPA was swept from 0 V to 450 V, and three successive scans were performed. The voltage with the largest d*I*/dV must be determined to acquire the plasma parameters, which are the acceleration voltages experienced by ions. Figure 73 illustrates that the maximum value achieved at the current operating condition was 256.5 V.

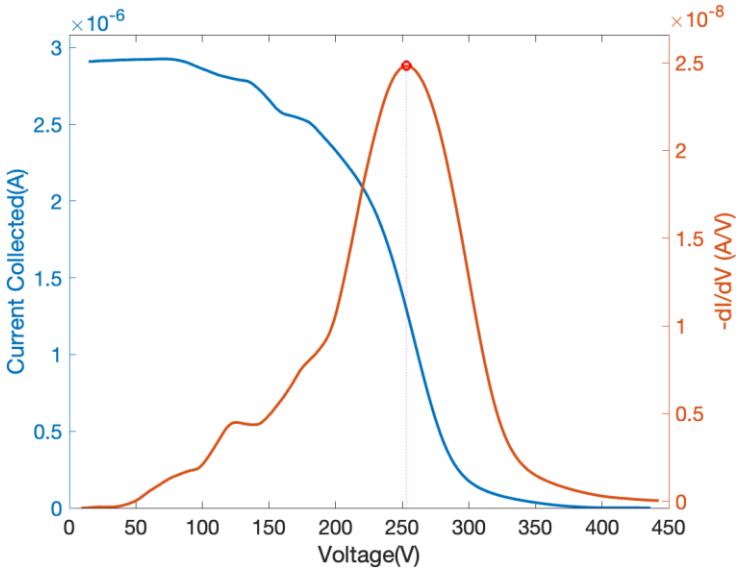

Figure 73 – Average I-V traces collected by RPA(left) and ion energy distribution function represented by -d*I*/dV (right) at gradient2 test condition

5.4.2.5 Oscilloscope

Table 41 shows time-resolved measurements of the thruster discharge characteristics under operating conditions. In order to eliminate any discrepancies in the measurements that may have resulted from plasma fluctuations, five measurements were recorded over a two-hour period and averaged to determine the final discharge characteristics.

Table 41 – Time-resolved measurements of discharge current at gradient2 test condition.

Test No.	Condition Name	I_d (A)	$I_{d,pk2pk}$ (A)	$I_{d,rms}$ (A)
3	gradient 2	7.94	5.01	7.92

5.4.2.6 Thrust Stand

Following the completion of measurements with all probes, thrust measurements were carried out. The average thrust value was determined by taking consecutive thruster measurements in a row. The thruster was permitted to achieve thermal stable state conditions between each measurement. The current operating condition yielded a thrust of 75.6 mN with an error of ±2 mN. Specific impulse obtained for the current operating condition was 1366 s.

5.4.3 Gradient 3 Test condition

5.4.3.1 Sweep Probe Apparatus

The Sweep Probe apparatus is operated after the thrust has achieved the thermal steady state condition. The apparatus consists of a Faraday probe that collects ion current across a hemispherical area. The collector and the guard ring of the Faraday are biased to -30V using the Keithley 2470 source meter. Measurements are conducted with a continuous sweep ranging from -41°to 46°for the probe with a resolution of 0.1 °for the measurements for data analysis. After three consecutive vertical sweeps, the sweep probe

apparatus mounted on the radial arm is swept horizontally with an angular spacing of 5°. This results in a total of 37 horizontally positioned scans ranging from -90° to 90°. The ion current measurements from the three-dimensional sweeping of the plume can be seen in Figure 74. An ion beam current of 2.23 A with a beam divergence of 26° was obtained from the raw data from the Faraday probe. The standard error associated with the reading is 1.8×10^{-7}, deeming the measurements to be highly reliable and accurate. In order to get the total ion beam current of the plume, a horizontal scan is conducted with the sweep probe apparatus with the position of the Faraday probe at 0° in vertical direction resulting in the probe being situated at the centerline. The three-dimensional scan yielded a 36.9% decrease compared to the horizontal sweep in the measurement of ion beam current due to the restricted vertical sweep range. The vertical scans were extrapolated using the horizontal scan measurements to determine the potential full-scale measurement of the ion beam current while preserving the trend of ion current density variation across the 37 vertical scans. The data extrapolation resulted in measurements that span from -90° to 90° in both the vertical and horizontal directions, thereby enabling the total estimation of the hemispherical ion current for P5 at 2.3 kW, as illustrated in Figure 75. An ion beam current measurement of 4.35 A and a divergence angle of 34° was obtained from the extrapolated three-dimensional ion current. The ion beam current measurements were evaluated after correcting for secondary electron emission and charge exchange at horizontal and vertical angles, yielding a 95% ion beam percentage.

Table 42 – Calculated ion beam properties at gradient3 test condition on krypton using sweep probe apparatus.

Test No.	Condition Name	I_d (A)	I_b (A)	θ_{div} (°)	η_b (%)
4	gradient 3	7.94	4.35	34	54.87

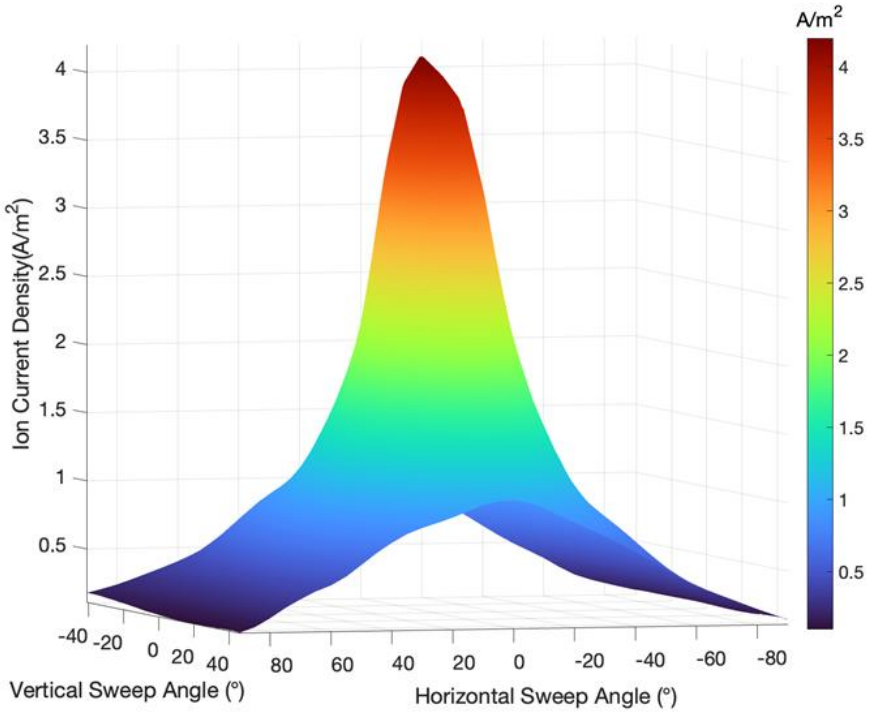

a)

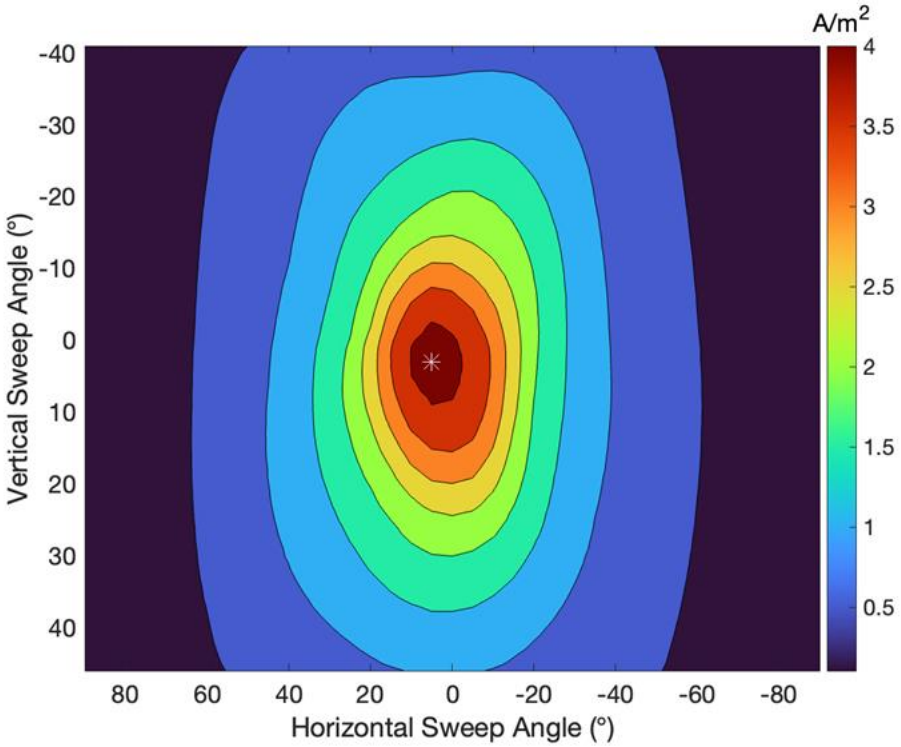

b)

Figure 74 – Raw measurements of a) Three-dimensional ion current density variation with horizontal and vertical sweep b) Contour map of ion current density at gradient3 test condition

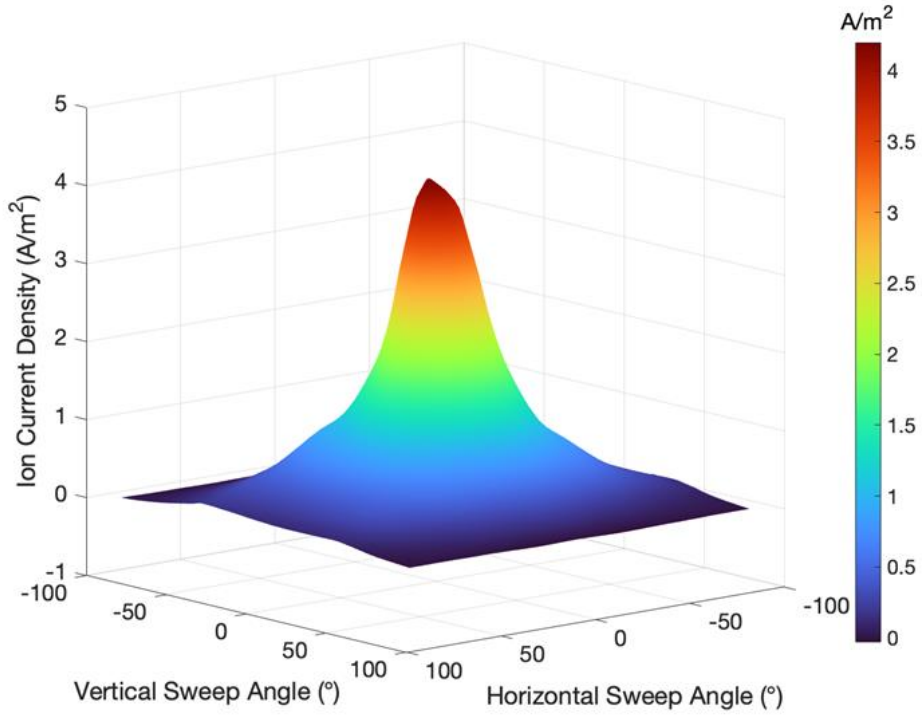

a)

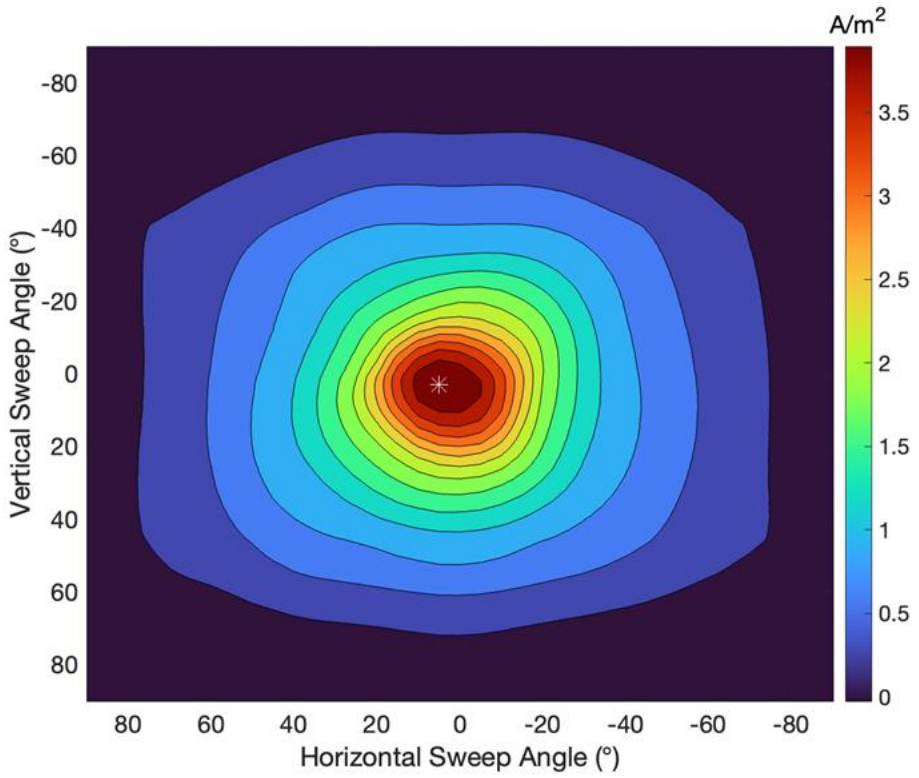

b)

Figure 75 – Extrapolated measurements of a)Three-dimensional ion current density variation with horizontal and vertical sweep b) Contour map of ion current density at gradient3 test condition

5.4.3.2 Faraday Probe

The Faraday probe is mounted on the radial arm and swept horizontally from -90° to 90° with a resolution of ±0.17°. The Collector and Guard of the Faraday are biased at -30 V to collect the ion current in the plume. The radial arm motion control system is subject to a systemic error of ±2%. The uncertainty associated with the scan measurements was determined by conducting three consecutive scans. Table 43 displays the thruster's current utilization, beam divergence, and ion beam current at the operating condition. Figure 76 displays the revised Faraday probe scan representing the ion current density.

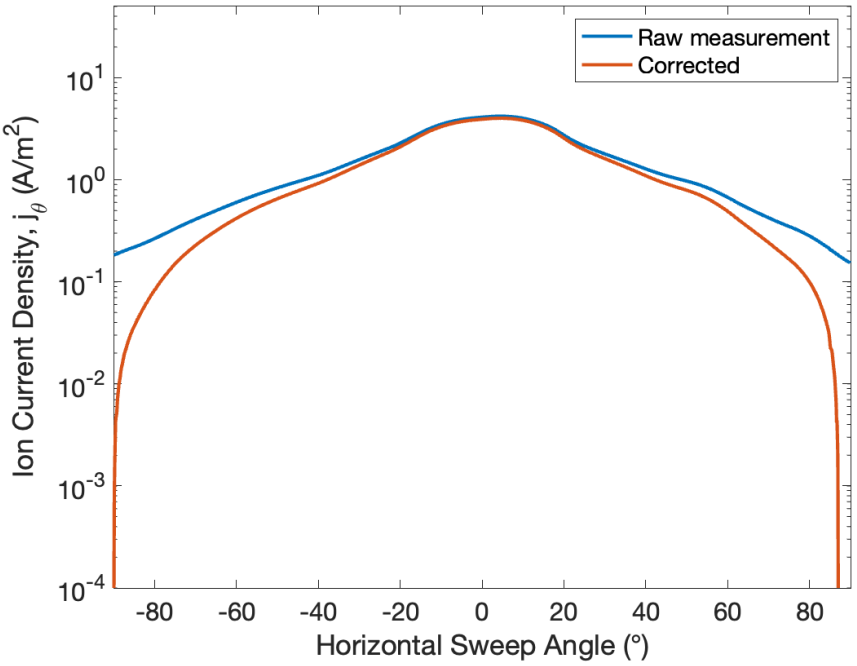

Figure 76 – Raw and corrected ion current density for a horizontal sweep at gradient3 test condition

Table 43 – Calculated ion beam properties at gradient3 test condition on krypton using Faraday probe

Test No.	Condition Name	I_d (A)	I_b (A)	θ_{div} (°)	η_b (%)
4	gradient 3	7.94	4.33	33.68	54.48

5.4.3.3 Langmuir Probe

The Langmuir probe is positioned on the radial probe arm to collect measurements at the thruster centerline. The radial arm is positioned at 0°at a horizontal sweep angle to allow the measurements to be conducted. The Langmuir probe undergoes three consecutive scans, sweeping from -50 V to 60 V.

Table 44 depicts plasma parameters such as electron density, temperature, and potential obtained from the data analysis of the I-V trace. The I-V traces obtained from the HET plume exhibited characteristics that resemble the principles of Langmuir probe theory, suggesting the presence of a Maxwellian electron distribution. The data processing for the trace obtained for the test condition as shown in Figure 77.

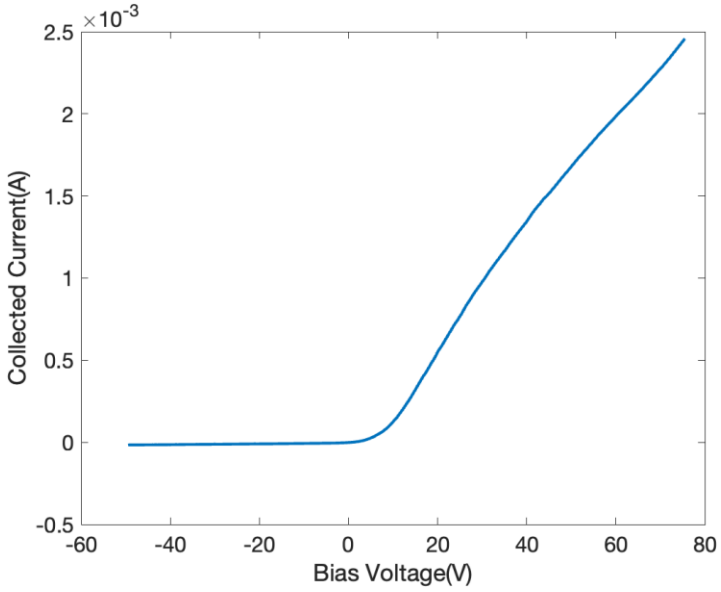

Figure 77 – Average I-V traces collected by Langmuir probe at gradient3 test condition.

Table 44 – Calculated plume properties at gradient3 test condition on krypton using Langmuir probe.

Test No.	Condition Name	T_e (eV)	n_e (m^{-3})	V_p (V)
4	gradient 3	3.85	1.63×10^{15}	14.14

5.4.3.4 RPA Probe

The RPA probe is located on the radial probe arm, and to take measurements at the thruster centerline, the radial arm is positioned at 0° in a horizontal sweep. The RPA was swept from 0 V to 450 V, and three successive scans were performed. The voltage with the largest d*I*/dV must be determined to acquire the plasma parameters, which are the acceleration voltages experienced by ions. Figure 78 illustrates that the maximum value achieved at the current operating condition was 254 V.

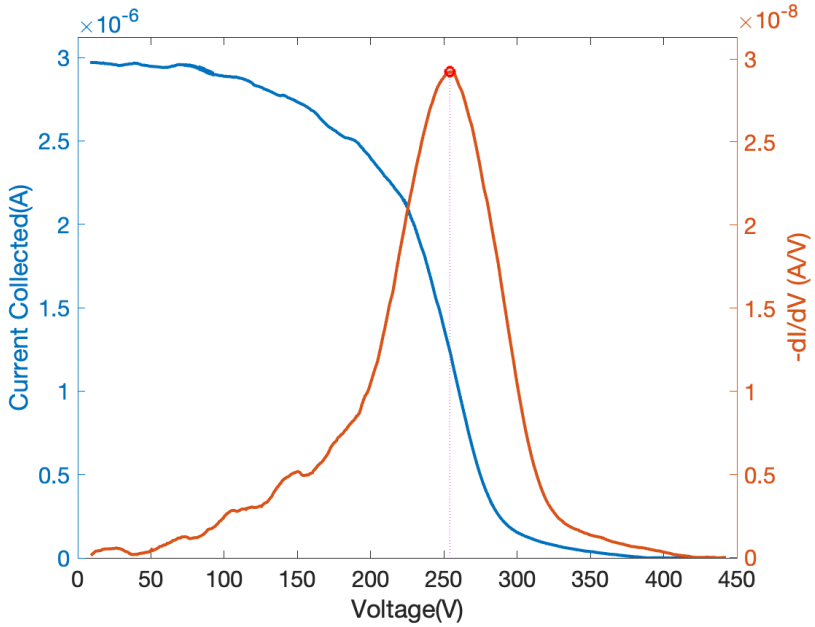

Figure 78 – Average I-V traces collected by RPA(left) and ion energy distribution function represented by -d*I*/dV (right) at gradient3 test condition

5.4.3.5 Oscilloscope

Table 45 shows time-resolved measurements of the thruster discharge characteristics under operating conditions. In order to eliminate any discrepancies in the measurements that may have resulted from plasma fluctuations, five measurements were

recorded over a two-hour period and averaged to determine the final discharge characteristics.

Table 45 – Time-resolved measurements of discharge current at gradient3 test condition.

Test No.	Condition Name	I_d (A)	$I_{d,pk2pk}$ (A)	$I_{d,rms}$ (A)
4	gradient 3	7.94	5.11	7.93

5.4.3.6 Thrust Stand

Following the completion of measurements with all probes, thrust measurements were carried out. The average thrust value was determined by taking consecutive thruster measurements in a row. The thruster was permitted to achieve thermal stable state conditions between each measurement. The current operating condition yielded a thrust of 75.9 mN with an error of ±2 mN. Specific impulse obtained for the current operating condition was 1371 s.

5.4.4 Gradient 4 Test Condition

5.4.4.1 Sweep Probe Apparatus

The Sweep Probe apparatus is operated after the thrust has achieved the thermal steady state condition. The apparatus consists of a Faraday probe that collects ion current across a hemispherical area. The collector and the guard ring of the Faraday are biased to -30 V using the Keithley 2470 sourcemeter. Measurements are conducted with a continuous sweep ranging from -41° to 46° for the probe with a resolution of 0.1° for the

measurements for data analysis. After three consecutive vertical sweeps, the sweep probe apparatus mounted on the radial arm is swept horizontally with an angular spacing of 5°. This results in a total of 37 horizontally positioned scans ranging from -90° to 90°. The ion current measurements from the three-dimensional sweeping of the plume can be seen in Figure 79. An ion beam current of 2.24 A with a beam divergence of 26° was obtained from the raw data from the Faraday probe. The standard error associated with the reading is 1.8×10^{-7}, deeming the measurements to be highly reliable and accurate. In order to get the total ion beam current of the plume, a horizontal scan is conducted with the sweep probe apparatus with the position of the Faraday probe at 0° in vertical direction, resulting in the probe being situated at the centerline. The three-dimensional scan yielded a 36.9% decrease compared to the horizontal sweep in the measurement of ion beam current due to the restricted vertical sweep range. The vertical scans were extrapolated using the horizontal scan measurements to determine the potential full-scale measurement of the ion beam current while preserving the trend of ion current density variation across the 37 vertical scans. The data extrapolation resulted in measurements that span from -90° to 90° in both the vertical and horizontal directions, thereby enabling the total estimation of the hemispherical ion current for P5 at 2.3 kW, as illustrated in

Figure 80. An ion beam current measurement of 4.33 A and a divergence angle of 34° were obtained from the extrapolated three-dimensional ion current. The ion beam current measurements were evaluated after correcting for secondary electron emission and charge exchange at horizontal and vertical angles, yielding a 95% ion beam percentage.

Table 46 – Calculated ion beam properties at gradient4 test condition on krypton using sweep probe apparatus.

Test No.	Condition Name	I_d (A)	I_b (A)	θ_{div} (°)	η_b (%)
5	gradient 4	8.05	4.33	34	53.74

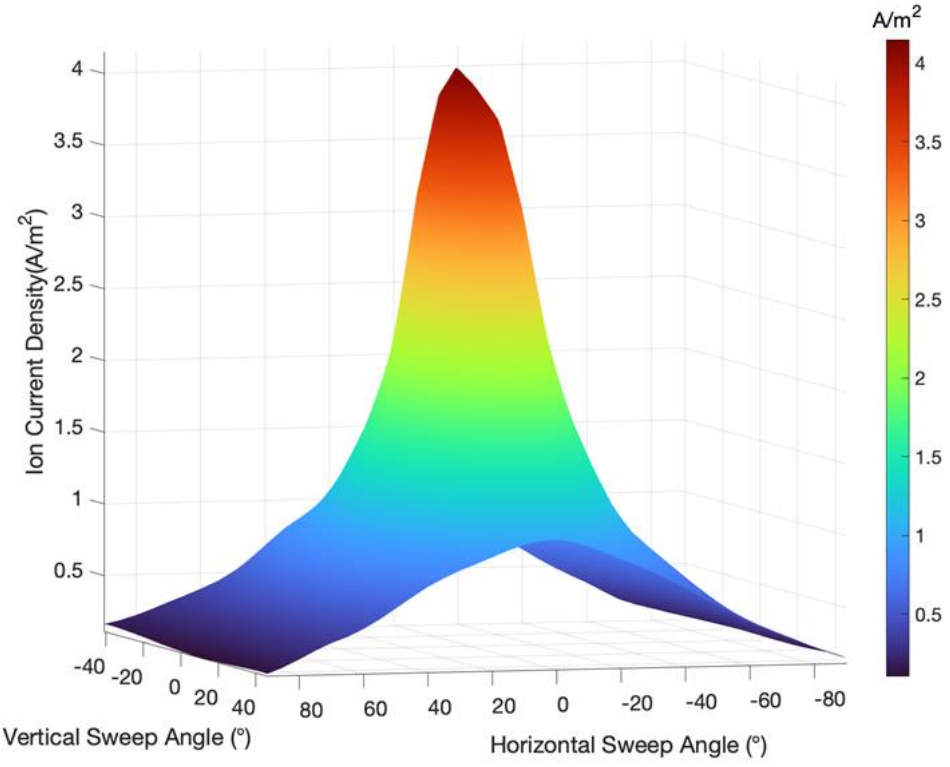

a)

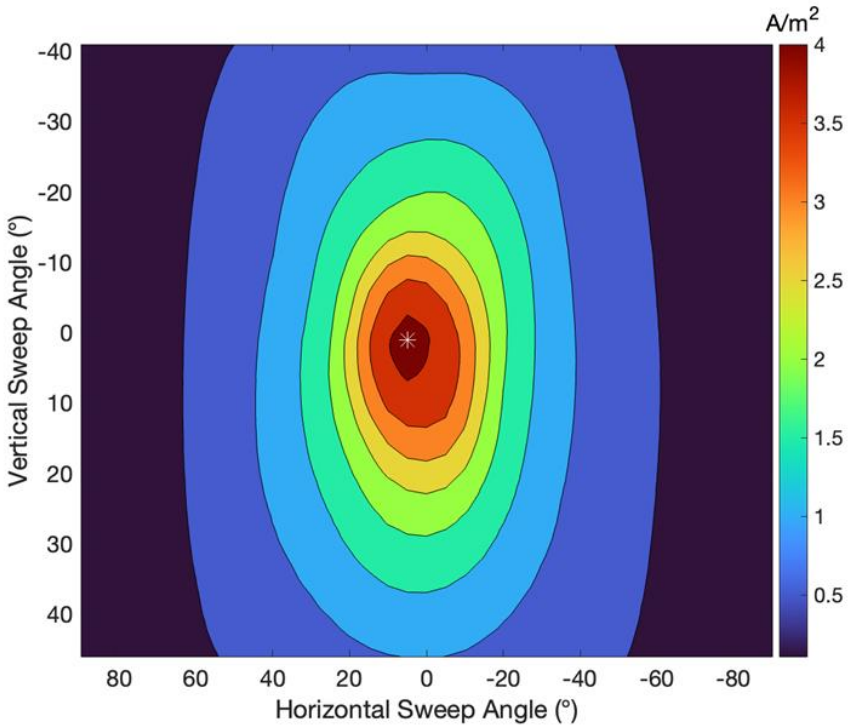

b)

Figure 79 – Raw measurements of a)Three-dimensional ion current density variation with horizontal and vertical sweep b) Contour map of ion current density at gradient4 test condition

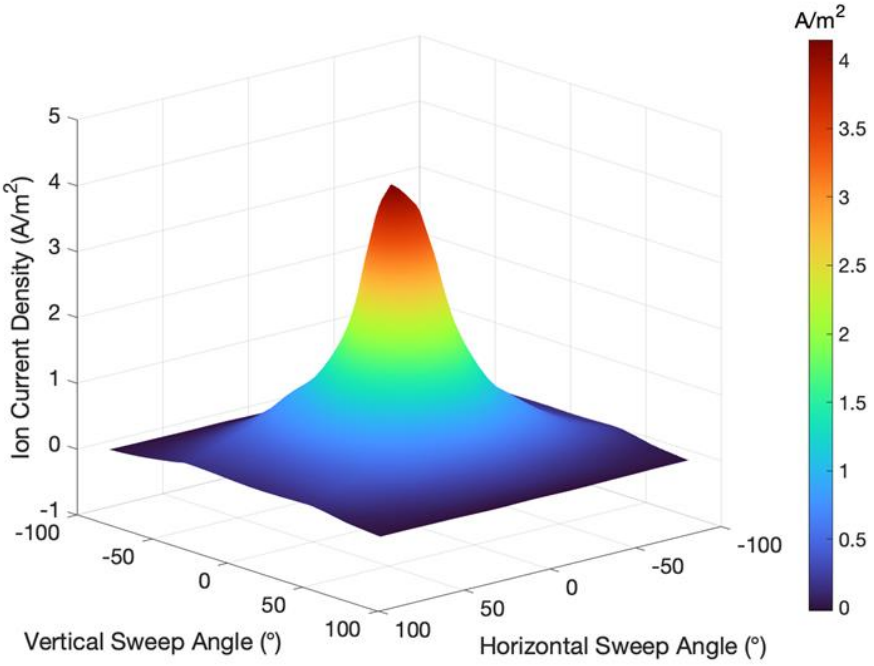

a)

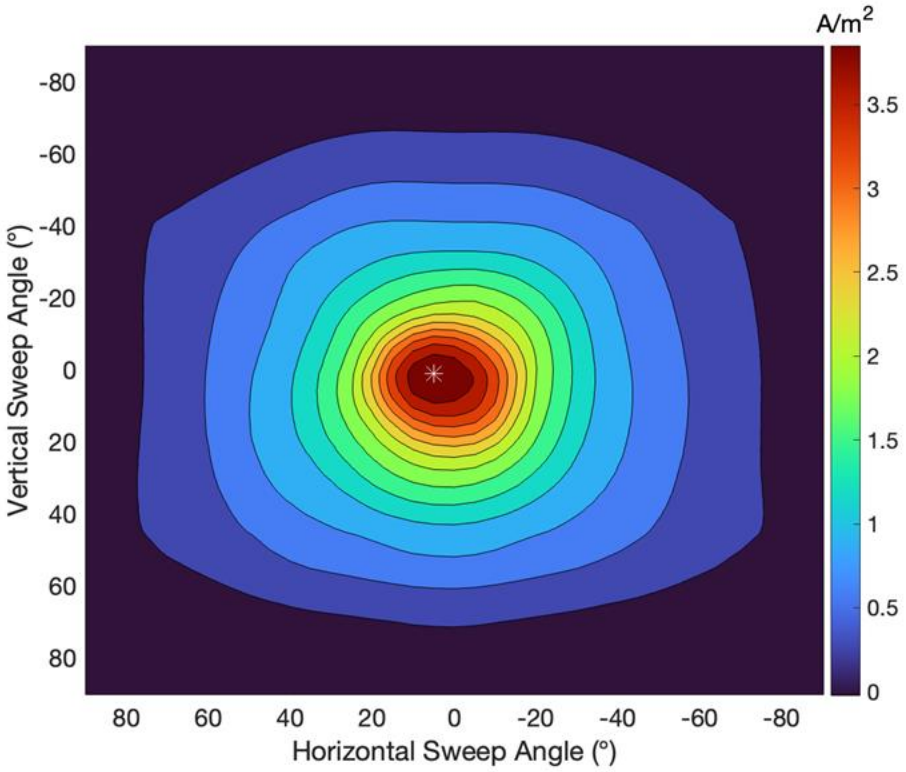

b)

Figure 80 – Extrapolated measurements of a)Three-dimensional ion current density variation with horizontal and vertical sweep b) Contour map of ion current density at gradient4 test condition

5.4.4.2 Faraday Probe

The Faraday probe is mounted on the radial arm and swept horizontally from -90°to 90°with a resolution of ±0.17°. The Collector and Guard of the Faraday are biased at -30 V to collect the ion current in the plume. The measurement of the Faraday probe is subject to the same uncertainty margin of ±10% as recommended in Faraday's best practices[77]. The radial arm motion control system is subject to a systemic error of ±2%. The uncertainty associated with the scan measurements was determined by conducting three consecutive scans. Table 47 displays the thruster's current utilization, beam divergence, and ion beam

current at the operating condition. Figure 81 displays the revised Faraday probe scan representing the ion current density.

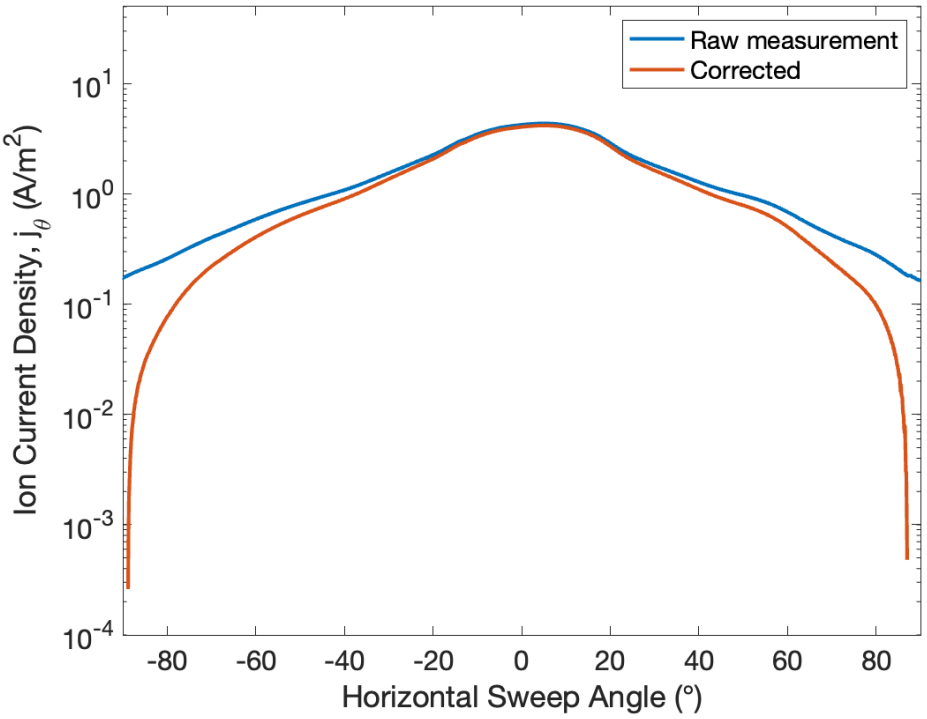

Figure 81 – Raw and corrected ion current density for a horizontal sweep at gradient4 test condition

Table 47 – Calculated ion beam properties at gradient4 test condition on krypton using Faraday probe

Test No.	Condition Name	I_d (A)	I_b (A)	θ_{div} (°)	η_b (%)
5	gradient 4	8.05	4.34	33.57	53.93

5.4.4.3 Langmuir Probe

The Langmuir probe is positioned on the radial probe arm to collect measurements at the thruster centerline. The radial arm is positioned at 0 °at a horizontal sweep angle to allow the measurements to be conducted. The Langmuir probe undergoes three consecutive scans, sweeping from -50 V to 60 V.

Table 48 depicts plasma parameters such as electron density, temperature, and potential obtained from the data analysis of the I-V trace. The I-V traces obtained from the HET plume exhibited characteristics that resemble the principles of Langmuir probe theory, suggesting the presence of a Maxwellian electron distribution. The data processing for the trace obtained for the test condition as shown in Figure 82.

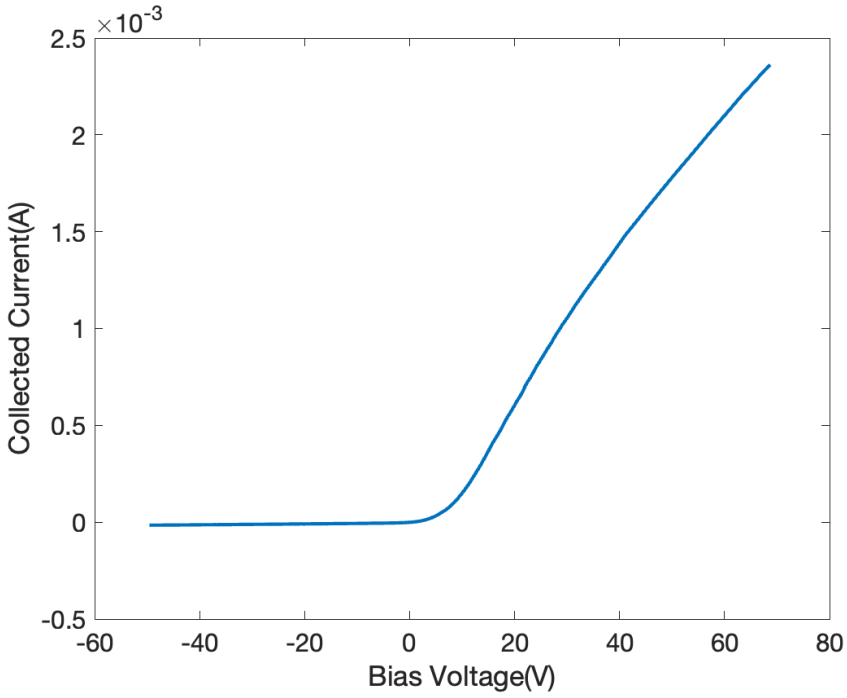

Figure 82 – Average I-V traces collected by Langmuir probe at gradient4 test condition

Table 48 – Calculated plume properties at gradient4 test condition on krypton using Langmuir probe.

Test No.	Condition Name	T_e (eV)	n_e (m^{-3})	V_p (V)
5	gradient 4	3.72	1.50×10^{15}	13.96

5.4.4.4 RPA Probe

The RPA probe is located on the radial probe arm, and to take measurements at the thruster centerline, the radial arm is positioned at 0 ° in a horizontal sweep. The RPA was swept from 0 V to 450 V, and three successive scans were performed. The voltage with the largest d*I*/dV must be determined to acquire the plasma parameters, which are the acceleration voltages experienced by ions. Figure 83 illustrates that the maximum value achieved at the current operating condition was 253.5 V.

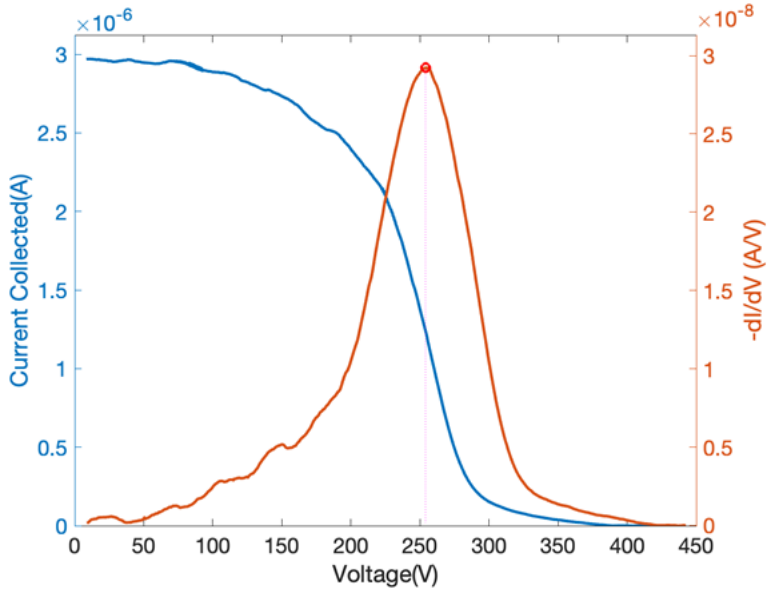

Figure 83 – Average I-V traces collected by RPA(left) and ion energy distribution function represented by -d*I*/dV (right) at gradient4 test condition

5.4.4.5 Oscilloscope

Table 49 shows time-resolved measurements of the thruster discharge characteristics under operating conditions. In order to eliminate any discrepancies in the measurements that may have resulted from plasma fluctuations, five measurements were recorded over a two-hour period and averaged to determine the final discharge characteristics.

Table 49 – Time-resolved measurements of discharge current at gradient4 test condition.

Test No.	Condition Name	I_d (A)	$I_{d,pk2pk}$ (A)	$I_{d,rms}$ (A)
5	gradient 4	8.05	5.32	7.94

5.4.4.6 Thrust

Following the completion of measurements with all probes, thrust measurements were carried out. The average thrust value was determined by taking consecutive thruster measurements in a row. The thruster was permitted to achieve thermal stable state conditions between each measurement. The current operating condition yielded a thrust of 75.3 mN with an error of ±2 mN. Specific impulse obtained for the current operating condition was 1360 s.

CHAPTER 6 DISCUSSION

This chapter analyzes the findings in Chapter 5 and offers valuable perspectives on the data. First, we investigate the change in thruster performance and stability caused by the change in uniform magnetic field and present a comparative study with respect to baseline conditions. Afterward, we address the thesis question by examining the impact of an azimuthal gradient in the magnetic field on thruster performance and the implications of an increase in gradient. Additionally, we offer an analysis of the changes in thrust vector caused by introducing a gradient utilizing the sweep probe apparatus.

6.1 Uniform Magnetic Field Effects on Thruster Performance

6.1.1 Experimental Results Analysis

As demonstrated in Chapter 5, the baseline test for the P5 thruster was conducted at a discharge current of 7.92 A and a voltage of 300 V, with an anode flow rate of 5.61 mg/s and a cathode flow rate of 0.44 mg/s. The inner and outer coil circuits supplied a current of 6 A and 4 A, respectively, to generate a magnetic field of 145 G for the baseline condition. Because of the thruster's construction, the magnetic coil's maximal current was 6 A and 4 A. Therefore, to assess the magnetic field's impact and prevent damage to the circuit, the current in the outer coil of the magnetic field was reduced to decrease the magnetic field. The inner and outer coil current ratio was maintained at 1.5:1 to ensure the trend remained consistent across the channel. Table 50 now offers the performance

parameters for the baseline and the six uniform magnetic field configurations, including thrust, impulse, efficiency, and stability.

Table 50 – Performance parameters of P5 for uniform magnetic field configurations at 300 V, anode flow of 5.61 mg/s and cathode flow of 0.44 mg/s krypton.

Test Condition No.	Condition Name	B (G)	T (mN)	I_{sp} (s)	$pk2pk$ (%)	η_b (%)	η_v (%)	η_m (%)	η (%)
1	baseline	145	78.03	1410	52.52	52.05	84.97	59.56	22.90
2	uniform 1	136	77.06	1392	72.40	50.80	83.91	59.08	21.97
3	uniform 2	130	76.8	1387	74.48	50.28	84.06	58.55	21.79
4	uniform 3	125	76.61	1384	69.03	50.88	83.85	59.03	21.77
5	uniform 4	120	76.51	1382	77.13	49.46	83.98	58.31	21.36
6	uniform 5	110	76.43	1381	125.31	48.05	83.89	58.17	20.76
7	uniform 6	93	75.7	1368	154.44	42.32	83.27	56.39	18.51

The baseline condition yielded the greatest thrust of 78.03 mN, with a current usage efficiency of 52.05% and peak-to-peak discharge current oscillation of 52.52%. As the magnetic field was reduced, the thrust, efficiency, and specific impulse decreased, as illustrated in Figure 84. The peak-to-peak percentage represents the stability of the thruster, with a higher peak-to-peak percentage indicating a lower level of stability. The stability also decreased, as seen by the increase in peak-to-peak percentage.

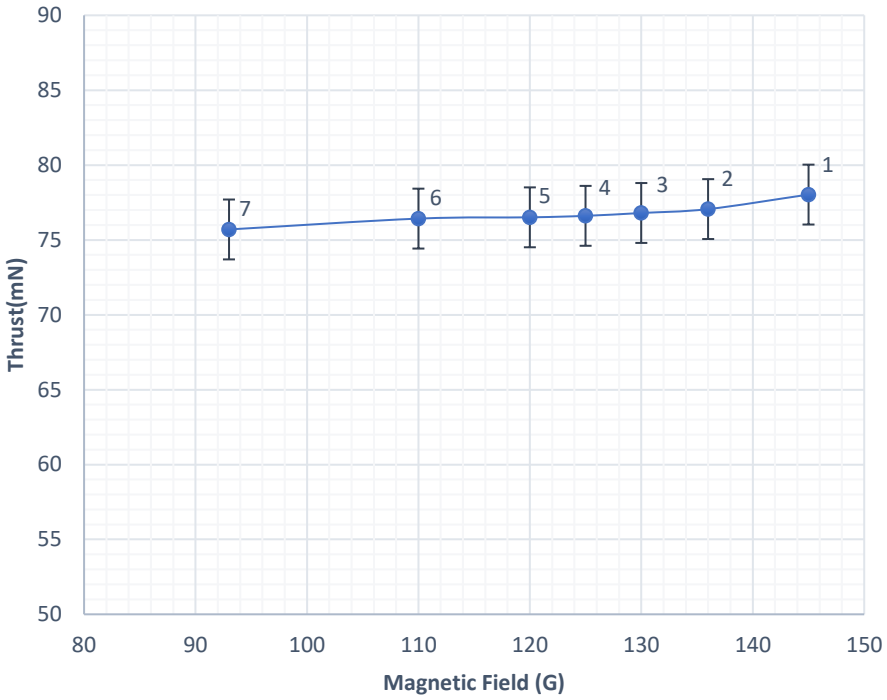
90
85
80
75
70
65
60
55
50
Thrust(mN)
80
90
100
110
120
130
140
150
Magnetic Field (G)
7
6
5
4
3
2
1

a)

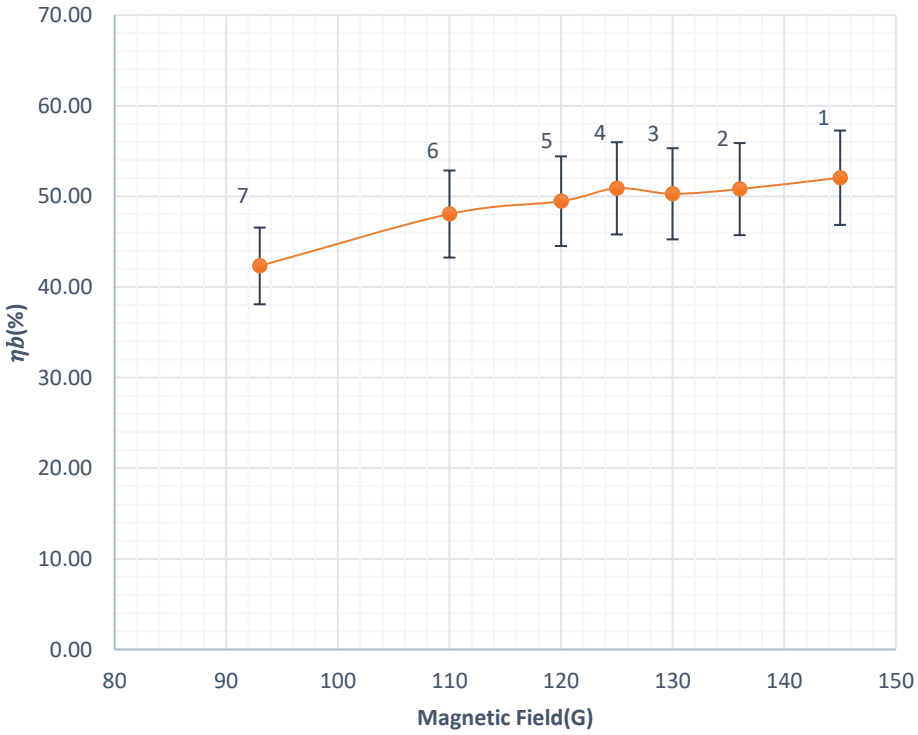
70.00
60.00
50.00
40.00
30.00
20.00
10.00
0.00
ηb(%)
80
90
100
110
120
130
140
150
Magnetic Field(G)
7
6
5
4
3
2
1

b)

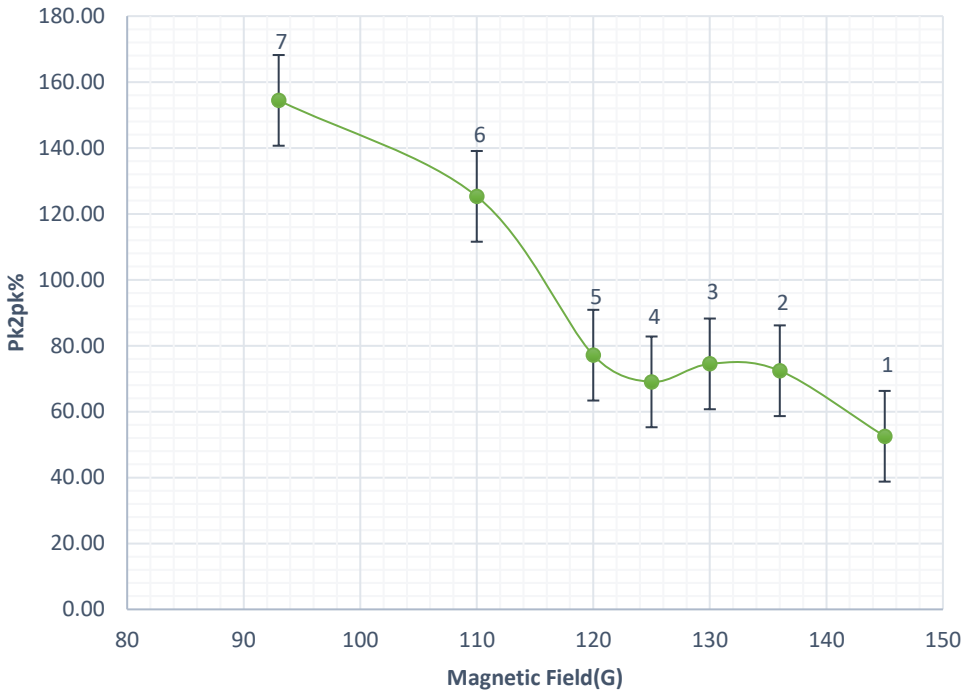

c)

Figure 84 – Variations of performance parameters a) thrust b) current utilization efficiency and c) pk-to-pk% of discharge current for uniform magnetic field test matrix 1 test conditions at 300 V, 5.61 mg/s anode mass flow rate and 0.44 mg/s cathode flow rate as a function of magnetic field strength.

Upon examining the performance change, it was evident in Figure 84 that the magnetic field's magnitude decreased by an average of 8.66 G incrementally across all operational conditions. This change led to an average decrement of 0.38 mN across all operational conditions, resulting in an average 0.50% decrease in thrust from the baseline for a magnetic field decrease of 7.02%. Acknowledging that the uncertainty surrounding the thrust measurement was ±2 mN is crucial. Consequently, the fluctuations in thrust were within the uncertainty bounds, indicating a minor impact of the magnetic field change on thrust.

Similarly, the impulse exhibited the same trend as the thrust, resulting in an average magnitude decrease of 7.01 s and a 1.01% decrease with a 7.02% decrease in the magnetic field compared to the baseline condition. As the magnetic field decreased by 7.02%, the current utilization efficiency experienced 1.62% average decrease in magnitude and 3.42% decrease compared to the baseline condition. Lastly, there was a 16.99% increase in the peak-to-peak% of the discharge current oscillation when the magnetic field decreased across the uniform magnetic field conditions. The uncertainty associated with the oscilloscope is taken as ±5%, thus depicting that the magnetic field affects the stability of the HET significantly. As outlined in section 5.1, the magnetic field magnitude was reduced to ensure that the decrease in magnitude experienced due to the azimuthal gradient in a magnetic field was uniformly applied to facilitate measurements using the OES diagnostics. Thus, the thruster experienced these operating conditions as extreme conditions, indicating the same magnetic field decrease. Upon examining the extreme conditions of one coil off and two coils off, as illustrated in the Table 50, condition 1 was the baseline condition, condition 3 represented one coil off (OC2 circuit), and operating condition 5 represented two coils off (OC2 and OC3 circuit). The thrust decreased by 1.23 mN and 1.57% as the HET operation transitioned from the baseline to the one coil-off condition. The current utilization efficiency decreased by 3.40%, peak-to-peak discharge current oscillations increased by 41.81%, and the magnetic field decreased by 10.34%. In the same way, the reduction of the magnetic field by 17.24% resulted in a decrease of 1.52 mN and 1.94% in thrust, a 4.97% decrease in efficiency, and a 46.84% increase in the peak-to-peak discharge current oscillations compared to the baseline condition.

In light of the model established in Chapter 3, the magnetic field is a critical factor in the influence of the ionization and acceleration processes. Changes in plasma parameters and thruster performance result from the influence of the magnetic field. The model illustrates the impact of the magnetic field magnitude at the departure plane on the various performance parameters. The electron confinement in the channel decreases as the magnetic field of the HET decreases. The reduction in confinement leads to decreased collision frequency, which induces ionization due to the reduced electron number density. Due to the reduction in the probability of ionization collision, the ohmic heating experienced by electrons decreases temperature. The electron's energy is less than that of the electron's in the baseline case as the collision frequency decreases and the electron temperature decreases. A decrease in the electron temperature results in a decrease in the energy possessed by the charged species, which leads to a less positive plasma potential at that location. The electron travels further within the channel to gain the energy required for ionization.

Consequently, the region responsible for ionization acceleration moves in the direction opposite to the flow, towards the anode. As a result of the electrons' movement causing the ionization acceleration region to move upstream, the length of the acceleration region that the ions observe increases. The ions are now generated at a location further upstream. The loss voltage has increased as a result of the increased likelihood of wall collisions and neutralization collisions among the ions. The rise in the voltage loss with a constant discharge voltage leads to a decrease in the acceleration voltage. The reduction in acceleration voltage indicates a decrease in ion velocity, which causes a change in efficiency, specific impulse, and thrust. Although the results presented emphasize the

alteration of plasma parameters within the channel, the experimental results indicate that the channel plasma parameters influenced the far-field plume measurement and can offer a comprehensive representation of the impact of the magnetic field on thruster performance.

Comparing the experimental results to the baseline condition, we observed an average 5.79% decrease in electron temperature and an average 0.34% decrease in acceleration voltage. These findings provide strong evidence for the model's capability to detect the impact of the magnetic field on the plasma parameters. The observed trends in Figure 85 further validate the model, depicting the real-world impact of the magnetic field on thruster performance.

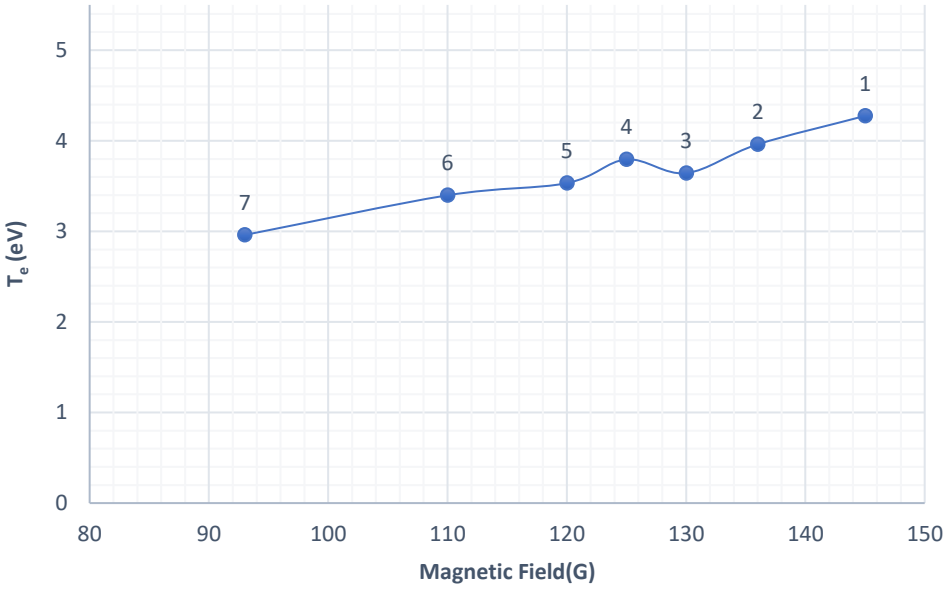

Figure 85 – Electron temperature variation as a function of magnetic field for uniform magnetic field test matrix 1 test conditions at 300 V, 5.61 mg/s anode flow rate, and 0.44 mg/s cathode flow rate.

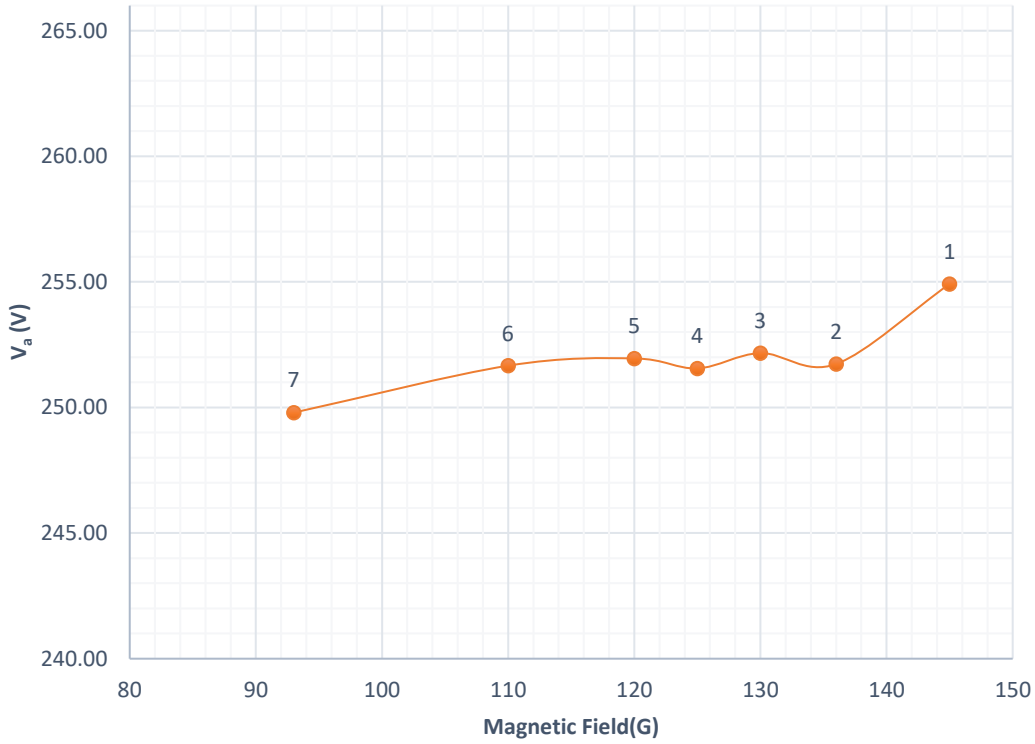

Figure 86 – Ion acceleration voltage variation as a function of magnetic field for uniform magnetic field test matrix 1 test conditions at 300 V, 5.61 mg/s anode mass flow rate, and 0.44 mg/s cathode flow rate.

The OES was employed to obtain measurements at 0, 5, and 10 mm downstream from the thruster exit plane to verify the postulated displacement of the ionization and acceleration region, as illustrated in section 3.2.2. The neutral emission wavelength, which emits the highest light intensity, was employed to monitor the alterations in response to varying magnetic fields. The maximal intensity light's wavelength, 811.24 nm, remained consistent throughout the test conditions.

An average decrease of 7.93% in light intensity was observed at the 0 mm condition, a 8.63% decrease in light intensity at the 5 mm condition, and a 5.68% decrease

in light intensity at the 10 mm condition. The collimator was then moved downstream of the exit plane using the linear motion stage. The light intensity of the neutral emission line decreased as the collimator receded from the exit plane. This decrease in intensity resulted from the principle that the plume primarily consists of neutralization collisions. Consequently, the other collisions result in energy emission due to the variation in metastasis of different particles, such as the excitation of neutrals, decreasing as we move away from the region of the maximum magnetic field. The light intensity of the neutral emission line decreased by 61.36% as the magnetic field was reduced by 17.93% as compared to the baseline, as illustrated in Figure 87. This decrease in light intensity illustrated the fluctuation in the ionization and acceleration region's location. When the intensity diminished, it indicated that the region had shifted upstream compared to the baseline.

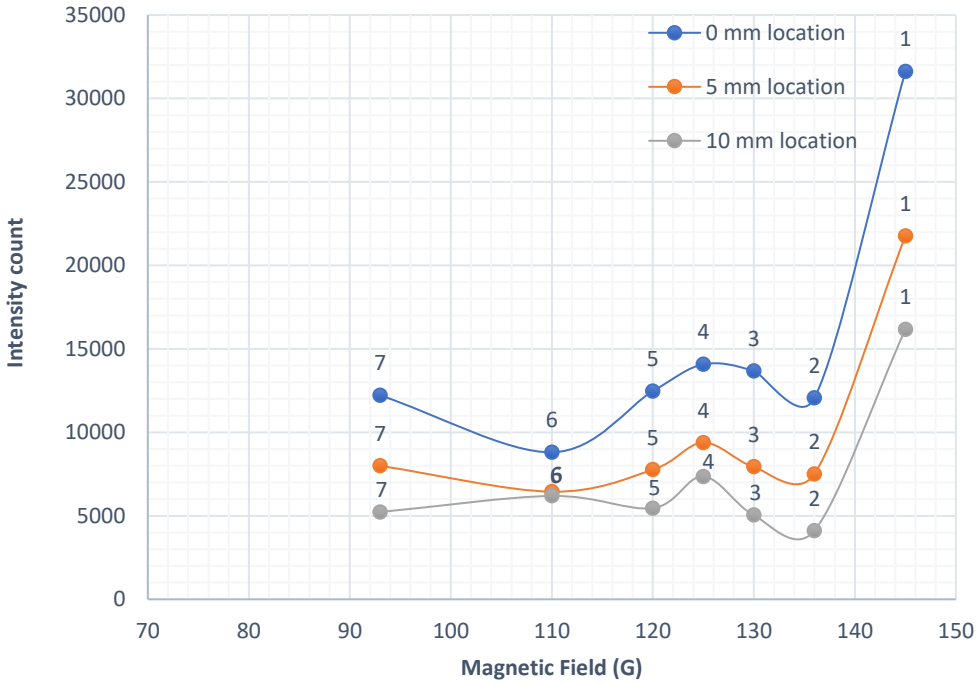

Figure 87 – Plume light intensity variation as a function of magnetic field at 0 mm, 5 mm, and 10 mm from thruster exit plane field for uniform magnetic field test matrix 1 test conditions at 300 V, 5.61 mg/s anode flow rate and 0.44 mg/s cathode flow rate.

Due to the collimator's placement outside the exit plane and the region of ionization and acceleration inside the channel, measurements of that region were unavailable. In conjunction with the high background noise, this led to an inability to observe any ion emission line that could provide a more precise understanding of the ionization process. A CRM model will be necessary for future studies to provide a detailed and accurate explanation of the processes that led to the observed trends resulting from a collision. Moreover, it is presently beyond the scope of the present investigation.

6.1.2 Summary

The model depicted in section 3.2.2 was validated by the evidence provided in this section, which illustrated the magnetic field's effect on the thruster's performance. The model indicates that a reduction in the magnetic field from the optimal magnetic field condition leads to a decrease in the stability and performance of the thruster. As the magnetic field decreases, the thrust and efficiency decrease as a result of the reduction in the ion beam current, which is a result of the effect of the magnetic field on ionization acceleration phenomena. The degree of oscillation in the discharge current, which is indicative of the instability of the HET operation, increases as the thruster deviates from the optimal magnetic field operating condition. Experimentally, magnetic field impact had the most influence on the thruster's stable operation and the least on the generated thrust. As opposed to a 0.50% decrease in thrust, a 7.02% decrease in magnetic field resulted in a 16.99% decrease in stability. The current utilization efficiency was the most significantly impacted by the change in magnetic field and significantly contributed to the overall

efficiency variations observed as the magnitude of the magnetic field decreased from the ideal operating condition of P5 in the current environment.

6.2 Azimuthal Magnetic Field Gradient Effects on Thruster Performance

6.2.1 Experimental Results Analysis

Evaluation of various uniform magnetic field configurations demonstrated the significant influence of the magnetic field on the performance of HET. Deviation from the optimal operating conditions reduced the performance and operation of the P5 thruster. In light of the findings of the preceding section, it is imperative to address the current research question. To quantify the change in HET performance caused by an azimuthal magnetic field gradient, an azimuthal magnetic field gradient was intentionally introduced into the channel, as described in section 4.1. The alteration in the current flow to the OC2 and OC3 coil circuits, which operated independently, facilitated the gradient in the channel. Table 51 presents the observed performance of the thruster under the baseline condition and four different operating conditions with varying magnitudes of the azimuthal magnetic field gradient. The four test scenarios range in the amount of current provided to the coils, resulting in variations in thrust, efficiency, and peak-to-peak% discharge current oscillation.

Table 51 – Performance parameters of P5 for azimuthal magnetic field gradient configurations at 300 V, anode flow rate of 5.61 mg/s, and cathode flow rate of 0.44 mg/s krypton.

Test No.	Condition Name	B_l (G)	$\nabla_\theta B_r$ (G/°)	T (mN)	I_{sp} (s)	$pk2pk$ (%)	η_b (%)	η_v (%)	η_m (%)	η (%)
1	baseline	145	0.00	78.03	1410	52.52	52.05	84.97	59.56	22.90
2	gradient1	137	0.18	77.06	1392	72.40	50.80	83.91	59.08	21.97
3	gradient2	131	0.31	76.8	1387	74.48	50.28	84.06	58.55	21.79
4	gradient3	125	0.30	76.61	1384	69.03	50.88	83.85	59.03	21.77
5	gradient4	121	0.36	76.51	1382	77.13	49.46	83.98	58.31	21.36

As detailed in section 5.1, the baseline condition for the P5 optimal operating condition was 300 V and 7.92 A, with a cathode mass flow of 5.61 mg/s and a cathode mass flow of 0.44 mg/s of krypton. The magnetic circuit configuration consisted of 6 A for the inner coil circuit and 4 A for the outer coil circuits. The baseline condition was the optimal operating condition for P5, resulting in the highest propulsion of the magnitude of 78.03mN, a current utilization efficiency of 52.05%, and a peak-to-peak% discharge current oscillation of 52.52%. With the introduction of the magnetic field gradient, the magnitude of the gradient increased throughout the operation condition, resulting in a decrease in thruster performance, as illustrated in Figure 88. The magnitude of the magnetic field in the localized region was reduced due to the reduction in current across the two independently operating coils. However, the area spans across which the gradient was observed was also increased. As the magnitude of the azimuthal gradient grew, the thrust and efficiency of the thruster both decreased due to the higher magnitude. The instability is indicated by the peak-to-peak percentage, where the higher the peak-to-peak percentage, the less stable the thruster operation. The thruster operation became more unstable as the

azimuthal gradient increased, increasing the peak-to-peak % of discharge current oscillation. The trends closely aligned with the uniform magnetic field test matrix outcomes. This variation in performance also indicated that a significant impact was observed despite the gradient being very small compared to the magnetic field's magnitude in the uniform portion of the channel.

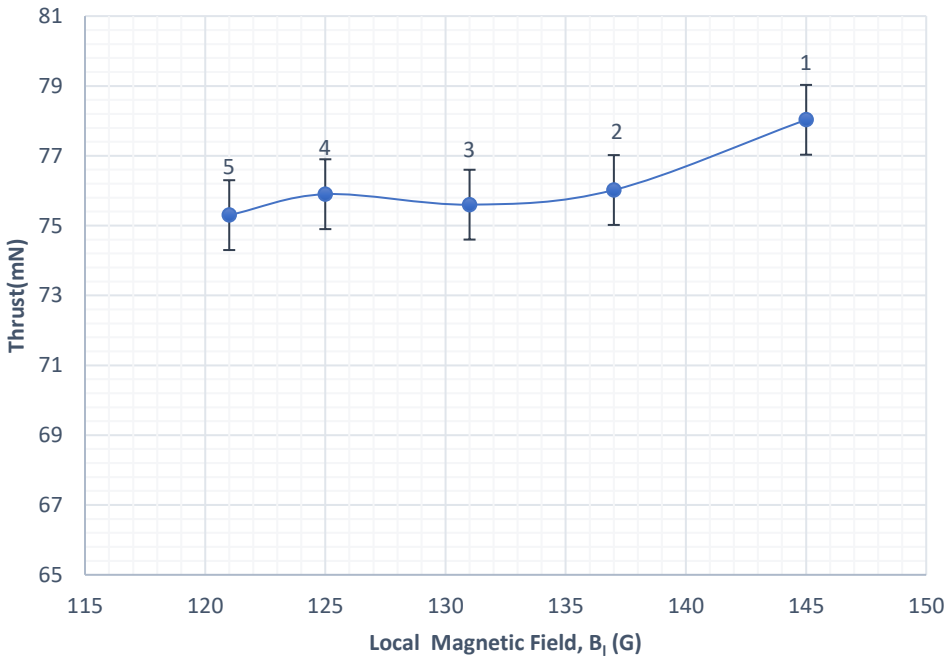

a)

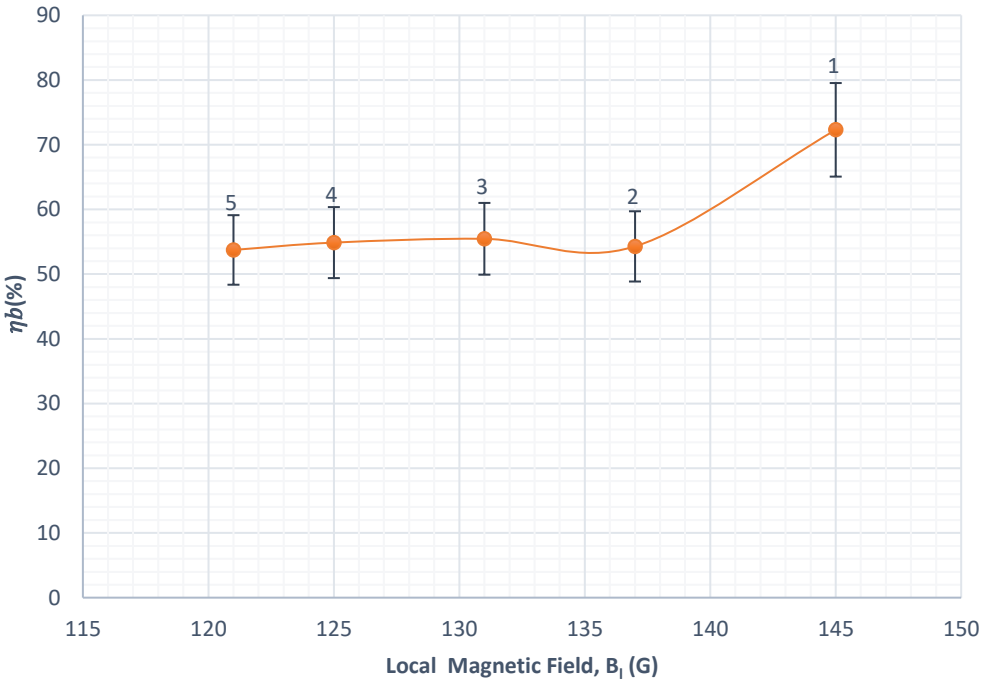

b)

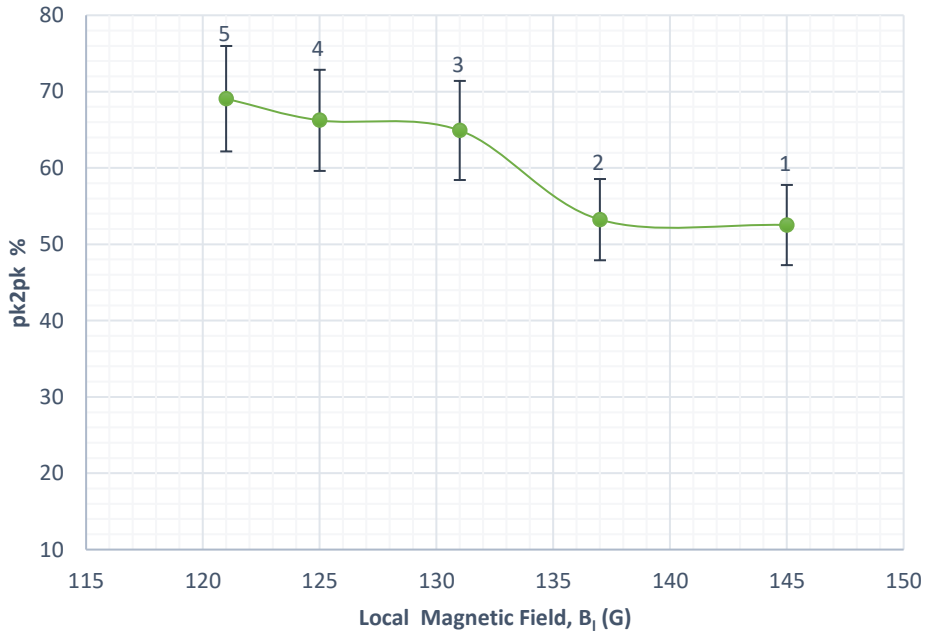

c)

Figure 88 – Variations of performance parameters a) thrust b) current utilization efficiency and c) pk-to-pk% of discharge current for azimuthal gradient magnetic field gradient test matrix 2 test conditions at 300 V, 5.61 mg/s anode flow rate and 0.44 mg/s cathode flow rate as a function of local magnetic field strength.

By examining the performance change, it is evident in Figure 88 that the magnitude of the magnetic field in the region of maximal gradient decreased by an average of 6.00 G across all operational conditions. Implementing the localized gradient led to an average reduction of 0.68 mN in thrust across all operational conditions, resulting in a 2.97% decrease from the baseline. Locally, the magnetic field experienced an average 4.41% decrease due to the gradients. As stated in the preceding section, the uncertainty associated with the thrust measurement is ±2 mN. Therefore, the changes in thrust lie slightly beyond the uncertainty ranges, indicating a minimal impact of magnetic field shifts on thrust.

Similarly, the impulse exhibited the same trend as the thrust, resulting in an average magnitude decrease of 12.32 s and a 2.97% decrease with a gradient in the magnetic field compared to the uniform condition. The current utilization efficiency experienced an average 4.64% decrease in magnitude for a 24.49% decrease with a gradient in the magnetic field compared to the baseline condition. Finally, the peak-to-peak % of the discharge current oscillation increased on average by 20.6% due to the gradient introduction. The azimuthal magnetic field gradient's influence on thruster stability illustrated that the stability of thruster operation is one of the thruster performance parameters that was most significantly influenced by non-uniformity.

The OES setup could not obtain radial measurements at the exit plane because the azimuthal magnetic field gradient was present only in a localized channel region. The measurements for the azimuthal gradient location will be obscured by the measurements obtained in the uniform region, as OES is a line-of-sight measurement technique. As provided in section 5.1, the magnetic field magnitude was reduced to ensure that the decrease in magnetic field due to the introduction of azimuthal gradient in the channel was

uniformly applied to facilitate measurements using the OES diagnostics. Thus, the thruster experienced these operating conditions as extreme conditions, indicating the same magnetic field decrease Figure 89. Section 5.3 presented experimental information acquired from the measurements.

To summarize the findings, the HET's thrust decreased by 2.43 mN and 3.11% as the operation transitioned from the baseline to the one coil-off condition. The efficiency also decreased by 23.29%, peak-to-peak discharge current oscillations increased by 23.59%, and the magnetic field decreased by 9.65%. In the same way, the reduction of the magnetic field by 16.55% for two coil off condition resulted in a decrease of 2.73 mN and 3.49% in thrust, a 25.67% decrease in efficiency, and a 31.51% increase in the peak-to-peak discharge current oscillations.

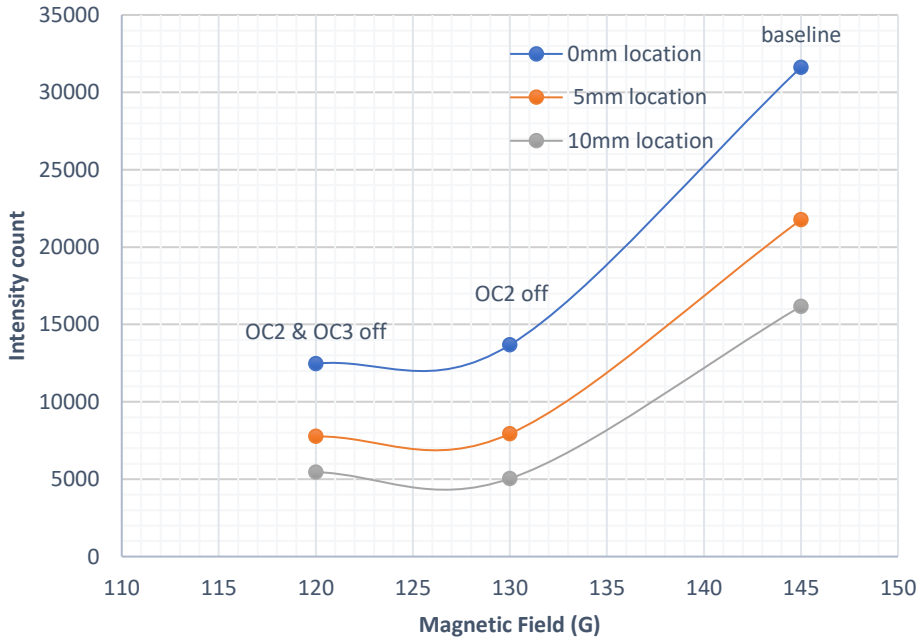

Figure 89 – Plume light intensity variation with decreasing magnetic field at 0 mm, 5 mm and 10 mm from thruster exit plane field at one coil off and two coils off condition synonymous conditions of test matrix1 at 300 V, 5.61 mg/s anode flow rate and 0.44 mg/s cathode flow rate as a function of magnetic field strength.

In light of the model established in Chapter 3, the magnetic field is a critical factor in the influence of the ionization and acceleration processes. As demonstrated in section 3.2.2, the impact of the magnetic field was translated into a change in plasma parameters and, consequently, the thruster's performance. The model now illustrates the impact of the azimuthal magnetic field on the performance parameters in the vicinity of the exit plane. The magnetic field experienced an azimuthal gradient due to the localized region's loss of magnetic field. The electron's confinement in the channel decreases as the electrons transition from the high uniform magnetic field region to a sectional lower magnetic field region as a result of the gradient's introduction in the HET channel. The lesser confinement of the electrons increases the electron flux in the gradient region. The reduction in confinement leads to a decrease in collision frequency, resulting in a decrease in ionization due to the reduced electron number density. Electrons undergo ohmic heating, leading to a decrease in temperature due to the decreased likelihood of ionization collisions. A decrease in the electron temperature results in a decrease in the energy possessed by the charged species, which leads to a less positive plasma potential at that location. Therefore, an azimuthal magnetic field gradient operating condition results in a non-uniform distribution of the electron number density and electron temperature in the channel. The electron temperature decreases along the collision frequency, leading to a decrease in the total energy the electrons acquire as they travel azimuthally. The decrease in energy causes the electron to travel upstream in the region of the azimuthal gradient to gather energy for ionization. This motion leads to a localized shift in the ionization acceleration region, which causes the region to move upstream towards the anode at the gradient's location.

The location of the ionization acceleration region is not uniform across the channel due to the azimuthal magnetic field gradient. The length of the acceleration region increases in the magnetic field gradient region due to the variations in the location of the ionization acceleration region. Consequently, the azimuthal gradient influences the ions, as they are now formed further upstream within the localized region. The loss voltage has increased as a result of the increased likelihood of wall collisions and neutralization collisions among the ions. The acceleration voltage decreases due to the increase in the loss voltage for a fixed discharge voltage. The decrease in acceleration voltage indicates a decrease in ion velocity, which causes a change in efficiency, specific impulse, and thrust. It is vital to note that an azimuthal magnetic field gradient influences plasma characteristics in the confined region and causes an overall decrease across the channel. The average integral of the energy distribution of the electron varies from the uniform magnetic field baseline condition as the electron transitions from the low magnetic field gradient region to the high magnetic field uniform region, resulting in reduced energy.

As observed, the introduction of an azimuthal magnetic field gradient leads to a reduction in current utilization efficiency, which has a significant impact on the thruster's stability, increasing discharge current oscillation. Further examination of the discharge current oscillation reveals that the electron motion can be characterized as a blend of thermal and kinetic energy. The kinetic energy of electrons increases, and thermal energy decreases as a result of a decrease in the magnetic field. In order to stabilize the discharge current oscillation, it is imperative to maintain the energy balance. The momentum transfer collision frequency decreases as the electrons propagate from the region of the high magnetic field to the low magnetic field, and the electron temperature decreases as a

consequence of reduced ohmic heating. This variation leads to non-uniformities throughout the channel during ionization collisions. The imbalance between Joules heating and the convection term associated with wall loss caused by enhanced oscillation increases as the electrons drift in the azimuthal and axial direction. A decrease in thermal energy indicates a decrease in ionization collision and an increase in atom excitation collision. Therefore, the azimuthal gradient results in a general decrease in the ion beam current, leading to a decrease in the efficiency of current utilization. Not only does the azimuthal gradient increase the mobility of electrons, but it also causes the gyroscopic frequency to fluctuate and increase in the region of the low magnetic field due to the variation of the magnetic field. The proper confinement of electrons in the axial and azimuthal directions is necessary to maintain or accomplish the stability of HET, as shown by discharge current oscillation. The reduction in electron confinement affects the frequency of ionization collisions, and electron generation near the anode results in a non-uniform length of the ionization acceleration area, resulting in variations in electron number density across the channel. The collision frequency and electron production rate influence the discharge current oscillation, resulting in the non-stable operation of HET, which attempts to maintain plasma discharge. The introduction of gradient has the most significant impact on discharge current oscillation, as the magnitude of the magnetic field significantly influences electron motion and collision processes.

The results presented emphasize the change in plasma parameters at the far field despite the azimuthal gradient resulting in the highest reduction in the magnitude of the magnetic field, which is 16.55% of the baseline magnetic. The model offers potential explanations for the processes taking place in the channel. The plume measurement serves

as evidence of the significant influence of in-channel non-uniformities. Thus, clearly establishing the impact of the azimuthal magnetic field gradient on thruster performance. The diagnostics discussed in section 4.4 were employed to conduct measurements to observe the far-field changes caused by the gradient. The experimental results demonstrated a reduction of 8.12% in electron temperature and a decrease of 5.09% in acceleration voltage compared to the baseline condition when one coil was turned off.

Additionally, there was a decrease of 12.90% in electron temperature and a decrease of 6.03% in acceleration voltage when two coils were turned off as seen in Figure 90. Examining the uncertainty linked to the Langmuir and RPA probe, there was a strong rationale for the capability to detect the impact of the azimuthal gradient on the plasma parameters. Figure 88 illustrates the model's validation of the thruster's efficiency in relation to the magnetic field. It is crucial to emphasize that the other magnetic circuit maintained sufficient operational stability to enable continuous thruster operation despite the thruster experiencing a decrease in stable operation due to the two coils in the circuit being off in the investigation.

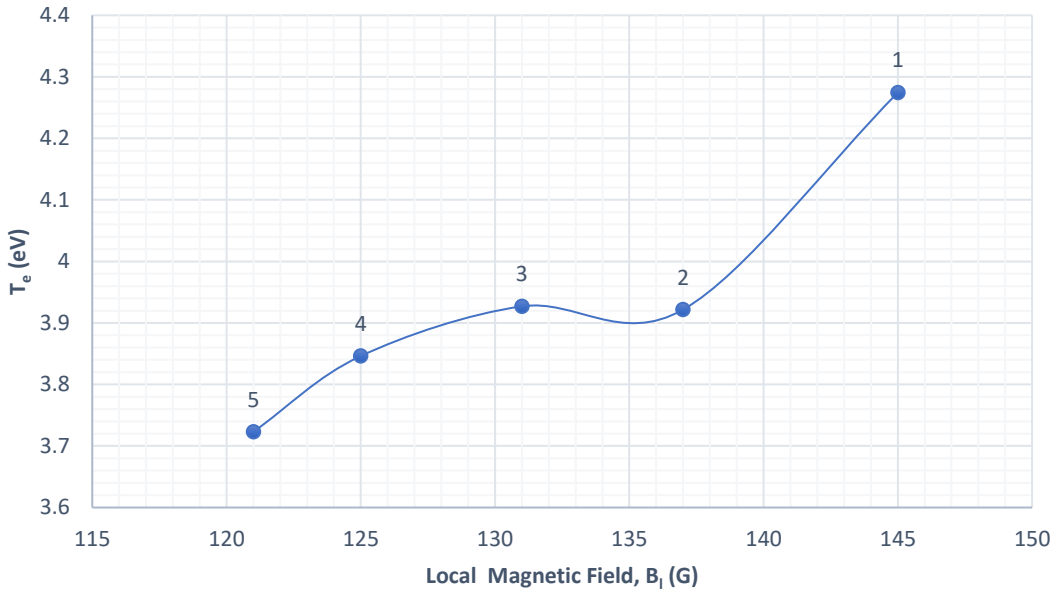

Figure 90 – Electron temperature variation as a function of local magnetic field for azimuthal magnetic field gradient test matrix 2 test conditions at 300 V, 5.61 mg/s anode flow rate and 0.44 mg/s cathode flow rate.

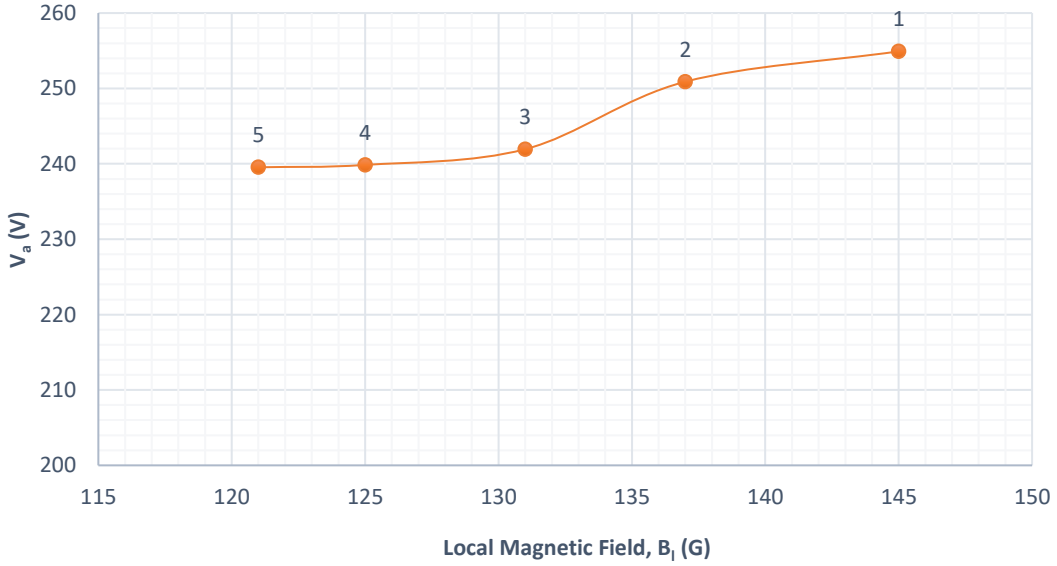

Figure 91 – Ion acceleration voltage variation as a function of local magnetic field for azimuthal magnetic field gradient test matrix 2 test conditions at 300 V, 5.61 mg/s anode flow rate, and 0.44 mg/s cathode flow rate.

The azimuthal magnetic field gradient influenced the thruster performance in terms of magnitude and the plume's orientation. We were able to monitor the position of the

maximum ion current collected by the sweeping Faraday probe by utilizing the three-dimensional measurement of the ion current density acquired through the custom-designed sweep probe apparatus. When a Faraday scan cannot pick up on the distinctive double peaks, the ion current density peak becomes a reliable substitute for them in finding the thrust vector[71]. Qualifying a thrust vector is an intricate process that requires using indirect measuring techniques to quantify the attributes associated with the thrust vector accurately. Plasma properties, including the ion beam current, are estimated to determine the location of the thrust vector. As a result of the indirect measurement techniques, it is necessary to make assumptions. It is presumed that the peak of the ion beam current density, which represents the maximum density present and provides the most significant contribution of the ions in the plume, represents the location of the thrust vector. Consequently, the experiment was conducted in the absence of a double peak. Table 52 displays the thrust vector's location for the baseline line condition and the varying azimuthal magnetic field gradient condition. Figure 92 illustrates the thrust vector position in a graphical format.

Table 52 – Thrust vector position for azimuthal magnetic field gradient test conditions at 300 V, 5.61 mg/s anode, and 0.44 mg/s cathode flow rates.

Test No.	Condition Name	B_l (G)	$\nabla_\theta B_r$ (G/°)	Horizontal (°)	Vertical (°)
1	baseline	145	0.00	0	4
2	gradient1	137	0.18	5	2
3	gradient2	131	0.31	5	3
4	gradient3	125	0.30	5	3
5	gradient4	121	0.36	5	1

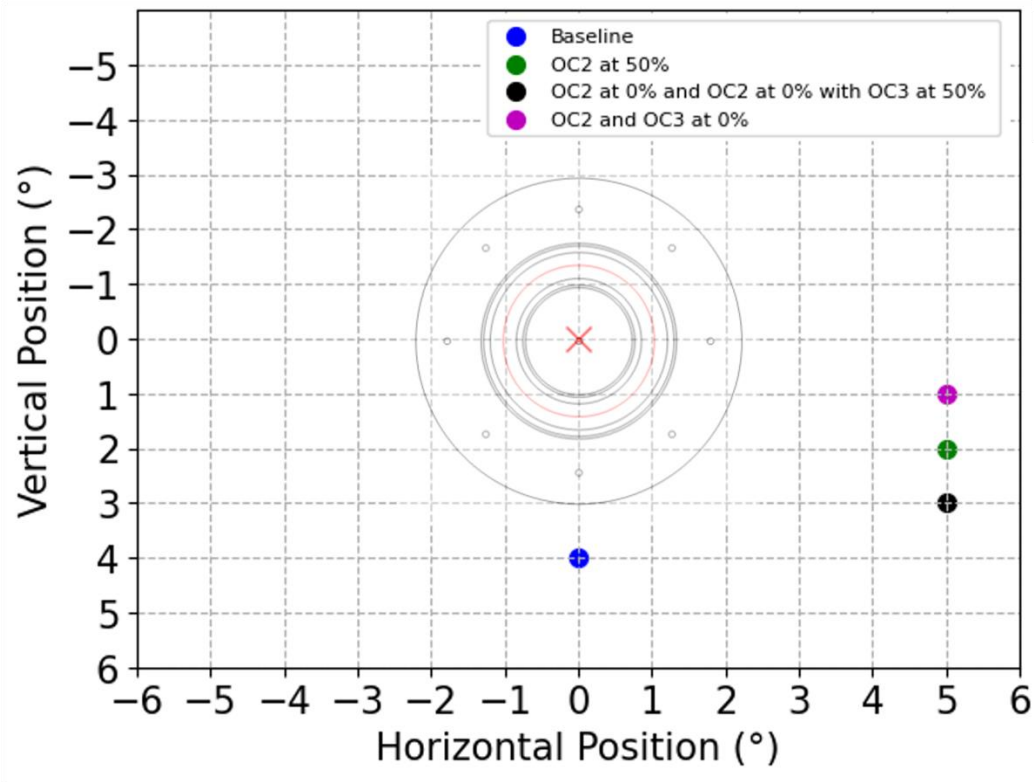

Figure 92 – Graphical representation of thrust vector position for azimuthal magnetic field gradient test conditions at 300 V, 5.61 mg/s anode flow rate and 0.44 mg/s cathode flow rate.

The thruster's inclination was measured during the installation process, and a vertically downward angular incline of 0.2° was determined. This inclination was 5% of the thruster vector value obtained for the baseline condition and, as a result, will be disregarded in the current analysis. The thrust vector for the baseline condition was determined to be 0° horizontally and 4° vertically downward. The two coils, independently actuated, were situated on the right side of the thruster when viewed from the front, as illustrated in Figure 16.The position of the thrust vector changed to 5° horizontally and 3° vertically when the OC2 circuit was off. The incorporation of azimuthal gradient in the magnetic field leads to a reduction in the frequency of ionization collisions. Furthermore, the alteration in length within the ionization acceleration region causes a decrease in the overall ion beam current observed during the scan conducted with the sweep probe

apparatus to measure ion current density. The ion current density peak was deviated due to the magnetic field lines passing through the inner coil being modified due to the OC2 circuit being turned off and tilted towards the outer coil rather than at the centerline location, which was probable for the magnetic field lines. As illustrated in Figure 93, this variation in the magnetic field topology was visible in the COMSOL simulation for the two extreme conditions. The change in the magnetic field line generates a deviation in the equipotential lines. The displacement of equipotential lines influences ion motion, causing the thrust vector to deviate in the direction of the area of the azimuthal gradient. The magnitude of the deviation is contingent upon the span/length of the gradient and the magnitude of the magnetic field. The OC2 and OC3 circuits being off corresponded to the two coils being turned off condition. It is evident that the presence of a 0.04 G/° higher gradient, as opposed to a single coil being off, caused a 2° vertical deviation in the thrust vector. The magnetic field experienced a greater magnitude decrease due to the additional coil's turning off. Additionally, the gradient was able to traverse a larger area, resulting in a fluctuation in the vertical position of the peak. After conducting experiments, it was also observed that the horizontal displacement of the thrust vector by 3° from the baseline condition led to an increase in erosion in the channel at the location of the azimuthal magnetic field gradient. As compared to the area of the channel containing a uniform magnetic field, the thickness of the channel at the site of gradient introduction decreased by 1mm during the 24-hour operation in a non-uniform magnetic field condition. The erosion in the channel resulted from the increase in ion beam current was observed in the gradient direction using the Sweep probe apparatus, which was substantiated by the increase in ion wall collisions.

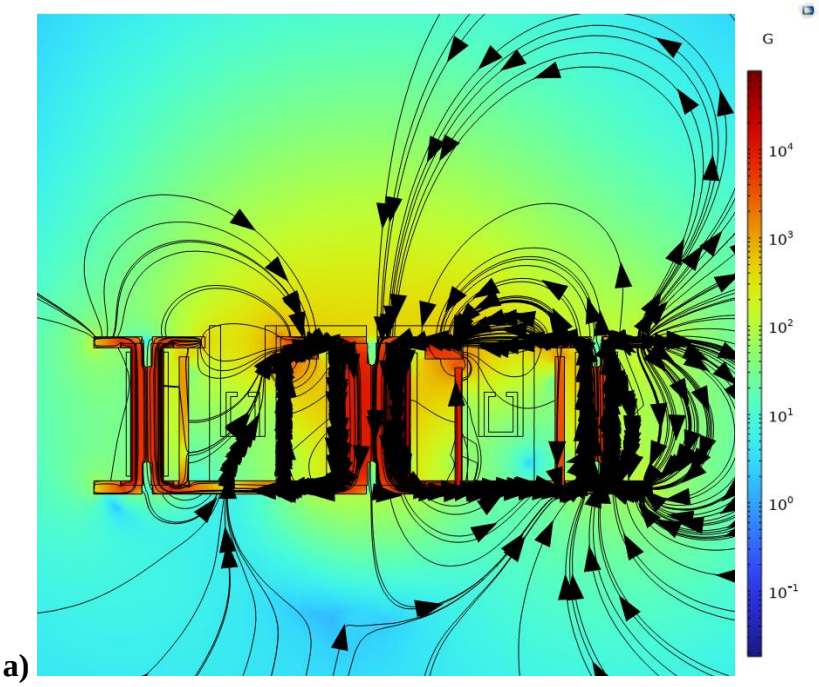

Figure 93 – COMSOL simulations of P5 magnetic field at a) one coil off condition b) two coils off condition showing tilt towards outer coil with increase in azimuthal gradient

6.2.2 Summary

This section presents the necessary evidence to validate the model shown in section 3.2.3, which illustrates the impact of the azimuthal magnetic field gradient on the thruster's performance. The quantification of the variation in the thruster performance and operation owing to the existence of the gradient was provided, answering the research question posed in the thesis. The thruster's efficacy and stability are reduced as the magnitude of the azimuthal magnetic field gradient in the HET channel increases, as indicated by the model. Upon the introduction of the azimuthal magnetic field, the thrust and efficacy decrease as a result of the impact of magnetic field non-uniformities on the electron motion, which in turn affects the associated ionization acceleration phenomena. The azimuthal magnetic field gradient has the most significant impact on the instability of the HET operation, which is characterized by the degree of oscillation in the discharge current. According to the model, this instability increases as the gradient's magnitude increases. Experimentally as well the azimuthal magnetic field gradient's presence had the greatest impact on the stable operation of the thruster and the least on the thrust it generated. In contrast to a 3.49% decrease in thrust, a 0.36 G/° gradient in the magnetic field leads to a 31.51% decrease in stability. As the magnitude of the azimuthal gradient of the magnetic field increased, the current utilization efficiency was the most significantly impacted and contributed significantly to the overall efficiency decrease.

CHAPTER 7 CONCLUSION AND FUTURE WORK

7.1 Conclusion and Contribution

The primary objective of the present study was to quantify the impact of incorporating an azimuthal magnetic field gradient on HET performance. To accomplish this objective, we divided the outer coil circuit into three segments: two independent coils and six coils connected in series. By deactivating the electrical current flowing through the separate coils, a magnetic field with a varied magnitude was created in the channel, resulting in an azimuthal gradient. The research aimed to address the following question:

"How does azimuthal magnetic field gradient affect Hall effect thruster performance and stability?"

It has been determined that a gradient in the azimuthal magnetic field reduces the performance of the HET. The current investigation yielded the subsequent findings:

1) According to the increase in the peak-to-peak percentage of discharge current oscillations, the gradient has the most significant impact on the stability of the HET. The thruster efficiency also decreased due to the gradient, while the thrust experienced the most negligible impact.

2) The exclusive development of the sweep probe apparatus for the current study facilitated the observation of the impact due to the non-uniformities by allowing for three-dimensional measurements of the plume. The significance of the current research question was underscored by our ability to provide experimental evidence

that the thrust vector, represented by the location of the highest ion current in the investigation, was displaced.

3) It is also important to note that the thruster continued to operate without shutting down, even though two coils were off, resulting in the peak-to-peak % of discharge current oscillations of 69.07%. This analysis offered a perspective on the close drift of electrons, which is a critical principle that should be employed in the development of thrusters to ensure that they operate reliably.

Through this study, we made a significant contribution to understanding the impact of non-uniformities in the azimuthal magnetic field gradient on the thruster's performance, specifically in terms of efficiency, thrust, and stability. Presence of an azimuthal magnetic field gradient in the channel leads to a localized drop in the magnetic field, affecting the electrons' mobility. The azimuthal magnetic field gradient induces an enhanced electron drift in both the azimuthal and axial directions. The aggregate kinetic energy increases due to the increased drift of electrons while the thermal energy of the electrons decreases. The ionization region moves upstream towards the anode as a result of the displacement of the ionization acceleration region caused by decrease in the thermal energy as indicated by the electron temperature. Ionization occurs near the anode as a consequence of the azimuthal magnetic field gradient, which leads to a decrease in the acceleration voltage observed by ions and an increase in wall losses. Therefore, the presence of an azimuthal gradient in the magnetic field leads to an increase in electron velocity and a decrease in the overall ion velocity, which consequently results in an increase in the discharge current oscillation and a decrease in the thrust provided by the thruster. In addition, the three-dimensional characterization of the P5 HET plume was another contribution of the current research.

This characterization offered a more precise depiction of the HET plume, serving as a versatile tool for measuring the plumes of individual thrusters and clusters of thrusters in the field of electric propulsion.

7.2 Future Work

Future work for this study entails measuring plasma parameters within the thruster channel to determine how local azimuthal magnetic field changes affect these parameters. The measurement conducted within the channel with a gradient will establish correlations between the recorded plasma properties and the far field measurements observed during changes in the magnetic field. Another aspect that requires to be verified is usage of non-invasive measurement techniques to provide more accurate measurements regarding the variation of plasma properties inside the channel. These techniques will allow us to verify the displacement of ionization acceleration region due to the introduction of azimuthal magnetic field gradient. Observing the impact to a greater extent is possible by introducing a higher magnitude of the gradient, which can result in the HET operating at its maximal gradient. Future studies will be critical in qualifying thrusters for space flights by the commercial sector, which produces large quantities of thrusters.

Another aspect of future work related to the investigation is to improve the sweep probe device. This improvement will enable readings at a faster velocity, which is crucial for real-time data analysis. Using the enhanced sweep probe apparatus for centrally mounted and externally mounted cathodes will show how cathode position affects plume characterization and demonstrate the benefits of centrally mounted cathodes, which EP research is promoting. Additionally, employing the improved sweep probe apparatus to

investigate cluster orientation and configuration would significantly enhance the precision of measurement capabilities for the evaluation of thrust and efficiency in commercially deployed cluster configurations, leading to more efficient and reliable plasma propulsion systems.

REFERENCES

[1] Vilela Salgado, M. C., Belderrain, C. M. N., and Devezas, T. C., "Space Propulsion: A Survey Study About Current and Future Technologies," *Journal of Aerospace Technology and Management*, Vol. 10, 2018. https://doi.org/10.5028/jatm.v10.829

[2] Thapa, R., "Evolution in Propellant of the Rocket Engine," *Journal of Materials Physics and Chemistry*, Vol. 11, No. 1, 2023, pp. 8–21. https://doi.org/10.12691/jmpc-11-1-2

[3] Boeuf, J.-P., "Tutorial: Physics and Modeling of Hall Thrusters," *Journal of Applied Physics*, Vol. 121, No. 1, 2017, p. 011101. https://doi.org/10.1063/1.4972269

[4] Greatrix, D., Leyva, I., Pastrone, D., Sanal Kumar, V., and Smart, M., "Chemical Rocket Propulsion," *International Journal of Aerospace Engineering*, Vol. 2012, 2012, pp. 1–2. https://doi.org/10.1155/2012/715706

[5] Mahjub, A., Mazlan, N. M., Abdullah, M. Z., and Azam, Q., "Design Optimization of Solid Rocket Propulsion: A Survey of Recent Advancements," *Journal of Spacecraft and Rockets*, Vol. 57, No. 1, 2020, pp. 3–11. https://doi.org/10.2514/1.A34594

[6] Trache, D., Klapötke, T. M., Maiz, L., Abd-Elghany, M., and DeLuca, L. T., "Recent Advances in New Oxidizers for Solid Rocket Propulsion," *Green Chemistry*, Vol. 19, No. 20, 2017, pp. 4711–4736. https://doi.org/10.1039/C7GC01928A

[7] Jens, E. T., Cantwell, B. J., and Hubbard, G. S., "Hybrid Rocket Propulsion Systems for Outer Planet Exploration Missions," *Acta Astronautica*, Vol. 128, 2016, pp. 119–130. https://doi.org/10.1016/j.actaastro.2016.06.036

[8] Mazouffre, S., "Electric Propulsion for Satellites and Spacecraft: Established Technologies and Novel Approaches," *Plasma Sources Science and Technology*, Vol. 25, No. 3, 2016, p. 033002. https://doi.org/10.1088/0963-0252/25/3/033002

[9] Lev, D., Myers, R. M., Lemmer, K. M., Kolbeck, J., Koizumi, H., and Polzin, K., "The Technological and Commercial Expansion of Electric Propulsion," *Acta Astronautica*, Vol. 159, 2019, pp. 213–227. https://doi.org/10.1016/j.actaastro.2019.03.058

[10] O'Reilly, D., Herdrich, G., and Kavanagh, D. F., "Electric Propulsion Methods for Small Satellites: A Review," *Aerospace*, Vol. 8, No. 1, 2021, p. 22. https://doi.org/10.3390/aerospace8010022

[11] Potrivitu, G.-C., Sun, Y., Rohaizat, M. W. A. B., Cherkun, O., Xu, L., Huang, S., and Xu, S., "A Review of Low-Power Electric Propulsion Research at the Space Propulsion Centre Singapore," *Aerospace*, Vol. 7, No. 6, 2020, p. 67. https://doi.org/10.3390/aerospace7060067

[12] Jahn, R. G., "Physics of Electric Propulsion," Dover Publication, Mineola, NY, 2006.

[13] Goebel, D. M., and Katz, I., "Fundamentals of Electric Propulsion: Ion and Hall Thrusters."

[14] Wollenhaupt, B., Le, Q. H., and Herdrich, G., "Overview of Thermal Arcjet Thruster Development," *Aircraft Engineering and Aerospace Technology*, Vol. 90, No. 2, 2018, pp. 280–301. https://doi.org/10.1108/AEAT-08-2016-0124

[15] Smith, P., "Resistojet Thruster Design and Development Programme," presented at the 42nd AIAA/ASME/SAE/ASEE Joint Propulsion Conference & Exhibit, Sacramento, California, 2006. https://doi.org/10.2514/6.2006-5210

[16] Chelem Mayigué, C., Kühn, C., and Groll, R., "Performance Investigation of an Argon Fueled Magnetoplasmadynamic Thruster with Applied Magnetic Field," *Journal of Applied Physics*, Vol. 124, No. 22, 2018, p. 223301. https://doi.org/10.1063/1.5038421

[17] Wu, Z., Huang, T., Liu, X., Ling, W. Y. L., Wang, N., and Ji, L., "Application and Development of the Pulsed Plasma Thruster," *Plasma Science and Technology*, Vol. 22, No. 9, 2020, p. 094014. https://doi.org/10.1088/2058-6272/aba7ac

[18] Bapat, A., Salunkhe, P. B., and Patil, A. V., "Hall-Effect Thrusters for Deep-Space Missions: A Review," *IEEE Transactions on Plasma Science*, Vol. 50, No. 2, 2022, pp. 189–202. https://doi.org/10.1109/TPS.2022.3143032

[19] Magaldi, B., Karnopp, J., Da Silva Sobrinho, A., and Pessoa, R., "A Global Model Study of Plasma Chemistry and Propulsion Parameters of a Gridded Ion Thruster Using Argon as Propellant," *Plasma*, Vol. 5, No. 3, 2022, pp. 324–340. https://doi.org/10.3390/plasma5030025

[20] Jovel, D., "Impedance Characterizatioon of Hall Effect Thruster Discharge in a Ground-Based Vaccum Test Facility," Georgia Institute of Technology, Atlanta, 2024.

[21] Choueiri, E., "A Critical History of Electric Propulsion: The First Fifty Years (1906-1956)," presented at the 40th AIAA/ASME/SAE/ASEE Joint Propulsion Conference and Exhibit, Fort Lauderdale, Florida, 2004. https://doi.org/10.2514/6.2004-3334

[22] Hofer, R. R., "Development and Characterization of High-Efficiency, High-Specific Impulse Xenon Hall Thrusters," Ph.D. University of Michigan, 2004.

[23] Jacobson, D., Manzella, D., Hofer, R., and Peterson, P., "NASA's 2004 Hall Thruster Program," presented at the 40th AIAA/ASME/SAE/ASEE Joint Propulsion Conference and Exhibit, Fort Lauderdale, Florida, 2004. https://doi.org/10.2514/6.2004-3600

[24] Brown, D. L., "Investigation of low discharge voltage hall thruster characteristics and evaluation of loss mechanisms.",Ph.D. Dissertation, University of Michigan,2009

[25] Goebel, D. M., Hofer, R. R., Mikellides, I. G., Katz, I., Polk, J. E., and Dotson, B. N., "Conducting Wall Hall Thrusters," *IEEE Transactions on Plasma Science*, Vol. 43, No. 1, 2015, pp. 118–126. https://doi.org/10.1109/TPS.2014.2321110

[26] Chhavi, C., and Walker, M. L. R., "Review of Non-Conventional Hall Effect Thrusters," *Journal of Electric Propulsion*, Vol. 3, No. 1, 2024, p. 11. https://doi.org/10.1007/s44205-024-00073-2

[27] Pérez Grande, D., "Fluid Modeling and Simulation of the Electron Population in Hall Effect Thrusters with Complex Magnetic Topologies," Ph.D. Dpto. de Bioingenería e Ingeniería Aeroespacial Escuela Politécnica Superior, 2018.

[28] Tahara, H., Goto, D., Yasui, T., and Yoshikawa, T., "Thrust Performance and Plasma Characteristics of Low Power Hall Thrusters," presented at the 27th International Electric Propulsion Conference, Pasedena, 2001.

[29] Xia, G., Liu, X., Li, H., Ding, Y., Wei, L., Chen, S., and Yu, D., "Performance Improvement of Hall Thrusters with High Discharge Voltage," *Vacuum*, Vol. 172, 2020, p. 109052. https://doi.org/10.1016/j.vacuum.2019.109052

[30] Ding, Y., Li, P., Zhang, X., Wei, L., Sun, H., Peng, W., and Yu, D., "Effects of the Magnetic Field Gradient on the Wall Power Deposition of Hall Thrusters," *Journal of Plasma Physics*, Vol. 83, No. 2, 2017, p. 905830205. https://doi.org/10.1017/S0022377817000241

[31] Morozov, A. I., Esipchuk, Y. V., Kapulkin, A. M., Nevrovskii, V. A., and Smirnov, V. A., "Effect of the magnetic field on a closed-electron-drift accelerator.," *Sov. Phys.-Tech. Phys. (Engl. Transl.) 17: No. 3, 482-7(Sep 1972).*, 1972. Retrieved 6 April 2024. https://www.osti.gov/biblio/4654554

[32] Gao, Y., Wang, W., Xue, S., Li, Y., and Cai, G., "Influence of the Upstream Axial Magnetic Mirror Field on the Plume Characteristics in the Full Cylindrical Hall Thruster," *Acta Astronautica*, Vol. 196, 2022, pp. 186–193. https://doi.org/10.1016/j.actaastro.2022.04.018

[33] Jiang, Y., Tang, H., Ren, J., Li, M., and Cao, J., "Magnetic Mirror Effect in a Cylindrical Hall Thruster," *Journal of Physics D: Applied Physics*, Vol. 51, No. 3, 2018, p. 035201. https://doi.org/10.1088/1361-6463/aa9e3e

[34] Keidar, M., and Boyd, I. D., "On the Magnetic Mirror Effect in Hall Thrusters," *Applied Physics Letters*, Vol. 87, No. 12, 2005, p. 121501. https://doi.org/10.1063/1.2053351

[35] Daren, Y., Hui, L., and Haiyang, F., "Effect of Magnetic Mirror on the Asymmetry of the Radial Profile of Near-Wall Conductivity in Hall Thrusters," *Plasma Science and Technology*, Vol. 11, No. 3, 2009, pp. 1–7. https://doi.org/10.1088/1009-0630/11/3/13

[36] Mahalingam, S., and Menart, J. A., "Particle-Based Plasma Simulations for an Ion Engine Discharge Chamber," *Journal of Propulsion and Power*, Vol. 26, No. 4, 2010, pp. 673–688. https://doi.org/10.2514/1.45954

[37] Brieda, L., Keidar, M., Raitses, Y., and Fisch, N., "Investigation of Electron Transport in a Cylindrical Hall Thruster Using a Kinetic Code," presented at the 45th AIAA/ASME/SAE/ASEE Joint Propulsion Conference & Exhibit, Denver, Colorado, 2009. https://doi.org/10.2514/6.2009-4811

[38] Liu, H., Wu, B., Yu, D., Cao, Y., and Duan, P., "Particle-in-Cell Simulation of a Hall Thruster," *Journal of Physics D: Applied Physics*, Vol. 43, No. 16, 2010, p. 165202. https://doi.org/10.1088/0022-3727/43/16/165202

[39] Liu, J., Li, H., Hu, Y., Liu, X., Ding, Y., Wei, L., Yu, D., and Wang, X., "Particle-in-cell Simulation of the Effect of Curved Magnetic Field on Wall Bombardment and Erosion in a Hall Thruster," *Contributions to Plasma Physics*, Vol. 59, No. 8, 2019, p. e201800001. https://doi.org/10.1002/ctpp.201800001

[40] Szabo, J., and Joseph, J., "Fully Kinetic Numerical Modeling of a Plasma Thruster," Ph.D. Massachusetts Institute of Technology, 2005.

[41] Kornberg, O., "Investigation of Magnetic Field Profile Effects in Hall Thrusters," Master of Science. Embry-Riddle Aeronautical University - Daytona Beach, 2007.

[42] Peterson, P., Gallimore, A., and Haas, J., "Experimental Investigation of Hall Thruster Interal Magnetic Field Topography," *37th Joint Propulsion Conference and Exhibit*, American Institute of Aeronautics and Astronautics. https://doi.org/10.2514/6.2001-3890

[43] Harvey, M. L., "The Effect of the 2-Dimensional Magnetic Field Profile in Hall Thrusters," Master of Science. Embry-Riddle Aeronautical University - Daytona Beach, 2014.

[44] Yang, L., Wang, P. Y., and Wang, T., "Study on the Influence of Magnetic Field on the Performance of a 5 kW Hall Thruster," *Frontiers in Materials*, Vol. 10, 2023, p. 1150802. https://doi.org/10.3389/fmats.2023.1150802

[45] Garrigues, L., Hagelaar, G. J. M., Bareilles, J., Boniface, C., and Boeuf, J. P., "Model Study of the Influence of the Magnetic Field Configuration on the Performance and

Lifetime of a Hall Thruster," *Physics of Plasmas*, Vol. 10, No. 12, 2003, pp. 4886–4892. https://doi.org/10.1063/1.1622670

[46] Fan, H., Xu, Y., Wang, L., Wei, L., Li, H., Guo, N., and Ding, Y., "Effects of Unsymmetrical Magnetic Field on Discharge Characteristics of Hall Thruster with Large Height-Radius Ratio," *Vacuum*, Vol. 203, 2022, p. 111261. https://doi.org/10.1016/j.vacuum.2022.111261

[47] Komurasaki, K., and Arakawa, Y., "Hall Current Ion-Thruster Performance," *Journal of Propulsion and Power*, Vol. 8, No. 6, 1992, pp. 1212–1216. https://doi.org/10.2514/3.11464

[48] Kim, V., "Main Physical Features and Processes Determining the Performance of Stationary Plasma Thrusters," *Journal of Propulsion and Power*, Vol. 14, No. 5, 1998, pp. 736–743. https://doi.org/10.2514/2.5335

[49] Hofer, R., and Jankovsky, R., "A Hall Thruster Performance Model Incorporating the Effects of a Multiply-Charged Plasma," presented at the 37th Joint Propulsion Conference and Exhibit, Salt Lake City,UT,U.S.A., 2001. https://doi.org/10.2514/6.2001-3322

[50] Andrenucci, M., Battista, F., and Piliero, P., "Hall Thruster Scaling Methodology," presented at the The 29th International Electric Propulsion Conference, Princeton University, 2005.

[51] Garrigues, L., Boyd, I. D., and Boeuf, J. P., "Computation of Hall Thruster Performance," *Journal of Propulsion and Power*, Vol. 17, No. 4, 2001, pp. 772–779. https://doi.org/10.2514/2.5832

[52] Boyd, I. D., "Review of Hall Thruster Plume Modeling," *Journal of Spacecraft and Rockets*, Vol. 38, No. 3, 2001, pp. 381–387. https://doi.org/10.2514/2.3695

[53] Taccogna, F., and Garrigues, L., "Latest Progress in Hall Thrusters Plasma Modelling," *Reviews of Modern Plasma Physics*, Vol. 3, No. 1, 2019, p. 12. https://doi.org/10.1007/s41614-019-0033-1

[54] Ahedo, E., and Escobar, D., "Influence of Design and Operation Parameters on Hall Thruster Performances," *Journal of Applied Physics*, Vol. 96, No. 2, 2004, pp. 983–992. https://doi.org/10.1063/1.1759790

[55] Hofer, R., Katz, I., Goebel, D., Jameson, K., Sullivan, R., Johnson, L., and Mikellides, I., "Efficacy of Electron Mobility Models in Hybrid-PIC Hall Thruster Simulations," presented at the 44th AIAA/ASME/SAE/ASEE Joint Propulsion Conference & Exhibit, Hartford, CT, 2008. https://doi.org/10.2514/6.2008-4924

[56] King, D., De Grys, K., and Jankovsky, R., "Multi-Mode Hall Thruster Development," presented at the 37th Joint Propulsion Conference and Exhibit, Salt Lake City,UT,U.S.A., 2001. https://doi.org/10.2514/6.2001-3778

[57] Dannenmayer, K., and Mazouffre, S., "Elementary Scaling Laws for the Design of Low and High Power Hall Effect Thrusters," presented at the Progress in Propulsion Physics, Versailles, France, 2011. https://doi.org/10.1051/eucass/201102601

[58] Ferreira, J. L., Martins, A. A., Miranda, R., Schelling, A., Alves, L. D. S., Costa, E. G., Junior, H. D. O. C., Branco, A. C., and Lopes, F. N. D. O., "Permanent Magnet Hall Thrusters Development and Applications on Future Brazilian Space Missions," *Journal of Physics: Conference Series*, Vol. 641, 2015, p. 012016. https://doi.org/10.1088/1742-6596/641/1/012016

[59] Thomas, C., Sommier, E., Gascon, N., and Cappelli, M., "The Magnetic Interference Hall Accelerator," presented at the 42nd AIAA/ASME/SAE/ASEE Joint Propulsion Conference & Exhibit, Sacramento, California, 2006. https://doi.org/10.2514/6.2006-4993

[60] Hofer, R., Peterson, P., Gallimore, A., and Jankovsky, R., "A High Specific Impulse Two-Stage Hall Thruster with Plasma Lens Focusing," presented at the the 27th International Electric Propulsion Conference, Pasadena, CA, 2001.

[61] Pote, B., Hruby, V., and Tedrake, R., "Performance of a Multi-Kilowatt Non-Circular Discharge Hall Thruster," presented at the 36th AIAA/ASME/SAE/ASEE Joint Propulsion Conference and Exhibit, Las Vegas,NV,U.S.A., 2000. https://doi.org/10.2514/6.2000-3249

[62] "Pseudo Linear Hall Effect Thruster Characterization through Potential, Magnetic, and Optical Measurements," Ph.D. Dissertation. Department of Aeronautics and Astronautics, Air Force Institute of Technology., 2018.

[63] Lazurenko, A., Kim, V., Bishaev, A., and Auweter-Kurtz, M., "Three-Dimensional Simulation of Atom and Ion Dynamics in a Stationary Plasma Thruster," *Journal of Applied Physics*, Vol. 98, No. 4, 2005, p. 043303. https://doi.org/10.1063/1.2009821

[64] Mazouffre, S., Bourgeois, G., Vaudolon, J., Garrigues, L., Hénaux, C., Harribey, D., Vilamot, R., Rossi, A., Zurbach, S., and Le Méhauté, D., "Development and Testing of Hall Thruster with Flexible Magnetic Field Configuration," *Journal of Propulsion and Power*, Vol. 31, No. 4, 2015, pp. 1167–1174. https://doi.org/10.2514/1.B35417

[65] Yamamoto, N., Komurasaki, K., and Arakawa, Y., "Erratum for 'Discharge Current Oscillation in Hall Thrusters,'" *Journal of Propulsion and Power*, Vol. 22, No. 2, 2006, pp. 478–478. https://doi.org/10.2514/1.22410

[66] Choueiri, E. Y., "Plasma Oscillations in Hall Thrusters," *Physics of Plasmas*, Vol. 8, No. 4, 2001, pp. 1411–1426. https://doi.org/10.1063/1.1354644

[67] Dutra, E. C., Koch, J. A., Presura, R., Wiewior, P., and Covington, A. M., "Electron Temperature and Electron Number Density Measurements in Laser Ablation Z-Pinch Experiments of Al2O3," *Physics of Plasmas*, Vol. 26, No. 8, 2019, p. 083506. https://doi.org/10.1063/1.5081152

[68] Baranov, V. I., Nazarenko, Yu. S., Petrosov, V. A., Vasin, A. I., and Yashnov, Yu. M., "Energy balance and role of walls in ACDE," presented at the International Electric Propulsion Conference, 1997.

[69] Gulczinski, Frank, "Examination of the structure and evolution of ion energy properties of a 5 kW class laboratory Hall effect thruster at various operational conditions," University of Michigan, 1999.

[70] Haas, J. M., and Gallimore, A. D., "Internal Plasma Potential Profiles in a Laboratory-Model Hall Thruster," *Physics of Plasmas*, Vol. 8, No. 2, 2001, pp. 652–660. https://doi.org/10.1063/1.1338535

[71] Benavides, G. F., Mackey, J., Ahern, D., and Thomas, R., "Diagnostic for Verifying the Thrust Vector Requirement of the AEPS Hall-Effect Thruster and Comparison to the NEXT-C Thrust Vector Diagnostic," presented at the 2018 Joint Propulsion Conference, Cincinnati, Ohio, 2018. https://doi.org/10.2514/6.2018-4514

[72] Sohl, G., and Fosnight, V. V., "Thrust Vectoring of Ion Engines.," *Journal of Spacecraft and Rockets*, Vol. 6, No. 2, 1969, pp. 143–147. https://doi.org/10.2514/3.29552

[73] HOMA, J., and WILBUR, P., "Ion Beamlet Vectoring by Grid Translation," *16th International Electric Propulsion Conference*, American Institute of Aeronautics and Astronautics. https://doi.org/10.2514/6.1982-1895

[74] Van Reijen, B., Weis, S., Lazurenko, A., Haderspeck, J., Genovese, A., Holtmann, P., Ruf, K., and Püttmann, N., "High Precision Thrust Vector Determination through Full Hemispherical RPA Measurements Assisted by Angular Mapping of Ion Energy Charge State Distribution," 2013.

[75] Pollard, J., and Welle, R., "Thrust Vector Measurements with the T5 Ion Engine," *31st Joint Propulsion Conference and Exhibit*, American Institute of Aeronautics and Astronautics. https://doi.org/10.2514/6.1995-2829

[76] Polk, J., Anderson, J., and Brophy, J., "Behavior of the Thrust Vector in the NSTAR Ion Thruster," *34th AIAA/ASME/SAE/ASEE Joint Propulsion Conference and Exhibit*, American Institute of Aeronautics and Astronautics. https://doi.org/10.2514/6.1998-3940

[77] Brown, D. L., Walker, M. L. R., Szabo, J., Huang, W., and Foster, J. E., "Recommended Practice for Use of Faraday Probes in Electric Propulsion Testing," *Journal of Propulsion and Power*, Vol. 33, No. 3, 2017, pp. 582–613. https://doi.org/10.2514/1.B35696

[78] "Electrical Facility Effects on Faraday Probe Measurements." https://doi.org/10.2514/1.B36467

[79] Brown, D. L., and Gallimore, A. D., "Evaluation of Facility Effects on Ion Migration in a Hall Thruster Plume," 2011. https://doi.org/10.2514/1.54143

[80] Xu, K. G., "Ion Collimation and In-Channel Potential Shaping Using in-Channel Electrodes for Hall Effect Thrusters," 2012. Retrieved 31 March 2024. http://hdl.handle.net/1853/44830

[81] Lobbia, R. B., and Beal, B. E., "Recommended Practice for Use of Langmuir Probes in Electric Propulsion Testing," *Journal of Propulsion and Power*, Vol. 33, No. 3, 2017, pp. 566–581. https://doi.org/10.2514/1.B35531

[82] King, L., "Transport-Property and Mass Spectral Measurements in the Plasma Exhuast Plume of a Hall-Effect Space Propulsion System," Ph.D. Dissertation. University of Michigan, Ann Arbor, 1998.

[83] Xu, K. G., and Walker, M. L. R., "High-Power, Null-Type, Inverted Pendulum Thrust Stand," *Review of Scientific Instruments*, Vol. 80, No. 5, 2009, p. 055103. https://doi.org/10.1063/1.3125626

[84] Pagnon, D., Lasgorceix, P., and Touzeau, M., "Control of the Ceramic Erosion by Optical Emission Spectroscopy: Results of PPS1350-G Measurements," Vol. 555, 2004, p. 23.1.